e-ISSN 2149-6366

Cilt 11, Sayı 4, Aralık 2022

Volume 11, Issue 4, December 2022

TDFD
TÜRK DOĞA ve FEN DERGİSİ

TURKISH JOURNAL OF NATURE AND SCIENCE

TJNS

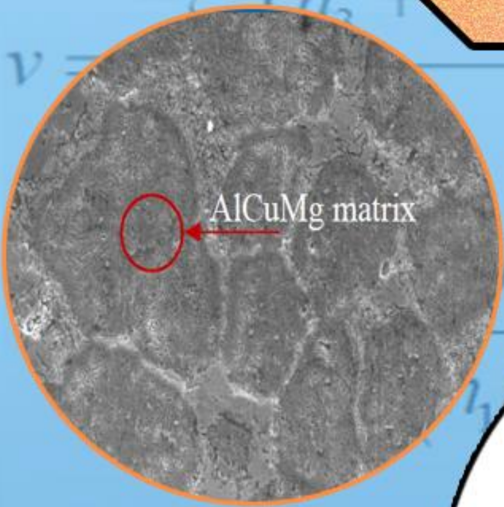

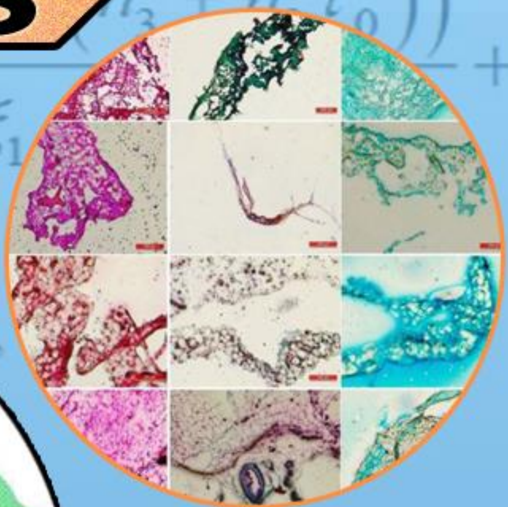

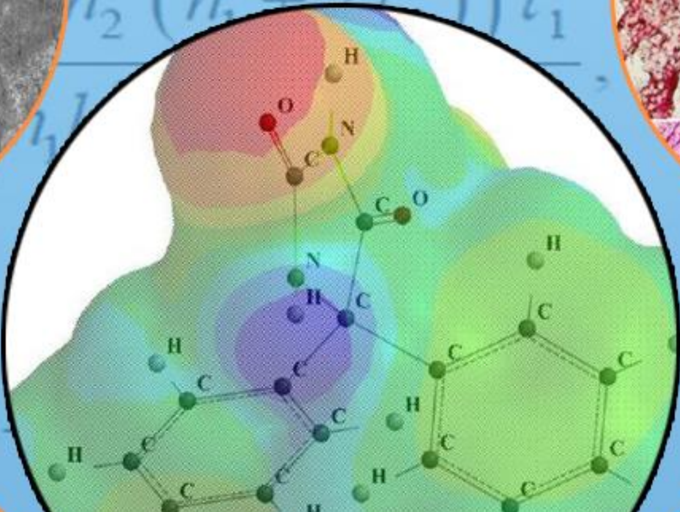

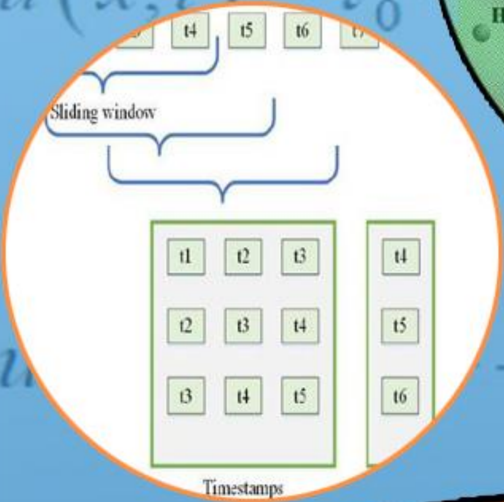

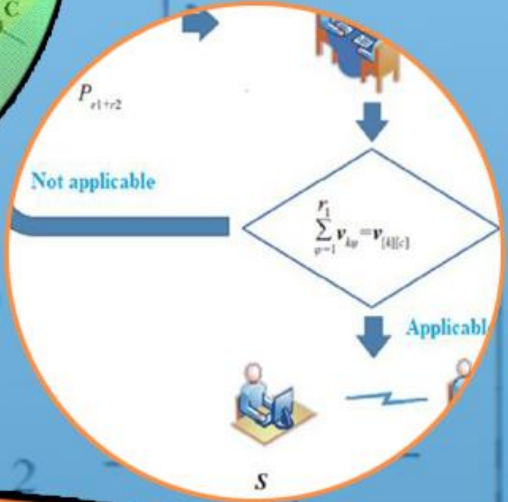

www.dergipark.gov.tr/tdfd

Bingöl Üniversitesi Fen Bilimleri Enstitüsü tarafından yayımlanmaktadır.

Published by Bingol University Institute of Science

TÜRK DOĞA VE FEN DERGİSİ

Amaç

Türk Doğa ve Fen Dergisi, Dergipark tarafından yayınlanan Bingöl Üniversitesi Fen Bilimleri Enstitüsüne ait ulusal ve hakemli bir dergidir. Türk Doğa ve Fen Dergisi, Türkiye ve dünyanın her yerinden gelen doğa ve fen bilimlerinin her alanında özgün, yayımlanmamış, yayımlanmak üzere başka yere gönderilmemiş makale, derleme ve sempozyum değerlendirmesi gibi çalışmaların bilim alemine sunulması amacıyla kurulmuştur.

Kapsam

Türk Doğa ve Fen Dergisinde Mühendislik, Ziraat, Veterinerlik, Fen ve Doğa Bilimleri alanlarından olmak üzere Türkçe ve İngilizce hazırlanmış orijinal makale, derleme ve sempozyum değerlendirmesi gibi çalışmalar yayımlanır. Türk Doğa ve Fen Dergisi sadece online sistemde yayınlanmakta olup ayrıca kağıt baskısı bulunmamaktadır.

Merhaba…

Türk Doğa ve Fen Dergisi, Dergipark tarafından yayınlanmakta olup Bingöl Üniversitesi Fen Bilimleri Enstitüsüne aittir. Bahar ve güz dönemi olmak üzere yılda iki defa çıkarılan ulusal hakemli bir dergi olarak ilk sayısını 2012 bahar döneminde yayımlamıştır. Türk Doğa ve Fen Dergisi, Türkiye ve dünyanın her yerinden gelen doğa ve fen bilimlerinin her alanında özgün, yayımlanmamış, yayımlanmak üzere başka yere gönderilmemiş makale, derleme ve sempozyum değerlendirmesi gibi çalışmaların bilim alemine sunulması amacıyla kurulmuştur. İlk sayısından bugüne kesintisiz olarak faaliyetlerini sürdürmektedir.

Türk Doğa ve Fen Dergisi sadece online sistemde yayınlanmakta olup ayrıca kağıt baskısı bulunmamaktadır. Dergimize gelen her çalışma öncelikle Turnitin intihal programında taranmaktadır. Dergimizde editörlerin, hakemlerin ve yazarların, uluslararası yayım etik kurallarına uyması ve makalelerin yazım kurallarına uyumlu olması zorunluluğu vardır.

Yazarlar yayımlanmak üzere dergimize gönderdikleri çalışmaları ile ilgili telif haklarını zorunlu olarak Bingöl Üniversitesi Türk Doğa ve Fen Dergisi'ne devretmiş sayılırlar. Yazarlardan herhangi bir ücret talep edilmemektedir. Yazarların değerlendirmeleri, dergimizin resmi görüşü olarak kabul edilemez. Çalışmaların her türlü sorumluluğu yazarlarına aittir. Araştırma ürünleri için etik kurul raporu gerekli ise, çalışma üzerinde bu raporun alınmış olduğu belirtilmeli ve kurul raporu sisteme kaydedilmelidir. Araştırma ile ilgili intihal, atıf manipülasyonu, sahte veri uydurma vb. suistimallerin tespit edilmesi halinde yayım ve etik ilkelerine göre davranılır. Bu durumda çalışmanın yayımlanmasını önlemek, yayımdan kaldırmak ya da başka işlemler yapmak için gerekli işlemler takip edilmektedir.

Dergimizde, kaynak gösteriminde uluslararası Vancouver sistemine geçilmiştir. Ayrıca dergimiz, Creative Commons ile lisanslanmak suretiyle dergimizde yayımlanan makalelerin paylaşımı, kaynak gösterimi ve yayımlanmasında dergi ve yazar haklarını korumaya almıştır. 2018 yılı güz döneminden itibaren makaleler, uluslararası yazar kimlik numarası ORCID No'su ile yayımlanmaktadır.

Dergi ekibi, dergimizin ulusal ve uluslararası indekslerce taranan bir dergi olması yönünde çalışmalarını titizlikle sürdürmektedir. Dergimize gösterilen ilgi bu yönde bizleri teşvik etmeye devam edecektir.

Bingöl Üniversitesi Fen Bilimleri Enstitüsü tarafından yayımlanmaktadır

Prof. Dr. Zafer ŞİAR

Bingöl Üniversitesi, Fen-Edebiyat Fakültesi, Matematik Bölümü
E-Mail: zsiar@bingol.edu.tr

Prof. Dr. Uğur ÇAKILCIOĞLU

Munzur Üniversitesi, Pertek Sakine Genç Meslek Yüksekokulu, Bitki Morfolojisi ve Anatomisi Bölümü
E-Mail: ucakilcioglu@yahoo.com

Doç. Dr. Kamuran DİLSİZ

Bingöl Üniversitesi, Fen-Edebiyat Fakültesi, Fizik Bölümü
E-Mail: kdilsiz@bingol.edu.tr

Doç. Dr. Şükran KONCA

Bakırçay Üniversitesi, Mühendislik ve Mimarlık Fakültesi, Temel Bilimler, Matematik Bölümü
E-Mail: sukran.konca@bakircay.edu.tr

Doç. Dr. İdris YAZGAN

Kastamonu Üniversitesi, Fen Edebiyat Fakültesi, Biyoloji

E-Mail: idrisyazgan@gmail.com

Doç. Dr. Abdulcabbar YAVUZ

Gaziantep Üniversitesi, Mühendislik Fakültesi, Metalurji ve Malzeme Mühendisliği
E-Mail: ayavuz@gantep.edu.tr

Doç. Dr. Bünyamin ALIM

Bayburt Üniversitesi, Teknik Bilimler Meslek Yüksekokulu, Elektrik ve Enerji Bölümü
E-Mail: balim@bayburt.edu.tr

Dr. Öğr. Üyesi Mustafa Şükrü KURT

Erzurum Teknik Üniversitesi, Fen Fakültesi, Temel Bilimler
E-Mail: mustafa.kurt@erzurum.edu.tr

Dr. Öğr. Üyesi Sinan SAĞIR

Karamanoğlu Mehmetbey Üniversitesi, Fizik

E-Mail: sinansagir@kmu.edu.tr / sinan.sagir@cern.ch

Doç. Dr. Murat AYDEMİR

Erzurum Teknik Üniversitesi, Fen Fakültesi, Temel Bilimler

E-Mail: murat.aydemir@erzurum.edu.tr

Mühendislik Bilimleri

Doç. Dr. Özgür ÖZGÜN

Bingöl Üniversitesi, Sağlık Bilimleri Fakültesi, İş Sağlığı ve Güvenliği Bölümü
E-Mail: oozgun@bingol.edu.tr

Prof. Dr. Figen KOREL

İzmir Yüksek Teknoloji Enstitüsü, Gıda Mühendisliği Bölümü
E-Mail: figenkorel@iyte.edu.tr

Prof. Dr. Kubilay ASLANTAŞ

Afyon Kocatepe Üniversitesi, Teknoloji Fakültesi, Makine Mühendisliği Bölümü
E-Mail: aslantas@aku.edu.tr

Prof. Dr. Hamit Özkan GÜLSOY

Marmara Üniversitesi, Teknoloji Fakültesi, Metalurji ve Malzeme Mühendisliği Bölümü
E-Mail: ogulsoy@marmara.edu.tr

Prof. Dr. Ali Adnan HAYALOĞLU

İnönü Üniversitesi, Mühendislik Fakültesi, Gıda Mühendisliği Bölümü
E-Mail: adnan.hayaloglu@inonu.edu.tr

Prof. Dr. Barbara SAWICKA

University of Life Sciences in Lublin, Department of Plant Production Technology and Commodities Sciences
E-Mail: barbara.sawicka@gmail.com

Prof. Dr. İbrahim GÜNEŞ

Giresun Üniversitesi, Mühendislik Fakültesi, İnşaat Mühendisliği Bölümü
E-Mail: ibrahim.gunes@giresun.edu.tr

Doç. Dr. Sırma YEĞİN

Ege Üniversitesi, Mühendislik Fakültesi, Gıda Mühendisliği Bölümü
E-Mail: sirma.yegin@ege.edu.tr

Doç. Dr. Hasan OĞUL

Sinop Üniversitesi, Mimarlık ve Mühendislik Fakültesi, Nükleer Enerji Mühendisliği
E-Mail: hogul@sinop.edu.tr

Doç. Dr. Murat YILMAZTEKİN

İnönü Üniversitesi, Mühendislik Fakültesi, Gıda Mühendisliği Bölümü
E-Mail: murat.yilmaztekin@inonu.edu.tr

Doç. Dr. Ferhat AYDIN

Sakarya Uygulamalı Bilimler Üniversitesi, Teknoloji Fakültesi, İnşaat Mühendisliği Bölümü
E-Mail: ferhata@subu.edu.tr

Dr. Öğr. Üyesi Nurullah DEMİR

Bingöl Üniversitesi, Mühendislik ve Mimarlık Fakültesi, Gıda Mühendisliği Bölümü
E-Mail: ndemir@bingol.edu.tr

Dr. Öğr. Üyesi Ahmet GÜNER

Bingöl Üniversitesi, Mühendislik ve Mimarlık Fakültesi, Elektrik ve Elektronik Mühendisliği Bölümü
E-Mail: aguner@bingol.edu.tr

Dr. Öğr. Üyesi Tahir AKGÜL

Sakarya Uygulamalı Bilimler Üniversitesi, Teknoloji Fakültesi, İnşaat Mühendisliği Bölümü
E-Mail: tahirakgul@subu.edu.tr

Dr. Erhan Sulejmani

University of Tetova, Faculty of Food Technology and Nutrition
E-Mail: erhan.sulejmani@unite.edu.mk

Dr. Valenti GOMEZ

UCL Cancer Institute, Faculty of Medical Sciences, Department of Oncology, UCL, London, UK
E-Mail: valentin.gomez@ucl.ac.uk

Veterinerlik Bilimleri

Doç. Dr. Cüneyt ÇAĞLAYAN

Bilecik Şeyh Edebali Üniversitesi, Tıp Fakültesi, Temel Tıp Bilimleri Bölümü, Tıbbi Biyokimya Anabilim Dalı
E-Mail: cuneyt.caglayan@bilecik.edu.tr

Prof. Dr. Fatih Mehmet KANDEMİR

Atatürk Üniversitesi, Veteriner Fakültesi, Veteriner Hekimliği Temel Bilimler
E-Mail: fmehmet.kandemir@atauni.edu.tr

Doç. Dr. Akın KIRBAŞ

Bozok Üniversitesi, Veteriner Fakültesi, Klinik Bilimler Bölümü
E-Mail: akindahiliye55@yahoo.com

Doç. Dr. Emrah Hicazi AKSU

Atatürk Üniversitesi, Veteriner Fakültesi, Klinik Bilimler Bölümü
E-Mail: emrahaksu@atauni.edu.tr

Ziraat Bilimleri

Dr. Öğr. Üyesi Zeynep DUMANOĞLU

Bingöl Üniversitesi, Ziraat Fakültesi, Biyosistem Mühendisliği Bölümü
E-Mail: zdumanoglu@bingol.edu.tr

Prof. Dr. Kağan KÖKTEN

Bingöl Üniversitesi, Ziraat Fakültesi, Tarla Bitkileri Bölümü
E-Mail: kahafe1974@yahoo.com

Prof. Dr. Mustafa SÜRMEN

Adnan Menderes Üniversitesi, Ziraat Fakültesi, Tarla Bitkileri Bölümü
E-Mail: mustafa.surmen@adu.edu.tr

Türk Doğa ve Fen Dergisi
Turkish Journal of Nature and Science
www.dergipark.gov.tr/tdfd

İÇİNDEKİLER/CONTENTS

Cilt 11, Sayı 4, Sayfa 1-10, 2022 Volume 11, Issue 4, Page 1-10, 2022

Araştırma Makalesi https://doi.org/10.46810/tdfd.1123517 Research Article

Türk Doğa ve Fen Dergisi
Turkish Journal of Nature and Science
www.dergipark.gov.tr/tdfd

Assessment of The Use of Artemisia Dracunculus L and Erigeron Canadensis in The Remediation of Heavy Metal Contaminated Soils and Their Ability to Phytoextraction and Biomass Yield

Ayhan KOCAMAN[1*]

[1] Karabük University, Engineering Faculty, Environmental Engineering Department, 78050, Karabük, Turkey,
Ayhan KOCAMAN ORCID No: 0000-0002-1597-7936

**Corresponding author: ayhankocaman@karabuk.edu.tr*

(Received: 31.05.2022, Accepted: 27.09.2022, Online Publication: 28.12.2022)

Keywords
Heavy Metals,
Translocation Factor,
Bioaccumulation Factor

Abstract: Different hyperaccumulator plants growing in the same contaminated soil may have excessive accumulation of different metals or produce biomass. Therefore, it is important to determine the ability of the plant to improve the soil under natural conditions in the improvement of heavy metal-contaminated lands with hyperaccumulator plants. This study focused on the phytoremediation and biomass production capabilities of *Artemisa Dracunculus L*. and *Erigeron Canadensis plants*. Considering this fact, *Erigeron Canadensis* was determined to have the highest phytoextraction potential between the two plants, as it produces more biomass (96%) and mineral content (169%) than *Artemisa Dracunculus L*. This shows that *Erigeron Canadensis* has more phytoremediation potential than *Artemisa Dracunculus L*. and that *Erigeron Canadensis* plant is one of the alternative hyperaccumulator plant candidates and is more effective for soil reclamation. In addition, when the plants were categorized according to their BAF values, accumulator (1<Cd-Pb<10), heavy metal exclusionary (Cr-Hg-Sn<1), and Hyperaccumulator (10<Ni) were identified for both plants. On the other hand, *Artemisa Dracunculus L.* was defined as the accumulator for Se, but *Erigeron Canadensis* was excluder for Se.

Artemisia Dracunculus L ve Erigeron Canadensis'in Ağır Metalle Kirlenmiş Toprakların İyileştirilmesinde Kullanımının ve Bunların Fitoekstraksiyon, Biyokütle Veriminin Değerlendirilmesi.

Anahtar Kelimeler
Ağır Metal,
Translokasyon Faktörü,
Biyobirikim Faktörü

Öz: Aynı kirlenmiş toprakta büyüyen farklı hiperakümülatör bitkiler, farklı metallerin aşırı birikimine sahip olabilir veya biokütle üretebilirler. Bu nedenle ağır metal kirlenmiş arazilerin hiperakümülatör bitkilerle ıslahında bitkinin tarla koşullarında toprağı iyileştirme kabiliyetinin belirlenmesi önemlidir. Bu çalışma, *Artemisa Dracunculus L.* ve *Erigeron Canadensis* bitkilerinin fitoremediasyon ve biokütle üretim yeteneklerine odaklanmıştır. Bu gerçek göz önüne alındığında, *Erigeron Canadensis*'in *Artemisa Dracunculus L.*'den daha fazla biokütle (%96) ve mineral içeriği (%169) ürettiği için en yüksek fitoekstraksiyon potansiyeline sahip olduğu belirlendi. *Erigeron Canadensis* bitkisi, *Artemisa Dracunculus L*. Bitkisine göre toprak ıslahında daha etkilidir. Bu nedenle ’de alternatif hiperakümülatör bitki adayıdır. Ayrıca bitkiler BAF değerlerine göre sınıflandırıldığında her iki bitki için Cd ve Pb akümülatör (1<Cd, Pb<10), Cr, Hg, Sn için ağır metal dışlayıcı özelliğinde (Cr-Hg-Sn<1) ve Ni için hiperakümülatör (10<Ni) bitkiler olarak belirlenmiştir. Öte yandan *Artemisa Dracunculus L*, Se için akümülatör olarak tanımlanırken, *Erigeron Canadensis* Se için dışlayıcı bitkidir.

1. INTRODUCTION

Soils contaminated by heavy metals occurred primarily following the industrial revolution and it has become a growing threat because of intense agriculture and rapid urbanization [1]. The presence of heavy metals affects not only soil quality, but plant health and crop productivity as well [2]. Moreover, it reduces soil, water, and crop quality, in additionally, it poses serious risks for human health in the food chain [3, 4]. In fact that they are a long-term environmental threat [5]. Therefore, remedial measures are required to prevent heavy metals from entering terrestrial, atmospheric and aquatic environments and to reduce soil contamination [6, 7]. Physical and chemical methods of removing heavy metals from contaminated areas on a large scale are generally not available. Because the cost is high and is not acceptable to the public [8]. There are also disadvantages, including irreversible soil properties and secondary pollution [9, 10]. Thus, this is a major environmental concern. Remediation of metal-contaminated sites usually involves excavation of contaminated soil and the next step is to immobilize metal contaminants using solidification or stabilization technology at a licensed landfill [11]. Consequently, phytoremediation has become an alternative method that removes pollutants from polluted environmental components such as water, soil and air [12]. There are currently more than 450 species of hyperaccumulator plants in 45 families that meet the criteria for hyperaccumulation. Most of them are Ni hyperaccumulators (75%) [13] and most of hyperaccumulator plant species can over accumulate and over tolerate a single metal. However, some plant species are capable of accumulating and tolerating multiple metals at elevated concentrations. As a solution, Plants with well-developed roots and large biomass that can tolerate elevated concentrations of metals [14] and their phytoremediation capacity should be determined. Because they can fix or remove heavy metals from contaminated soil [14].

The aim of this study was to compare the accumulative capacity of heavy metals and the remediation capacity of two plants grown in soils polluted with industrial waste. Their biomass production was also compared due to heavy metal buildup. As a result, the translocation factor (TF), the bioaccumulation factor (BAF) for determining the phytoextraction and the hyperaccumulation capacity of *Artemisa Dracunculus L.* (AD) and *Erigeron Canadensis* (EC) from the family *Astéraceae* was studied. As well, it was assessed together pollution loads of the sampling sites.

2. MATERIAL AND METHOD

2.1. Sampling Area

Karabuk is a province where steel industries and their sub-industries are active in Turkey. It is located on the western side of the Black Sea region. it consists of mountains and forest regions to an elevation of 240. Plant and soil samples were collected from the landfill where the waste from the steel and construction industries (PS) was discharged (N 410 10' 42,60146' and E 320 38'42,07808'). As a reference sampling (RS) was carried out on agricultural land without industrial pollution (N 410 12' 45,47' and E 320 40' 38,09"). All samples were collected in the last quarter of July 2021.

2.2. Plant and Soil Sampling

Plant and soil samples in five random replicates were collected from both two plant varieties on a square hectare area. First, soil surface was swept away from organic residual as 2-3 cm thin, and soil samples were then taken around the plant roots by 20 cm deep. The same procedure was applied to the reference area plant and soil samples.

2.3. Preparing Soil and Plant Samples for Analysis

AD and *EC* collected in their natural environment were brought to the laboratory. They were washed 3 times with distilled water to clean the contaminants in them. Allowed to dry for one day at ambient temperature. Following weighing of the plant samples, they were divided into leaves, stems, and roots. Plant parts were dried in the oven at 80ºC for 48h until it reached a constant weight. Dried plant samples were granulated to small particles using a blender and stored in closed containers for analysis. The root or other residues were cleaned in soil samples collected on the root surface. Soil samples was sieved using a 2 mm sieve and dried at 105^{0}C for 48h until it reached a constant weight. The dried soil samples were stored in closed containers for analysis.

.

2.4. Analysis of Heavy Metal Concentrations

For the heavy metal contents of the 1 g dried samples, 3 ml HNO_3 +9 ml HCl was incinerated in 3 different steps and prepared for analysis. First step; (5 minutes at 145 ºC at 75% microwave power), second Step; (10 minutes at 180 ºC at 90% microwave power) and third step (10 min. at 100 ºC at 40% microwave power) were kept in a microwave, burning unit resistant to 40 bars (speedwave MWS-2 Berghof products + Instruments Harresstr.1. 72800 Enien Gernmany) [15]. After the samples were prepared for analysis, the ICP OES spectrophotometer (Perkinelmer, Optima 2100 DV, ICP/OES, Shelton, CT 06484-4794, USA) was used to determine the heavy metal content of the plant.

2.5. Plant Combustion

0.5 g of dried plant sample was weighed and placed in melting pots. Combustion was conducted in an electric furnace at 550°C and 900°C in the atmosphere. A temperature of 550 °C was selected. Because (i) it is enough to decompose the organic material and is the conventional temperature of the determination of the ash yield of the biomass. (ii) There is no significant loss of inorganic volatiles at this temperature [16]. The temperature of 900°C is the estimated temperature achieved in the boiler used for the pilot to burn tests [17]. Incineration was performed under conditions consistent with NF EN ISO 18122 to determine the ash content. the temperature was raised to 250°C at 25°C min^{-1}. It was kept constant for 60 minutes. It was then elevated to 550 at 10°C min^{-1} and kept constant for 120 minutes, then 900 ^{0}C at 10 ^{0}C min^{-1} and kept constant for 120 min. The crucibles were put into a desiccator until their temperature decreased to room temperature (20°C), and the sample was measured [18]. It was repeated three times for each plant.

2.6. SEM-EDX Characterization

Zeiss sigma 300 field emission gun scanning electron microscope (SEM), energy dispersive X-Ray (EDX) analysis and UV-1280 UV–VIS Spectrophotometer were used. The morphology of heavy metals between plant cells was analyzed. These analyzes were carried out in Van Yüzüncü Yıl University laboratories in Turkey.

2.7. Translocation Factor (TF)

The translocation factor is evaluated translocation of metals from roots to shoots by equation (1). it was computed as the ratio of metal concentration in the shoots to those in the roots [19-21]. as follows:

$$TF = \frac{heavy\ metal\ concentration\ in\ shoot}{heavy\ metal\ concentration\ in\ root} \quad (1)$$

TF > 1 signifies that the plant effectively translocated metals from the roots to the shoots [22].

2.8. Bioaccumulation Factor (BAF)

The Bioaccumulation factor (BAF) is determined for quantitative expression of metal accumulation in the plant shoots from the soil by equation (2) [23].

$$BAF = \frac{heavy\ metal\ concentration\ in\ shoot}{heavy\ metal\ concentration\ in\ soil} \quad (2)$$

Plants with different BAF values are categorized as (excluder)1<(accumulator)<10 (hyperaccumulator) [24].

2.9. Phytoremediation Efficiency

The Translocation Factor and Bioaccumulation Factor were calculated to evaluate the efficiency of phytoextraction of heavy metals [24, 25]. TF is the ability of a plant to move metal from roots to shoots. But the bioaccumulation factor refers to the capacity of a plant to accumulate soil metals. An accumulator of plants with BAF shoot values >1 according to the classification of existing plants used as phytoremediation media [26]. The plants for which the BAF shoot value < 1 is assumed to be metal excluder. Moreover, plants are classified as potential hyperaccumulators if the shoot values of BAF >10 [24].

2.10. Contamination Factor (CF)

Contamination Factor is also called single pollution index (PI). CF is the quotient obtained by dividing the concentration of metals related to the target area by reference area. The contamination factor can be calculated by equation 3 [27].

$$\text{CF} = \frac{concentration\ of\ metals\ in\ the\ target\ area}{concentration\ of\ metals\ in\ the\ reference\ area.} \quad (3)$$

Contamination factor categorized [28]. as below.

(LP) Low (CF < 1), (MP) Moderate (1≤ CF<3), (CP) Considerate (3≤CF<6), (VHP) Very high (CF>6).

2.11. Pollution Load Index

Pollution Load Index (PLI) is simple statistical technique used to determine elemental contents in soil beyond the reference concentration [29, 30]. PLI can be determined by equation (4)

$$PLI = \sqrt[n]{CF1xCF2xCF3 \ldots CFn} \quad (4)$$

PLI represents the pollution load index, CF is the contamination factor, and “n” is the number of elements. The indicates polluted (PLI >1), no pollution (PLI <1).

2.12. Enrichment Factor (EF)

The Enrichment factor is identified as an effective tool for evaluating the amount of pollutants in the environment [31]. The EF for each component was calculated to assess anthropogenic effects on hazardous soil components by equation (5) [32, 33].

$$EF = \frac{\frac{concentration\ of\ heavy\ metal\ in\ the\ soil\ sample}{Fe\ content\ in\ the\ soil\ sample}}{\frac{heavy\ metal\ content\ in\ Geo\ ref.}{Fe\ content\ in\ Geo\ ref.}} \quad (5)$$

Classification of enrichment factors (EF).
EF < 2 Low enrichment, 2 ≤ EF < 5 Medium enrichment, 5 ≤ EF < 20 Significant enrichments, 20 ≤ EF < 40 Very high enrichment, EF ≥ 40 Excessive enrichments.

2.13. The Rate of Phytoextraction

The rate of phytoextraction was calculated using by equation (6) [34]. Metal contamination was assumed to occur only in the active root zone, in the top 20 cm of soil. It results in a total soil mass of 2600 t ha^{-1} (Supposing a soil mass density of 1,3 t m^{-3}).

$$\%\ soil\ metal\ removed\ by\ plant\ = \frac{(Plant\ metal\ concentration\ Biomass)\ x100}{(Soil\ metal\ concentration\ x\ Soil\ mass\ in\ the\ rooting\ zone)} \quad (6)$$

2.14. Statistical Analysis

Data were analyzed by One-Way ANOVA using SPSS software (version 22.0). Duncan's test was used to identify significant differences between the means ($p < 0.05$).

3. RESULTS AND DISCUSSIONS

The mean pH for two plant soils sampled from PS were 6.80-7.07, while it was 7.92–7.21 in two soil samples from RS. The EC values of soil sampled from PS was 92.19 and 100.57 µs cm^{-1}. The EC values for the RS samples was 67.64 and 64.49 µs cm^{-1}. The concentration of $CaCO_3$% of the two plant soils from the PS was 0.36 and 0.39, whereas it was 0.59 and 0.84 in soil samples from the RS. Organic Matter content of sampled soils from RS for *AD* and *EC* (1.90-2.21%) was higher than PS (1.48-0.89%) (Table 1).

Table 1. Soil samples taken from plant root zones

	***AD* (PS)**	***EC* (PS)**	***AD* (RS)**	***EC* (RS)**
pH	6.80	7.07±0.15	7.92±0.04	7.21±0.06
EC mikromhos cm^{-1}	92.19±7.03	100.57±6.03	67.64±1.86	64.49±1.69
Calc. %	0.36±0.24	0.39±0.08	0.59±0.04	0.84±0.04
OM %	1.48±0.11	0.89±0.04	1.90±0.07	2.12±0.09
Total N %	0.10±0.04	0.03±0.01	0.06±0.03	0.06
P ppm	21.33±2.36	26.51±0.58	32.16±1.49	59.20±7.34
K cmol kg^{-1}	2.05±1.20	1.24±0.08	2.64±0.08	2.94±0.12
Ca	11.40±0.41	6.88±0.11	14.70±8.29	16.36±0.67
Mg cmol kg^{-1}	7.66±1.20	9.36±1.87	15.16±0.51	17.24±0.80
Na cmol kg^{-1}	2.56±0.41	2.29±0.11	3.68±0.22	1.01±0.08
Total Ni	2786.01±222.88	2291.25±160.37	255.21±12.75	210.02±14.7
Total Cd	335.83±23.45	323.07±22.61	23.21±9.28	22.55±1.58
Total Pb	1297.80±90.79	1157.25±92.56	29.85±2.67	30.30±1.72
Total Cr	3319.12±165.95	4209.92±294.63	268.84±21.51	245.96±14.76

Depending on the contaminant factor categorized by [28]. The levels of contamination of heavy metals where studied area was determined by Cd (very high), Hg (considerate), Se-Pb (moderate), Ni-Cr and Sn (low). The CF of PS area was calculated as the mean of the results of the two sampled soils because of represents in the same area. CF of heavy metals were computed as (Cd 99.4, Hg 5.29, Se 1.78, Pb 1.17, Ni 0.37, Cr 0.13, Sn 0.05). The pollution load index was determined 22.91 (means of two soil samples) because of contamination factors. According to these results, soils sample of *AD* and *EC* plant from PS, the pollution factor was very high (PLI 26,76-19,05). The enrichment factor (EF) is often used to assess soil contamination by HM [35, 36]. The total EF was also computed to understand the pollution dimension. It was 63.33 on PS soil samples. Our results showed that anthropological pollution because of high EF and PLI value was caused by waste from the iron and steel industry in Karabük province. The EF value focuses on the fact that it adequately represents our field of study and may serve as a reference in the future.

Moreover, these results showed that the studied plants could be able to detoxify heavy metals and the capacity of the hyperaccumulator. As a result of heavy metal analysis of soil and plant samples taken from both PS and RS fields, there were statistically significant differences in heavy metal accumulation between organs of both *AD* and *EC* plants ($p<0.05$) (Table 2, Figure 1).

Table 2. Heavy metal concentrations in AD and EC plants (leaf-stem-root) and soils.

Plants	**Area**	**Site**	**Cd**	**Cr**	**Hg**	**Pb**	**Ni**	**Sn**	**Se**
			mg g^{-1} dry weight						
AD	**PS**	**Leaf**	13.28±1.14**a**	0.90±0.10**b**	0.13±0.01**b**	32.47±1.12**a**	11.31±0.56**a**	0.21±0.01**b**	2.95±0.12**a**
		Stem	8.66±0.74**b**	0.74±0.08**b**	0.11±0.01**b**	24.15±0.83**b**	7.37±0.36b	0.16**b**	1.92±0.08**ab**
		Root	5.66±0.45**c**	0.14±0.02**b**	0.01**c**	13.10±0.58**d**	0.21±0.01**d**	0.03**c**	1.17±0.05**b**
		Soil	2.93**d**	5.89±1.20**a**	2.31±0.11**a**	16.80±3.32**c**	1.04±0.15**c**	0.56±0.10**a**	2.96±1.75**a**
	RS	**Leaf**	0.97±0.10a	0.06±0.01b	0.00c	0.80±0.11a	0.13b	0.02b	0.00b
		Stem	0.63±0.07b	0.07±0.01b	0.00c	0.60±0.08b	0.09bc	0.01c	0.00b
		Root	0.43±0.04c	0.16±0.02a	0.02b	0.30±0.02c	1.56±0.07a	0.03a	0.00b
		Soil	0.08d	0.18±a	0.05±0.01a	0.29±0.04c	0.03±0.01c	0.02±b	0.07±0.06a
EC	**PS**	**Leaf**	12.39±1.36**a**	0.78±0.07**b**	0.10**b**	27.93±1.12**a**	9.02±1.50a	0.22±0.04**b**	2.06±0.04**ab**
		Stem	8.08±0.88**b**	0.64±0.06**c**	0.09**b**	20.77±0.91**b**	5.88±0.97**b**	0.16±0.03**b**	1.34±0.03b
		Root	5.85±0.18**c**	0.13±0.02**d**	0.01**b**	11.32±0.16**d**	0.19±0.03**d**	0.02±0.01**c**	0.8±0.04**b**
		Soil	3.05±0.07d	5.81±0.05**a**	2.53±0.35**a**	17.13±2.43**c**	1.16±0.21**c**	0.64±0.03**a**	4.34±2.68**a**
	RS	**Leaf**	0.96±0.11a	0.06±0.01c	0.00c	0.81±0.03a	0.11±0.01b	0.02b	0.00b
		Stem	0.62±0.07b	0.05±0.01c	0.00c	0.60±0.02b	0.08±0.01b	0.01b	0.00b
		Root	0.39±0.02c	0.15±0.01b	0.02b	0.32±0.01c	1.28±0.22a	0.03±0.01a	0.00b
		Soil	0.08d	0.17a	0.06±0.01a	0.29±0.04c	0.03±0.01b	0.02±b	0.10±0.06a
Duncan abc ($p<0.05$)									

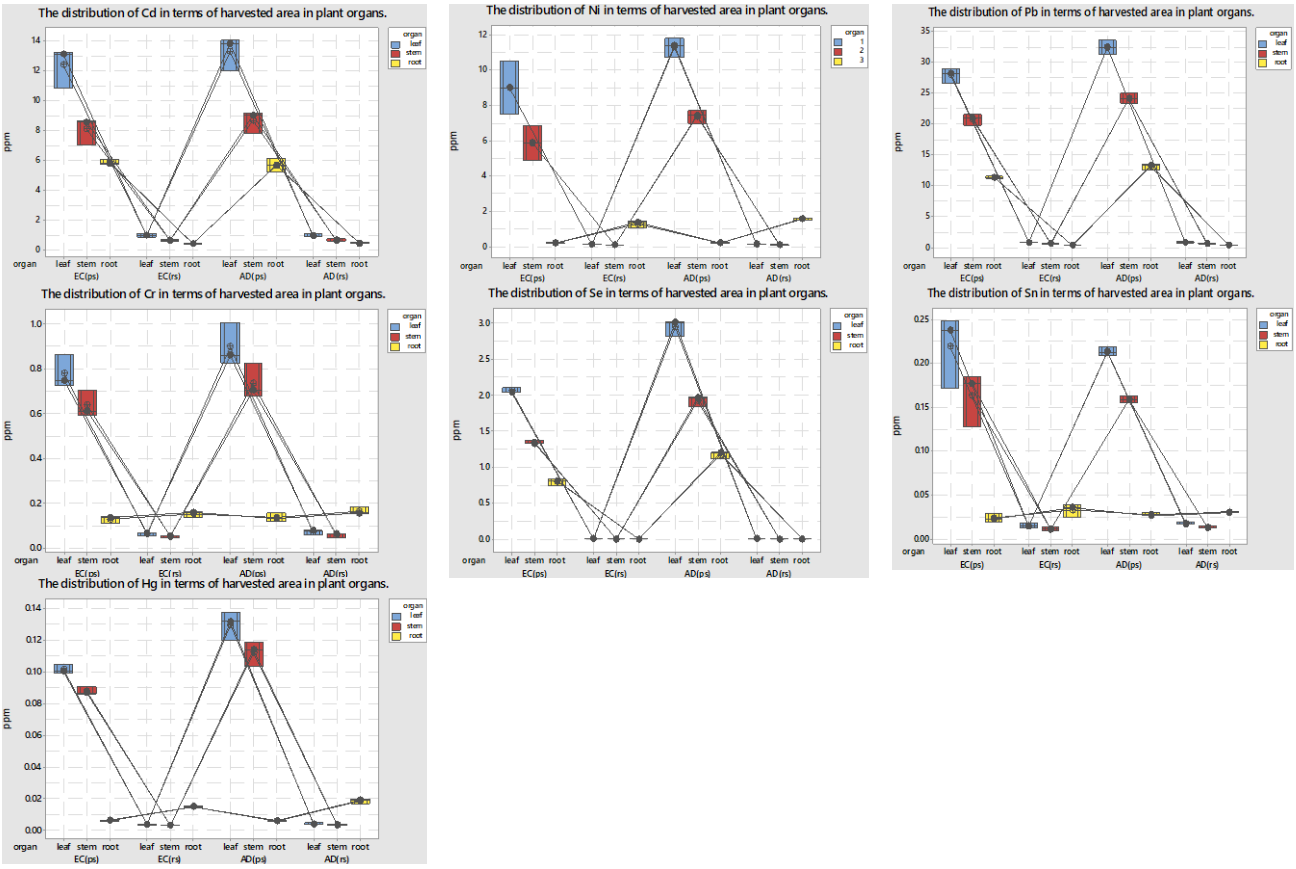

Figure 1. The distribution of heavy metals in terms of harvested area in plant organs.

On the other hand, the nutrient concentration of plant samples collected from the PS was lower than plant samples collected in RS areas (Figure 2). According to the *AD* and *EC* plant leaves from PS had a high accumulation of heavy metal compared to the RS. These increases in the *AD* leaves were at Cd 1269%, Cr 1400%, Hg 3150%, Pb 3959%, Ni 8600%, Sn 950%, Se 98233%. It was for the *EC* leaves at Cd 1270%, Cr 1200%, Hg 2400%, Pb 3348%, Ni 8100%, Sn 1000%, Se 102900%. These increases in the xylem of *AD* and *EC* were at Cd 1274-1203%, Cr 957-1200%, Hg 2650-2400%, Pb 3925-3361%, Ni 8088-7250, % Sn 1500-1000%, Se 95900-66900%. Therefore, it was determined that was the ability to accumulate more heavy metals into aerial components.

TF is an indicator of the accumulation of heavy metals in plants or the mobility of heavy metals in soil. It is also quantified the differences in metal bioavailability for the plant. According to the results of samples from PS, the accumulation of heavy metals was the highest in the aerial parts of plant. Both *AD* and *EC* samples showed the mobility of HMs from root to stem and leaf. TF (stem<leaf) was obtained at TF_{Cd} (1.53-1.38<2.34-2.12), TF_{Cr} (5.29-4.92<6.42-6), TF_{Hg}(18.34-15<21.67-1667), TF_{Pb}(1.84<2.48-2.47), TF_{Ni} (35.01-30.95<53.86-47.47), TF_{Sn}(5.3-8<7-11), TF_{Se}(1.64-1.68<2.52-2.58). Moreover, the BAF values were computed for phytoremediation efficiency for both plants. BAF value was as BAF_{Cd} (7.5-6.71), BAF_{Cr} (0.28-0.24), BAF_{Hg} (0.10-0.08), BAF_{Pb} (3.37-2.84), BAF_{Ni} (17.96-12.85), BAF_{Sn} (0.71-0.6), BAF_{Se} (4.17-0.78) (Table 3). BAF and TF have been widely used to assess heavy metal transport in growing plant tissues [37]. In both samples, the accumulation capacity of heavy metals in plants was determined by the absorption of metal ions and their transport to the aerial parts. Depending on the results of the analysis, the accumulation of heavy metals in plant samples from the polluted area was highest in the aerial parts and especially leaves. The highest concentration of heavy metals was as Pb>Cd>Ni>Se>Cr>Sn>Hg respectively. BAF values for both plants showed that accumulator (1<Cd-Pb<10), heavy metal excluder (Cr-Hg-Sn<1), Hyperaccumulator (10<Ni). On the other hand, *AD* was identified as accumulator for Se, whereas *EC* was Se excluder plant property (Table 3). Some plant species may absorb and over-accumulate metal contaminants and/or excess nutrients in roots and shoots from growing substrate to plant extraction [38]. In research in Iran, the maximum bioaccumulation of Pb was observed in *Artemisia Dracunculus L.* [39] and it was also reported that new natural Se accumulator was identified by [40]. Another study showed that low levels of Cd accumulated by Artemisa Dracunculus, but they have not been identified as heavy metal accumulator by [41]. In a study was found that the BAF and TF of C. canadensis (L.) Cronq. were all <1. it was indicated that C. canadensis (L.) Cronq. was not a hyperaccumulator [42]. Furthermore, it reported that was strong resistance to heavy metal stress and high concentration of heavy metal. Therefore, as a candidate species for phytoremediation, *C.Canadensis* (L.) *Cronq.* has a certain application prospect in phytoremediation of cadmium-contaminated soil [43].

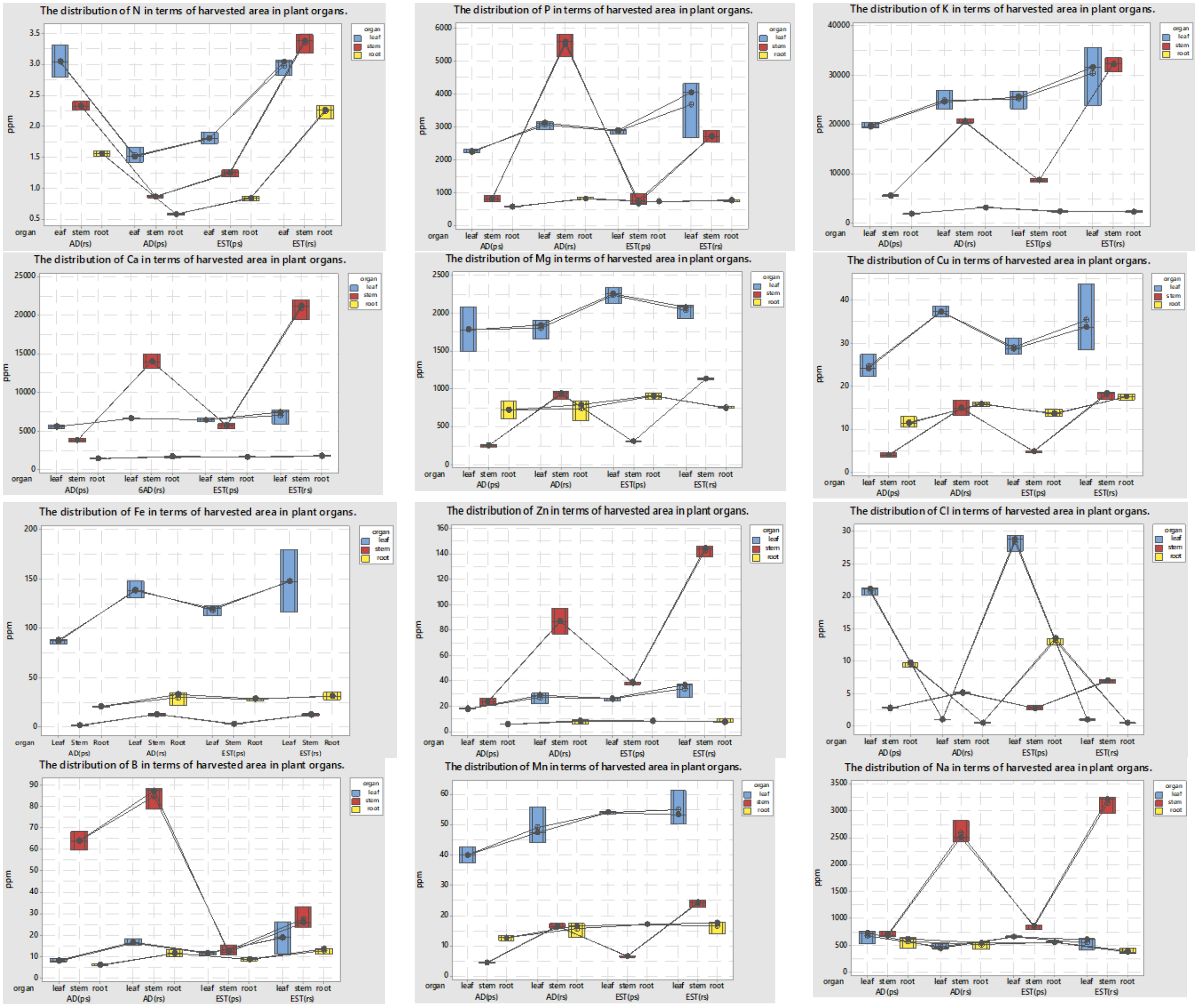

Figure 2. The distribution of nutrients concentration in terms of harvested area in plant organs

Table 3. Phytoremediation efficiency charts

	AD				EC			
	TF_{leaf}	TF_{stem}	CF	BAF	TF_{leaf}	TF_{stem}	CF	BAF
Cd	2.34	1.53	101^{VHP}	7.5^{A}	2.12	1.38	97.98	6.71^{A}
Cr	6.42	5.29	0.13^{LP}	0.28^{E}	6	4.92	0.12	0.24^{E}
Hg	21.67	18.34	5.12^{CP}	0.10^{E}	16.67	15	5.45	0.08^{E}
Pb	2.48	1.84	1.24^{MP}	3.37^{A}	2.47	1.84	1.10	2.84^{A}
Ni	53.86	35.01	0.4^{LP}	17.96^{H}	47.47	30.95	0.33	12.85^{H}
Sn	7	5.3	0.05^{NP}	0.71^{E}	11	8	0.05	0.6^{E}
Se	2.52	1.64	1.8^{MP}	4.17^{A}	2.58	1.68	1.76	0.78^{E}
PLI	26.76				19.05			

Plant biomass of AD and EC was computed using bio consumption methods.0.45 g biomass and 0.05 g mineral content were obtained from AD (RS) plants. 0.47 g biomass and 0.03 g mineral content were also obtained from EC (RS) plant, after 0.5 g dry plant samples were put in a 550 0C ash kiln. The total biomass rate for AD, EC sampled from the RS was 90-94%. In addition, the mineral content was 10-6 %. The volatiles content of mineral ash was 72.60-93.77%. In contrast, 0.39 g biomass and 0.11 g mineral content were obtained from EC (PS) plants. 0.42 g biomass and 0.08 g mineral content were also obtained from AD (PS) plant, after 0.5 g dry plant samples were put in a 550 0C ash kiln. EC and AD plants collected from PS had lower biomass, and higher mineral content. EC and AD biomass % were achieved at 78-84%. The mineral content for AD and EC from PS was 22-16%. The volatiles content of mineral ash was 81.35-72.43%. In additionally, the mineral content of the where sampled soil from PS was 76.53%. The distribution of heavy metal accumulation in plant organs was shown in Figure 3, 4, 5 and 6 by SEM-EDX observation.

In additionally, bright points in the images showed the distribution of heavy metals observed SEM. Heavy metal residues were identified in the tissues of plant organs. Therefore, these investigations could show the possibility of heavy metal chelation in the leaf and stem of the plant. Furthermore, the EDX detection proved to be close to our real results. The amount of AD biomass (% wt) was 72.96-94.47% (leaf-stem), for EC (% wt) was 80.33-71.22% (leaf-stem).

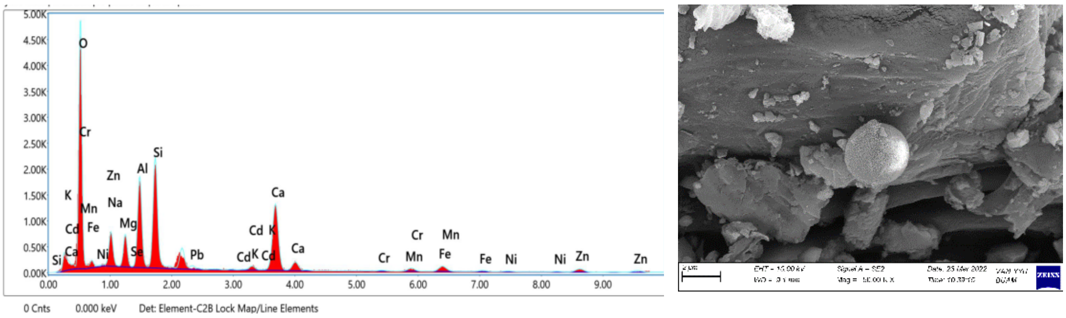

Element	Weight %
O K	40.55
NaK	0.59
MgK	3.66
K K	0.77
CaK	17.72
MnK	1.98
ZnK	7.69

Figure 3. SEM and EDX investigation of the distribution of heavy metals in the tissues of AD leaves (PS)

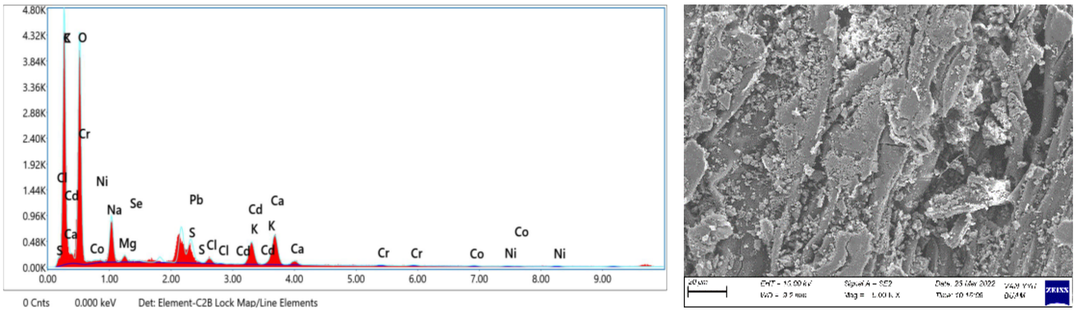

Element	Weight %
C K	32.50
O K	41.47
NaK	6.16
MgK	0.62
S K	1.52
ClK	0.48
K K	4.36
CaK	7.36

Figure 4. SEM and EDX investigation of the distribution of heavy metals in the tissues of AD stem (PS)

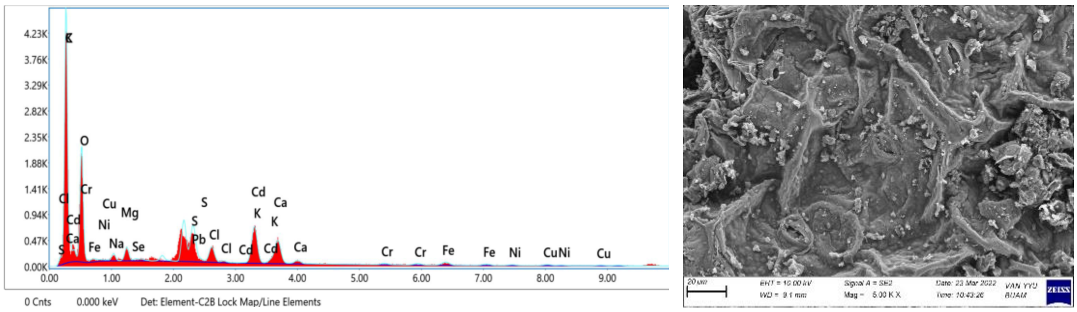

Element	Weight %
O K	52.56
NaK	1.40
MgK	0.74
AlK	7.69
SiK	23.05
AuM	7.96
ClK	0.40
K K	2.36
CaK	1.50
FeK	2.34

Figure 5. SEM and EDX investigation of the distribution of heavy metals in the tissues of EC leaves (PS)

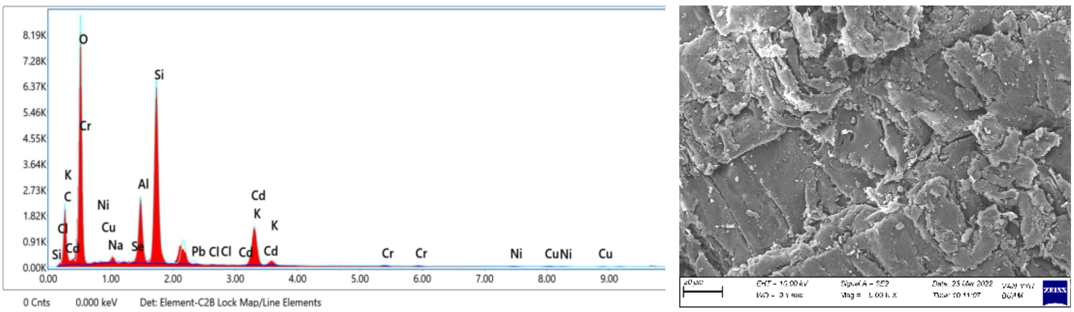

Element	Weight %
C K	17.27
O K	43.89
NaK	1.01
ClK	0.01
K K	9.04

Figure 6. SEM and EDX investigation of the distribution of heavy metals in the tissues of EC stem (PS)

According to plants organs of biomass rate for AD collected from PS, it was 94.98-94.95-72.63% (Root>stem>leaf), mineral content 5.02-5.05-27.37%, volatile minerals range in mineral content 49.54-69.31-98.43% (Root-Stem-Leaf) respectively. For the AD collected from RS, it was 94.10-92.91-92.83% (Leaf>stem>root), mineral content 5.90-7.09-7.17%, the volatiles content of mineral ash 83.01-58.43-76.36% (leaf>stem>root) respectively. Plants organs of % biomass for EC collected from PS, it was 85.89-79.02-67.62-% (Root>stem>leaf), mineral content 14.11-20.98-32.38%, the volatiles content of mineral ash 72.11-73.51-98.41% (root-stem-leaf) respectively. For the EC collected from RS, it was 93.05-94.94-93.53% (Leaf> stem>root), mineral content 6.95-6.47-5.06%, the amount of volatile minerals in mineral content 99.72-95.38-86.22% respectively.

The means of collected AD and EC plant samples of dry weight from PS was 27.14 ±7.78 plant-1 0.20m2, 74.

50±13.23 plant-1 0.25 m². The biomass of AD and EC was determined to be 23.61 g plant^{-1} 0. 20m2 and 57.75 g plant-1 0. 25m2. 1.181kg ha^{-1} and 2.310 kg ha^{-1} of biomass were determined from the AD, EC samples from PS, respectively. It was also calculated on 188.96 kg ha^{-1}, 508.2 kg ha^{-1} mineral content. Moreover, 1989.80 t ha^{-1} mineral content was determined soil sampled area.

Assuming both plant of biomass ha-1 year-1, AD and EC plant had a capable of eliminating heavy metals from the soil at Cd (0.34-0.60%), Cr (0.01-0.02%), Hg (0.005%), Pb (0.15-0.25%), Ni (0.82-1.14%), Sn (0.03-0.05%), Se (0.08-0.7%). In terms of results, the rate of Phytoextraction of AD and EC was determined at 9.5%-25.54% for one harvesting in a year. Research determined that it took 14 years to eliminate low concentrations of Cd in soil [44]. It was also reported that T. Caerulescens remove approximately (200 and 8 ppm) Zn and Cd from industrial contaminated soil for 391 days [45]. Another study indicated that V. Baoshanens removed about (20, 268 and 15 ppm) of contaminated Pb, Zn and Cd for more than 140 days [44]. EC generated more biomass (96%) and mineral content (169%) than the AD. This suggests that EC has more phytoremediation potential than AD.

EC plant was determined one of alternative candidate of hyperaccumulator plant and more effective for the soil remediation. Moreover, it presents a possibility of secondary productions. Apart from the removal of heavy metals from the ground, hyperaccumulating plants have the advantage of secondary uses of the biomass they produce. Thus, they contribute to countries' economies and contribute to reducing carbon emissions. [46]. As biochar, bio-brick, bio-hydrogen, Biomethane, bioethanol, bioethanol, organic acids, bioelectricity, etc. For example, Bio-brick is carbon-negative and sustainable. It is a cost-effective and profitable alternative to incineration of crop residues. Furthermore, Bio-bricks have a lower thermal conductivity of about 0.27 W mk-1 and can be used as a good source of sound and heat insulation in walls. In additionally, During the development of the bio-brick, the researchers revealed that a single block of bio-brick can hold 322.2 gm of CO2.

4. CONCLUSION

This study focused on the phytoremediation and biomass production capabilities of AD and EC plants. In the process of determining of the phytoremediation potential, not only the BAF and TF values, but also the biomass of the plants are very important, because the amount of metal absorbed increases sufficiently in parallel with its increase of Biomass. Considering this fact, the highest phytoextraction potential of between two plants was determined that was EC. It was also generated more biomass (96%) and mineral content (169%) than the AD. This suggests that EC has more phytoremediation potential than AD. Therefore, EC plant was determined one of alternative candidate of hyperaccumulator plant and more effective for the soil remediation. Moreover, it presents a possibility of secondary productions. Apart from the removal of heavy metals from the ground, hyperaccumulating plants have the advantage of secondary uses of the biomass they produce. Thus, they contribute to countries' economies and contribute to reducing carbon emissions.

The EC plant has an important Phyto chelator potential to tolerate soils contaminated by heavy metals. It is also able to survive under different environmental conditions and may accumulate large quantities of metal in its harvestable parts. This would allow researchers to choose this plant as a plant remediation tool.

Acknowledgement

I would like to thank my supervisor Prof. Metin Turan for his consistent support and guidance during the running of this project. Furthermore, I would also like to acknowledge the Karabuk University Scientific Research Center (BAP) for their participation and engagement in the study.

Funding: This research was funded by Karabuk University Scientific Research Center (BAP), grand number FOA-2020-2280.

REFERENCES

[1] Cozma P, Hlihor R-M, Roșca M, Minuț M, Diaconu M, Gavrilescu M, editors. Coupling Phytoremediation with Plant Biomass Valorisation and Metal Recovery: an Overview. 2021 International Conference on e-Health and Bioengineering (EHB); 2021: IEEE.Carlson BM. Human embryology and developmental biology. 4th ed. St. Louis: Mosby; 2009.
[2] ÖZKUTLU F, Kara Şm. Cd concentration of durum wheat grain as influenced by soil salinity. Akademik Ziraat Dergisi. 2019;8(1):97-100.
[3] Zhou B, Zhao L, Sun Y, Li X, Weng L, Li Y. Contamination, and human health risks of phthalate esters in vegetable and crop soils from the Huang-Huai-Hai region of China. Science of the Total Environment. 2021; 778:146281.
[4] Lv G, Yang T, Chen Y, Hou H, Liu X, Li J, et al. Biochar-based fertilizer enhanced Cd immobilization and soil quality in soil-rice system. Ecological Engineering. 2021; 171:106396.
[5] Suman J, Uhlik O, Viktorova J, Macek T. Phytoextraction of heavy metals: a promising tool for clean-up of polluted environment? Frontiers in plant science. 2018:1476.
[6] Murray EW, Greenberg BM, Cryer K, Poltorak B, McKeown J, Spies J, et al. Kinetics of phytoremediation of petroleum hydrocarbon contaminated soil. International journal of phytoremediation. 2019;21(1):27-33.
[7] Hasan M, Uddin M, Ara-Sharmeen I, F Alharby H, Alzahrani Y, Hakeem KR, et al. Assisting phytoremediation of heavy metals using chemical amendments. Plants. 2019;8(9):295.

[8] Khalid S, Shahid M, Niazi NK, Murtaza B, Bibi I, Dumat C. A comparison of technologies for remediation of heavy metal contaminated soils. Journal of Geochemical Exploration. 2017; 182:247-68.
[9] Xin J, Ma S, Li Y, Zhao C, Tian R. Pontederia cordata, an ornamental aquatic macrophyte with great potential in phytoremediation of heavy-metal-contaminated wetlands. Ecotoxicology and Environmental Safety. 2020; 203:111024.
[10] Salas-Moreno M, Marrugo-Negrete J. Phytoremediation potential of Cd and Pb-contaminated soils by Paspalum fasciculatum Willd. ex Flüggé. International Journal of Phytoremediation. 2020;22(1):87-97.
[11] Liu L, Li W, Song W, Guo M. Remediation techniques for heavy metal-contaminated soils: Principles and applicability. Science of the Total Environment. 2018; 633:206-19.
[12] Kaur L. Role of Phytoremediation Strategies in Removal of Heavy Metals. Emerging Issues in the Water Environment during Anthropocene. 2020:223-59.
[13] Verbruggen N, Hermans C, Schat H. Molecular mechanisms of metal hyperaccumulation in plants. New phytologist. 2009;181(4):759-76.
[14] Wang J, Xiong Y, Zhang J, Lu X, Wei G. Naturally selected dominant weeds as heavy metal accumulators and excluders assisted by rhizosphere bacteria in a mining area. Chemosphere. 2020; 243:125365.
[15] Mertens D. AOAC official method 922.02. Plants preparation of laboratuary sample. Official Methods of Analysis. Chapter. 2005; 3:20877-2417.
[16] Koppejan J, Van Loo S. The handbook of biomass combustion and co-firing: Routledge; 2012.
[17] Houzelot V, Laubie B, Pontvianne S, Simonnot M-O. Effect of up-scaling on the quality of ashes obtained from hyperaccumulator biomass to recover Ni by agromining. Chemical Engineering Research and Design. 2017; 120:26-33.
[18] Cassayre L, Hazotte C, Laubie B, Carvalho Jr W, Simonnot M-O. Combustion of nickel hyperaccumulator plants investigated by experimental and thermodynamic approaches. Chemical Engineering Research and Design. 2020; 160:162-74.
[19] Lin H, Liu J, Dong Y, He Y. The effect of substrates on the removal of low-level vanadium, chromium and cadmium from polluted river water by ecological floating beds. Ecotoxicology and Environmental Safety. 2019; 169:856-62.
[20] Qian Y, Gallagher FJ, Feng H, Wu M, Zhu Q. Vanadium uptake and translocation in dominant plant species on an urban coastal brownfield site. Science of the Total Environment. 2014; 476:696-704.
[21] Liu J-g, Qu P, Zhang W, Dong Y, Li L, Wang M-x. Variations among rice cultivars in subcellular distribution of Cd: the relationship between translocation and grain accumulation. Environmental and experimental botany. 2014; 107:25-31.
[22] Baker AJ, Brooks R. Terrestrial higher plants which hyperaccumulate metallic elements. A review of their distribution, ecology and phytochemistry. Biorecovery. 1989;1(2):81-126.
[23] Deram A, Denayer F-O, Petit D, Van Haluwyn C. Seasonal variations of cadmium and zinc in Arrhenatherum elatius, a perennial grass species from highly contaminated soils. Environmental Pollution. 2006;140(1):62-70.
[24] Ma LQ, Komar KM, Tu C, Zhang W, Cai Y, Kennelley ED. A fern that hyperaccumulates arsenic. Nature. 2001;409(6820):579-.
[25] Yang X, Li T, Yang J, He Z, Lu L, Meng F. Zinc compartmentation in root, transport into xylem, and absorption into leaf cells in the hyperaccumulating species of Sedum alfredii Hance. Planta. 2006;224(1):185-95.
[26] Baker AJ. Accumulators and excluders-strategies in the response of plants to heavy metals. Journal of plant nutrition. 1981;3(1-4):643-54.
[27] Harikumar P, Nasir U, Rahman M. Distribution of heavy metals in the core sediments of a tropical wetland system. International Journal of Environmental Science & Technology. 2009;6(2):225-32.
[28] Inengite A, Abasi C, Walter C. Application of pollution indices for the assessment of heavy metal pollution in flood impacted soil. International research journal of pure & applied chemistry. 2015;8(3):175-89.
[29] Tomlinson D, Wilson J, Harris C, Jeffrey D. Problems in the assessment of heavy-metal levels in estuaries and the formation of a pollution index. Helgoländer meeresuntersuchungen. 1980;33(1):566-75.
[30] Yang Z, Lu W, Long Y, Bao X, Yang Q. Assessment of heavy metals contamination in urban topsoil from Changchun City, China. Journal of Geochemical Exploration. 2011;108(1):27-38.
[31] Franco-Uría A, López-Mateo C, Roca E, Fernández-Marcos ML. Source identification of heavy metals in pastureland by multivariate analysis in NW Spain. Journal of hazardous materials. 2009;165(1-3):1008-15.
[32] Zheng L, Zhou Z, Rao M, Sun Z. Assessment of heavy metals and arsenic pollution in surface sediments from rivers around a uranium mining area in East China. Environmental Geochemistry and Health. 2020;42(5):1401-13.
[33] Proshad R, Kormoker T, Islam S. Distribution, source identification, ecological and health risks of heavy metals in surface sediments of the Rupsa River, Bangladesh. Toxin reviews. 2019.
[34] Zhao F, Lombi E, McGrath S. Assessing the potential for zinc and cadmium phytoremediation with the hyperaccumulator Thlaspi caerulescens. Plant and soil. 2003;249(1):37-43.
[35] Wang L, Dai L, Li L, Liang T. Multivariable cokriging prediction and source analysis of potentially toxic elements (Cr, Cu, Cd, Pb, and Zn)

in surface sediments from Dongting Lake, China. Ecological Indicators. 2018; 94:312-9.
[36] Wang X, Fu R, Li H, Zhang Y, Lu M, Xiao K, et al. Heavy metal contamination in surface sediments: A comprehensive, large-scale evaluation for the Bohai Sea, China. Environmental Pollution. 2020; 260:113986.
[37] Alaboudi KA, Ahmed B, Brodie G. Phytoremediation of Pb and Cd contaminated soils by using sunflower (Helianthus annuus) plant. Annals of agricultural sciences. 2018;63(1):123-7.
[38] Tang H, Li T, Yu H, Zhang X. Cadmium accumulation characteristics and removal potentials of high cadmium accumulating rice line grown in cadmium-contaminated soils. Environmental Science and Pollution Research. 2016;23(15):15351-7.
[39] Ghasemidehkordi B, Malekirad AA, Nazem H, Fazilati M, Salavati H, Shariatifar N, et al. Concentration of lead and mercury in collected vegetables and herbs from Markazi province, Iran: a non-carcinogenic risk assessment. Food and chemical toxicology. 2018; 113:204-10.
[40] Golubkina N, Shevchuk O, Logvinenko L, Molchanova A, Plugatar YV, editors. Macro and trace element accumulation by species of genus Artemisia on the southern coast of the Crimea. VIII International Scientific and Practical Conference on Biotechnology as an Instrument for Plant Biodiversity Conservation 1324; 2018.
[41] Ozyigit II, Yalcin B, Turan S, Saracoglu IA, Karadeniz S, Yalcin IE, et al. Investigation of heavy metal level and mineral nutrient status in widely used medicinal plants' leaves in Turkey: Insights into health implications. Biological trace element research. 2018;182(2):387-406.
[42] Yu S, Sheng L, Mao H, Huang X, Luo L, Li Y. Physiological response of Conyza Canadensis to cadmium stress monitored by Fourier transform infrared spectroscopy and cadmium accumulation. Spectrochimica Acta Part A: Molecular and Biomolecular Spectroscopy. 2020; 229:118007.
[43] Xia H, Liang D, Chen F, Liao Ma, Lin L, Tang Y, et al. Effects of mutual intercropping on cadmium accumulation by the accumulator plants Conyza canadensis, Cardamine hirsuta, and Cerastium glomeratum. International journal of phytoremediation. 2018;20(9):855-61.
[44] Zhuang P, Ye Z, Lan C, Xie Z, Shu W. Chemically assisted phytoextraction of heavy metal contaminated soils using three plant species. Plant and Soil. 2005;276(1):153-62.
[45] Lombi E, Zhao F, Dunham S, McGrath S. Phytoremediation of heavy metal–contaminated soils: Natural hyperaccumulation versus chemically enhanced phytoextraction. Journal of Environmental Quality. 2001;30(6):1919-26.
[46] Koul B, Yakoob M, Shah MP. Agricultural waste management strategies for environmental sustainability. Environmental Research. 2022; 206:112285.

Cilt 11, Sayı 4, Sayfa 11-17, 2022 Volume 11, Issue 4, Page 11-17, 2022

Araştırma Makalesi https://doi.org/10.46810/tdfd.1116882 Research Article

Türk Doğa ve Fen Dergisi
Turkish Journal of Nature and Science
www.dergipark.gov.tr/tdfd

Synthesis and Characterization of $MoSi_2$ Particle Reinforced AlCuMg Composites by Molten Salt Shielded Method

Mehmet AKKAŞ[1,2*]

[1] Kastamonu University, Faculty of Engineering and Architecture, Department of Mechanical Engineering, Kastamonu, Türkiye
[2] Istanbul Technical University, Faculty of Chemical and Metallurgical Engineering, Department of Metallurgical and Materials Engineering, İstanbul, Türkiye
Mehmet AKKAŞ ORCID No: 0000-0002-0359-4743

**Corresponding author: mehmetakkas@kastamonu.edu.tr, akkasmehmet@itu.edu.tr*

(Received: 15.05.2022, Accepted: 03.09.2022, Online Publication: 28.12.2022)

Keywords
Molten salt shielded,
AlCuMg composite,
Powder metallurgy,
Microstructure,
Sintering,
Mechanical properties,
$MoSi_2$

Abstract: AlCuMg and its alloys are the most preferred composite materials in areas such as automotive, aerospace and aerospace industries due to their positive properties such as high corrosive properties, heat resistance, high strength and toughness. However, the inadequacy of these alloys in terms of wear and mechanical properties is one of the problems encountered in the industry. As a result of the literature review, it has been determined that there are almost no studies to improve the mechanical properties of these alloys. In this study, $MoSi_2$ particles in different percentages were added to AlCuMg matrix and produced by powder metallurgy method. The aim is to improve the mechanical properties of AlCuMg matrix composite material and to perform characterization processes. Molten salt shielded synthesis/sintering process was used as a protective atmosphere environment for the produced samples to protect them from oxidation during sintering. In salt-protected synthesis, potassium bromide (KBr) was preferred as the salt. After the synthesis process, Scanning Electron Microscope (SEM), Energy Dispersion Spectroscopy (EDS), X-Ray Diffractometry (XRD) analyzes were applied respectively as characterization processes. In addition, microhardness test was performed to determine the mechanical properties of the produced composites. It has been determined that $MoSi_2$ particles reinforced to AlCuMg alloy increase the mechanical properties of AlCuMg composite material because they have high values in terms of hardness and melting temperature. The hardness of the unreinforced sample is approximately 90 $HV_{0.1}$. According to the addition of 5, 10 and 15% $MoSi_2$, the hardness of the samples is 266, 317 and 422 $HV_{0.1}$, respectively. The hardness of the $MoSi_2$ added samples was higher than the non-reinforced sample.

$MoSi_2$ Parçacık Takviyeli AlCuMg Kompozitlerin Erimiş Tuz Korumalı Yöntem ile Sentezi ve Karakterizasyonu

Anahtar Kelimeler
Erimiş tuz korumalı,
AlCuMg kompozit,
Toz metalurjisi,
Mikroyapı,
Sinterleme,
Mekanik özellikler,
$MoSi_2$

Öz: AlCuMg ve alaşımları yüksek korozif özellikleri, ısıl direnci, yüksek mukavemet ve tokluk gibi pozitif özelliklerinden dolayı otomotiv, havacılık ve uzay endüstrisi gibi alanlarda en çok tercih edilen kompozit malzemeler olarak karşımıza çıkmaktadır. Ancak, bu alaşımların aşınma ve mekanik özellik bakımından yetersiz olmaları endüstride karşılaşılan problemlerden biridir. Literatür taraması sonucunda bu alaşımların mekanik özelliklerini iyileştirmeye yönelik neredeyse yok denecek kadar az çalışmaların mevcut olduğu tespit edilmiştir. Bu çalışmada AlCuMg matrisine farklı yüzde oranlarında $MoSi_2$ parçacıkları takviye edilerek toz metalurjisi yöntemi ile üretilmiştir. Amaç, AlCuMg matrisli kompozit malzemenin mekanik özelliklerini iyileştirerek karakterizasyon işlemlerinin yapılmasıdır. Üretilen numuneler için koruyucu atmosfer ortamı olarak, sinterleme esnasında oksidasyondan korumak için erimiş tuz korumalı sentez/sinterleme (molten salt shielded synthesis/sintering process) işlemi uygulanmıştır. Tuz korumalı sentez uygulamasında tuz olarak potasyum bromür (KBr) tercih edilmiştir. Sentezleme işlemi sonrasında karakterizasyon işlemleri olarak sırasıyla, Taramalı Elektron Mikroskobu (SEM), Enerji Dağılım Spektroskopisi (EDS), X-Işını Difraktometresi (XRD) analizleri uygulanmıştır. Buna ek olarak, üretilen kompozitlerin mekanik özelliklerini belirlemek için mikrosertlik testi yapılmıştır. AlCuMg alaşımına takviye edilen $MoSi_2$ parçacıkları, sertlik ve ergime sıcaklığı olarak yüksek değerlere sahip olduğu için AlCuMg kompozit malzemesinin mekanik özelliklerini arttırdığı tespit edilmiştir. Takviyesiz olan numunenin sertliği yaklaşık 90 $HV_{0,1}$'tir. % 5, 10 ve 15 $MoSi_2$ ilavesine göre numunelerin sertliği sırasıyla 266, 317 ve 422 $HV_{0,1}$'tir. $MoSi_2$ katkılı numunelerin sertliği, takviyesiz üretilen numuneden daha yüksek çıkmıştır.

1. INTRODUCTION

Among the recently applied methods, AlCuMg alloys produced by powder metallurgy (PM) were found to be remarkable. Chemical composition control of the alloy can be achieved with the PM method. Powder metallurgy has been developed as an alternative to production methods such as casting, machining, hot and cold pressing. By obtaining composites by powder metallurgy method, materials such as wear resistance, corrosion resistance, surface friction and surface tension can be increased. Composite materials have an indispensable place among the material groups used in engineering applications. As a result of the development of thinner and lighter composites by increasing the strength/weight ratio, the unit cost of production and operating expenses is reduced. Composite materials with very good mechanical properties are produced with AlCuMg alloys, which are successful in terms of lightness and strength. AlCuMg and its alloys are preferred as high engineering alloys in fields such as aerospace, automotive and biomedical due to their excellent heat resistance, corrosion resistance, toughness and strength [1-6]. In addition, these materials are used in industrial and medical applications such as machinery equipment and building materials, medical devices and vehicles, as well as advanced applications such as electronic devices, spacecraft, and many products that facilitate daily life such as super-elastic eyeglass frames, telephone antennas [7,8]. In recent years, it has become widespread in applications in the field of robotics. However, in the industrial use of AlCuMg and its alloys, problems are encountered in terms of mechanical properties and wear properties [9]. Due to these problems, since the mechanical properties and wear properties of AlCuMg alloy are low, it has been produced by adding $MoSi_2$ particles to this alloy by powder metallurgy method. As the abrasion resistance and mechanical properties of the produced samples will increase, a gap needed in the industry will be closed.

Tang et al. In 1997, they carried out the study. In experimental studies, mechanical alloying, SEM, XRD and DSC analyzes were performed. As a result, they successfully produced the Cu-Al-Ni alloy. In their results, they emphasized that the microhardness values increased with the increase of mechanical time [10]. Du et al. In 2017, they carried out the study. The materials used in this experimental study include commercial purity Al, commercial purity crystalline Si, Al-5C master alloys were used. Al-Si based composites reinforced with SiCp can be used in automotive, aerospace and aerospace industries. As a result, in this study, Al-Si composites were made and the effect of SiC on microstructures, mechanical properties and heat treatment procedures were investigated [11]. Karakulak et al. In 2014, they carried out the study. In this experimental study, alloying elements (Si, Ti, Cr, Cu, Mg, Ni) were added to Aluminum. They aimed to improve the mechanical properties of Al alloys and aluminum. As a result, the wear and hardness resistances of aluminum were higher than the matrix composites. Their microstructure and processing details have been studied in the literature [12]. Alizadeh et al. In 2017, they conducted a study. It is aimed to strengthen super high strength nanostructured B4C, Al-2Cu aluminum alloy matrix composites. As a result, they found that increasing the content of B_4C particles increased the matrix grain size [13]. Mandala and Viswanathanb conducted a study. In this experimental study, the effect of heat treatment on microstructure and SiC Aluminum-based 2124 alloy with 10% by weight silicon carbide (SiC) particle reinforced composite was prepared. As a result, they emphasized that the size of SiC particles was reduced after hot rolling [14]. Elkady et al. In 2019, they carried out a study. In this experimental study, Al / Ni-SiC composite was prepared and it was aimed to absorb the Al matrix composite by microwave. As a result, they found that Ni-SiC particles were homogeneously distributed throughout Al [15]. Vrsalović et al. In 2018, they carried out the study. In the experimental study, the effects of heat treatment on the corrosion properties of CuAlNi alloy were analyzed. As a result, the increase in the polarization resistance values of the heat-treated CuAlNi alloy revealed a beneficial effect on the corrosion resistance of the CuAlNi alloy in NaCl solution [16].

The aim of this study is to investigate the effect of the addition of $MoSi_2$ particles on the microstructure and mechanical properties of AlCuMg alloy produced by powder metallurgy method. In this study, the changes in the microstructure and mechanical properties of $MoSi_2$ reinforced AlCuMg composites pressed at constant pressing pressure and sintered at constant temperature were compared.

2. EXPERIMENTAL STUDIES

To be used in the experiments, 4 (four) kinds of alloys were produced by powder metallurgy method. Al, Cu, Mg and $MoSi_2$ powders with approximately 99.9% purity and a grain size of 325 mesh were used in the production of the alloys. In this study, it was produced by powder metallurgy method by adding $MoSi_2$ particles at different rates (5, 10 and 15%) to AlCuMg alloy. For this purpose, firstly, powders for AlCuMg alloy $MoSi_2$ particles were prepared by weighing according to the percentage chemical composition given in Table 1.

Table 1. Chemical compositions of the produced test samples

Sample No	Al (wt %)	Cu (wt %)	Mg (wt %)	$MoSi_2$ (wt %)
1	90	5	5	-
2	85	5	5	5
3	80	5	5	10
4	75	5	5	15

In order to prepare the mixtures, in order to obtain a homogeneous mixture by mixing the pure metal powders thoroughly with each other, an 88 type, closed powder chamber, two kg powder capacity, three-dimensional rotary mixing mixer was used. The powder chamber of this mixer is especially closed type, and after the powder is placed in it, its lid is tightly closed in order to cut off the relationship between the external environment and the powders. After the mixer is started, the powder chamber can rotate 360 degrees in all directions so that the powder can be mixed thoroughly, thus ensuring that the powders are thoroughly mixed with each other. In the pressing application, 600 MPa pressure was applied to the samples as pressing pressure. The sintering process of the produced pellets was carried out with an atmosphere-controlled heat treatment furnace (Protherm) in the Mechanical Engineering Laboratories of the Faculty of Engineering and Architecture of Kastamonu University. The sintering process was carried out in an argon atmosphere at 550 °C for 1 hour.

The sintering process was completed in a total of 180 minutes. In order to discharge the wastes, the sintering temperature was increased to 550 °C in 60 minutes at a rate of 10 °C/minute. Then, the sintering temperature was kept at 550 °C for 60 minutes at a constant temperature. The cooling process of the samples was cooled to room temperature in 60 minutes under atmosphere control.

Metallographic processes were applied to the samples for scanning electron microscopy (SEM) and Energy Dispersive Spectrum (EDS) analyzes of the samples. These applied metallographic processes were performed as sanding, polishing and etching, respectively. The surfaces of the samples were sanded with 200, 360, 600, 1000, 1200 and 2000 mesh abrasives, respectively. Afterwards, the surfaces of the samples were polished with 3 and 1 μ diamond suspensions, respectively. Finally, the etching reagent was prepared by using 95 ml of distilled water, 2.5 ml of nitric acid (HNO3), 1.5 ml of Hydrochloric acid (HCl), 1 ml of Hydrofluoric acid (HF), and they were etched with this reagent by immersion for 20 seconds.

After the samples were etched, SEM images were taken from the "FEI QUANTA 250 FEG" brand device in Kastamonu University Central Research Laboratories. XRD measurements of the samples were made with the Bruker D8 Advance brand device in Kastamonu University Central Research Laboratories. It was investigated as a mechanical property how the hardness values due to the applied pressing pressure and MoSi2 reinforcement and sintering temperature for the samples produced in this study were affected. In order to determine the hardness measurements of the samples in a healthy way, measurements were made from at least 5 points and the average results of the measurements were taken into consideration.

3. RESULTS AND DISCUSSION

3.1. SEM Analysis Results

SEM images of $MoSi_2$ reinforced AlCuMg composites produced by powder metallurgy method were taken and evaluations were made according to the obtained images. When the SEM images of the sample number 1 given in Figure 1 are examined, the AlCuMg matrix structure is clearly seen.

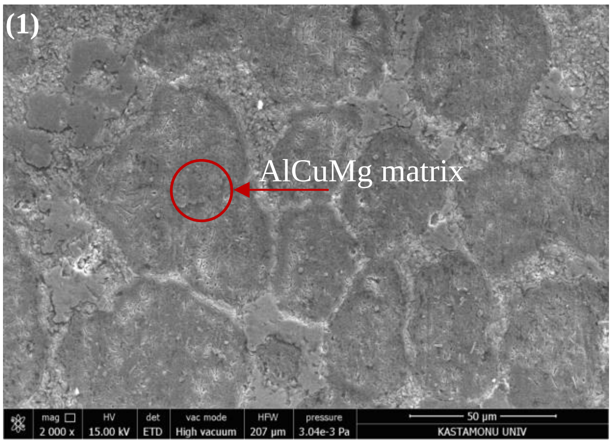

Figure 1. SEM image of sample number 1 produced

SEM images of AlCuMg composites reinforced with MoSi2 in different ratios (5, 10 and 15%) produced by powder metallurgy method were taken and evaluations were made according to the obtained images. When the SEM images of samples 2, 3 and 4 given in Figure 2 are examined, the AlCuMg matrix structure is clearly seen. In addition, it is seen that $MoSi_2$ particles are homogeneously dispersed in the AlCuMg matrix [1,17,18].

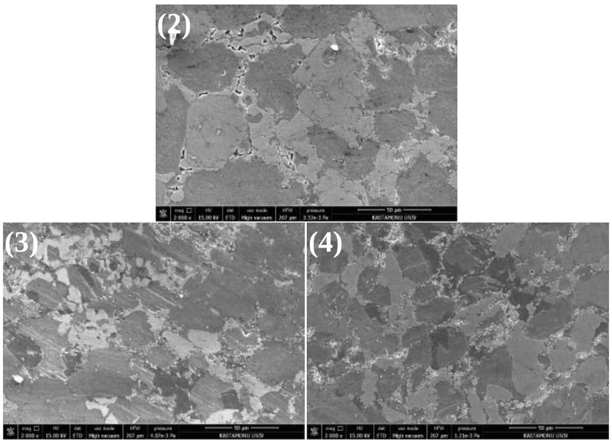

Figure 2. SEM images of samples 2, 3 and 4 produced

Partially cracks and pores are seen in the produced samples. When the SEM images given are examined, it is clearly seen that the amount of pores decreases as the addition of $MoSi_2$ increases. Besides, in the SEM images given, it is seen that MoSi2 particles are homogeneously distributed in the internal structure. It was interpreted that the homogeneous distribution of $MoSi_2$ particles in the internal structure resulted from the mixing and sintering process. This is an expected situation. There are studies in the literature that support this result. In addition, when the SEM images given are examined, the AlCuMg structure used as the matrix is clearly seen. $MoSi_2$ particles used as reinforcements are similar to each other and generally have sharp corners and irregular geometry [19-21]

3.2. SEM-EDS Analysis Results

SEM-EDS analyzes of AlCuMg, AlCuMg-$MoSi_2$ composite samples produced by powder metallurgy method are given in Figures 3, 4 and 5, respectively. When the given SEM-EDS analysis results are examined, it is clearly seen that the results support the chemical composition of the produced samples. In addition, different ratios of Al, Cu, Mg, Mo and Si were found in the internal structures of the produced samples.

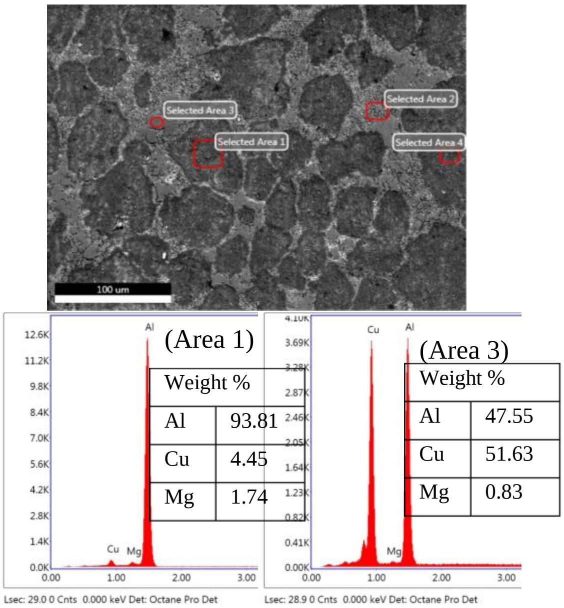

Figure 3. SEM-EDS analysis result of sample number 1 produced

When the SEM-EDS analysis results given in Figure 3 were examined, it was determined that the produced AlCuMg composite sample supported the chemical compositions. According to the results of EDS analysis taken from the selected area 1 in the internal structure of the produced AlCuMg composite sample, it was determined that it was 93.81% Al, 4.45% Cu and 1.74% Mg. In addition, according to the results of the EDS analysis taken from the selected area 3, it was determined that there are 47.55% Al, 51.63% Cu and 0.83% Mg.

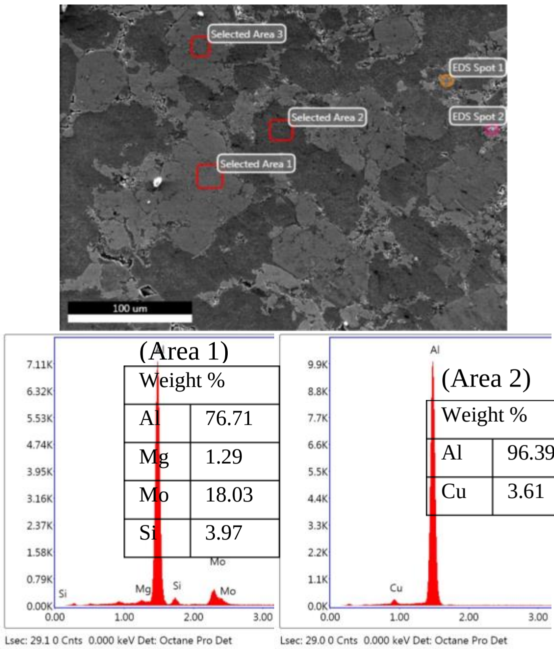

Figure 4. SEM-EDS analysis result of the 2nd sample produced

When the SEM-EDS analysis results given in Figure 4 were examined, it was determined that the produced AlCuMg-$MoSi_2$ composite sample supported the chemical compositions. In the internal structure of the produced AlCuMg-$MoSi_2$ composite sample, it was determined that 76.71% Al, 1.29% Mg, 18.03% Mo and 3.97% Si were determined according to the EDS analysis result taken from the region specified as selected area 1. In addition, it was determined that 96.39% Al and 3.61% Cu were obtained according to the EDS analysis result taken from the region specified as selected area 2.

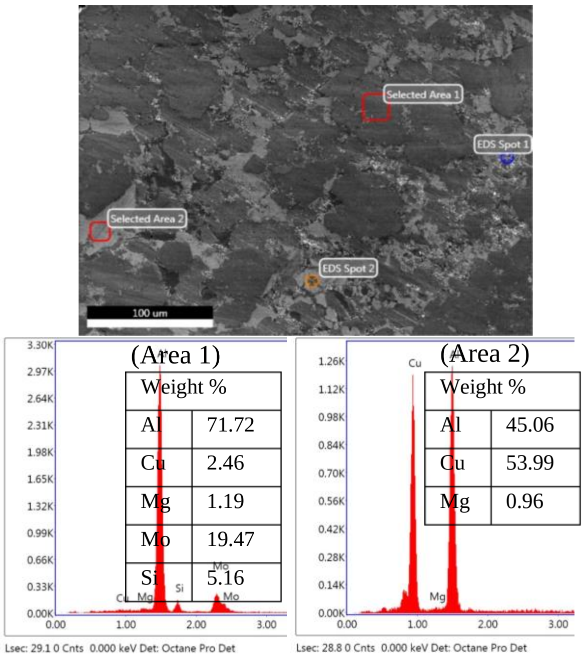

Figure 5. SEM-EDS analysis result of the 3rd sample produced

When the SEM-EDS analysis results given in Figure 5 were examined, it was determined that the produced AlCuMg-$MoSi_2$ composite sample supported the chemical compositions. According to the results of the EDS analysis taken from the selected area 1 in the internal structure of the produced AlCuMg-$MoSi_2$ composite sample, it was determined that there are 71.72% Al, 2.46% Cu, 1.19% Mg, 19.47% Mo and 5.16% Si. In addition, according to the results of the EDS analysis taken from the region specified as selected area 2, 45.06% Al, 53.99% Cu and 0.96% Mg were determined.

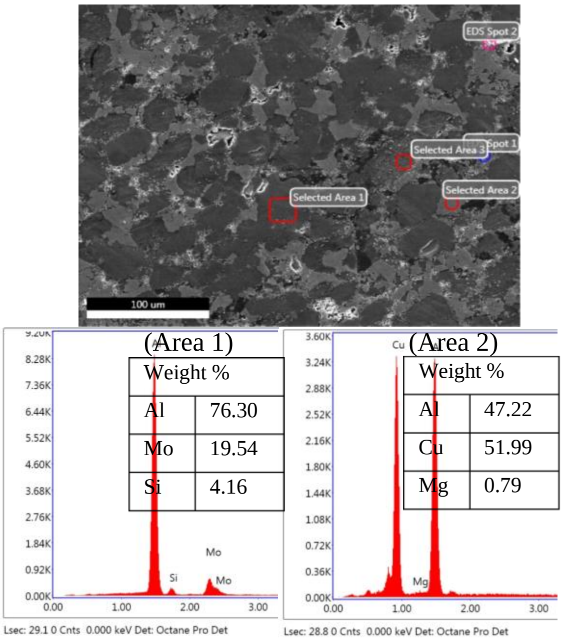

Figure 6. SEM-EDS analysis result of sample number 4 produced

When the SEM-EDS analysis results given in Figure 6 were examined, it was determined that the produced AlCuMg-$MoSi_2$ composite sample supported the chemical compositions. According to the results of EDS analysis taken from the selected area 1 in the internal structure of the produced AlCuMg-$MoSi_2$ composite sample, 76.30% Al, 19.54% Mo and 4.16% Si were determined. In addition, according to the results of the EDS analysis taken from the selected area 2, it was determined that there are 47.22% Al, 51.99% Cu and 0.79% Mg.

3.3. XRD Analysis Results

XRD graphics of AlCuMg and AlCuMg-$MoSi_2$ composites produced by powder metallurgy method are given in Figure 7. When the given XRD graph was examined, it was determined that Al_2CuMg, AlCuMg, Al_2Cu, $Al_{22}Mo_5$, $Mg_{3.78}Al_{4.22}$, Cu_3Mo_2, Cu_6Mo_5, $Si_{1.91}Al_{4.09}$, $Mg_2Al_4Si_5$, MgMo and Al phases were formed. In addition, it is clearly seen that the Cu_3Mo_2, $Al_{22}Mo_5$, Al_2CuMg phases are dominant. Similar peaks are also seen in studies conducted in the literatüre [22-25]

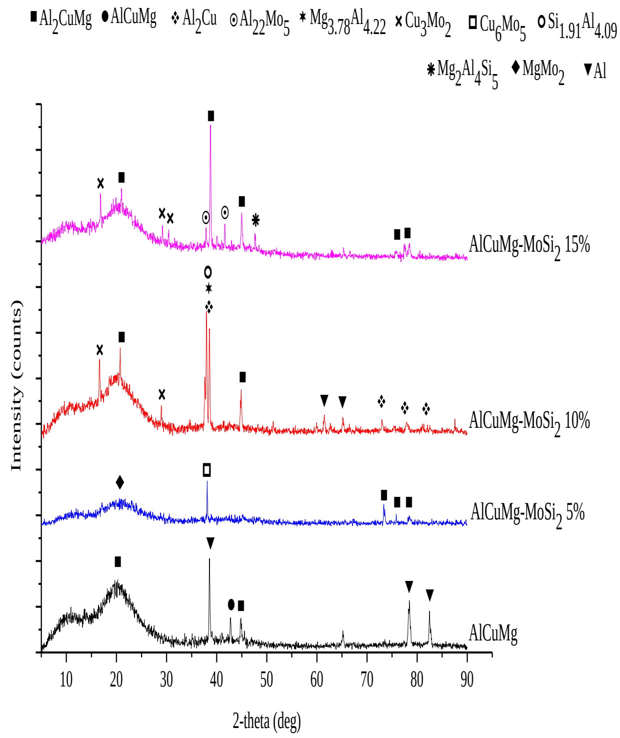

Figure 7. XRD graphs of AlCuMg and AlCuMg-MoSi2 composites

During the sintering process, the above-mentioned phases were formed between Al, Cu, Mg, Mo and Si. In addition, it was determined that the intensity of Cu3Mo2, Al22Mo5, Al2CuMg phases increased as the MoSi2 reinforcement ratios increased in the produced composite samples. The peaks detected in this study were also supported by other studies in the literatüre [22,25]. In addition, whether these precipitates formed in these structures are formed or not is proved by XRD, and the results obtained from the XRD analysis have been found to support the results of point and area EDS analysis made in SEM examinations.

3.4. Microhardness Analysis Results

The microhardness graph of the produced samples is given in Figure 8. Hardness measurements were taken from the sample surface along a line line at 100 μm intervals. The hardness of the unreinforced sample is approximately 90 $HV_{0.1}$. According to the addition of 5, 10 and 15% $MoSi_2$, the hardness of the samples is 266, 317 and 422 $HV_{0.1}$, respectively. The hardness of $MoSi_2$ added samples is higher than the sample produced without reinforcement. This increase was interpreted to be related to the presence of carbide and formed hard phases [26-30]. The use of $MoSi_2$ as reinforcement led to the formation of Cu_3Mo_2, $Al_{22}Mo_5$ and Al_2CuMg phases, and as a result it was found to contribute to the increase in hardness.

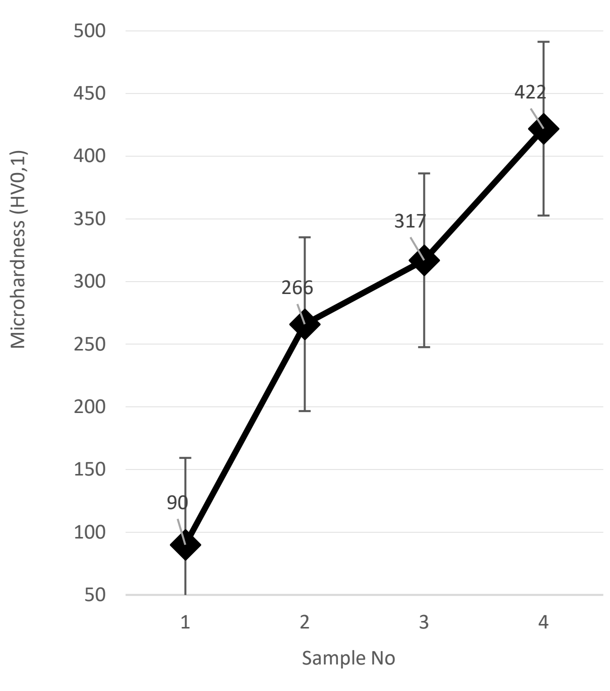

Figure 8. Microhardness graph for the composites

4. GENERAL RESULTS

In this study, $MoSi_2$ reinforced AlCuMg composites were successfully produced by powder metallurgy method. As the production parameter, cold pressing at 600 MPa pressure and sintering process at 550 ℃ in argon atmosphere for 1 hour were performed. SEM, SEM-EDS, XRD and microhardness analysis results of these produced samples were examined. As a result of the studies carried out; $MoSi_2$ reinforced AlCuMg composites were successfully subjected to pressing and sintering by powder metallurgy method. As a result of SEM analysis, it was clearly determined that the amount of pores decreased as the addition of $MoSi_2$ increased. In addition, it was determined that $MoSi_2$ particles were homogeneously distributed in the internal structure in the SEM images taken. It was interpreted that the homogeneous distribution of $MoSi_2$ particles in the internal structure resulted from the mixing and sintering process in the three-dimensional turbula. In the SEM-EDS analysis results of the produced samples, it was clearly determined that the samples supported the chemical compositions. In addition, it has been reported that the produced samples have different ratios of Al, Cu, Mg, Mo and Si in their internal structures. From the XRD analysis results, it was determined that Al_2CuMg, AlCuMg, Al_2Cu, $Al_{22}Mo_5$, $Mg_{3.78}Al_{4.22}$, Cu_3Mo_2, Cu_6Mo_5, $Si_{1.91}Al_{4.09}$, $Mg_2Al_4Si_5$, MgMo and Al phases were formed. In addition, it was determined that Cu_3Mo_2, $Al_{22}Mo_5$, Al_2CuMg phases were dominant. It was determined that the intensity of the Cu_3Mo_2, $Al_{22}Mo_5$, Al_2CuMg phases increased as the $MoSi_2$ reinforcement ratios increased in the produced composite samples. The hardness of the unreinforced sample is approximately 90 $HV_{0.1}$. According to the addition of 5, 10 and 15% $MoSi_2$, the hardness of the samples is 266, 317 and 422 $HV_{0.1}$, respectively. The hardness of the $MoSi_2$ added samples was higher than the non-reinforced sample.

Acknowledgement

This study was conducted within the scope of the KÜ-BAP01/2020-8 projects supported by Kastamonu University Scientific Research Projects Unit.

REFERENCES

[1] Sharma S, Patyal V, Sudhakara P, Singh J, Petru M, Ilyas RA. Mechanical, morphological, and fracture-deformation behavior of MWCNTs-reinforced (Al–Cu–Mg–T351) alloy cast nanocomposites fabricated by optimized mechanical milling and powder metallurgy techniques. Nanotechnology Reviews. 2022;11(1):65-85.

[2] Wang SC, Starink MJ, Gao N. Precipitation hardening in Al–Cu–Mg alloys revisited. Scripta Materialia. 2006;54(2):287-291.

[3] Varol T, Canakci A, Ozsahin S. Modeling of the prediction of densification behavior of powder metallurgy Al–Cu–Mg/B4C composites using artificial neural networks. Acta Metallurgica Sinica (English Letters). 2015;28(2):182-195.

[4] Farajollahi R, Aval HJ, Jamaati R, Hájovská Z, Nagy Š. Effects of pre-and post-friction surfacing heat treatment on microstructure and corrosion behavior of nickel-aluminide reinforced Al-Cu-Mg alloy. Journal of Alloys and Compounds. 2022;906:164211.

[5] Rodríguez-Cabriales G, Lometo-Sánchez AM, Guía-Tello JC, Medrano-Prieto HM, Gutiérrez-Castañeda EJ, Estrada-Guel I, Martínez-Sánchez R. Synthesis and characterization of Al-Cu-Mg system reinforced with tungsten carbide through powder metallurgy. Materials Today Communications. 2020;22:00758.

[6] Qiu T, Wu M, Du Z, Chen G, Zhang L, Qu X. Microstructure evolution and densification behaviour of powder metallurgy Al–Cu–Mg–Si alloy. Powder Metallurgy. 2020;63(1):54-63.

[7] Al-Nima RRO, Al-jiboori MAH. Manufacturing Al-Cu-Mg Alloys and Studying Various Mechanical Properties. Advances in Mechanics. 2021;9(3):91-311.

[8] Wu R, Zhou K, Yang Z, Qian X, Wei J, Liu L, Wang L. Molten-salt-mediated synthesis of SiC nanowires for microwave absorption applications. CrystEngComm. 2013;15(3):570-576.

[9] Gezici LU, Özer E, Sarpkaya İ, Çavdar U. The effect of SiC content on microstructural and tribological properties of sintered B4C and SiC reinforced Al–Cu–Mg–Si matrix hybrid composites. Materials Testing. 2022;64(4):502-512.

[10] Tang SM, Chung CY, Liu WG. Preparation of CuAlNi-based shape memory alloys by mechanical alloying and powder metallurgy method. Journal of materials processing technology. 1997;63(1-3):307-312.

[11] Du X, Gao T, Liu G, Liu X. In situ synthesizing SiC particles and its strengthening effect on an Al–Si–Cu–Ni–Mg piston alloy. Journal of Alloys and Compounds. 2017; 695:1-8.
[12] Karakulak E, Yamanoğlu R, Erten U, Zeren A, Zor S, Zeren M. Investigation of corrosion and mechanical properties of Al–Cu–SiC–xNi composite alloys. Materials & Design. 2014;59:33-37.
[13] Alizadeh A, Maleki M, Abdollahi A. Preparation of super-high strength nanostructured B4C reinforced Al-2Cu aluminum alloy matrix composites by mechanical milling and hot press method: microstructural, mechanical and tribological characterization. Advanced Powder Technology. 2017;28(12):3274-3287.
[14] Mandal D, Viswanathan S. Effect of heat treatment on microstructure and interface of SiC particle reinforced 2124 Al matrix composite. Materials Characterization. 2013;85:73-81.
[15] Elkady OA, Abolkassem SA, Elsayed AH, Hussein WA, Hussein KF. Microwave absorbing efficiency of Al matrix composite reinforced with nano-Ni/SiC particles. Results in Physics. 2019;12:687-700.
[16] Vrsalović L, Ivanić I, Kožuh S, Gudić S, Kosec B, Gojić M. Effect of heat treatment on corrosion properties of CuAlNi shape memory alloy. Transactions of nonferrous metals society of china. 2018;28(6):1149-1156.
[17] Akkaş M, Boushiha, KFI. Investigation of WC Reinforced CuNiSi Composites Produced by Mechanical Alloying Method. El-Cezeri Journal of Science and Engineering. 2021;8(2):592-603.
[18] Guo X, Deng Y, Zhang J, Zhang X. Effect of grain boundary on the precipitation behavior and hardness of Al-Cu-Mg alloy bicrystals during stress-aging. Materials Science and Engineering: A. 2017;683:129-134.
[19] Gao YY, Qiu F, Geng R, Zhao WX, Yang DL, Zuo R, Jiang QC. Preparation and characterization of the Al-Cu-Mg-Si-Mn composites reinforced by different surface modified SiCp. Materials Characterization. 2018;141:156-162.
[20] Manohar G, Pandey KM, Maity SR. Characterization of Boron Carbide (B4C) particle reinforced aluminium metal matrix composites fabricated by powder metallurgy techniques–A review. Materials Today: Proceedings. 2021;45:6882-6888.
[21] Sameezadeh M, Farhangi H, Emamy M. Structural characterization of AA 2024-MoSi2 nanocomposite powders produced by mechanical milling. International Journal of Minerals, Metallurgy, and Materials. 2013;20(3):298-306.
[22] Susila AB, Sugihartono I, Marpaung MA. Study on mechanical properties of Metal Matrix Composites (MMCs) Al-Cu-Mg/SiCp with Powder Metallurgy. In Journal of Physics: Conference Series. 2019;1402(4):044109.
[23] Mann RED, Hexemer RL, Donaldson IW, Bishop DP. Hot deformation of an Al–Cu–Mg powder metallurgy alloy. Materials Science and Engineering: A. 2011;528(16-17):5476-5483.
[24] Witusiewicz VT, Bondar AA, Hecht U, Stryzhyboroda OM, Tsyganenko NI, Voblikov VM, Velikanova TY. Thermodynamic re-modelling of the ternary Al–Mo–Ti system based on novel experimental data. Journal of Alloys and Compounds. 2018;749:1071-1091.
[25] Li Z, Chen L, Zhang X, Zhao G, Zhang C. Strengthening mechanism and anisotropy of mechanical properties of Si3N4p/Al-Mg-Si composites fabricated by sintering and extrusion. Materials & Design. 2021;210:110111.
[26] Özgün Ö, Erçetin A. Toz metalurjisi metoduyla üretilen Cr-C takviyeli Cu matrisli kompozitlerin mikroyapı ve mekanik özellikleri . Türk Doğa ve Fen Dergisi. 2017;6(2):1-6 .
[27] Kim YK, Yu JH, Kim HS, Lee KA. In-situ carbide-reinforced CoCrFeMnNi high-entropy alloy matrix nanocomposites manufactured by selective laser melting: Carbon content effects on microstructure, mechanical properties, and deformation mechanism. Composites Part B: Engineering. 2021;210:108638.
[28] Zamharir MJ, Zakeri M, Razavi M, Asl MS. Effect of co-addition of WC and MoSi2 on the microstructure of ZrB2–SiC–Si composites. International Journal of Refractory Metals and Hard Materials. 2022;103:105775.
[29] Polat S. Production of ZnFe2O4 Doped Carbon Cloth-Based Flexible Composite Electrodes for Supercapacitors. Türk Doğa ve Fen Dergisi. 2021;10:199-205.
[30] Ercetin A. Application of the hot press method to produce new Mg alloys: Characterization, mechanical properties, and effect of Al addition. Journal of Materials Engineering and Performance. 2021;30(6):4254-4262.

Cilt 11, Sayı 4, Sayfa 18-22, 2022 Volume 11, Issue 4, Page 18-22, 2022

Araştırma Makalesi https://doi.org/10.46810/tdfd.1097682 Research Article

Türk Doğa ve Fen Dergisi
Turkish Journal of Nature and Science
www.dergipark.gov.tr/tdfd

The Western Maksurah of the Great Mosque of Diyarbakir, Research and Excavation

Fatma Meral HALİFEOĞLU[1*], Martine ASSENAT[2]

[1] Dicle University, Architecture Faculty, Architecture Department, Diyarbakır, Türkiye
[2] Paul-Valery University, Archaeological Faculty, Histoire Department, Montpellier, France
Fatma Meral HALİFEOĞLU ORCID No: 0000-0003-2032-3774
Martine ASSENAT ORCID No: 0000-0001-8143-8511

Corresponding author: mhalife@gmail.com

(Received: 04.04.2022, Accepted: 03.09.2022, Online Publication: 28.12.2022)

Keywords
Diyarbakır Great Mosque, Western Maksurah, research excavation, restoration, conservation

Abstract: The Great Mosque of Diyarbakır is located in the district of Cami-i Kebir, in the northwestern quarter of the walled ancient city. The space occupied by the mosque has been recognized as the ancient forum of the city of Amida. To the east, it is located along the urban cardo opposite the Han of Hasan Pasa. The south of the monumental complex overlooks the traditional bazaar of Sipahi. To the north and east the mosque is surrounded by walls. Currently, around the courtyard, the Hanefi prayer room is located to the south, two maksurahs to the west and east and the Mesudiye medressa with its portico to the north, as well as the Shafi's section. The mosque has three entrances to the east, west and north. In the center, on the square, there is a conical octagonal and pyramidal pointed fountain as well as a prayer room and a pool. The courtyard also contains a sun clock. Many ancient spolia can still be seen. Excavations in the Western Maksurah have provided important information for the restoration of the Great Mosque and for the understanding of its history. The results obtained for both of these issues are presented here. The evaluations made for the preservation of the excavation findings, which were deemed necessary during the restoration works in the Great Mosque, will also be explained in this study.

Diyarbakır Ulu Cami Batı Maksuresinde Araştırma Kazıları

Anahtar Kelimeler
Diyarbakır Ulu Cami, Batı Makuresi, araştırma kazısı, restorasyon, koruma

Öz: Diyarbakır Ulu Camii, surlarla çevrili antik kentin kuzeybatısında, Cami-i Kebir mahallesinde yer almaktadır. Caminin kapladığı alan, Amida şehrinin antik forumu olarak kabul edilmiştir. Doğuda, Hasan Paşa Hanı'nın karşısındaki kentsel meydan boyunca yer almaktadır. Yapı topluluğunun güneyi Sipahi Çarşısı'na bakmaktadır. Cami kuzey ve doğudan duvarla çevrilidir. Hâlihazırda avlu çevresinde güneyde Hanefiler Bölümü, batı ve doğuda iki maksure, kuzeyde Mesudiye Medresesi ile Şafiler Bölümü yer almaktadır. Caminin doğu, batı ve kuzeyden olmak üzere üç girişi vardır. Merkezde, meydanda, konik sekizgen ve piramidal sivri uçlu şadırvanın yanı sıra namazgâh ve havuz bulunmaktadır. Avluda ayrıca bir güneş saati bulunmaktadır. Birçok antik devşirme malzeme hala görülebilmektedir. Batı Maksura'da yapılan kazılar, Ulu Cami'nin restorasyonu ve tarihinin anlaşılması için önemli bilgiler sağlamıştır. Bu iki konu için elde edilen sonuçlar burada sunulmaktadır. Ulu Cami'deki restorasyon çalışmaları sırasında gerekli görülen kazı buluntularının korunması için yapılan değerlendirmeler de bu çalışmada anlatılacaktır.

1. INTRODUCTION

Between 2010 and 2017 major restoration works were carried out in the Great Mosque. They coincided with the preparation of the UNESCO nomination file, which resulted in the classification of "the cultural landscape of Diyarbakır Fortress and Hevsel Garden" as a world heritage site [1].

In order to obtain detailed information necessary for the restoration of the site, the members of the scientific committee wanted research excavations. The purpose of these was to obtain information in each section of the building before the intervention. The first interventions concerned the Hanafi prayer hall and the eastern Maksurah. In 2015 the Shafi prayer hall was excavated as well as the plot behind the Western Maksurah. Excavations were carried out behind the Shafi section and the Western Maksurah. Numerous remains were uncovered.

These excavations have provided new information about the mosque and the history of the city and have contributed to the preservation and enhancement of the city center.

These results and the information obtained present the original value of the study.

2. MATERIAL AND METHOD

In this study, first of all, the architectural features of Diyarbakır Great Mosque are briefly explained. Brief information is given from the research excavations carried out during the extensive restoration work of the building between 2010-2017. The importance of the research excavation in the restoration works is explained and the excavations made in the back area of the Western Maksurah are explained. The importance and evaluation of the findings were made.

2.1. The Location and The Structural Plan of The Great Mosque of Diyarbakır

The Great Mosque of Diyarbakir is a group of structures in Cami-i Kebir neighborhood located in the northwest quarter of the traditional urban area. The mosque is in front of Hasan Pasha public house on Gazi Street. The mosque is located off the street and its east entrance opens to a square, while its north and west wings are surrounded by a street, its south wing looks towards the traditional Sipahi (cavalry) Bazaar (figure 1).

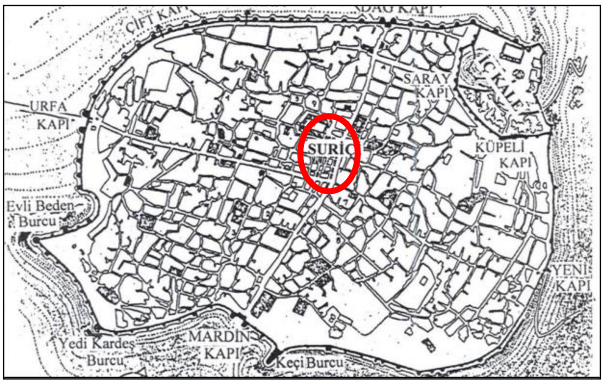

Figure 1. The Great Mosque of Diyarbakir on the Suriçi map (Gabriel,1940)

Although the construction period of the structure is not well known, we can find in each section, interventions from various periods which can infer from the inscriptions in the structure Gabriel 1940:184-194 [2]. Despite all these interventions, we have been able to keep the traditional features of the construction by integrating the art and techniques of the concerned periods.

Around the large courtyard of the building we can find to the south, the Hanafi's Section; to the east, an eastern portico (eastern maksurah), containing the library which may have been a muvakkithane and the eastern entrance; to the north, the Shafi's Section, the northern entrance, the cloister of the Mesudiye Madrasa, a traditional house and toilets; to the west another portico (western maksurah), containing the Qur'anic classrooms, and the western entrance. Some other features of the large courtyard are: the pointed octagonal pyramidal Shadirvan with a sharp pyramidal tip, the fountain built in the Ottoman period, an open-air prayer space and a pool raised by a few steps. There is also a sundial in front of the portico of the Mesudiye Madrasa (figure 2).

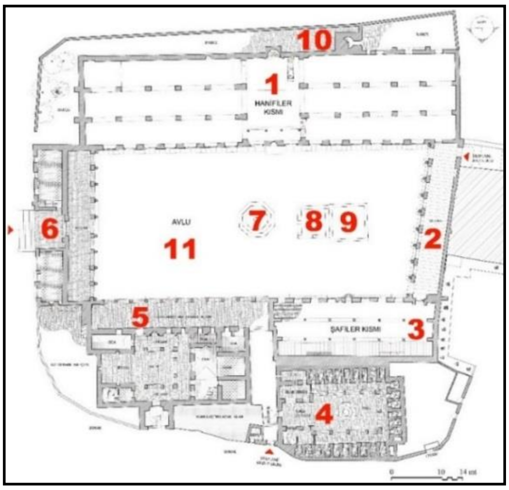

Figure 2. Plan of the Great Mosque: 1. Hanafi Section; 2. Western Maksurah; 3. Shafi Section; 4. Latrines; 5. Mesudiye Madrasa; 6. Eastern Maksurah; 7. Shadirvan; 8. Prayer Hall; 9. Pool; 10. Minaret; 11. Sundial

2.2. The Western Maksurah and Its Situation at The Rear of The Western Maksurah Before The Restoration Work

The Shafi's Section is located on the north of the ground floor, and we can find the Hanafi's entrance in the south. The entrance door of the mosque, which opens to a street, is located to the west. A significant part of the building leans on a traditional house on the outside. The stoa used to have another door, which is currently closed, near the Shafi's Section.

The façade of the courtyard of the Western Maksurah seems to have the same features as The Eastern Maksurah, but the construction period is different Assenat 2018 [3]. The ground floor consists of decorated columns, arches, and inscriptions. The same decoration can be found on the second floor but there are windows between the columns. However, we can also find windows built in the later periods on the outer façade. On the ground floor behind the stoa, there is a mortuary, a ghusl room, and a warehouse also constructed in the later periods.

Before the restoration work, as in the other sections, some damages can be seen. During the recent intervention, the mezzanine floor and the upper covering were changed into reinforced concrete, the pressure from the reinforced concrete roof led to erosion and crackings of the columns. All the decorated areas have erosion and crackings. There was significant urban pollution on the limestones' surfaces, and inappropriate work on the cement-based seals was carried out (figure 3).

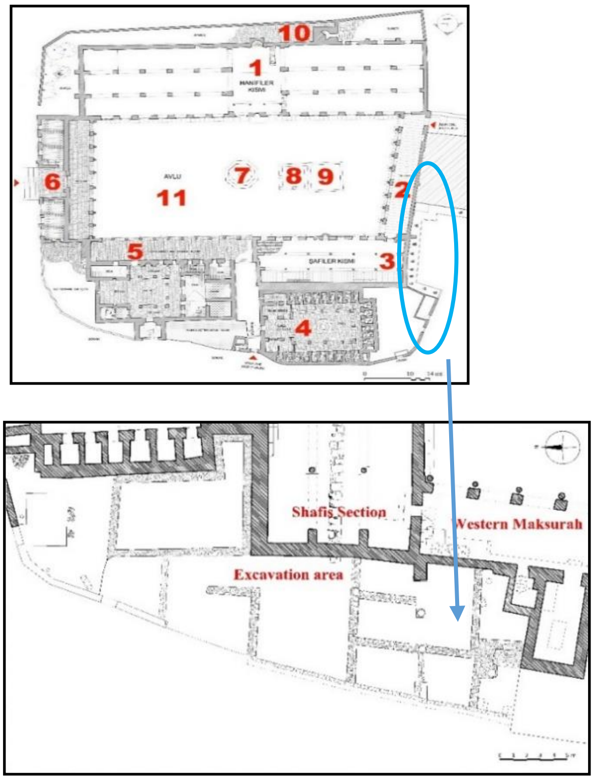

Figure 3. Excavation area

3. RESULTS

The objective of all the works carried out in the Great Mosque of Diyarbakir is the transmission of the posterity. In accordance with the recommendations of the scientific committee, the detailed information provided by the excavations made it possible to understand the originality of the structure and to preserve it. Elements that threatened the authenticity of the monument have been removed. Useful documentation and conservation work has been carried out and the rear area has been refurbished.

Furthermore various structures belonging to the Byzantine and medieval periods have been unearthed and document the history of the mosque and its immediate surroundings.

4. DISCUSSION AND CONCLUSION

The objective of all the works carried out in the Great Mosque of Diyarbakir is the transmission of the monument to the following generations. To this end, excavations, carried out in accordance with the authorized project and in accordance with the decisions taken by the scientific committee, have provided detailed information in order to preserve the historical interventions made on the structure and its originality. The elements that threatened the authenticity of the monument were removed.

Research excavations were important to preserve the historical monuments, to obtain information about them during the restoration work, and to choose the correct restoration method. As it had been done in the other parts of the Grand Mosque of Diyarbakir, the excavations behind the western maksurah have led to a useful method of conservation and correct restoration works.

So, the excavation was conducted in an area of approximately 300 square meters. The façade of a three-arched wall, taken from the frame of a traditional house, was uncovered to the south of the excavated area Ertunç 2015a; 2015b [4,5]; Aktay et alii 2015 [6]. The basalt columns and capitals of the façade were intact.

The excavations also led to numerous discoveries. Various structures belonging to the Byzantine and medieval periods have been brought to light.

In this area, walls, arches, columns, capitals, columns' bases, buttresses and rows of tiles from different periods were uncovered.

Useful documentation and conservation work was carried out, and the area at the back was reorganized.

The arch gaps were filled with mortar and stones. In the Shafi's Section, an arch door was uncovered. An elevation adjustment was made in the area of the western maksurah arc that took into account the ground level of the excavation. The door in the stoa of the western maksurah has been opened.

The cause of the humidity on the western wall of the Shafi's Section was found. Necessary drainages were installed. Restoration, conservation, and regulations works were carried out in the excavation area. Moreover, the restoration work made it possible to make correct decisions concerning the originality of the structure and its current use.

Figure 4. View of the excavated area. On the left the condemned door

*In this excavation work, some structures from different periods were uncovered. Some of them were grossly built and some others were carefully built, particularly a basalt wall that is approximately 60 cm wide.

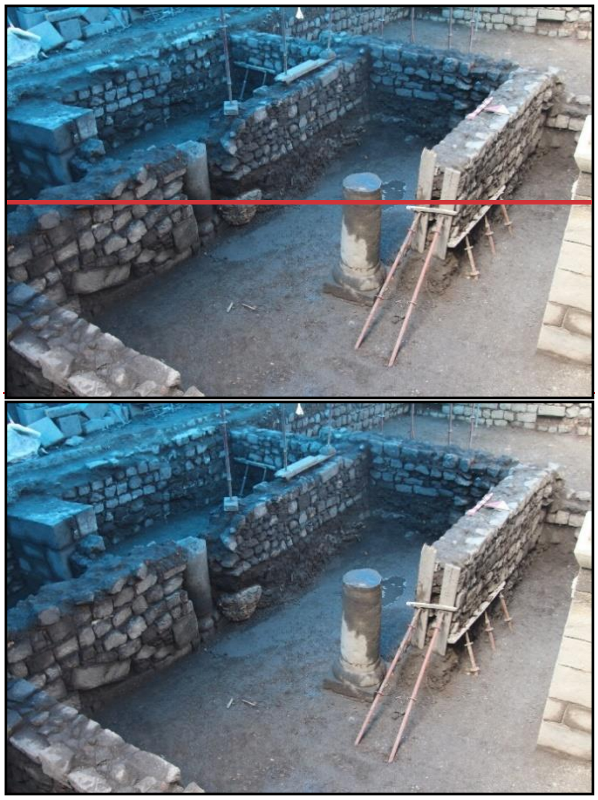

Figure 5. View of the excavations behind the Western Maksurah

* On the axis of the wall that separates the Shafi's Section from the western maksurah, in an east/west direction, a basalt buttress, a basalt column, and a basalt capital dating from the Byzantine period were uncovered.

*Parallel to the street, in a north/south direction, basalt stone walls between 150 and 200 cm high were discovered. A late-period building is located in the central area. Additionally, in the central area, basalt walls, that could be the foundation of a building of a later period, were uncovered.

Figure 6. A basalt wall that is approximately 60 cm wide.

*The use of bricks can be observed in the north of the excavation area, but the period is not determined.

In the north of the excavation area, from an undetermined period, basalt stonework.

*The arch door, which had a distinct circumference, located inside of the Shafi's Section has been entirely uncovered during the excavations.

Figure 7. Basalt stone walls between 150 and 200 cm

Excavation Conservation and Reclamation: The restoration work began in 2010 and ended in 2017. The complex is planned for both praying and visiting purposes. Therefore, during the restoration work, the complex was not completely closed. After the excavation and conservation works of the Hanifis section and the eastern maksurah, the same works were extended to the Shafi's Section and to the western maksurah Halifeoğlu 2019 [7]; Halifeoğlu & Assenat 2019 [8]; 2020 [7,9,10]. The work carried out in the western maksurah can be defined as cleaning, reinforcement, complementation, and reconstruction work. In the western maksurah, a suspension project was carried out before the intervention and the structure was suspended. Samples of mortar and dirt have been analyzed by experts. According to the new information, the project has been reshaped.

Cleaning: In all plastered surfaces and stone surfaces cleaning work was carried out. Cement-based plaster and joints were removed. The intermediate floor slab was removed by fragments with a core drilling machine. The work was carried out without causing vibrations. On the western side of the maksurah closer to the Shafi's Section, the closed-door has been opened.

Reinforcement work: The entire structure has been reinforced by injecting mortar. Metal bracelets are attached to the joints of columns. The stones have been consolidated.

Complementation work: After the cleaning work, complementation work was conducted for the missing materials.

Reconstruction: After the removal of the reinforced concrete roof, a slight wooden roof has been installed. Its surface is covered by lead sheets as in the other parts. Wooden beams were installed in the place of removed intermediate floor slabs. Wooden covers are installed. The intermediate floor slabs are reconstructed with wood. All windows and doors were reconstructed. After the removal of joint mortars, joint seals were done.

After the excavation work, a plan was drawn. Documentation and photo-shootings have been finalized. Due to the excavations, we have adjusted the difference in ground levels. A stair to climb to the street elevation level was built. In the south area, the water tank behind the lavatories has been removed. A women's bathroom and a room to perform ablution were built in this area.

The findings from the excavation were inspected by the museum's archaeologists, the science committee, and an art historian. The above-mentioned unqualified elements were removed. The conservation work was done on the wall pieces, arch wall, and the other details.

The floor was covered with basalt stones. Steps were installed because of the level differences. At the same time, wheelchair ramps were built.

REFERENCES

[1]https://www.unesco.org.tr/Home/AnnouncementDetail/303 (10.08.2020).
[2] Gabriel A. Voyages Archeologiques en Turquie Orientale. Paris: de Boccard; 1940.
[3] Assenat M. Matieres, modules et modèles: ébauches pour un lexique de la pierre, et de ses emplois historiques à Diyarbakır. In: Assenat M, editor. Les jardins de l'Hevsel: paradis intranquilles. Istanbul: Institut francais d'etudes anatoliennes. 2018.https://doi.org/10.4000/books.ifeagd.2266.
[4] Ertunç B. Diyarbakır Merkez Ulu Cami Yapı Topuluğu, Mesudiye Medresesi ve Müştemilatları Kadınlar Tuvaleti Bölümü Kazi Alanı Rölöve Raporu. Diyarbakır: Rapor Müze Müdürlüğü; Nisan 2015a.
[5] Ertunç B. Kadınlar Tuvaleti Bölümü Kazı Alanı Fotoğraf Albümü. Diyarbakır: Rapor Müze Müdürlüğü; 2015b.
[6] Aktay M, Gül A, Bedirhanoğlu Yalçınkaya E. Ulu Cami Batı Maksuresi Arka Cephesi ve Şafiler Bölümü Doğu Duvarı Önü Sondaj Kazısı. Diyarbakir: Rapor Müze Müdürlüğü; 03.03.2015.
[7] Halifeoğlu FM. Restorasyon Çalışmalarında Araştırma Kazılarının Önemi: Tarihi Diyarbakır Ulu Camı Şafiler Bölümü. 2nd Erasmus International Academic Research Symposium. Paris 11-13 October 2019. Elazığ December/Aralık; 2019. p.175-186.
[8] Assenat M, Halifeoğlu FM. Archeological Evaluation in the Shafi's Section of the Great Mosque of Diyarbakır. 2nd Erasmus International Academic Research Symposium. Paris 11-13 October 2019. Elazığ December/Aralık: 2019. p.175-186.
[9] Halifeoğlu FM, Assenat M. Evaluation of the Excavations Carried Out between 2010 and 2017 in Diyarbakır Great Mosque Complex for Restoration Work; Hanafi's Section and Eastern Maksurah. International Journal of Architectural Heritage; 2020. p. 163-181. DOI: 10.1080/15583058.2020.1765050
[10] Halifeoğlu FM, Assenat M. The Great Mosque of Diyarbakir: a contribution to understanding the monumental development of a site from antiquity to the Arab conquest Anatolian Studies, 2021 , pp. 141 – 156 DOI: 10.1017/s0066154621000089

Araştırma Makalesi https://doi.org/10.46810/tdfd.1099664 Research Article

Türk Doğa ve Fen Dergisi
Turkish Journal of Nature and Science
www.dergipark.gov.tr/tdfd

Phenolic Compounds, Organic Acid Profiles and Antioxidant Potential of *Salvia verticillata* L.

Züleyha ALMAZ[1*]

[1]Mus Alparslan University, Arts and Sciences Faculty, Molecular Biology and Genetics Department, Mus, Turkey
Züleyha ALMAZ ORCID No: 0000-0002-4532-4311

**Corresponding author: z.turkoglu@alparslan.edu.tr*

(Received: 06.04.2022, Accepted: 05.09.2022, Online Publication: 28.12.2022)

Keywords
Salvia verticillata L.,
Phenolic acid,
Organic acid,
Antioxidant

Abstract: *Salvia* genus, which is widely used in folk medicine and attracts great attention, is a rich source of polyphenols, which has been the subject of many chemical studies. Leaf and root ethanol extracts of *Salvia verticillata* L. plant sampled from Muş region were obtained by using the soxhlet extraction method. Antioxidant profiles of these extracts were defined by five different methods. Although *S. verticillata* L. leaf extract showed the best activity in all tests, it was lower than the antioxidants we used as standard. The presence of 17 phenolics, 13 organic acids, and sugars in these extracts was screened by HPLC and correlated with their antioxidant potential. In this context, the difference between the organs of the species examined and collected from a region was also revealed. Leaf extracts have been found to be rich in curcumin, which has anti-inflammatory, anti-cancer, and strong antioxidant capacity. It was determined that acetic acid, an organic acid that is also used as a food preservative, was found in very high amounts in root and leaf extracts. According to the results obtained, it can be thought that the phenolic and organic acid contents of *S. verticillata* L. may be among the parameters responsible for antioxidant activity, and they are also natural sources for pharmacological processes and the food industry.

Salvia verticillata L.'nin Fenolik Bileşikleri, Organik Asit Profilleri ve Antioksidan Potansiyeli

Anahtar Kelimeler
Salvia verticillata L,
Fenolik asit,
Organik asit,
Antioksidan

Öz: Zengin bir polifenol kaynağı olan ve çok sayıda kimyasal araştırmaya konu olan ada çayı, büyük ilgi gören ve halk hekimliğinde yaygın olarak kullanılan bir cinstir. Muş yöresinden örneklenen *Salvia verticillata* L. bitkisinin yaprak etanol ve kök etanol ekstraktları soxhlet ekstraksiyon yöntemi kullanılarak elde edilmiştir Bu ekstraktların antioksidan profili, beş farklı metod kullanılarak belirlendi. *S. verticillata* L. yaprağı ekstresi tüm testlerde en iyi aktiviteyi göstermesine rağmen standart olarak kullandığımız antioksidanlardan daha düşüktü. Bu ekstraktlarda 17 fenolik, 13 organik asit ve şekerin varlığı HPLC ile taranmış ve antioksidan potansiyelleri ile ilişkilendirilmiştir. Bu bağlamda bir bölgeden toplanan ve incelenen türlerin organları arasındaki fark da ortaya konulmuştur. Yaprak özlerinin, anti-inflamatuar, anti-kanser ve güçlü antioksidan kapasiteye sahip kurkumin açısından zengin olduğu bulunmuştur. Gıda koruyucu olarak da kullanılan bir organik asit olan asetik asidin kök ve yaprak ekstraktlarında çok yüksek miktarlarda bulunduğu belirlendi. Elde edilen sonuçlara göre *S. verticillata* L.'nin fenolik ve organik asit içeriğinin antioksidan aktiviteden sorumlu parametreler arasında olabileceği, ayrıca farmakolojik süreçler ve gıda endüstrisi için doğal kaynaklar olduğu düşünülebilir.

1. INTRODUCTION

Since ancient times, people have used plants as a solution to nutrition and health problems. With the expansion of alternative medicine and the increasing demand for health treatment, the use of therapeutic plants has increased all over the world. Among the plants that are often the subject of research to determine their health benefits is the genus *Salvia*, which belongs to the mint family. *Salvia*, which contains about 900 species and belongs to the Lamiaceae family, is an important genus used as a folk medicine in many diseases such as coronary heart disease, neuroasthenic insomnia, hepatitis, and chronic kidney failure [1]. It has been reported that different species of *Salvia* have biological activities such as antidiabetic, antioxidant, antimicrobial, anti-inflammatory, anticarcinogenic, anxiolytic, antiplasmodial, and produce various phenolic metabolites that attract attention with these properties [2, 3]. In addition, many types of *Salvia*, which are frequently used in the food industry due to herbal teas, flavoring and preservative properties, also attract great attention in the cosmetics, perfumery and pharmaceutical sectors [4, 5]. Although antioxidants such as BHT, BHA, and *ter*-butyl hydroperoxide (TBH) are widely used today to reduce the damage caused by free radicals, they are unsuitable for use in health and food fields as they can cause tumors and toxicities in the animal body [6]. *Salvia* species, one of the most common members of its family, and their isolated components have significant antioxidant activity [7]. Phenolics are the main compounds that make up the antioxidant effect of widely used sage [8]. Phenolic antioxidants scavenge free radicals by an electron transfer mechanism. The presence of the methoxy group in the phenolic structure of curcumin, which is one of them, causes its antioxidant and anti-inflammatory activity to be high. It is also a phenolic compound with strong antitumor, antiseptic, anti-carcinogenic activity [9]. In clinical studies, it has been reported that curcumin is not dangerous for humans even at high doses [10]. For these and other reasons, the desire for natural foods has led to the search for naturally occurring antioxidants.

In this study, root and leaf ethanol extracts of *S. verticillata* L. were prepared and their phenolic and organic acids profiles were investigated by HPLC. In addition, *in vitro* antioxidant tests such as DPPH and ABTS radical scavenging activities, CUPRAC and FRAP methods, reducing capacities of copper and iron ions and metal chelating activities of these extracts were performed. The results of the study and analysis were correlated with each other.

2. MATERIAL AND METHOD

2.1. The Extraction of Plant Samples

S. verticillata L. plant was collected in Mus province during the vegetation period in 2021 (38° 43' 33.0996" N; 41° 30' 44.4384" E). The identification of the collected plant samples according to the Flora of Turkey was done by Murat Kurşat (Bitlis, Turkey). The plant samples that was made into herbarium material was encoded (Z. Almaz: 4900). The leaves and roots of the plant were removed and left to dry in shade. *S. verticillata* L. leaf (*Sv*L) and root ethanol (*Sv*R) extracts were prepared by using the soxhlet extraction method.

2.2. Antioxidant Activity

2.2.1. Fe^{3+} reducing activity according to the FRAP method

The reduction of total Fe^{3+} power was performed according to the assay of Savci et al. [11]. *S. verticillata* L. extracts (15, 30 and 45 µg/mL) were added to test tubes at different concentrations and adjusted to 1 mL with deionized water. For each test tube, 500 µL of potassium ferricyanide [$K_3Fe(CN)_6$] and phosphate buffer (0.2 M, pH: 6.6) as well as plant extracts of different concentrations were added. The solution was incubated at 50°C for 20 minutes before the 500 µL of trichloroacetic acid (TCA) was added to the reaction mixture.and 500 µL of the phase was taken at the top of the mixture, 500 µL of deionized H_2O and 100 µL of $FeCl_3$ were added. The absorbances of the samples were measured by adjusting the UV visible spectrophotometer to 700 nm.

2.2.2. Cu^{2+} reducing activity according to the CUPRAC method

The copper ion (Cu^{2+}) reducing capacities of *S.verticillata* L. extracts and standard antioxidants were performed similar to the procedure used by Apak et al. [12]. Different concentrations *S. verticillata* L. extracts (15, 30, and 45 µg/mL) were added to test tubes and made up to 1 mL with deionized H_2O water. Firstly, 250 µL of $CuCl_2$ solution (0.01 M) and neocuproine solution (7.5x10^{-3} M), 1 mL of CH_3COONH_4 (1 M) buffer were transferred to each tube. After half an hour of incubation to clearly determine their reducing capacity, absorbance at 450 nm was measured.

2.2.3. $ABTS^{\cdot+}$ scavenging activity

Re [13] method was used for calculation of 2,2′-Azino-bis-3-ethylbenzothiazoline-6-sulfonic acid (ABTS) radical scavenging activities of *S. verticillata* L. extracts. First of all, solutions of potassium persulphate (2.45 mM) and ABTS (7 mM) were mixed in a 1:1 ratio. It was incubated for 12 h at room temperature in the dark. Then the absorbance of the mixture was measured at 734 nm and diluted with ethanol until an absorbance of 0.700±0.02 was reached. After adding different concentrations of extracts to the test tubes, it was made up to 200 µL with ethanol. 800 µL of ABTS was added to them. It was incubated for up to two hours. The absorbance of the extracts was measured at 734 nm.

2.2.4. $DPPH^{\cdot}$ scavenging activity

1,1-diphenyl-2-picrylhydrazyl (DPPH) radical scavenging activity of the *S. verticillata* L. extracts and standards were done to an assay of Koçpınar et al. [14]. This method is based on the removal of DPPH free radicals by reacting with antioxidants. According to this assay, the extracts at different concentrations (15, 30, and 45 µg/mL) were placed in the test tubes, were made up to be adjusted to 600 µL with ethanol. 200 µL of 1 mM DPPH radical solution was added to each test tubes. The mixture was incubated for 30 minutes at room temperature and in the dark and absorption spectra were calculated at 517 nm against the ethanol blank.

2.2.5. Fe^{2+} chelating activity

The Fe^{2+} chelating activity of *S. verticillata* L. extracts and standard antioxidants was studied, modifying the method performed by Alhafez et al. [15]. It was prepared from samples at concentrations of 15, 30 and 45 µg/mL. 2 mM solution containing 120 µL of $FeCl_2.4H_2O$ and 80 µL of distilled water was added to 60 µL of solution containing samples. After this step, the total volume was made up to 1000 µL with ethanol. To initiate the reaction, 60 µL of 5 mM ferrozine solution prepared earlier was added to the samples. The resulting solution was mixed by rapid vortexing and incubated for 10 minutes at room temperature. In the next step, the absorbance of the samples at 562 nm was measured by UV/VIS spectrophotometer.

2.3. Phenolic Substance Analysis by HPLC

Concentrations of 1 mg/mL were prepared by diluting the leaf (*Sv*L) and root (*Sv*R) extracts of *S. verticillata* L. for loading in HPLC. To determine the phenolic content by HPLC, the final concentrations of the standards were adjusted to 10 mg/mL. Then, 1% acetonitrile and acetic acid (1/9 ratio, respectively) were added to prepare the standards. Methanol was added at the same rate and stock standards were prepared. Different concentrations of 10, 25, 50, 75, and 100 µg/mL of the stock solution prepared for the standards were created to draw the standard graph [16]. The *S. verticillata* L. plant extracts we prepared earlier were diluted at 20 mg/mL concentration using standard solutions and filtered using a 0.45 µm membrane filter. HPLC analyses used for phenolic content determination were performed using 1260 Infinity II HPLC Agilent Tech. Standard chromatograms and curves generated by HPLC were used to determine the concentrations of 17 different phenolics. ACE 5 C18 (250 x 4.6 mm id) is the analytical column used for the analysis. The HPLC configuration used includes a 1260 DAD WR detector (272 nm, 280 nm, and 310 nm wavelength), a 1260 Quat Pump VL pump (flow rate 1.0 mL/min), a 1260 Vial sampler (20 µL injected), and a G7130A column furnace (28 °C).

2.4. Organic Acid and Sugar Content in The Extracts

The standards used to determine the sugar and organic acid content of *S. verticillata* L. extracts are fructose, glucose, rhamnose, tartaric acid, pyruvic acid, citric acid, maleic acid, malic acid, acetoin, fumaric acid, 2,3-butanediol, acetic acid, and succinic acid. The concentrations of the standards used were weighed to be 1 mg/mL. The standards that we will use as stocks were dissolved in falcon tubes with 0.03M H_2SO_4 (sulfuric acid). Stock standard solutions were prepared in 8 different dilutions (5, 10, 25, 50, 100, 200, 300 and 400 ppm). It was loaded on HPLC (Agilent Technologies 1260 Infinity II) and the calibration curve was calculated [17]. 0.2 ml was taken from the extracts. It was vortexed by adding 0.03M 1.8 mL H_2SO_4. The resulting mixture was centrifuged at 2000 rpm for 5 minutes and 100 µL was taken from the supernatant. It was added to ependorph containing 0.9 µL of 0.03 M H_2SO_4 and mixed. The resulting mixture was filtered through 0.45 µm pore diameter filters and transferred to approximately 0.5 mL bottles. The extracts we prepared to determine the amount of sugar and organic acid in HPLS were given to the device. 0.03 M H_2SO_4 was used as carrier phase.

2.5. Statistical Analysis of The Antioxidants

All antioxidant tests were repeated three times. Fe^{3+} and Cu^{2+} reducing activity, Fe^{2+} chelating activity results were calculated as µM Trolox equivalent in g extract (µM TE/g Extract). In other tests, the results of both the extract and the standards (DPPH· and ABTS·+ radical scavenging activities) were calculated as % radical removal, and the standards and extract results were compared. All comparisons were made using One-way ANOVA followed by Dunnett's multiple comparisons test, and values were given as mean±standard deviation (Mean±Standard Deviation). "●" symbol in comparison against BHA standard, "■" symbol in comparison against BHT standard, and "◆" symbol in comparison against ascorbic acid (AA) were used as degrees of significance, and comparison results that did not change significantly were expressed as "ns". Accordingly, one symbol (● or ■ or ◆) was expressed as meaningful, two symbols (●● or ■■ or ◆◆) were expressed as very meaningful, and three symbols (●●● or ■■■ or ◆◆◆) were expressed as highly meaningful. ●/■/◆P<0.05 (meaningful); ●●/■■/◆◆ P<0.01 (very meaningful); ●●●/■■■/◆◆◆P<0.001 (highly meaningful).

3. RESULTS AND DISCUSSION

3.1. Results of *In Vitro* Antioxidant Activity

Since various mechanisms of action may play a role in the antioxidant effects of studies on plant extracts, it is generally accepted that the application of a single antioxidant method is not sufficient to determine the free radical scavenging potential of the samples and is a limited approach. Therefore, it is considered useful to use simultaneous methods for a real test, that is, to understand the full antioxidant potential [18]. The current study has demonstrated the ability of leaf and root extracts from *S. verticillata* L. to capture DPPH· and ABTS·+ radicals, as well as reduce ferric to ferrous form (FRAP assays), to reduce Cu^{2+} into Cu^{+} (CUPRAC assay) and the analyzed antioxidant activity potentials such as the capacity to chelate (Fe^{2+} chelating activity). The antioxidant potential of the extracts is compared with standard antioxidants such as butylated hydroxyanisole (BHA), butylated hydroxytoluene (BHT), and ascorbic acid (AA) are given in Table 1. In the FRAP results obtained, it was determined that the leaf extract had better metal reducing power than the root extract, but it was weaker than BHT with the lowest activity. However, it was determined that the same extract showed better activity than AA in the CUPRAC results. ABTS radical scavenging activities were found to be similar to the antioxidants used as standard in leaf extract and even stronger than BHT. It was also found that leaf extract showed better activity than root extract in DPPH scavenging activity. In the metal chelation results of the study, the extracts showed very low activity compared to the standard antioxidants, but the activity of the leaf extract was quite good compared to the root extract. Considering the results obtained, it was found that the leaf extract of the *S. verticillata* L. plant showed better antioxidant activity compared to the root extract and some standard antioxidants. *In vitro* antioxidant activity results of the highest concentrations of *Sv*L and *Sv*R extracts compared with standard antioxidants as µg TE/ml and percentages are presented in Figures 1 and 2.

Table 1. *In vitro* Antioxidant Activities of *S. verticillata* L. extracts.

Samples	FRAP (µg TE/ml)	CUPRAC (µg TE/ml)	DPPH scavenging (IC_{50})	ABTS scavenging (IC_{50})	Fe-chelating (IC_{50})
***Sv*L**	10.83±0.01	29.72±0.11	40.03±0.02	23.51±0.01	139.78±0.01
***Sv*R**	8.05±0.01	15.28±0.01	97.94±0.20	79.20±0.11	580.04±0.02
BHA	90.34±0.01	101.47±0.03	20.14±0.30	18.29±0.01	38.29±0.01
BHT	18.16±0.01	72.81±0.04	26.86±0.03	24.65±0.21	38.12±0.02
AA	38.71±0.02	21.33±0.01	19.40±0.01	20.19±0.01	32.41±0.01

*FRAP and CUPRAC results as µg TE / ml Extract, DPPH, ABTS, and Fe-chelating activity results as IC_{50}

In a study investigating the antioxidant activity of extracts of *S. verticillata* ssp. *verticillata* and *S. verticillata* spp. *amasiaca*, prepared using different solvents, it was reported that methanol extracts showed strong DPPH radical scavenging activity compared to other extracts and BHT [19]. In another study evaluating the biological activities of 7 *Salvia* species, they reported that all species had a strong DPPH clearance potential, and *S. verticillata* L. showed the strongest antioxidant activity. The ability of these *Salvia* species to chelate transition metal ions was determined by the iron-chelating activity assay, and *S. verticillata* L. had the weakest activity, consistent with our study. They reported that *S. verticillata* L. showed high activity in accordance with our study in the antioxidant activity experiment performed by reducing the power assay [4].

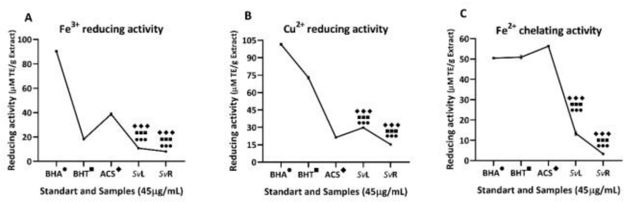

Figure 1. *In vitro* antioxidant activities of *S. verticillata* L. extracts as Trolox Equivalent (TE), BHA, BHT and ACS

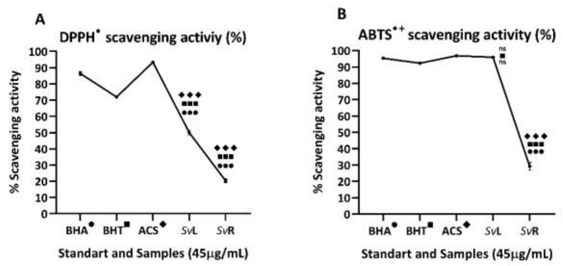

Figure 2. *In vitro* antioxidant activities of *S. verticillata* L. extracts as a percentage, BHA, BHT and ACS

3.2. Results of Phenolic Concentration

The phenolic concentration of root (*Sv*R) and leaf (*Sv*L) extracts of *S. verticillata* L. was determined using HPLC and the results are given in Table 2 in µg/mL. Leaf extract had the highest concentration of curcumin and root extract had the highest concentration of abscisic acid. The lowest concentrations for leaf and root extracts were seen in rosmarinic acid and catechol, respectively. The phenolic concentration of the leaf extract of *S. verticillata* L. appears to be significantly higher than the root extract. It is known that the pharmaceutical properties of *Salvia* plant species originate from phenolic compounds. Significant differences are observed in terms of the distribution and content of phenolic compounds, both within and between species of the plant. In addition, in our study, it was determined that there are more and different types of phenolic compounds in the leaves than in the roots, similar to the literature. In a previous study, it was determined that the leaves of *S. verticillata* are very rich in rosmarinic acid and salvianolic acid A [20]. Again, in a study evaluating the *S. verticillata* subsp. *amasiaca* of Turkey in the literature, it was reported that the leaves were quite rich in rosmarinic acid compared to the roots [3]. The part of our study, which is similar to the literature, is that the above-ground parts of *Salvia* species have high phenolic content. Differences with the current study may be due to the extraction method, the solvent used, and the differences in intra- and inter-species components. HPLC chromatogram results of leaf and root extracts are given in Figures 3 and 4, respectively.

Table 2. The concentrations (µg/mL) of phenolics in the *S. verticillata* L. extracts

Phenolic Compounds	Phenolic amounts (µg/mL)	
	*Sv*L	*Sv*R
Ascorbic acid	-	1.1197
Gallic acid	-	-
Myricetin	-	-
4-Hydroxybenzoic acid	1.2571	-
Trans-*p*-coumaric acid	-	-
3,4-Dihydroxybenzoic acid	-	-
Abscisic acid	1.1033	**1.4756**
Quercetin	-	-
Apigenin	-	-
Kaempferol	-	-
Curcumin	**39.2766**	-
Catechol	0.5635	0.1926
Vanillin	-	-
Caffeic acid	-	-
Cinnamic acid	0.7852	-
Rosmarinic acid	0.6375	0.7946
Salicylic acid	-	-
Total phenolic	**43.6232**	**3.5825**

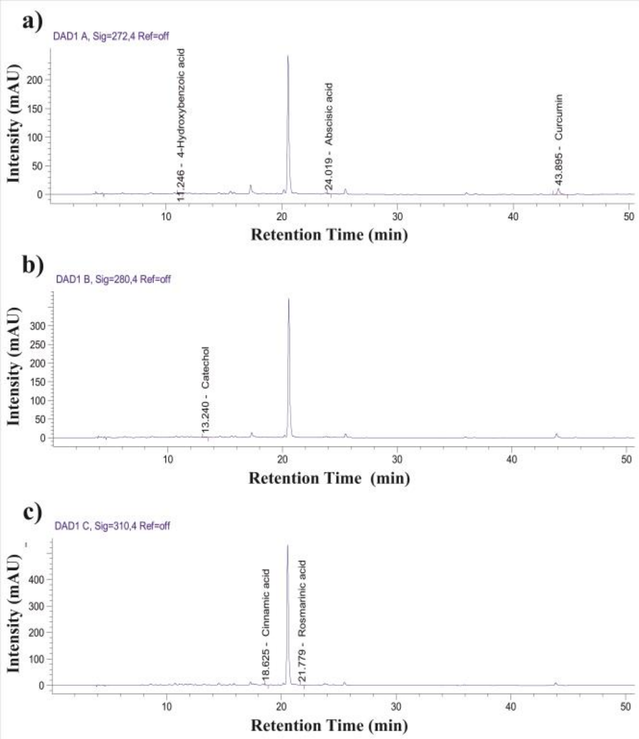

Figure 3. HPLC phenolic chromatogram of *Sv*L ethanol extracts

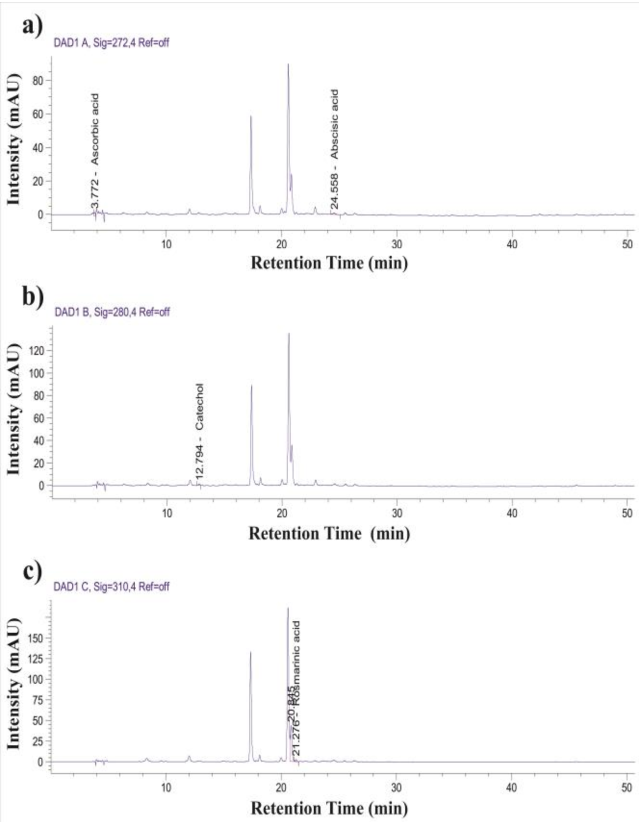

Figure 4. HPLC phenolic chromatogram of *Sv*R ethanol extracts

3.3. Results of Organic Acids and Sugars Concentration

Researchers often emphasize that organic acids and sugars are bioactive compounds, play important roles in antioxidant defense, and therefore have enormous therapeutic potential. They reported that organic acids reduce the pH, prevent food spoilage caused by organisms, and thus are widely used in the food industry, and they do not have negative effects on the body because they are rapidly oxidized in metabolism [21, 22]. In addition to organic acids, glucose and fructose are accepted as positive molecules in terms of antioxidant capacity [23]. In the current study, it was determined that the root and leaf ethanol extracts of *Salvia* contain a very high amount of acetic acid, followed by high amounts of maleic acid for both extracts. These two organic acids appear to be higher in root extract than in leaf extract. In addition to these, tartaric acid in leaf extract and fumaric acid in root extract were found at significant levels. According to the results, the ratios of glucose and fructose, which are free sugars, were found to be close to each other and moderately high in both extracts. In addition to organic acids, acetoin, a secondary metabolite with significant biological activity, was detected in leaf extract in lower amounts compared to other components. The results are given in Table 3 in µg/mL. In the literature review, no study was found on the organic acid and sugar content of the *Salvia* genus. HPLC chromatogram results of *Sv*L and *Sv*R ethanol extracts are given in Figure 5.

Table 3. The concentrations (µg/mL) of organic acids and sugars in the *S. verticillata* extracts

Organic acid and sugar compounds	Organic acid and sugar amounts (µg/mL)	
	***Sv*L**	***Sv*R**
Maleic acid	107.1578	139.0724
Citric acid	-	-
Tartaric acid	13.7790	-
Pyruvic acid	-	-
Glucose	51.6690	42.4277
Malic acid	-	-
Fructose	35.1951	52.1044
Rhamnose	-	-
Suksinic acid	-	-
Fumaric acid	-	-
Acetic acid	**1268.6395**	**1092.7171**
Acetoin	6.1567	23.8874
2-3 bütan	-	-
Total compounds	**1482.5975**	**1350.2090**

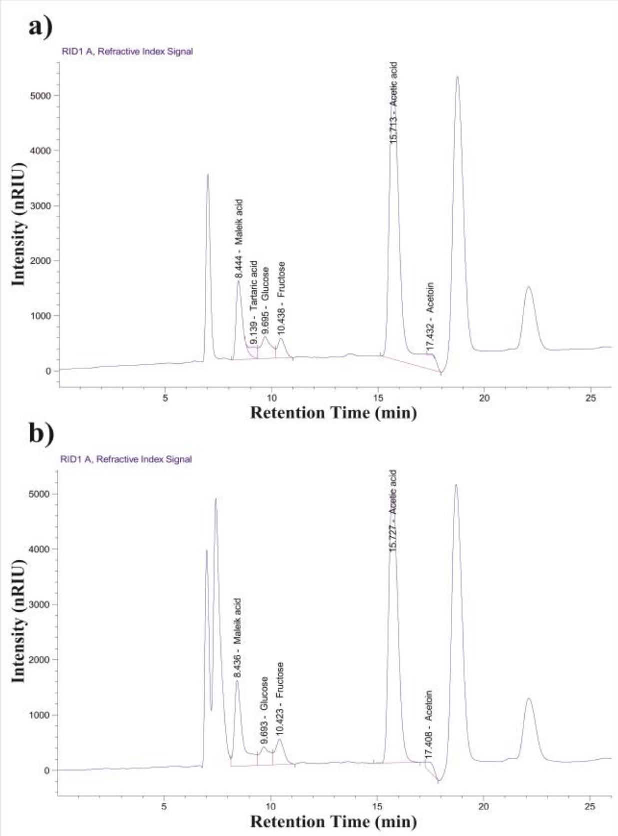

Figure 5. HPLC organic acid and sugar chromatogram results of *Sv*L (a) and *Sv*R (b) ethanol extracts

4. CONCLUSION

Research on the biological potential of plant phenolic compounds continues to be extremely interesting today. Determination of antioxidant properties in order to identify natural sources, including wild species, for use in functional foods, pharmaceuticals, and industry, is also one of the subjects that should be investigated. As a result, antioxidant activities, phenolic, organic acid, and sugar components of *S. Verticillata* L. were investigated. This strain exhibited good antioxidant activity. It has various phenolic and organic acids, including curcumin and acetic acid, as well as glucose content. It has been found to have reasonable and variable activities according to the antioxidant method used. It was also understood that *Salvia* species collected from different regions may have different phenolic contents and concentrations. This study provides a valuable reference for further biological activity research of *Salvia*, such as isolating and characterizing active compounds and conducting in vivo studies to better understand their activity.

REFERENCES

[1] Lu Y, Foo LY. Polyphenolics of Salvia—a review. Phytochemistry. 2002;59(2):117-40.

[2] Jeshvaghani ZA, Rahimmalek M, Talebi M, Goli SAH. Comparison of total phenolic content and antioxidant activity in different Salvia species using three model systems. Industrial Crops and Products. 2015;77:409-14.

[3] Zengin G, Llorent-Martínez EJ, Fernández-de Córdova ML, Bahadori MB, Mocan A, Locatelli M, et al. Chemical composition and biological activities of extracts from three Salvia species: S. blepharochlaena, S. euphratica var. leiocalycina, and S. verticillata subsp. amasiaca. Industrial Crops and Products. 2018;111:11-21.

[4] Mervić M, Bival Štefan M, Kindl M, Blažeković B, Marijan M, Vladimir-Knežević S. Comparative Antioxidant, Anti-Acetylcholinesterase and Anti-α-Glucosidase Activities of Mediterranean Salvia Species. Plants. 2022;11(5):625.

[5] Tosun M, Ercisli S, Sengul M, Ozer H, Polat T, Ozturk E. Antioxidant properties and total phenolic content of eight Salvia species from Turkey. Biological Research. 2009;42(2):175-81.

[6] Scott G. Antioxidants. Bulletin of the Chemical Society of Japan. 1988;61(1):165-70.

[7] Zupko I, Hohmann J, Rédei D, Falkay G, Janicsák G, Máthé I. Antioxidant activity of leaves of Salvia species in enzyme-dependent and enzyme-independent systems of lipid peroxidation and their phenolic constituents. Planta Medica. 2001;67(04):366-8.

[8] Schwarz K, Ternes W. Antioxidative constituents ofRosmarinus officinalis andSalvia officinalis. Zeitschrift für Lebensmittel-Untersuchung und Forschung. 1992;195(2):99-103.

[9] Raheem SMA. Evaluate the Efficiency of Sage (Salvia Officinalis) and Curcumin Mouthwash in the Treatment of Recurrent Aphthous Stomatitis (Comparative Study). Al-Rafidain University College For Sciences. 2021(48).

[10] Vitaglione P, Barone Lumaga R, Ferracane R, Radetsky I, Mennella I, Schettino R, et al. Curcumin bioavailability from enriched bread: the effect of microencapsulated ingredients. Journal of Agricultural and Food Chemistry. 2012;60(13):3357-66.

[11] Savcı A, Koçpınar E, Alan Y, Kurşat M. Antioxidant, antimicrobial, and DNA protection activities of some Tanacetum species and phenolic richness in their ethanolic extracts. International Food Research Journal. 2020;27(1).

[12] Apak R, Güçlü K, Özyürek M, Esin Karademir S, Erçağ E. The cupric ion reducing antioxidant capacity and polyphenolic content of some herbal teas. International journal of food sciences and nutrition. 2006;57(5-6):292-304.

[13] Re R, Pellegrini N, Proteggente A, Pannala A, Yang M, Rice-Evans C. Antioxidant activity applying an improved ABTS radical cation decolorization assay. Free radical biology and medicine. 1999;26(9-10):1231-7.

[14] Koçpınar EF, Kürşat M, Savcı A, Alan Y. Some biological properties of ethanol extract prepared from the aerial parts of Scutellaria albida L. subsp. condensata (Rech. f.) JR Edm. Bitlis Eren University Journal of Science and Technology. 2020;10(2):43-8.

[15] Alhafez A, Savci A, Alan Y, Söylemez R, Kilic A. Preparation of Cu (II), Ni (II), Ti (IV), VO (IV), and Zn (II) Metal Complexes Derived from Novel vic Dioxime and Investigation of Their Antioxidant and

Antibacterial Activities. Chemistry & Biodiversity. 2022:e202100768.
[16] Seal T. Quantitative HPLC analysis of phenolic acids, flavonoids and ascorbic acid in four different solvent extracts of two wild edible leaves, Sonchus arvensis and Oenanthe linearis of North-Eastern region in India. Journal of Applied Pharmaceutical Science. 2016;6(2):157-66.
[17] Ball S, Lloyd L. Agilent Hi-Plex columns for carbohydrates, alcohols, and acids. Application Note Pub. 2011;4:5990-8264.
[18] Tabart J, Kevers C, Pincemail J, Defraigne J-O, Dommes J. Evaluation of spectrophotometric methods for antioxidant compound measurement in relation to total antioxidant capacity in beverages. Food chemistry. 2010;120(2):607-14.
[19] Yumrutas O, Sokmen A, Ozturk N. Determination of in vitro antioxidant activities and phenolic compounds of different extracts of Salvia verticillata ssp. verticillata and spp. amasiaca from Turkey's flora. Journal of Applied Pharmaceutical Science. 2011;1(10):43.
[20] Fotovvat M, Radjabian T, Saboora A. HPLC fingerprint of important phenolic compounds in some Salvia L. species from Iran. Records of Natural Products. 2018;13(1).
[21] Lamani S, Anu-Appaiah KA, Murthy HN, Dewir YH, Rikisahedew JJ. Analysis of Free Sugars, Organic Acids, and Fatty Acids of Wood Apple (Limonia acidissima L.) Fruit Pulp. Horticulturae. 2022;8(1):67.
[22] Angonese M, Motta GE, de Farias NS, Molognoni L, Daguer H, Brugnerotto P, et al. Organic dragon fruits (Hylocereus undatus and Hylocereus polyrhizus) grown at the same edaphoclimatic conditions: Comparison of phenolic and organic acids profiles and antioxidant activities. LWT. 2021;149:111924.
[23] Hu W, Sun DW, Pu H, Pan T. Recent developments in methods and techniques for rapid monitoring of sugar metabolism in fruits. Comprehensive reviews in food science and food safety. 2016;15(6):1067-79.

Cilt 11, Sayı 4, Sayfa 30-35, 2022 Volume 11, Issue 4, Page 30-35, 2022

Araştırma Makalesi https://doi.org/10.46810/tdfd.1169601 Research Article

Türk Doğa ve Fen Dergisi
Turkish Journal of Nature and Science
www.dergipark.gov.tr/tdfd

Isolation of a Novel Amylase Producing *Brachybacterium paraconglomeratum* Strain FAD4 and Optimization of the Enzyme Production Conditions

Dilsat Nigar COLAK[1*]

[1]Giresun University, Dereli Vocational School, Department of Forestry, Giresun, 28950 Türkiye
Dilsat Nigar COLAK ORCID No: 0000-0001-9544-3733

**Corresponding author: dilsat.nigar@giresun.edu.tr*

(Received: 01.09.2022, Accepted: 17.10.2022, Online Publication: 28.12.2022)

Keywords
Amylase,
Brachy-bacterium,
Starch

Abstract: A novel amylase producing bacterium FAD4 was isolated from the wastewater of a textile factory located in Soke (Aydın/Turkey). The amylase production ability of gram positive, coccoidal FAD4 strain was confirmed with plate assay. Morphological and 16S rRNA sequence analyses revealed that FAD4 belongs to the genus *Brachybacterium* with a sequence similarity of 99.8% with *B. paraconglomeratum.* The optimal conditions for amylase production were determined as 72 h at 30 °C with supplementation of 1% starch. Optimum temperature and pH of the amylase were 50 °C and 7.0 respectively. Different starch, carbon and nitrogen sources were investigated for amylase production. A high enzyme production was observed with 1% potato starch and among nitrogen sources peptone was induced the production of amylase. Lactose, galactose, and fructose were also increased the enzyme production as carbon sources.

Yeni Bir Amilaz Üreticisi *Brachybacterium paraconglomeratum* FAD4'ün İzolasyonu ve Enzim Üretim Koşullarının Optimizasyonu

Anahtar Kelimeler
Amilaz,
Brachy-bacterium,
Nişasta

Öz: Yapılan bu çalışmada Aydın (Türkiye)'ın Söke ilçesinde bulunan bir tekstil fabrikasının atık suyundan amilaz üreten bir suş; FAD4 izole edilmiştir. Gram pozitif ve kokoid olan FAD4'ün amilaz üretme yeteneği petri deneyi ile belirlenmiştir. FAD4'ün morfolojik özellikleri ve 16S rRNA dizin analizi sonuçları bu suşun %99.8 oranında *Brachybacterium paraconglomeratum* türüne benzediğini göstermiştir. Amilaz üretimi için optimum koşullar %1 nişasta ilavesi ile 30 °C'de 72 saat olarak belirlenmiştir. FAD4 amilazının optimum aktivite sıcaklığı 50 °C ve pH'sı 7.0'dir. Amilaz üretimi için farklı nişasta, karbon ve azot kaynaklarının etkisi incelenmiştir. %1 patates nişastası varlığında yüksek oranda amilaz üretimi gözlenmiştir. Ayrıca azot kaynaklarından peptonun amilaz üretimini artırdığı, karbon kaynaklarından ise laktoz, galaktoz ve fruktozun enzim üretimini artırdığı gözlenmiştir.

1. INTRODUCTION

Microbial enzymes have been used in industrial applications for decades because of their high activity and stability. They also cost-effective and economically friendly. Many of these microbial enzymes are used in various industries such as food, detergent, textile, paper, medicine etc. [1]. Amylases (EC 3.2.1.1) are one of the most significant enzymes used in industry. These extracellular enzymes catalyse the breakdown of starch into glucose and oligosaccharides via hydrolysing the internal α-1,4 glycosidic linkages in a random manner [2]. Sequence similarity analyses of the catalitic domain revealed that most of the α-amylases are belong to glycoside hydrolase (GH) family 13 [3]. The conserved structure of GH13 include a $(\beta/\alpha)_8$ barrel that contains the active site and extra domains can vary based on the type of amylase [4]. Although amylases can be produced by a variety of organsisms (microorganisms, animals, and plants), microorganisms are the best source for industrial applications due to mild growth conditions and cost-effectiveness [5]. However, the demand of growth conditions differ significantly depending on the producers like temperature, time, nutritional source, metal ions etc.

Starch is produced by most of the plants for energy storage and constitutes an important part of the human and animal diet. The enzymatic hydrolysis of starch has a broad range of applications in industry. α-amylases are one of the major enzymes used in starch processing and they utilized in glucose syrup, brewing, baking as well as detergent, paper and pulp, textile, leather, and distilling industries for decades [6]. A variety of bacteria have been reported for α-amylase production. Bacillus species are the most common bacterial sources, however amylases from Geobacillus, Lactobacillus, Pseudomonas, Corynebacterium, Nesterenkonia species were also reported [5, 7, 8, 9].

In this work an amylase producing bacterium *Brachybacterium paraconglomeratum* was isolated from wastewater samples. Species of *Brachybacterium* are rod-cocci shaped, Gram-positive, nonmotile, aerobic or weakly anaerobic bacteria. They were isolated from various environments, such as garden soil, oil-contaminated sand, seawater, poultry deep litter, mouse liver, fermented cheese and seafood, and roots [10, 11, 12, 13]. There is only one report about amylase producing *Brachybacterium* that is a maltooligosaccharide-forming amylase from *Brachybacterium* sp. strain LB25 [14]. In present study we aimed to determine the optimum conditions of α-amylase production from the newly isolated strain *Brachybacterium paraconglomeratum.*

2. MATERIAL AND METHOD

2.1. Bacterial Strain

In a previous work wastewater and contaminated soil samples were collected from a textile factory located in Soke (Aydın/Turkey). Samples were diluted, inoculated into nutrient agar medium (NA, 105450, Merck Millipore) and incubated at 30 °C for 18 h. Growing colonies were subcultured into NA plates to obtain single colonies. Based on coloni morphologies 13 isolates were selected. Gram staining was performed and colony morphologies were determined using an Olympus CX21 light microscope. Amylase production capacities of the isolates were screened via plate assay. Four of the isolates (FAD2, FAD3, FAD4, and FAD12) were amylase positive. The 16S rRNA sequences of the strains were amplified by PCR using universal UNI16S-L as forward and UNI16S-R as reverse primers for identification. Sequence similarities were analysed with online databases NCBI Genbank and EzTaxon. After identification of the strains, FAD4 was choosen for amylase production.

2.2 Qualitative Screening of Amylase Production

The method of Atlas et al. [15] was used for amylase activity screening. Bacterial strains were inoculated into NA medium containing 1% (w v^{-1}) of soluble starch and incubated at 30 °C for two days. After incubation plates were flooded with 1% of Iodine solution and kept at room temperature for 5 minutes. The formation of dark-blue color represented the precence of starch and clear zones indicated the hydrolysis of starch around colonies.

2.3. Enzyme Production and Amylase Assay

Enzyme production was carried out in a shake flask containing NB medium enriched with 2% of soluble starch. 2 ml overnight culture of FAD4 was inoculated into enriched medium and incubated at 30 °C for two days. Samples were centrifuged at 11.000 rpm for 6 min and supernatant was used as crude enzyme extract.
DNS (3.5-dinitro salicyclic acid) method [16] was used for determination of amylase activity, soluble starch (0.5% w v^{-1}) in 0.05 M Tris-HCl buffer (pH:7.0) was the substrate. The reaction mixture containing 50 µl of crude enzyme and 50 µl of substrate was incubated at 50 °C for 30 min. 500 µl of DNS (1%) was added to stop the reaction and boiled in a water bath for 10 min. The release of reducing sugar was measured spectrophotometrically at 540 nm, the amount of liberated maltose was calculated by a standard curve.

2.4. Effects of Temperature and Incubaion Time on Enzyme Production

The strain FAD4 is a mesophilic bacterium, thats why it can not grow at high temperatures. Incubations at room temperature, 30 °C, and 37 °C were performed for determining optimum enzyme producing temperature. The effect of incubation time was determined by cultivating FAD4 at different times ranging from 18 hours to 4 days.

2.5. Optimum Temperature and pH of Amylase

Optimum temperature of FAD4 amylase was determined by incubating the reaction mixture including crude enzyme extract and substrate (soluble starch; 0.5% w v^{-1} in Tris-HCl buffer) at different temperatures ranging from 30 – 80 °C. The effect of pH on enzyme activity was measured by using following buffers: sodium acetate buffer (pH 5.0), sodium phosphate buffer (pH 6.0 – 8.0), Tris-HCl buffer (pH 7.0 – 9.0), glycine buffer (pH 9.0 – 12.0). Soluble starch (0.5%) was dissolved in each buffer (50 mM), mixed with enzyme and the reaction performed as mentioned above. Each experiment was carried out three times.

2.6. Effects of Starch Sources

Optimal strach concentration was determined by supplementing NB medium with 0.5, 1, 2, and 5% (w v^{-1}) of soluble starch. The effect of different starch sources on bacterial growth and enzyme production was analysed by using 2% (w v^{-1}) of each starch source (soluble starch, corn starch, wheat starch, and potato starch) dissolved in NB medium. After inoculation with 2 ml of overnight FAD4 bacterial culture and incubation at 30 °C for 2 days, crude enzyme extract was obtained as mentioned above. Enzyme production was measured with Bradford [17] method and DNS method was used for enzyme activity.

2.7. Effects of Various Carbon and Nitrogen Sources on Enzyme Production

Various carbon sources (glucose, galactose, glycerol, sucrose, fructose, lactose, maltose, and starch) and nitrogen sources (peptone, tryptone, yeast extract, urea, casein, ammonium chloride, ammonium sulphate) were tested for enzyme production. Each source was dissolved in NB medium at a concentration of 1% w v^{-1}, and autoclave sterilized. After an incubation period of 2 days at 30 °C, crude enzyme extracts were obtained via centrifugation and enzyme activity assay was performed.

3. RESULTS AND DISCUSSION

3.1. Identification of Bacteria

Based on qualitative screening of amylase, strain FAD4 was choosen for this study because of better starch hydrolising capacity than other three amylase producing strains. FAD4 was Gram positive and the cells were round-shaped. 16S rRNA sequence analyses revealed that FAD4 has a 99.8% sequence similarity with *Brachybacterium paraconglomeratum*. Clear zones around colonies in amylase plate assay represented that FAD4 has the ability of amylase production (Figure 1).

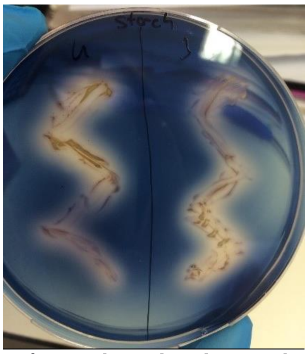

Figure 1. After washing the plates with 1% of iodine solution, formation of clear zones around strain FAD4 colonies indicates the starch hydrolysis

Microbial amylases have been used in industry for decades due to their starch hydrolysing capacity. Detergent, textile, paper, food and alcohol industries are some of the industries that amylases widely used [18]. Though most commonly used bacterial amylase sources are Bacillus species such as *B. subtilis*, *B. licheniformis*, *B. amyloliquifaciens*, *B. stearotherpophilus* [19], some other strains are also capable of amylase production. For example *Chromohalobacter* sp., *Caldimonas taiwanensis*, *Halobacillus* sp., *Haloarcula hispânica*, *Halomonas meridiana*, *Rhodothermus marinus*, *Geobacillus thermoleovorans*, *Lactobacillus fermentum* are also reported as amylase producing strains [20]. In our study we identified a new amylase producing bacterium *Brachybacterium paraconglomeratum* strain FAD4 from wastewater of a textile factory. In addition to 16S rRNA sequence similarities, the Gram staining feature and the coccoidal form is also similar with *B. paraconglomeratum*. There is only one report about amylase producing Brachybacterium presented by Doukyu et all. [14, 21]. They cloned a maltooligosaccharide-forming amylase gene from *Brachybacterium* sp. strain LB25 into *E. coli* and expressed but the specific activity of the clonned enzyme was lower than the crude enzyme extract.

3.2. Effects of Temperature and Incubaion Time on Enzyme Production

Industrial enzyme production is affected by various factors like fermentation procedure, growing media, carbon and nitrogen sources, temperature, pH, etc. *Brachybacterium paraconglomeratum* FAD4 was incubated at room temperature, 30 and 37 °C from 18 hours to 4 days and followed by crude enzyme extraction. Spectrophotometric measurements at 540 nm for protein concetration and 489 nm for amylase activity revealed that maximum yield of amylase was obtained from *B. paraconglomeratum* FAD4 at 30 °C for 72 h. When incubation period decreased to 48 hours there was only a 10% decrease observed in enzyme production, and halved when incubated for 24 h. After third day there was no increase in enzyme production. The optimum growing duration of industrial amylase producing *Bacillus* strains is range from 24 to 72 h [22]. The temperature needed for bacterial amylase production is between ~25 °C to around 100 °C [23]. Based on these data it can be said that the growing conditions of strain FAD4 is suitable for industrial applications.

3.3. Optimum Temperature and pH of Amylase

The activity and stability of the bacterial enzymes are highly related to the pH and temperature. The amylase activity of FAD4 was examined at different temperatures ranging from 30 – 80 °C, and different pH values ranging from pH 5.0 – 12.0. The optimum temperature and pH of the crude amylase extract were determined as 50 °C and pH 7.0 respectively (Figure 2). Optimum pH of the bacterial amylases were range from 4.0 (*Bacillus sp.* KR-8104) to 10.0 (*Bacillus subtilis* DM-03), and mostly 7.0. The temperature optima is varied from 33 °C (*Bacillus amyloliquefaciens*) to 135 °C (*Bacillus subtilis*) [20]. The results obtained from strain FAD4 were similar with literature.

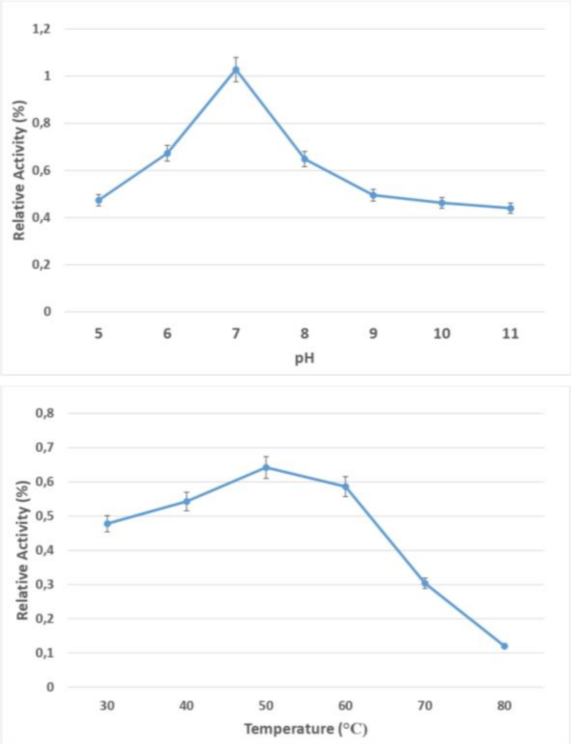

Figure 2. Optimum pH and temperature of the amylase of strain FAD4

3.4. Effects of Starch Sources on Enzyme Production

Starch concentration optimization was performed by using 0.5, 1, 2, and 5% (w v^{-1}) of soluble starch. FAD4 can grow in NB medium but there was very slight amylase production without starch supplementation. With 0.5% starch there was 1.6 mg ml^{-1} maltose liberation, and it was 2 mg ml^{-1} with 1 and 2% starch. Increasing the starch concentration to 5% did not effect the yield so much, which means using FAD4 for amylase production is cost effective.

Commercial starch sources (soluble starch, corn starch, wheat starch, and potato starch) with different concentrations were tested for amylase production. After an incubation period of 2 days, enzyme activity was measured. The most effective starch source was determined as potato starch with a maltose liberation of 1.0 mg ml^{-1}. The yield for soluble starch was 0.35 mg ml^{-1} while 0.2 mg ml^{-1} maltose liberation were observed for both corn starch and wheat starch in same conditions. Some of the Bacillus strains can produce good amount of amylase with the supplementation wheat bran [24] which is a cheap starch source. Strain FAD4 is also produce amylase with the supplementation of wheat starch. Besides, some other strains utilize potato starch for amylase production. *B. licheniformis* and *B. amyloliquefaciens* were used for maltose manufacture, and potato starch was one of their starch sources [25]. High amount of amylase production was observed also for *Anoxybacillus* sp. [26] and *A. flavithermus* SO-13 [27] with potato starch. The only *Brachybacterium* strain reported in the literature *B. paraconglomeratum* Strain LB 25 was studied with potato starch [14].

3.5. Effects of Carbon Sources on Enzyme Production

Commercial carbon and nitrogen sources are known to be effective on amylase production. Different carbon sources were used for determining the effects on amylase production. After incubation at 30 °C for 2 days, cells were harvested and supernatant was used as crude enzyme extract. Standart reaction conditions were performed for each amylase. Among various carbon sources, the best results obtained from lactose (Figure 3). 1.70 mg ml^{-1} of maltose liberation observed when lactose used in growing medium. It was 1.35 mg ml^{-1} for galactose, and 0.85 mg ml^{-1} for fructose. There was no enzyme production when glucose used as carbon source. Similar results were obtained from other bacterial strains in the literature. Supplementation of the medium with 5g l^{-1} of lactose increased the amylase production from *Bacillus amyloliquefaciens* [28]. In another study, the highest amylase production from *Anoxybacillus* sp. AH1 was observed with maltose supplementation, glucose, and lactose were also increased the enzyme production [26]. The inhibitory effect of glucose on FAD4 was also observed for *Anoxybacillus flavithermus*. Aguloglu Fincan et all., [29] determined that using glucose and sucrose in growing media decreased the amylase production from *A. flavithermus* [29].

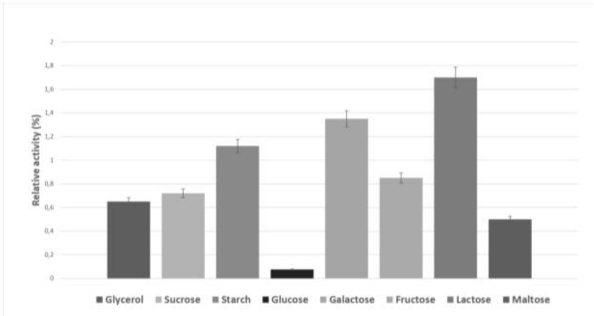

Figure 3. Effects of different carbon sources on amylase production from strain FAD4

3.6. Effects of Nitrogen Sources on Enzyme Production

Some of the nitrogen sources were also exhibited enhancing effects on amylase production from strain FAD4 (Figure 4). Among nitrogen sources used in this study peptone was the best source for enzyme production. Using 1% of peptone was increased the yield in a rate of 5.15% when compared with soluble starch, and yeast extract supplementation was also yielded a good enzyme production (only 4% lower than peptone). Other nitrogen surces decreased the enzyme production in a rate of 50% or more. Peptone and yeast extract were also suitable for the production of amylase from *Bacillus amyloliquefaciens* [28]. In another study amylase production from *Streptomyces* sp. MSC702 was induced by pepton [30]. The increasing effect of yeast extract was also observed for *Bacillus subtilis* MB6 [31] and *Bacillus* sp. [32].

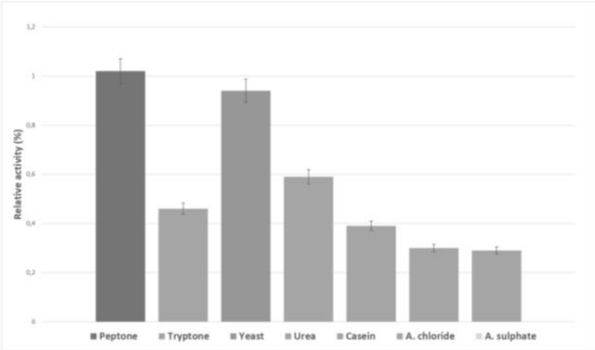

Figure 4. Effects of different nitrogen sources on amylase production from strain FAD4

4. CONCLUSION

Brachybacterium paraconglomeratum strain FAD4 was isolated from the wastewater of a textile factory located in Soke (Aydın/Turkey). FAD4 was able to hydrolyse starch with amylase production. The optimal conditions for amylase production were 72 h at 30 °C. Optimum temperature and pH of the amylase were suitable for industrial applications. A high enzyme production was observed with 1% potato starch and other starch sources (soluble, wheat, corn) were also suitable for amylase production. Among nitrogen sources peptone and yeast extract were induced the enzyme production. Lactose, galactose and fructose were also increased the enzyme production as carbon sources. The amylase production features of *B. paraconglomeratum* strain FAD4 were similar with the other amylase producing strains used in industry, and it can be said that the amylase produced by *B. paraconglomeratum* FAD4 colud be a useful tool for industrial applications.

Acknowledgement

The author is grateful to Ali Osman BELDUZ for useful discussions and suggestions.

REFERENCES

[1] Li S, Yang X, Yang S, Zhu M, Wang X. Technology prospecting on enzymes: application, marketing and engineering. Comput. Struct. Biotechnol. J. 2012;2:1–11.

[2] Gomes I, Gomes J, Steiner W. Highly thermostable amylase and pullulanase of the extreme thermophilic eubacterium *Rhodothermus marinus*: production and partial characterization. Bioresour. Technol. 2003;90 (2);2 07-214.

[3] Cantarel BL, Coutinho PM, Rancurel C, Bernard T, Lombard V, Henrissat B. The Carbohydrate-Active EnZymes database (CAZy): an expert resource for Glycogenomics. Nucleic Acids Res. 2009;37;233–238.

[4] Nagano N, Orengo C.A, Thornton JM. One fold with many functions: the evolutionary relationships between TIM barrel families based on their sequences, structures and functions. J. Mol. Biol. 2002;321;741-765.

[5] Gupta R, Gigras P, Mohapatra H, Goswami VK, Chauhan B. Microbial α-amylases: a biotechnological perspective. Process Biochem. 2003;38;1599 – 1616.

[6] Ma Y, Yang H, Chen X, Sun B, Du G, Zhou Z, et al. Significantly improving the yield of recombinant proteins in Bacillus subtilis by a novel powerful mutagenesis tool (ARTP): Alkaline α-amylase as a case study. Protein Express. Purif. 2015;114;82-88.

[7] Shafiei M, Ziaee AA, Amoozegar MA. Purification and characterization of an organic-solvent-tolerant halophilic α-amylase from the moderately halophilic Nesterenkonia sp. strain F. J. Ind. Microbiol. Biotechnol. 2011;38;275–81.

[8] Hussain I, Siddique F, Mahmood MS, Ahmed SI. A Review of the Microbiological Aspect of α-amylase Production. IJAB. 2013;15(5);1029-1034.

[9] Sundarram A, Murthy TPK. α-Amylase production and applications: a review. J. Appl. Environ. Microbiol. 2014; 2;166-175.

[10] Collins MD, Brown J, Jones D. Brachybacterium faeciumgen. nov., sp. nov., a coryneform bacterium from poultry litter. Int. J. Syst. Bacteriol. 1988;38; 45–48.

[11] Lapidus A, Pukall R, Labuttii K, Copeland A, Glavina Del Rio T, Nolan M, et al. Complete genome sequence of *Brachybacterium faecium* type strain (Schefferle 6-10). *Stand. Genomic Sci.* 2009;1;3–11.

[12] Park SK, Kim MS, Jung MJ, Nam YD, Park EJ, Roh SW. et al. *Brachybacterium squillarum* sp. nov., isolated from salt-fermented seafood. *Int. J. Syst. Evol. Microbiol.* 2011;61;1118–1122.

[13] Singh H, Du J, Yang JE, Yin CS, Kook M, Yi TH. *Brachybacterium horti* sp. nov., isolated from garden soil. *Int. J. Syst. Evol. Microbiol.* 2016;66;189–195.

[14] Doukyu N, Yamagishi W, Kuwahara H, Ogino H, Furuki N. Purification and characterization of a maltooligosaccharide-forming amylase that improves product selectivity in water-miscible organic solvents, from dimethylsulfoxide-tolerant Brachybacterium sp. strain LB25. Extremophiles. 2007;11;781–788.

[15] Atlas RM, Parks LC, Brown AE. Laboratory Manual of Experimental Microbiology. St Louis: Mosby-Year Book Inc.; 1995.

[16] Bernfeld P. Amylases, *α* and *β*. Methods. Enzymol. 1955;1;149–158.

[17] Bradford MM. A rapid and sensitive method for the quantitation of microgram quantitation of microgram quantities of protein utilizing the principle of protein-dye binding. Anal. Biochem. 1976;72;248-254.

[18] Mageswari A, Subramanian P, Chandrasekaran S, Sivashanmugam K, Babu S, Gothandam KM. Optimization and immobilization of amylase obtained from halotolerant bacteria isolated from solar salterns. J. Genet. Eng. Biotechnol. 2012;10(2);201-8.

[19] Konsoula Z, Liakopoulou-Kyriakides M. Co-production of alpha-amylase and beta-galactosidase

by *Bacillus subtilis* in complex organic substrates. Bioresour. Technol. 2007;98;150–157.
[20] Souza PMD, Pérola OM. Application of Microbial α-Amylase in Industry-A Review. Braz. J. Microbiol. 2010;41;850-861.
[21] Doukyu N, Yamagishi W, Kuwahara H, Ogino H. A Maltooligosaccharide-Forming Amylase Gene from Brachybacterium sp. Strain LB25: Cloning and Expression in Escherichia coli. Biosci. Biotechnol. Biochem. 2008;72(9);2444–2447.
[22] Farooq MA., Ali S, Hassan A, Tahir HM, Mumtaz S, Mumtaz S. Biosynthesis and industrial applications of α-amylase: a review. Arch. Microbiol. 2021;203;1281–1292.
[23] Mehta D, Satyanarayana T. Bacterial and archaeal α-amylases: diversity and amelioration of the desirable characteristics for industrial applications. Front. Microbiol. 2016;7;1129.
[24] Yildirim Akatın M. An Overview of Amylase Production by Solid State Fermentation (SSF) since 2010. JTST. 2019;9(1);1-7.
[25] Aiyer PV. Amylases and their applications. Afr. J. Biotechnol. 2005;4 (13);1525-1529.
[26] Acer O, Pirinccioglu H, Bekler FM, Gul-Guven R, Güven K. Anoxybacillus sp. AH1, an α-amylase-producing thermophilic bacterium isolated from Dargecit Hot Spring. Biologia. 2015;70(7);853-862.
[27] Ozdemir S, Okumus V, Ulutas MS, Dundar A, Akarsubası AT, et al. Isolation of a Novel Thermophilic *Anoxybacillus flavithermus* SO-13, Production, Characterization and Industrial Applications of its Thermostable α-Amylase. J. Bioprocess Biotech. 2015;5;237.
[28] Sharma N, Vamil R, Ahmad S, Agarwal R. Effect of Different Carbon and Nitrogen Sources on A-Amylase Production from *Bacıllus Amyloliquefacıens.* IJPSR. 2012;3(4);1161-1163.
[29] Fincan SA, Enez B, Ozdemir S, Bekler FM. Purification and characterization of thermostable a-amylase from thermophilic Anoxybacillus flavithermus. Carbohydr. Polym. 2014;102;144-150.
[30] Singh R, Kapoor V, Kumar V. Influence of Carbon and Nitrogen Sources on the α-amylase Production by a Newly Isolated thermophilic Streptomyces sp. MSC702 (MTCC 10772). Asian J. Biotechnol. 2011;3;540-553.
[31] Lall BM, Paul JS, Jadav SK, Tiwari KL. Effect of Carbon and Nitrogen Source α-Amylase Enzyme Production from *Bacillus Subtilis* MB6. Indian J. Aerobiol. 2016;29;37-41.
[32] Qader SAU, Bano S, Aman A, Syed N, Azhar AA. Enhanced productionand extracellular activity of commercially important amylolytic enzyme by anewly isolated strain of Bacillus sp. AS-1. TJB. 2006;31;135–140.

Cilt 11, Sayı 4, Sayfa 36-41, 2022 Volume 11, Issue 4, Page 36-41, 2022

Araştırma Makalesi https://doi.org/10.46810/tdfd.1170755 Research Article

Türk Doğa ve Fen Dergisi
Turkish Journal of Nature and Science
www.dergipark.gov.tr/tdfd

Production of α-amylase from Bacillus megaterium MD-1

Sema AGÜLOĞLU FİNCAN*, Barış ENEZ[2]

[1]Dicle University, Science Faculty, Biology Department, Diyarbakır, Türkiye
[2]Bingöl University, Vocational School of Food, Agriculture and Livestock, Veterinary Health Department, Bingöl, Türkiye
Sema AGÜLOĞLU FİNCAN ORCID No: 0000-0003-0147-4411
Barış ENEZ ORCID No: 0000-0003-4730-3458

**Corresponding author: semaagul@dicle.edu.tr*

(Received: 04.09.2022, Accepted: 25.10.2022, Online Publication: 28.12.2022)

Keywords
Bacillus megaterium, α-Amylase, Enzyme production, Carbon and nitrogen sources,

Abstract: The alpha-amylase is used extensively in many different industrial sectors and is renowned for modifying starch by rupturing 1-4 glycosidic bands. Depending on the intrinsic properties of the microorganism, several alpha-amylases with thermostable and halotolerant properties are expressed. In the current study, the bacteria were isolated from Ergani Makam Mountain. Identification and optimization of the isolated bacteria were performed. As a result of the 16S rRNA analysis, physiological, morphological and biochemical analyis were carried out for the identification of the isolated microorganism and consequently the bacterium was defined as *Bacillus megaterium* MD-1.

Following its identification, α-Amylase, was isolated from *B. megaterium*. Optimal conditions for bacteria and enzyme production were determined as 48 hours, 35°C and pH 7.0. Maximum enzyme activity was optained at 40°C and pH 8.0. The effects of various carbon and nitrogen sources on enzyme production were investigated by adding to the nutrient medium. Compared to the control regarding enzyme production, it was determined that carbon sources, particularly sucrose, fructose and lactose inhibited enzyme production by 75%, all carbon sources inhibited production. It was also observed that urea and sodium nitrate from nitrogen sources had an inhibitory effect on enzyme production whereas other nitrogen sources did not. The highest amylase production among nitrogen sources was obtained with peptone addition.

In our study, it was determined that an increase in amylase activity could be achieved by using the optimum values of physical parameters. These findings displayed that enzyme could be utilized in fruit juice industries for clarification of apple juice, textile industry and raw starch hydrolyzing.

Bacillus megaterium MD-1'den α-amilaz üretimi

Anahtar Kelimeler
Bacillus megaterium, α-Amylase, Enzim üretimi, Karbon ve azot kaynakları

Öz: Alfa-amilaz, birçok farklı endüstriyel sektörde yaygın olarak kullanılmaktadır ve 1-4 glikozidik bantları parçalayarak nişastayı modifiye etmesiyle ünlüdür. Mikroorganizmanın içsel özelliklerine bağlı olarak, termostabil ve halotolerant özelliklere sahip birkaç alfa-amilaz ifade edilir. Mevcut çalışmada, bakteriler Ergani Makam Dağı'ndan izole edilmiştir. İzole edilen bakterilerin tanımlanması ve optimizasyonu yapıldı. 16S rRNA analizi sonucunda izole edilen mikroorganizmanın tanımlanması için fizyolojik, morfolojik ve biyokimyasal analizler yapılmış ve sonuç olarak bakteri *Bacillus megaterium* MD-1 olarak tanımlanmıştır.

Tanımlanmasının ardından α-amilaz, *B. megaterium* MD-1'den izole edildi. Bakteri ve enzim üretimi için optimum koşullar 48 saat, 35°C ve pH 7.0 olarak belirlendi. Maksimum enzim aktivitesi 40°C'de ve pH 8.0'da elde edildi. Besin ortamına ilave edilerek çeşitli karbon ve azot kaynaklarının enzim üretimine etkileri araştırıldı. Enzim üretimi ile ilgili kontrol ile karşılaştırıldığında, başta sakaroz, fruktoz ve laktoz olmak üzere karbon kaynaklarının enzim üretimini %75 oranında inhibe ettiği, buna karşın glukoz, nişasta ve galaktozda herhangi bir değişiklik olmadığı belirlendi. Azot kaynaklarından gelen üre ve sodyum nitratın enzim üretimi üzerinde inhibitör etkisi olduğu, diğer azot kaynaklarının ise olmadığı gözlemlendi. Azot kaynakları arasında en yüksek amilaz üretimi pepton ilavesiyle elde edilmiştir.

Çalışmamızda fiziksel parametrelerin optimum değerleri kullanılarak amilaz aktivitesinde artış sağlanabileceği belirlendi.

1. INTRODUCTION

The enzyme known as alpha-amylase (α-amylase; 1,4-α-D-glucan glucanohydrolase; EC 3.2.1.1) hydrolyses the alfa bonds in massive, alfa-linked polysaccharides such as starch and glycogen to form shorter chains, dextrins, and maltose [1]. Alpha-amylase can be produced by a broad variety of organisms, including micro-organisms such aquatic bacteria, fungi, actinomycetes, plants and mammals [2, 3]. Microbial organisms are the principal source of alpha-amylase, producing a large amount of the enzyme at a high ratio of growth and proliferation. Additionally, the microorganisms that have undergone genetic manipulation are made to produce α-amylase with unique properties such as thermostability. The microbes also produce a lot of enzyme, which may easily be improved using different techniques including response surface methodology [4-7]. Alpha amylases are used today in biotechnology-important industries such as paper, food, textile, detergent, and in alcohol fermentation, starch hydrolysis, silage production, clinical, pharmaceutical, medical, analytical chemistry. They are industrial enzymes that are widely used in the field [8, 9].

Following the development of enzyme technology, the industrial enzymes have gained more attention in recent years. Majority of the enzymes (approximately 90%) used in industry are of microbial origin. Microorganisms are preferred for reasons such as being an important source of enzymes, biochemical diversity, being able to be produced by methods that will enable large-scale production and being suitable for genetic [10-13]. In addition, such bacteria are preferred in enzyme production due to their short fermentation cycle, stability, safe use, strong enzyme activity in stress situations and being environmentally friendly [14].

Among the bacterial enzymes, majority of the industrial enzymes are produced by different types of *Bacillus* strains [12]. Gram-positive *bacillus* and aerobic spore-forming *Bacillus megaterium* are among the largest group of the bacteria [15, 16]. Despite being utilised for industrial purposes over half century owing to its ability to produce key enzymes, it has recently been preferred in the field of biotechnology due to its capacity of recombinant protein production [17]. Amylases are the leading enzymes synthesized by *Bacillus*. Amylases are of 3 types; α-amylase, β-amylase and γ-amylase [18].

The aim of the current study was to isolate α-amylase, which constitutes the majority of the industrially important enzymes of the bacteria isolated from the soil. The second aim of our study was to increase the production of the enzyme obtained through optimization of the several parameters including temperature and pH.

2. MATERIAL AND METHOD

Morphological and biochemical analysis were carrıed out on *Bacillus megaterium* MD-1, a bacteria isolated from soil samples brought from Ergani Makam mountain. Optimum conditions for bacterial growth and α-amylase production were also determined within the scope of our work. To obtain the best amylase activity, optimum pH and temperature values were also investigated.

2.1. Isolation of Bacteria and its Phylogenetic Tree

Bacillus megaterium MD-1 was isolated from the soil sample in the Ergani Makam mountain, Diyarbakır in Turkey. Along with performing the morphological and biochemical investigations of the enzyme properties, we also performed 16s rRNA analysis of these bacteria were via Refgen. In order to collect the microbes from the soil, we took one gram of sample and added 9 ml of sterile water on the collected sample. Via application of that methodology, the sample was diluted 10 folds. A serial dilution procedure was applied and the sample was further diluted as follow: 10^{-2}, 10^{-3}, 10^{-4}, 10^{-5}, 10^{-6}, 10^{-7}. For the purpose of obtaining a single colony, smear sowing procedure was applied to the serially diluted samples instead of Nutrient Agar (NA) and incubated at 37 ºC.

2.2. Enzyme Production and Determination of Protein Amount

Bacillus megaterium MD-1 was regularly cultured through shaking at following experimental conditions: 120 rpm, pH 7.0 and 35 °C. After a 24-hour incubation period, the culture sample was centrifuged (Sigma Christ 2K15) for 10 min at 10 rpm. After centrifugation, the supernatant was used to measure the enzyme activity. The Lowry technique was used for protein quantification [19].

2.3. Determination of Enzyme Activity

The Bernfeld method [20] developed in 1955 was modified to determine the amylase activity. For 30 minutes at 70 °C, either a 100 µL crude enzyme solution or a 10 µL purified enzyme solution was added to a 200 µL 0.5% solvable starch solution (dissolved in a Tris-HCl buffer at 0.1 M pH 7.0). At the conclusion of this period, 400 µL of 3,5-dinitro salicylic acid (DNS) was added, and it was then heated in a water bath for 5 minutes to cease the substrate-enzyme reaction. The decreasing sugar was calculated using DNS, which also creates color. After boiling, test tubes were held for chilling, and 3 mL of distilled water was added for dilution. UV-VIS spectrophotometric (SPD-20A UV) detection of the enzyme activity at 489 nm. For amylase activity, the amount of enzyme resulting the production of 1 μmole glucose per minute was defined as one unit.

2.4. Effect of Temperature, pH and Incubation Time on Microorganism and Amylase Production

Bacteria were inoculated into 100 ml flasks. In order to determine the optimum bacterial and enzyme production values at 25-55 ºC temperature ranges, they were kept in a shaking water bath at 120 rpm and absorbance measurements were made in the spectrophotometer. Bacteria and enzymes were produced at different pHs between pH 4.0 and 11.0 in 0.5 increments in the prepared NB medium. To determine the effect of incubation time on microorganism growth and enzyme production; Absorbance measurements were made in spectrophotometer by taking samples at 4-hour intervals between 4-96 hours in NB medium.

2.5. Influence of temperature and pH on enzyme activity and stability

Using the aforementioned techniques, solvable starch was used as the substrate and temperatures ranging from 20 to 80°C were used to determine the purified α-amylase's optimal temperature. By preincubating the purified enzyme at various temperatures (40-70°C) for 0–180 min, the enzyme's thermostability was discovered. The Bernfeld approach was used to calculate the residual activity under ideal conditions [20].

During a 30-minute period at optimal temperature and a range of pH values (pH 3.0-11.0), the effect of pH on amylase activity was examined. Enzyme activity was determined for pH stability using the Bernfeld method [20] by maintaining the enzyme solution at various pH ranges (4.0-8.0) for 0-240 min.

2.6. Effect of Carbon and Nitrogen Sources on Amylase Production

After adding glucose, galactose, fructose, lactose, soluble starch and sucrose as carbon source to NB media at 1% concentration, bacteria were cultivated and incubated at 37°C for 48 hours. Nitrogen sources such as peptone, tryptone, urea, ammonium sulfate, ammonium chloride, ammonium nitrate, sodium nitrate and yeast extract were added to NB broths at the rate of 1% and incubated under optimal conditions for enzyme production.

3. RESULTS

B. megaterium MD-1 (YC2) was determined as the bacterium with 16 s rRNA analysis. The related phylogenetic tree is shown in Figure 1. 16S rRNA analysis to identify the bacterium was performed by Ref-Gen (METU Technocity/Ankara).

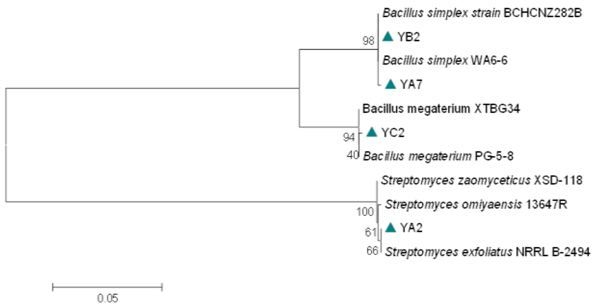

Figure 1. Phylogenetic tree of bacteria

In order to identify B. megaterium MD-1, biochemical tests such as starch, gelatin, catalase, casein, urease, lipase, hydrolysis, motility, indole, phosphatase, hemolysis, as well as morphological and physiological analyzes were performed. (Table 1).

Characters	***Bacillus megaterium***
Optimal pH	7
Hemolysis	-
Motile	+
Hydrolysis	
Starch	+
Casein	-
Gelatine	-
Activity	
Urease	+
Catalase	+
Lipase	+
Amylase	+
Indole	+
Phosphatase	+

Table 1: Morphological, Physiological and Biochemical Tests

To examine the effect of incubation time on enzyme production and growth of *B. megaterium* MD-1, bacterial growth curve was followed for 92 hours and enzyme activity was measured every 4 hours. As a result of the analysis, it was determined that bacterial growth and maximum enzyme production were at 48 hours (Figure 2).

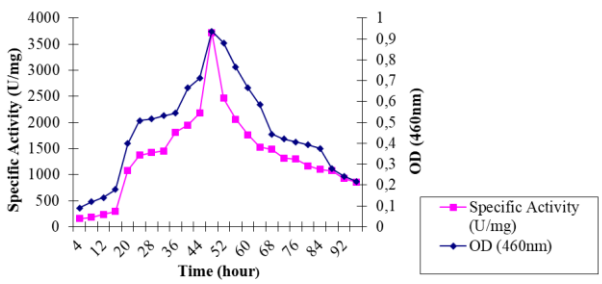

Figure 2. The effect of time on bacteria and amylase production

For the purpose of determination of the impact of temperature, bacteria culture was incubated in NB medium (pH 7.0) at 30 to 55°C for 48 hours. At the conclusion of the incubation time, it was discovered that the bacterial growth and enzyme synthesis were at their highest levels at 35°C. (Figure 3). A wide temperature range of 35°C to 80°C is given for optimum bacterial growth and α-amylase production in bacteria.

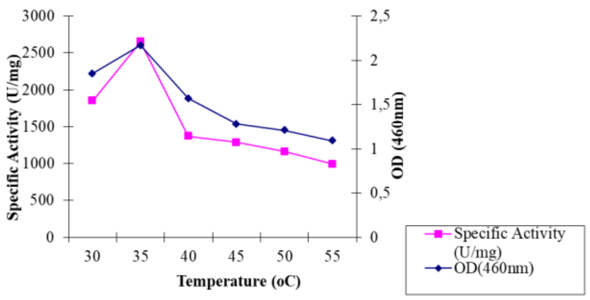

Figure 3. The effect of temperature on bacteria and amylase production

On the other hand, in order to determine the effect of pH on amylase production and bacteria growth, the bacteria culture was grown in the presence of different pH ranging between 4.0 to11.0 and the optimum pH value was determined as pH 7.0 for both analysis (Figure 4).

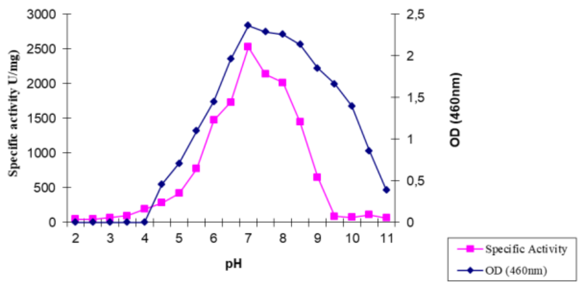

Figure 4. The effect of pH on bacteria and amylase production

The impacts of heat and pH on α-amylase activity isolated from *B. megaterium* MD-1 were also studied within the scope of current. In order to determine the effect of temperature on enzyme activity, it was determined that the maximum α-amylase activity was at 40°C in the experiment performed between 30-55°C temperature ranges. (Figure 5).

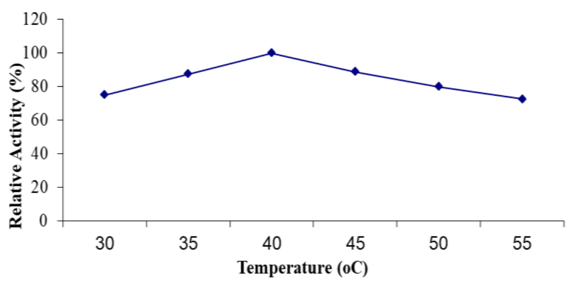

Figure 5. Effect of temperature on α-amylase

When the effect of pH on enzyme activity was studied, it was found out that the maximum α-amylase activity was achieved at pH 8.0. (Figure. 6).

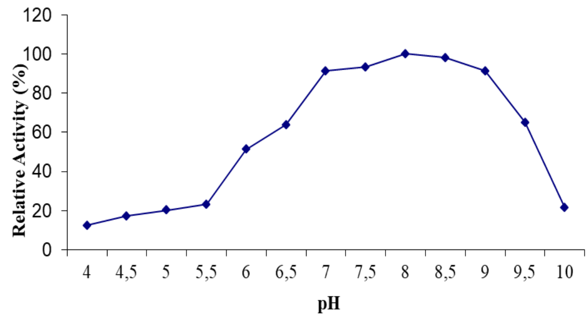

Figure 6. Effect of pH on α-amylase

The effect of carbon sources on amylase activity was also studied. Our results demonstrated that, the activity of the control for which no extra carbon sources added into the growth media was 1728 Umg-1 while after adding more glucose and starch added to the media the activity was 1577 Umg-1 and 1584 Umg-1 suggesting that the activity of the enzyme was not significantly changed in the presence of these carbon sources. The enzyme activity was decreased in the presence of sucrose, galactose, lactose and fructose (Figure 7).

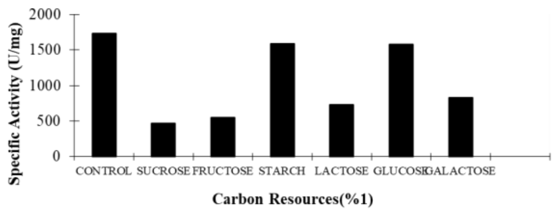

Figure 7. Effect of Nitrogen Sources on enzyme production

The effect of nitrogen sources on amylase activity revealed following results: When compared to the control (2227 Umg-1), suppression of amylase production was observed in media containing nitrogen sources urea (798 Umg-1), sodium nitrate (883 Umg-1) and yeast extract (896 Umg-1) (Figure 8).

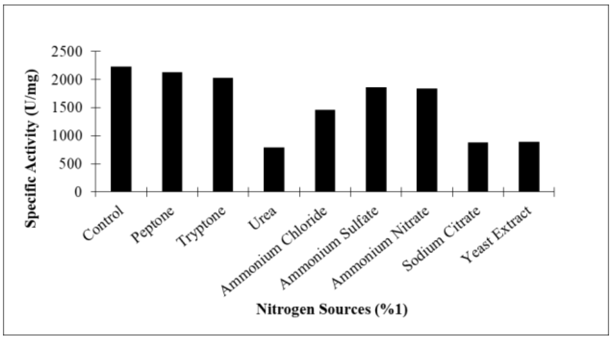

Figure 8. Effect of Nitrogen Sources on enzyme production

4. DISCUSSION AND CONCLUSION

Agüloğlu Fincan et al. [9] isolated a new thermo-tolerant bacteria named as *Bacillus licheniformis* SO-B3 from the mud sample of Şırnak-Meyrem deresi thermal spring and isolated amylase from the bacteria. 35°C and a pH of 7.0 were found to be the best conditions for enzyme generation. Özdemir et al. [21] found the maximum α-amylase production conditions from *Bacillus mojavensis* SO-10 bacteria to be 36 hour, 35°C and 7.0. Al Johani et al. [22] achieved maximum amylase production from *B.subtilis* at 45°C and pH 8.5 in agitated environment. Ortakaya et al. [23] isolated amylase from *Bacillus simplex*. While they determined the most suitable conditions for bacterial growth as 32. hour, 37°C and pH 7.0, they reported that they obtained the highest enzyme production at 72. hours, 37°C and 7.0. Agüloğlu Fincan and Enez [24] purified and characterized *Geobacillus stearotermophilus* α-amylase and they reported that maximum enzyme production was reached at pH 7.0 and 55°C at 24 hours and the enzyme was active in a wide temperature range between 50°C and 80°C.

α-Amylase's activity at alkaline pH is crucial in terms of its use in important areas such as detergent, food industry, liquefaction of starch and dry cleaning. Rakaz et al. [25] defined two species isolated from Omdurman Toti Island as *Bacillus cereus* and *Bacillus licheniformis*. They stated that *B. cereus* and *B. licheniformis*, which are alkalophilic and thermophilic, gave the best amylase activity at pH 8.0 and at 45°C and 65°C, respectively. Najafi et al. [26] determined the optimum temperature of *Bacillus subtilis* AX20 α-amylase, which they isolated from the soil, as 55°C and the optimum pH as 6.0. Kannan and Kanagaraj [27] named the bacteria they isolated from soil samples as *Bacillus licheniformis* and stated that they obtained the maximum amylase activity at pH 7.0 and 35°C after incubation at 48th hour. The results obtained in the studies carried out support the findings of our study.

Behal et al. [28] studied the effect of carbon and nitrogen sources on the production of α-amylase from *Bacillus sp*. AB 04, and obtained the maximum enzyme production by adding fructose as carbon source and meat extract as nitrogen source. Saxena et al. [29] *Bacillus sp*. maximum specific activity for PN5 thermostable amylase was obtained in media containing starch, peptone and yeast extract. Carvalho et al. [30] *Bacillus sp*. They achieved maximum enzyme production from SMIA-2 with peptone and soluble starch as carbon and nitrogen sources. Prakash et al. [30] obtained the maximum α-amylase production by adding tryptone. Agüloğlu Fincan and Enez [24] achieved the highest specific activity with ammonium nitrate among the nitrogen sources they used. Du [12] achieved maximum amylase production when they used peptone as N source and glucose as C source from *B. amyloliquefaciens* BH1. Asgher et al. [32] observed that 1% glucose suppressed amylase production from *Bacillus subtilis*. Al-Johani et al. [22] achieved maximum amylase production in culture medium supplemented with peptone and starch from B. subtilis. The findings we obtained in our study carbon and nitrogen sources are in agreement with the results of other researchers.

In our study, it was determined that temperature, pH and incubation time were effective on amylase activity and an increase in amylase activity could be achieved by using the optimum values of these physical parameters The maximum activity of the α-amylase we obtained at 40ºC will help especially in the washing sector. In addition, by adding the enzyme to detergents, a significant amount of energy will be saved as a result of maximum cleaning at low temperatures, and heat-induced wear will be prevented and the service life of the clothes will be extended.

REFERENCES

[1] Sun L, Warren FJ, Gidley MJ. Natural products for glycaemic control: Polyphenols as inhibitors of alpha-amylase. Trends Food Sci Technol. 2019; 91:262-273.

[2] Sundarram A, Murthy TPK. α-Amylase production and applications: a review. J Appl Environment Microbiol. 2014;2(4):166-175.

[3] Abou-Elela GM, El-Sersy NA, Wefky SH. Statistical optimization of cold adapted α-amylase production by free and immobilized cells of *Nocardiopsis aegyptia*. J Appl Sci Res. 2009;5(3):286-292.

[4] Farooq MA, Ali S, Hassan A, Tahir HM, Mumtaz S, Mumtaz S. Biosynthesis and industrial applications of α-amylase: A review. Arch Microbiol. 2021;203(4)1281-1292.

[5] Papoutsis K, Zhang J, Bowyer MC, Brunton N, Gibney ER, Lyng J. Fruit, vegetables, and mushrooms for the preparation of extracts with α-amylase and α-glucosidase inhibition properties: A review. Food Chem. 2021;338: 128119.

[6] Zheng Y, Tian J, Yang W, Chen S, Liu D, Fang H, Ye X. Inhibition mechanism of ferulic acid against α-amylase and α-glucosidase. Food Chem. 2020;317:126346.

[7] Far BE, Ahmadi Y, Khosroshahi AY, Dilmaghani A. Microbial alpha-amylase production: progress, challenges and perspectives. Advance Pharma Bull. 2020;10(3):350.

[8] Gupta R, Gigras P, Mohapatra H, Goswami VK, Chauhan B. Microbial α-Amylase: a Biotechnological Perspective. Process Biochem. 2003;1-18.

[9] Agüloğlu Fincan S, Özdemir S, Karakaya A, Enez B, Demiroğlu Mustafov S, Ulutaş MS, Şen, F. Purification and characterization of thermostable α-amylase produced from *Bacillus licheniformis* So-B3 and its potential in hydrolyzing raw starch. Life Sci. 2021;1:264.

[10] Woodley JM. Advances in enzyme technology-UK Contributions (Th.scheperi editör). Advance Biochem Eng/Biotechnol, Springer-Verlag. Berlin Heidelberg. 2000;94.

[11] Agüloğlu S, Ensari NY, Uyar F, Otludil B. The effects of amino acids on production and transport

of α-amylase through bacterial membranes. Starch/Starke, 2000;52, 290-295.
[12] Du R, Zhao F, Qiao X, Song Q, Ye G, Wang Y, Wang B, Han Y, Zhou Z. Optimization and partial characterization of ca-independent α-amylase from *Bacillus amyloliquefaciens* BH1, Prep Biochem Biotechnol.2018;48(8):768–774.
[13] Enez B. Purification and Characterization of Thermostable α-Amylase from Soil Bacterium *Bacillus* sp.Prot. Peptid Let. 2021;28(12):1372-1378.
[14] John RJD, Elangovan N. Molecular identification of amylase producing *Bacillus subtilis* and detection of optimal conditions. J Pharm Res 2013;6: 426-30.
[15] De Vos P. et al. Bergey's Manual of 1.Systematic Bacteriology: Volume 3: The Firmicutes. Springer, 2009.
[16] Vary PS, Biedendieck R, Fuerch T, Meinhardt F, Rohde M, Deckwer WD, Jahn D. *Bacillus megaterium* — from simple soil bacterium to industrial protein production host. Appl Microb Biotechnol. 2007;76: 957–967.
[17] Bunk B, Schulz A, Stammen S, et al. A short story about a big magic bug Boyke. Bioengineered Bugs. 2010; 1(2):85-91.
[18] Simair AA, Khushk I, Qureshi AS, Bhutto MA, Chaudhry HA, Ansari KA, Lu C. Amylase production from thermophilic *Bacillus* sp. BCC 021-50 isolated from a marine environment. Fermentation, 2017;3(2):25.
[19] Lowry OH, Rosebrough NJ, Farr AL. et al. Protein measurement with the Folin phenol reagent. J Biol Chem. 1951;193:265-275.
[20] Bernfeld P. Enzymes carbohydrate metabolism, ln Methods ln Enzymology, Academic Press. 1955;17:149-158.
[21] Özdemir S, Agüloğlu Fincan S, Karakaya A, Enez B. A novel raw starch hydrolyzing thermostable α-amylase produced by newly isolated *Bacillus mojavensis* SO-10: purification, characterization and usage in starch industries. Brazil Arch Bio Technol. 2018: 61.
[22] Al-Johani NB, Al-seeni MN, Ahmed YM. Optimization of alkaline α-amylase production by thermophilic *Bacillus subtilis*. Afr J Trad, Compl Alternati Meedici. 2017;14(1):288-301.
[23] Ortakaya V, Agüloğlu Fincan S, Enez B. α-Amylase from *Bacillus simplex* production, characterization and partial purification. Fresenius Environ Bull. 2017;26:4446–4455.
[24] Agüloğlu Fincan S, Enez B. Production, purification, and characterization of thermostable α-amylase from thermophilic *Geobacillus stearothermophilus*, Starch/Stärke. 2014;66:182-189.
[25] Rakaz MA, Hussien MO, Ibrahim HM. Isolation, Extraction, Purification, and Molecular Characterization for Thermostable α-Amylase from Locally Isolated *Bacillus* Species in Sudan. Biochemistry Res Int. 2021: 6670380.
[26] Kannan TR, Kanagaraj C. Molecular characteristic of α-amylase enzymes producing from *Bacillus lichenformis* (JQ946317) using solid state fermentation. Biocatal Agri Biotechnol. 2019;20:101240.
[27] Najafi MF, Deobagkar D, Deobagkar D. Purification and characterization of an extracellular α-amylase from *Bacillus subtilis* AX20. Protein Expr Purif. 2005;41:349–354.
[28] Behal A, Sınghj J, Sharma MK, Puri P, Batra N. Characterization of alkaline α-amylase from *Bacillus* sp. AB04. Int J Agri Biol. 2006; 8: 80–83.
[29] Saxena RK, Dutt K, Agarwal L, Nayyar P. A highly thermostable and alkaline amylase from a *Bacillus* sp. PN5. Biores Technol. 2007;98: 260–265.
[30] Carvalho RV, Cõrrea TLR, Silva JCM, Mansur LRCO, Martins MLL. Properties of an amylase from thermophilic *Bacillus* sp., Brazil J Microbiol. 2008; 39: 102–107.
[31] Prakash B, Vidyasagar M, Madhukumar MS, Muralikrishna G, Sreeramulu K. Production, purification, and characterization of two extremely halotolerant thermostable, and alkali-stable α-amylases from *Chromohalobacter* sp. TVSP 101. Process Biochem. 2009; 44:210–215.
[32] Asgher M, Javaid Asad M, Rahman SU, Legge RL. A thermostable α-amylase from a moderately thermophilic *Bacillus subtilis* strain for starch processing. J Food Eng. 2007; 79: 950–955.

Cilt 11, Sayı 4, Sayfa 42-49, 2022 Volume 11, Issue 4, Page 42-49, 2022

Araştırma Makalesi https://doi.org/10.46810/tdfd.1179350 Research Article

Türk Doğa ve Fen Dergisi
Turkish Journal of Nature and Science
www.dergipark.gov.tr/tdfd

Effect of Azimuth Angle on The Performance of a Small-Scale on-Grid PV System

Muharrem Hilmi AKSOY[1*], İsmail ÇİYLEZ[2], Murat İSPİR[1]

[1] Konya Technical University, Faculty of Engineering and Natural Sciences, Department of Mechanical Engineering, 42250, Konya, Türkiye
[2] Konya Technical University, Graduate Education Institute, Department of Mechanical Engineering, 42250, Konya, Türkiye
Muharrem Hilmi AKSOY ORCID No: 0000-0002-6509-8112
İsmail ÇİYLEZ ORCID No: 0000-0002-1113-5512
Murat İSPİR ORCID No: 0000-0001-5238-6011

**Corresponding author: mhaksoy@ktun.edu.tr*

(Received: 26.09.2022, Accepted: 08.11.2022, Online Publication: 28.12.2022)

Keywords
Azimuth angle,
Performance ratio,
PV performance,
Solar energy

Abstract: In this study, the effective solar irradiation on the PV surface, electricity generation, and performance ratios were investigated for a 100 kW small-scale on-grid PV system in Konya, Turkey. Five different azimuth angles -30°, -15°, 0°, 15°, and 30° were investigated for no-shading simulations with a fixed optimum tilt angle of 33°. As a result, the highest effective solar radiation is obtained at an azimuth of 0° as 1966.4 kWh/m², which is 2.12%, 0.46%, 0.79%, and 2.66% greater than the other azimuth angles of -30°, -15°, 15°, and 30°, respectively. On the other hand, it is seen that the highest energy production is obtained from the system with an azimuth angle of 0° with annual energy of 174.33 MWh. This value is 1.91%, 0.37%, 0.89%, and 2.8% greater than the other azimuth angles of -30°, -15°, 15°, and 30°, respectively. In addition, to evaluate the shading effect on the performance of the PV panels, two different panel spacings as, 4 m and 8 m, were also considered. It was seen that the electricity generation with an 8 m span system was 8.88% better than the 4 m. Another finding is that the height of the panels is negligible according to electricity generation. Finally, the highest performance ratio is obtained from the azimuth angle of 0°, as 0.857.

Azimut Açısının Küçük Ölçekli Şebekeye Bağlı Bir PV Sisteminin Performansına Etkisi

Anahtar Kelimeler
Azimut açısı,
Performans oranı,
PV performansı,
Güneş enerjisi,

Öz: Bu çalışmada, Konya, Türkiye'de 100 kW'lık şebekeye bağlı küçük ölçekli bir PV sistemi için efektif güneş ışınımı, elektrik üretimi ve performans oranları PVsyst yazılımı ile incelenmiştir. Optimum 33° sabit eğim açısı ile gölgelemesiz simülasyonlar için -30°, -15°, 0°, 15° ve 30° olmak üzere beş farklı azimut açısı incelenmiştir. En fazla efektif ışınım, -30°, -15°,15° ve 30° azimut açılarından sırasıyla %2.12, %0.46, %0.79 ve %2.66 daha büyük olarak 1966,4 kWh/m² değeriyle 0° azimut açısında gerçekleşmiştir. En iyi sonuçların 0° azimut açısında yıllık toplam 174.33 MWh enerji üretilebileceği belirlenmiştir. Bu üretim değeri -30°, -15°, 15° ve 30° olan diğer azimut açılarından sırasıyla %1.91, %0.37, %0.89 ve %2.8 daha büyüktür. Ayrıca, PV panellerin performansı üzerindeki gölgeleme etkisini değerlendirmek için 4 m ve 8 m olmak üzere iki farklı panel aralığı da dikkate alınmıştır. 8 m aralık sisteminin 4 m aralık sistemine göre %8.88 daha iyi olduğu görüldü. Ancak 8 m aralıklı sistemin daha fazla kurulum alanına ihtiyaç duyduğu bilinmektedir. Diğer bir bulgu ise panellerin elektrik üretimindeki yüksekliğinin ihmal edilebilir düzeyde olmasıdır. Son olarak en yüksek performans oranı 0° azimut açısı konumunda 0.857 olarak elde edilmiştir.

1. INTRODUCTION

With the development of science and technology, the current energy crisis and carbon emissions goals have turned to renewables as more binding energy globally. Developed and developing countries cooperate to prevent harmful practices such as emissions and greenhouse gases. In December 2020, the European Union target to reduce greenhouse gas effects by at least 55% by 2030, which is an essential step toward reducing emissions [1]. While renewable energy sources are available in many countries, it also depends on the geographical location according to the type of renewable sources [2,3].

Solar energy systems developed significantly over the last two decades are one of the most popular renewable energy sources [4]. PV cells are divided into three groups: silicon-based, thin-film, and third-generation, currently under development and not commercially available [5]. Silicon-based PV cells constitute approximately 85-90% of the market share and are still widely used [6]. PV Cell efficiency is one of the most critical parameters that give information about the system. The efficiency of silicon-based cells has increased year by year. The experimental efficiencies of the monocrystalline cell, one of the silicon-based cells, is approximately 15% in the 1950s, 17% in the 1970s, and 28% today taken under laboratory conditions. [7]. Today, application efficiencies are around 15-20% for monocrystalline, 11-15% for polycrystalline, and 6-7% for amorphous. [8,9]. In addition to the PV system's efficiency, production cost plays a vital role. In experiments conducted in 1974, cells had an efficiency value only of 4-5%, and the price of these cells was \$100/Wp [10]. In 2010, silicon-based cells' prices were between 3-3.5 USD/Wp [11]. In January 2018, the cost of installing a PV system varied between 1.73 USD/Wp and 1.23 USD/Wp depending on location [12]. In April 2020, the average price of PV cells was 0.177 USD/Wp for polycrystalline, 0.2 USD/Wp for monocrystalline, and 0.221 USD/Wp for thin film technologies [13]. As seen, the prices of PV cells have decreased, and their efficiency has increased over the years.

Turkey has a very advantageous position with an annual sunshine duration of 7.2 hours/day and annual total daily average irradiation of 3.6 kWh/m^2 [14,15]. Solar energy potential is relatively high in the Mediterranean Region and the South of the Central Anatolia Region, including Konya, as shown in Fig. 1 [16,17]. Turkey has reached a level of solar energy where it can compete with EU countries using the advantages of its geographical location. In 2019, PV systems were installed with a power of 3.9 GWp in Germany, 4.5 GWp in Spain, and 2.4 GWp in the Netherlands. Poland followed these countries with a new PV capacity of 800 MWp and Belgium, France, Hungary, and Italy with a PV capacity of 500 MWp [18]. The installed PV in Turkey was only 40 MW. This value has reached tremendous progress with a value of 7816 MW, with an increase of 19540% by 2021. While PV systems met 0.06% of electricity generation (E_G) in 2014, they accounted for 7.83% by 2021 [19,20]. The government's tax reductions in PV imports and incentives for plant establishment have a large share in this increase [21]. Also, in 2016, it made a tender for a 1000 MW PV plant in the renewable energy resource area (YEKA) in the Karapınar district of Konya [22]. Today, 756.05 MW of this facility has been completed, and, in this state, it meets the electricity needs of an average of 200000 people. The project is planned to be completed in August 2023. It is foreseen that the electricity needs of approximately 550.000 people will be met with an annual E_G of 2300 GWh upon the completion of the project [23]. This annual E_G is expected to meet 24% of Konya's and 0.6% of Turkey's electricity needs.

The tilt angle, which plays an important role in the performance of PV systems, is the ability to capture irradiation from the sun. This angle varies geographically. The optimum value of this angle is approximately equal to the latitude angle (φ) of the location. In addition, the optimum value of this angle changes seasonally. While this angle is 15° greater in latitude in summer season applications, it is 15° smaller in winter season applications. In addition to the tilt angle, the azimuth angle, representing the angle between the PV system and the south-north direction, greatly impacts the system's performance [25,26]. The tilt angle has a greater effect on the system performance than the azimuth angle [27]. However, while the tilt angles are adjustable, the azimuth angles can only be adjusted in field applications and cannot be adjusted much in roof applications.

Some studies investigate and examine the effects of tilt and azimuth angles on the performance of the systems. For example, the annual average E_G was calculated using ten different tilt angles including from 0° to 90° and five different azimuth angles including -90°, -45°, 0°, 45°, and 90° in Hong Kong, which has a latitude angle of 22°.

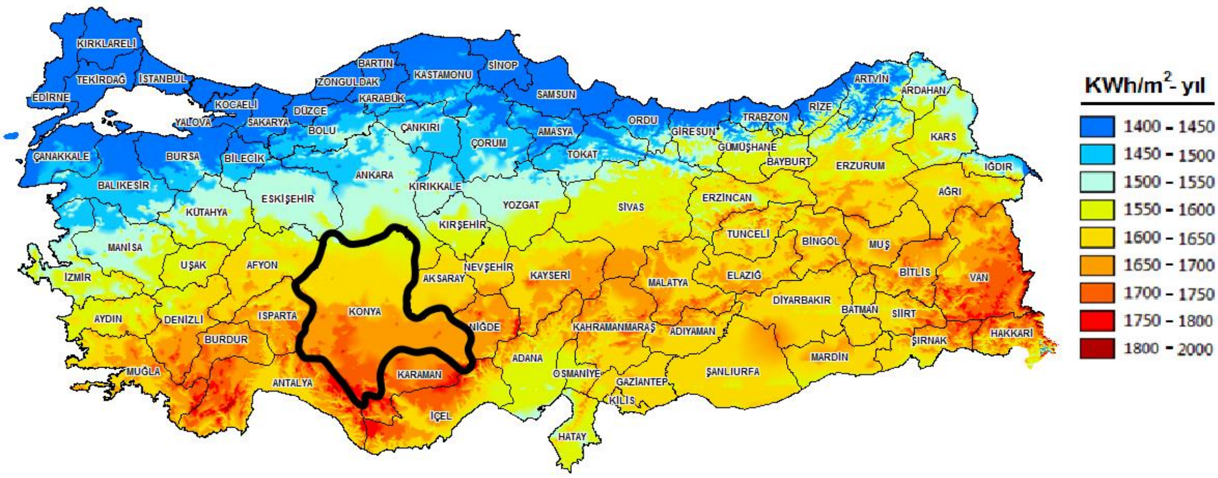

Figure 1. The solar energy potential map of Turkey and Konya [24]

In the study, when the tilt angle is constant, it has been observed that the most E_G is obtained with an azimuth angle of 0°. Furthermore, when the azimuth angle is constant, it has been observed that most E_G is obtained with a tilt angle of about 20° degrees [28].

In addition to tilt and azimuth angles, the shading area is one of the parameters affecting system performance [29,30]. According to an indoor experimental study, the model area is shaded with eight different percentage areas from 10% to 80%. It was concluded that the system efficiency and the output power decreased with the increase in the shading percentage [31]. A shading experiment with monocrystalline and polycrystalline cells was performed for five shading areas, 0%, 25%, 50%, 75%, and 100%. It was observed that the current produced decreased as the shading increased. In addition, it was concluded that if the system is shaded by 50%, E_G decreases by approximately 30% [32].

There are six mainly used software for modeling and analysis of PV systems, including PVsyst, RETScreen, HOMER, TRNSYS, INSEL, and PV F-Chart [33]. Developed by the University of Geneva, Switzerland, PVsyst software is a simulation and analysis program whose results can be obtained by performing on-grid or off-grid PV system design modeling. Compared to other software, this one has advantages such as containing more parameters and giving more detailed results. [34,35]. A study was conducted to compare E_G of Berlin and Kathmandu with the same PV cells with 60 kWp power using PVsyst software. While the tilt angle is 40^0 in Berlin, it is 30^0 in Kathmandu. According to the study, since Kathmandu receives more solar irradiation, the electricity produced is 70% more than in Berlin [36]. A power analysis was conducted at 1 MW with 3924 polycrystalline modules using PVsyst in Morocco. A study was conducted with tilt angles varying according to the seasons, 15° in summer and 48° in winter. In addition, analyses were made using a fixed tilt angle of 32° throughout the year. The fixed tilt angle system, with a performance ratio of 77.3%, was better than the seasonally different tilt angle system, with a performance ratio of 76.9% [37]. A study was carried out with bifacial PV cells on different surface grounds, including white, sand, and asphalt, using PVsyst Software in Konya. The bifacial system with white, sand and asphalt grounds has 8.86%, 4.55%, and 2.68% higher PR than the monofacial system. [38] Other findings from PVsyst in Algeria with a performance ratio of 83.9% [39], Poland with a performance ratio of about 88% [40], India with a performance ratio ranging from 74.9% to 52.57% [41], laboratory with a performance ratio 81% [42], simulation with a performance ratio 72.4% [43], and more.

This study investigates the effects of panel height and spacing on system performance and efficiency using a fixed tilt angle of 33° and different azimuth angles. In this way, it will be possible to comment on the amount of energy obtained from a system installed on the roofs of houses facing different directions.

2. MATERIAL AND METHOD

In this study, an installed capacity of 99 kW PV system is considered in Konya province with a latitude of 38.3°. The optimum tilt angle was determined as 33°, close to the latitude angle, using the METEO 8.0 program, which includes meteorological data and is included in PVsyst. A monocrystal panel with a 300 Wp capacity and a Solectria brand inverter with 50 kW 300-850 V 60 Hz were selected for the system. The system capacity has reached 330 cells, 22 on the horizontal axis and 15 on the vertical axis. Because it affects the output power, overload loss varies according to the array. For example, the 22 x 15 array has a 0.5% overload loss, which is acceptable. This array obtained a surface area of 537 m^2 as an on-grid system, where no batteries are needed.

Horizontal irradiation is independent of panels and angles. The amount of irradiation coming to the panel surface increases according to the coating material of the panel surfaces. However, contrary to irradiation reaching the horizontal plane, the irradiation incident on the panel surface depends on the angles and affects the system efficiency [44]. The amount of irradiation to the panel decreases significantly with a factor called the Incidence Angle Modifier (IAM). When the irradiation passing through the glass reaches the cell, it is reflected and reaches the glass surface again. IAM, dependent on b_0, surface glass quality, glass number, and albedo, is calculated as follows [45,46].

$$F_{IAM} = 1 - b_o \left(\frac{1}{\cos i} - 1 \right) \tag{1}$$

Where, i is the panel tilt angle. One of the essential pieces of information about the system is the Performance Ratio (PR). The PR is the ratio of the energy effectively produced with respect to the energy produced if the system continuously worked at its nominal STC efficiency. The PR is defined in the norm IEC EN 61724 [47].

$$PR = \frac{E_G}{G_I \times P_{PV}} \tag{2}$$

Where, E_G, is the amount of electricity supplied to the grid in kWh, G_I is the amount of irradiation coming into the panel in kWh m² and P_{PV} is the power of the system in kWp.

The sun is known to move from east to west. Therefore, hourly, the sun's radiation reaches the earth at a certain angle. This angle is called the hour angle (ω), defined as the hourly angle of the sun's irradiance with the location's meridian due to the earth's rotation of 15° per hour around its axis and the sun's movement from east to west. It is calculated as follows.

$$\omega = 15(ST - 12) \tag{3}$$

Where, ST is local time and equals 12 at midday. In addition, the sun's rays come daily at a certain angle to the equatorial plane. This angle is called the declination angle (δ), which is the angle between the sun irradiation coming to the earth and the earth's equator. This angle varies between -23.45° and 23.45° and is calculated as follows.

$$\delta = 23.45\, sin\left(360\frac{284+n}{365}\right) \quad (4)$$

Where, n is the number of days as of January 1. Also, the altitude angle (α) is the angle between the sun irradiation and the horizontal plane and is calculated as follows.

$$sin(\alpha) = sin(\varphi)sin(\delta) + cos(\varphi)\, cos(\delta)cos(HA) \quad (5)$$

The optimum azimuth angle of a location is calculated using Eqs. 3, 4 and 5 as follows.

$$sin(\gamma) = \frac{cos(\delta)\, sin(\omega)}{\cos(\alpha)} \quad (6)$$

3. RESULTS AND DISCUSSION

It is known that the amount of irradiation dramatically affects the performance of PV cells. The monthly average horizontal diffuse irradiation (G_{DH}) and global horizontal irradiation (G_H) from the sun to the horizontal plane in Konya using PVsyst are shown in Table 1.

Table 1. Monthly average total irradiation variations in Konya

Month	G_H [kWh/m²]	G_{DH} [kWh/m²]	Ambient Temperature [°C]
January	68.4	27.38	-1.43
February	86.6	32.85	0.55
March	129.8	50.26	5.55
April	165.9	65.31	9.72
May	209.7	67.94	14.87
June	222.8	63.59	19.63
July	229.6	70.10	23.86
August	207.5	57.67	23.58
September	169.0	42.77	18.16
October	118.8	39.98	12.14
November	78.4	31.1	5.28
December	62.1	22.9	0.27
Year	1748.7	571.83	11.08

The observance of highest ambient temperature is 23.86 °C, and the highest irradiation G_{DH} is 70.1 kWh/m² and G_H is 229.6 kWh/m² in July. So, an increase in irradiation values and ambient temperature towards summer in Table 1, while these values decrease towards winter, can be seen.

In this study, five different azimuth angles -30°, -15°, 0°, 15°, and 30°, were investigated for the effects on the system using PVsyst software. The monthly average irradiation amount coming to the panel surface is defined as G_I and varies according to the azimuth angles calculated using PVsyst and given in Table 2.

Table 2. Monthly average total G_I values with different azimuth angles

Month	Monthly average annual G_I [kWh/m²]				
	-30°	-15°	0°	15°	30°
January	104.2	110.1	112.7	111.8	107.4
February	117.7	122.6	124.3	122.9	118.3
March	154.7	159.2	160.9	159.6	155.7
April	177.9	178.1	177.1	174.5	171.2
May	205.2	203.3	201.7	200.5	199.0
June	204.8	202.9	202.8	203.6	206.1
July	219.7	216.7	215.6	214.7	215.3
August	213.5	214.9	216.0	215.3	213.8
September	198.4	202.2	202.9	200.1	195.2
October	156.9	162.5	164.3	162.1	156.3
November	114.4	120.3	122.8	121.8	117.2
December	99.9	105.3	107.3	105.8	100.8
Year	1967.4	1998	2008.5	1992.7	1956.2

Among considered cases, the highest monthly G_I was obtained in July as 219.7 kWh/m² from the system with an azimuth angle of -30°, while the lowest monthly G_I was received in December as 99.9 kWh/m² from the system with an azimuth angle of -30°. However, the highest annual G_I obtained as 2008.5 kWh/m² for the 0° azimuth case, while the lowest one, 1956.2 kWh/m², was received for the 30° azimuth case, which is more meaningful for comparison

The G_I reaching the earth is affected by losses like shading and IAM. The obtained irradiation after these effects is called Effective Global Irradiation (G_E) and given in Table 3.

Table 3. Monthly total average G_E values with different azimuth angles

Month	Monthly average G_E [kWh/m²]				
	-30°	-15°	0°	15°	30°
January	102.0	108.4	111.2	110.2	105.4
February	115.3	120.4	122.3	120.7	116.0
March	151.7	156.4	158.2	156.9	152.7
April	174.3	174.4	172.8	170.3	167.3
May	200.5	198.4	196.7	195.6	194.7
June	199.7	197.7	197.4	198.3	201.1
July	214.4	211.4	210.0	209.2	210.2
August	209.1	210.5	210.9	210.6	209.6
September	194.6	198.2	198.6	195.9	191.4
October	154.2	159.8	161.7	159.4	153.4
November	112.0	118.3	121.0	119.8	114.9
December	97.8	103.6	105.8	104.1	98.8
Year	1925.5	1957.4	1966.4	1951	1915.4

Like G_I, the highest monthly G_E was received in July as 214.4 kWh/m² with an azimuth angle of -30°. However, the highest annual G_E as 1966.4 kWh/m² was received with an azimuth angle of 0°. Since the irradiation intensity is higher in the summer, the value difference is enormous in summer than in winter. With a decrease of 2.66%, the most significant difference occurred in June, while the lowest was in January as 1.33%.

The monthly average annual E_G with a fixed tilt angle of 33° and various azimuth angles is given in Table 4.

Table 4. Monthly average electricity generations with different azimuth angles in Konya

Month	-30°	-15°	0°	15°	30°
January	0.930	0.931	0.932	0.933	0.935
February	0.918	0.916	0.915	0.914	0.916
March	0.890	0.889	0.888	0.887	0.887
April	0.871	0.871	0.868	0.868	0.870
May	0.848	0.847	0.846	0.845	0.846
June	0.827	0.826	0.824	0.823	0.822
July	0.811	0.810	0.808	0.807	0.807
August	0.811	0.810	0.806	0.806	0.807
September	0.828	0.825	0.823	0.822	0.823
October	0.867	0.864	0.864	0.864	0.863
November	0.903	0.904	0.903	0.901	0.899
December	0.924	0.925	0.924	0.923	0.921
Year	0.858	0.858	0.857	0.856	0.855

The highest annual E_G was obtained at an azimuth angle of 0° as 174.33 MWh, which is %2.8 higher than the azimuth angle of the 30° case. However, the highest monthly E_G was obtained from an azimuth of -30° as 18.09 MWh in July. In other words, in all cases, while the highest E_G is observed in the summer months, especially in July and August, and the lowest is observed in the winter months, especially in December and January.

The performance ratio gives information about the system. The monthly average annual performance ratios of the systems calculated with various azimuth angles are given in Table 5 using the PVsyst software.

Table 5. Monthly average annual PRs with different azimuth angles

Month	-30°	-15°	0°	15°	30°
January	0.930	0.931	0.932	0.933	0.935
February	0.918	0.916	0.915	0.914	0.916
March	0.890	0.889	0.888	0.887	0.887
April	0.871	0.871	0.868	0.868	0.870
May	0.848	0.847	0.846	0.845	0.846
June	0.827	0.826	0.824	0.823	0.822
July	0.811	0.810	0.808	0.807	0.807
August	0.811	0.810	0.806	0.806	0.807
September	0.828	0.825	0.823	0.822	0.823
October	0.867	0.864	0.864	0.864	0.863
November	0.903	0.904	0.903	0.901	0.899
December	0.924	0.925	0.924	0.923	0.921
Year	0.858	0.858	0.857	0.856	0.855

The highest PR was found as 0.935 at an azimuth of 30° in January, while the lowest one was obtained in August as 0.806 at an azimuth of 0° and 15°. Namely, the PR values are seen at low levels in the summer and at high levels in the winter months. When viewed annually, there is no significant change in the PRs with various azimuth angles. In addition, annual performance rates are at satisfactory levels.

In addition, by keeping the 33° tilt and 0° azimuth angles constant, four different systems were created for shading analysis by using two different PV panel distances, 4 m, and 8 m, and two different panel heights as 0.1 m and 1 m to evaluate their effect on the efficiency. In comparison, it was understood that the height of the panels had no significant effect on the system. In contrast, it was concluded that panel spacing significantly affects the system's performance. These two shading systems are compared with the no-shading system at 0° azimuth angle. The tilt angle is 33° for both shading and no-shading systems. Since the positions of both shading and no-shading systems are the same, G_I values do not change. However, the changes occur in G_E value, mainly due to some losses especially shading losses. The monthly average G_E values of shading and no-shading systems at 0° azimuth and 33° tilt angles are given in Fig. 2.

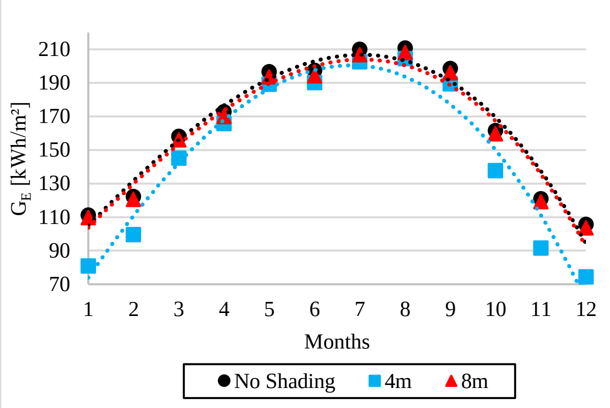

Figure 2. Monthly average of the G_E for no-shading case, 4 m and 8 m panel spans

As expected, the G_E of the no-shading system is higher than the other cases. In addition, since the losses will decrease with the increase of the panel spacing, the G_E value of the system with 8 m spacing is higher than that of the system with 4 m spacing. While there is not much G_E change in the 4 m panel spacing system in the summer months and considerable changes in the winter months, especially in December and January. The system with an 8 m panel span shows little change between the summer and winter. Because G_E comes to the panel surface more horizontally than in summer months in the 4 m panel space system, and the shorter panel spacing causes shadows. The monthly variations of the average E_G of the systems with 0° azimuth angle without shading and the shading systems with 4 m and 8 m panel distances are given in Fig. 3.

Because of the G_E coming to the panel surface in the summer months, as shown in Figure 2, is higher than in the winter months; more electricity is produced in the summer. As expected, E_G at the no-shading system is higher than in other cases. Because the G_E changes according to the months and shadows, the difference in E_G is huge in the winter, especially in December and January at the 4 m panel space case. The PRs of shading systems with 4 m and 8 m panel spacing are given in Fig. 4.

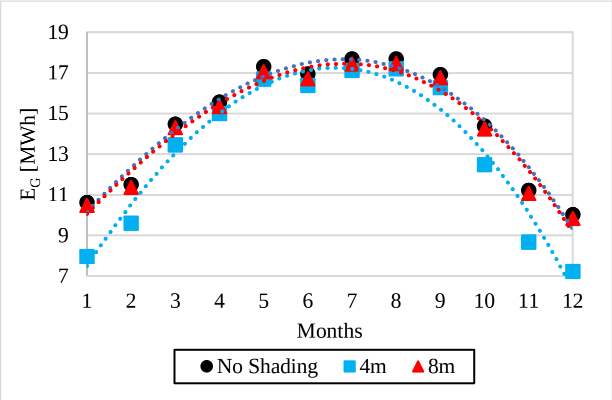

Figure 3. Monthly average variation of E_G of shading and no-shading cases

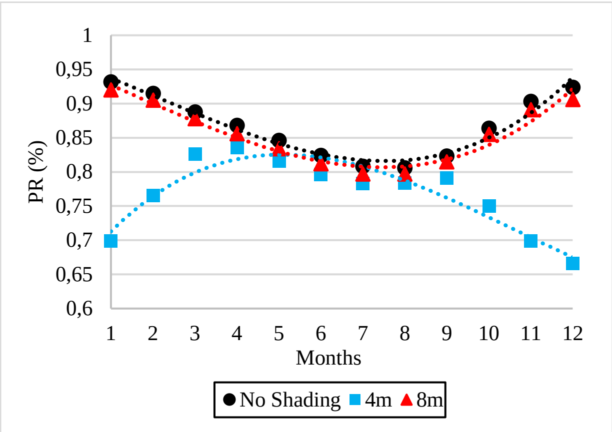

Figure 4. PRs of systems with 4 m and 8 m panel spacing and no shading cases

The PR of the system with 8 m panel spacing is higher in winter and lower in summer. Contrary to this system, the PR of the 4 m panel spacing system is lower in winter and higher in summer. When both systems are compared, the PR of the system with 8 m panel spacing is higher than that of the system with 4 m panel spacing in all months. However, the performance rates of these two systems in the summer months are very close. The PR of the system with panel spacing of 4 m decreased to 27.92% compared to the system without shading. The PR of the system with 8 m panel spacing shows a decrease between 0.97% and 1.95% throughout the year.

4. CONCLUSION

In this study, the effects of no-shading systems with a fixed tilt angle of 33° and five different azimuth angles, -30°, -15°, 0°, 15°, and 30°, were investigated for an on-grid PV system using PVsyst software.

- It was observed that the highest G_E, as 1966.4 kWh/m² occurred at an azimuth angle of 0°, while the lowest one as 1915.4 kWh/m² at an azimuth angle of 30°.
- Similarly, the annual highest E_G was obtained from the system with an azimuth angle of 0° as 174.33 MWh. The lowest E_G was obtained as 169.57 MWh with an azimuth angle of 30°, which is 2.74% lower than the 0° case.
- The highest PR, 0.858, was obtained from the systems with an azimuth angle of -30^0 and -15°. Similarly, for the system with an azimuth angle of 0°, PR was obtained as 0.857, which is approximately the same.

As a result, it is seen that the most proper system is the azimuth angle of 0° for PV applications in Konya.

Furthermore, by keeping a constant tilt angle of 33° and azimuth angle of 0°, the shading systems' effects consist of two different panel heights of 0.1 m, 1 m, and two different panel spacings 4 m, and 8 m, were examined. The obtained results are listed below.

- Although there should be some cooling differences in PV surface temperatures, for these simulations, it is seen that the panel height does not affect the system's performance.
- It is seen that the annual G_E at 4 m panel spacing case was decreased by 11%, while the reduction for the system with 8 m panel spacing was 1.45% compared to no shading case.
- The annual E_G with 4 m and 8 m, panel spacing cases were 154.47 MWh and 168.14 MWh, respectively, 12.85% and 3.68% lower than a no-shading system.
- Similarly, the PR of the systems with 4 m and 8 m panel spacing cases was calculated as 0.777 and 0.846, which are also lower than the no shading case.

It is seen that the results obtained from the system with 8 m panel spacing are better than the one with 4 m panel spacing. However, it should be considered that more land is needed for the system with the 8 m panel spacing case.

REFERENCES

[1] Tudor C, Sova R. EU Net-Zero Policy Achievement Assessment in selected members through Automated Forecasting Algorithms. ISPRS International Journal of Geo-Information. 2022;11:232-261.

[2] Gross R, Leach M, Bauen A Progress in renewable energy. Environment International. Pergamon. 2022;29:105-102.

[3] Kose F, Aksoy MH, Ozgoren M., Experimental investigation of solar/wind hybrid system for irrigation in Konya, Turkey. Thermal Science. 2019;23: 4129–4139.

[4] Bull SR. Renewable energy today and Tomorrow. Proceedings of the IEEE. 2001;89: 1216–1226.

[5] Bagher AM, Valid MMA, Mohsen M. Types of solar cells and application. American Journal of Optics and Photonics. 2015;3(5):94-113.

[6] Powell DM, Winkler MT, Choi HJ, Simmons CB, Needleman DB, Buonassisi T. Crystalline silicon photovoltaics: A cost analysis framework for determining technology pathways to reach baseload

electricity costs. Energy & Environmental Science. 2012;5(3):5874-5883.

[7] Tyagi VV, Rahim NAA, Rahim NA, Selvaraj JAL. Progress in solar PV technology: Research and achievement. Renewable and Sustainable Energy Reviews. 2013;20:443–461.

[8] Nogueira CE, Bedin J, Niedzialkoski RK, De Souza SN, Das Neves JC. Performance of monocrystalline and polycrystalline solar panels in a water pumping system in Brazil. Renewable and Sustainable Energy Reviews. 2015;51:1610–1616.

[9] Karaağac MO, Oğul H, Bulut F. Evaluation of Monocrystalline and Polycrystalline Photovoltaic Panels in Sinop Province Conditions. Turkish Journal of Nature and Science. 2021;10:176-181.

[10] Green MA. Silicon Photovoltaic Modules: A brief history of the first 50 years. Progress in Photovoltaics: Research and Applications. 2005;13:447–455.

[11] IRENA, Renewable Power Generation Costs in 2018 [Internet], International Renewable Energy Agency, Abu Dhabi, 2019 [cited 2022 September 20]. Available from: https://www.irena.org/publications/2019/May/Renewable-power-generation-costs-in-2018

[12] Jäger-Waldau A. Snapshot of photovoltaics − February 2018. EPJ Photovoltaics. 2018;9:6–11.

[13] Benda V, Černá L. PV cells and modules – state of the art, limits and Trends. 2020;6(12): e0566.

[14] Kaya MN, Aksoy MH, Köse F. Renewable Energy in Turkey: Potential, Current Status and Future Aspects. Annals of Faculty Engineering Hunedoara – International Journal of Engineering Tome. 2017;15:65–69.

[15] Babayigit O, Aksoy MH, Ozgoren M, Solmaz O. Investigation of absorption cooling application powered by solar energy in the South Coast region of Turkey. EPJ Web of Conferences. 2013;45:01100.

[16] Yilmaz Cakmak B. Solar energy potential of Konya and Architectural Design Criterias for solar energy efficiency. 2015 International Conference on Renewable Energy Research and Applications (ICRERA). 2015. p. 1463-1469.

[17] Sözen A, Arcaklioğlu E, Özalp M, Kanit EG. Solar-energy potential in Turkey. Applied Energy. 2005;80:367–381.

[18] Kougias I, Taylor N, Kakoulaki G, Jäger-Waldau A. The role of photovoltaics for the European Green Deal and the recovery plan. Renewable and Sustainable Energy Reviews. 2021;44:111017.

[19] Republic of Türkiye Ministry of Energy and Natural Resources [cited 2022 September 20]. Available from: https://enerji.gov.tr/eigm-yenilenebilir-enerji-kaynaklar-gunes.

[20] Çeçen M, Yavuz C, Tırmıkçı CA, Sarıkaya S, Yanıkoğlu E. Analysis and evaluation of distributed photovoltaic generation in electrical energy production and related regulations of Turkey. Clean Technologies and Environmental Policy. 2022;24:1321–1336.

[21] Doğan S, Yağmur S. Aksoy MH, Köse F. Solmaz O. Solar Energy Potential in Turkey and Manufacturability Research for Equipments of Photovoltaic Panel in Konya Province, III. International Congress on Environmental Research and Technology (Icerat), 2017. p 35.

[22] Karaveli AB, Soytas U, Akinoglu BG., The role of legislations and incentives in the growth of a PV market in a developing country. 2017 International Renewable and Sustainable Energy Conference (IRSEC). 2017.

[23] Enerji Atlası [internet]. Karapınar YEKA-1 GES [cited 2022 September 20]. Available from: https://www.enerjiatlasi.com/gunes/karapinar-yeka-11.html

[24] Republic of Türkiye Ministry of Energy and Natural Resources [cited 2022 September 20]. Available from:https://gepa.enerji.gov.tr/MyCalculator/pages/42.aspx

[25] Ahmed W, Sheikh JA, Ahmad S, Farjana SH, Mahmud MAP. Impact of PV system orientation angle accuracy on greenhouse gases mitigation. Case Studies in Thermal Engineering. 2021;23:100815.

[26] Yiğit A, Atmaca İ. Güneş Enerjisi Mühendislik Uygulamaları. 2nd ed. Bursa: Dora; 2018.

[27] Barbón A, Bayón-Cueli C, Bayón L, Rodríguez-Suanzes C. Analysis of the tilt and azimuth angles of photovoltaic systems in non-ideal positions for Urban Applications. Applied Energy. 2022;35:117802.

[28] Sun L, Lu L, Yang H. Optimum design of shading-type building-integrated photovoltaic claddings with different surface azimuth angles. Applied Energy. 2012;90:233–240.

[29] Yadav S, Hachem-Vermette C, Panda SK, Tiwari GN, Mohapatra SS. Determination of optimum tilt and azimuth angle of BiSPVT system along with its performance due to shadow of adjacent buildings. Solar Energy. 2021;215:206–219.

[30] Ramaprabha R, Mathur BL. Impact of Partial Shading on Solar PV Module Containing Series Connected Cells, 2019.

[31] Mamun MA, Hasanuzzaman M, Selvaraj J. Experimental investigation of the effect of partial shading on photovoltaic performance. IET Renewable Power Generation. 2017;11:912–921.

[32] Dolara A, Lazaroiu GC, Leva S, Manzolini G. Experimental investigation of partial shading scenarios on PV (photovoltaic) modules. Energy. 2013;55:466–475.

[33] Sharma, D. K., Verma, V., Singh, A. P. Review and Analysis of Solar Photovoltaic Softwares. International Journal of Engineering and Technology. 2017;4(2):725–731.

[34] Etci A, Bilhan A. PVSyst ile Konya ilinde sabit ve çift Eksenli Güneş Takip Sisteminin modellenmesi. European Journal of Science and Technology. 2022;32:142–147.

[35] Akcan E, Kuncan M, Minaz M. R. PVsyst Yazılımı ile 30 kw şebekeye Bağlı Fotovoltaik sistemin modellenmesi ve Simülasyonu. European Journal of Science and Technology. 2020;18:248–261.

[36] Karki P, Adhikary B, Sherpa K., Comparative study of grid-tied photovoltaic (PV) system in Kathmandu

and Berlin using PVsyst. 2012 IEEE Third International Conference on Sustainable Energy Technologies (ICSET). 2012.

[37] Belmahdi B, Bouardi AE., Solar potential assessment using PVSYST software in the Northern Zone of Morocco. Procedia Manufacturing. 2020;46:738–745.

[38] Aksoy MH, Çalik MK. Çift Yüzlü Fotovoltaik Panellerin Farklı Zemin Koşullarında Performansının incelenmesi. Konya Journal of Engineering Sciences. 2022;10(3):704–718.

[39] Soualmia A, Chenni R. Modeling and simulation of 15MW grid-connected photovoltaic system using PVsyst software. 2016 International Renewable and Sustainable Energy Conference (IRSEC). 2016.

[40] Boduch A, Mik K, Castro R, Zawadzki P., Technical and Economic Assessment of a 1 MWP floating photovoltaic system in Polish conditions. Renewable Energy. 2022;196:983–994.

[41] Bansal N, Jaiswal SP, Singh G., Long Term Performance Assessment and loss analysis of 9 MW grid tied PV plant in India. Materials Today: Proceedings. 2022;60:1056–1067.

[42] Sharma S, Kurian CP, Paragond LS., Solar PV system design using PVsyst: A case study of an Academic Institute. 2018 International Conference on Control, Power, Communication and Computing Technologies (ICCPCCT). Kannur, India: IEEE; 2018. p. 123–128.

[43] Yadav P, Kumar N, Chandel SS., Simulation and performance analysis of a 1kWp photovoltaic system using PVsyst. 2015 International Conference on Computation of Power, Energy, Information and Communication (ICCPEIC). Melmaruvathur, India: IEEE; 2015. p. 358–363.

[44] Öztürk D, Dener A. Power Generation Variation Analysis Of Solar Panels Coated With TiO2. Turkish Journal of Nature and Science. 2022;11:108-115.

[45] Boppana S, Passow K, Sorensen J, King BH, Robinson C. Impact of Uncertainty in IAM Measurement on Energy Predictions. 2018 IEEE 7th World Conference on Photovoltaic Energy Conversion (WCPEC). Waikoloa, HI, USA: IEEE; 2018. p. 2276–2281.

[46] PVsyst Help [cited 2022 September 20]. Available from: https://www.pvsyst.com/help/iam_loss.htm

[47] PVsyst Help [cited 2022 September 20]. Available from: https://www.pvsyst.com/help/performance_ratio.htm

Araştırma Makalesi https://doi.org/10.46810/tdfd.1120664 Research Article

Türk Doğa ve Fen Dergisi
Turkish Journal of Nature and Science
www.dergipark.gov.tr/tdfd

The Effect of Ca-Bentonite Application on Cadmium Uptake and Shoot Dry Matter of Bread Wheat

Dilek ECE[1*], Özlem ETE AYDEMİR[1], Faruk ÖZKUTLU[1]

[1] Ordu University, Agriculture Faculty, Soil Science and Plant Nutrition Department, Ordu, Türkiye
Dilek ECE ORCID No: 0000-0002-8928-0728
Özlem ETE AYDEMİR ORCID No: 0000-0002-6055-4908
Faruk ÖZKUTLU ORCID No: 0000-0002-8651-3346

**Corresponding author: dilekece5201@gmail.com*

(Received: 24.05.2022, Accepted: 08.11.2022, Online Publication: 28.12.2022)

Keywords
BreadWheat,
Bentonite,
Cadmium

Abstract: Cadmium (Cd) is a non-essential heavy metal that is highly toxic even at very low concentrations. Although Cd is a non-essential trace metal, when reached to high levels in agricultural soils, it can be easily absorbed by plants. Cadmium accumulation in wheat (*Triticum aestivum* L.) and its subsequent transfer to food chain is an important problem worldwide. Bentonite is a material essentially composed by montmorillonite and related clay minerals of the smectite group. The purpose of this study was to investigate the effects of bentonite (0, 3, 6 and 12%) application on Cd uptake of bread wheat growing in high Cd (0, 5 and 10 mg kg^{-1} soil) application. The experiment was conducted randomized block design with three replicates. The results revealed that shoot dry weight of bread was significantly increased with increasing doses of bentonite applications. While the dry weight of shoot without bentonite application was 480 mg/plant, it increased approximately 2 fold with 12% bentonite application. Cadmium concentration with the bentonite of control application decreased 4 times from 20.74 mg kg^{-1} to 5.07 mg kg^{-1} with application of 12% bentonite. The results show that Cd toxicity in the shoot was alleviated by bentonite treatment.

Ca-Bentonit Uygulamasının Ekmeklik Buğdayın Kadmiyum Alımına ve Yeşil Aksam Kuru Madde Verimi Üzerine Etkisi

Anahtar Kelimeler
Ekmeklik buğday,
Bentonit,
Kadmiyum

Öz: Kadmiyum (Cd), çok düşük konsantrasyonlarda bile oldukça toksik olan, mutlak gerekli olmayan bir ağır metaldir. Kadmiyum gerekli olmayan ağır metal olmasına rağmen, tarım topraklarında yüksek seviyelere ulaştığında bitkiler tarafından kolaylıkla alınabilir. Buğday 'da (*Triticum aestivum* L.) Cd birikiminin olması ve ardından besin zinciri vasıtasıyla insanlara geçişi global bir sorundur. Bentonit, esas olarak montmorillonit ve smektit grubuna ait kil minerallerinden oluşmaktadır. Bu çalışmanın amacı, bentonit (0, %3, %6 ve %12) ve Cd (0, 5 ve 10 mg kg^{-1} toprak) uygulaması altında yetiştirilen ekmeklik buğdayın Cd alımı üzerine etkilerini araştırmaktır. Deneme tesadüf blokları deneme deseninde üç tekerrürlü olarak yürütülmüştür. Sonuçlar, artan dozlarda bentonit uygulamaları ile ekmeğin yeşil aksam kuru madde verimini önemli ölçüde arttığını ortaya koymuştur. Bentonit uygulanmayan kontrol grubunda yeşil aksam kuru madde miktarı 480 mg/bitki iken, %12 bentonit uygulaması ile kuru madde verimi yaklaşık 2 kat artmıştır. Kontrol uygulamasında Cd konsantrasyonu 20.74 mg kg^{-1} iken %12 bentonit uygulamasında 4 kat azalarak 5.07 mg kg^{-1} olarak belirlenmiştir. Sonuçlar, bentonit uygulaması ile yeşil aksam Cd toksititesinin hafifletildiğini göstermektedir.

1. INTRODUCTION

Contamination of agricultural soils with heavy metals is an important problem worldwide, but also poses a serious threat to crop yields [1, 2, 3, 4, 5]. Cadmium (Cd), one of the heavy metals, is a toxic metal found almost everywhere, negatively affecting both plant and human health, and is very harmful even at very low levels [5, 6]. In the last 50 years, it has been announced that 22.000 tons of Cd has been released into the environment and 82%-94% of this is mixed into the soil [7]. It is also an important source of phosphorus fertilizers for the introduction of Cd into agroecosystems [8, 9]. Therefore, balanced fertilization of phosphorus is rather important in agricultural production [10]. While normal Cd levels in the soil range from 0 to 1 mg kg^{-1}, today the soils are at 1 to 3 mg kg^{-1} Cd levels and show a light pollution level. It has been explained that cadmium can accumulate in the plant tissue very easily even at very low concentrations in the soil and inhibit plant growth [11, 12, 13, 14, 15, 16]. It is possible for herbal products to be contaminated with Cd and to enter and accumulate in the human body by the food chain [17, 18]. Cadmium can be easily transported to grain products grown all over the world, especially in wheat grains [19]. When high Cd accumulates in wheat grains, serious health problems may occur as a result of people's consumption of these grains. For this reason, research on reducing Cd in cereal-based foods has been accelerated in recent years. There is a need to identify and apply the factors that reduce the transport of Cd, especially in agricultural soils. Clay minerals, which are an integral part of the soil system, are non-toxic, inexpensive, have a large specific area, and are widely used as soil conditioners [20, 21, 22]. The high metal adsorption capacity and low cost of clay minerals make them one of the most common treatment options for heavy metal adsorption [23, 24]. Bentonite is a natural soil conditioner that is mainly composed of clay minerals of the montmorillonite and smectite group, which can reduce water loss in the soil and increase crop yield [25]. Bentonite has a strong adsorption capacity for Cd in the soil, it can immobilize this metal and reduce the uptake of these metals by agricultural products [26, 27]. Wheat is the most important grain in the world after rice and corn, and approximately 60% is consumed as food [28]. As the human population grows, demand for wheat is expected to increase by an estimated 70% over the next few decades (2020-2050) [29]. Compared to other grains, wheat can accumulate more Cd in the root and grain [30, 31]. Therefore, with the intake of wheat-derived food products with the food chain, it also causes a small amount of Cd to be taken into the human body. Wheat, which meets the daily nutritional needs of people, should be of high quality and harmful metals should be reduced. The aim of this study is to investigate the effect of bentonite application to soils on cadmium uptake of bread wheat.

2. MATERIAL AND METHOD

2.1. Some Physical and Chemical Properties of Soil Used In The Experiment

The soil used for the pot experiment was loamy in texture with organic matter content of 1.52%. The soil used properties were determined soil pH 4.81, lime 0.8%, salinity 652 µs/cm, available P 3.74 mg/kg, available K 222 mg/kg, availability Mg 166 mg/kg and total Cd concentrations 0.51 mg Cd/kg. The analysis of all chemical and physical properties of the soils was carried out using standard methods given by [32].

2.2. Growth Conditions

Plants were grown under greenhouse conditions in plastic pots containing 1.7 kg soil. Seeds of bread wheat (*Triticum aestivum* L. cv. Bayraktar) were sown in plastic pots. The soil used was obtained from Ordu Province in Black Sea Region. About 12 seeds were sown in each pot and after emergence the seedlings were thinned to 6 per pot at the two leaf stage. For the Cd treatment, Cd were applied at a rate of 0, 5.0 and 10 mg kg^{-1} soil in the form of $3CdSO_4.8H_2O$ and Bentonite treatments consisted of four doses of (0%, 3%, 6% and 12%) bentonite, together with a basal treatment of 200 mg N kg^{-1} soil as $Ca(NO_3)_2$ and 100 mg P kg^{-1} soil as KH_2PO_4. After 45 day of growth in the greenhouse, the shoots were harvested and dried at 65 ºC for determination of dry matter weight and Cd concentration in the shoot. The shoot of Cd concentration was determined with Inductively Coupled Plasma-Atomic Emission Spectrometry (ICP-OES; Varian Vista-pro) instrument.

In order to determine whether there is a relationship between the analysis results determined in the leaf samples, analysis of variance using SPSS and lettering with LSD test were made according to Tukey.

3. RESULTS AND DISCUSSION

3.1. Shoot Dry Matter Weight, Mg $Plant^{-1}$

This research was carried out to determine the effects of different doses and application times of Cd and bentonite on bread wheat. The experiment was carried out in greenhouse conditions in the design of randomized plots with 3 replications. Plants were grown in strongly acid soil treated with increasing Cd (0, 5 and 10 mg kg^{-1}) and Bentonite (0%, 3%, 6% and 12%) and harvested after 45 days of growth under greenhouse conditions. Although shoot dry matter weight decreased with increasing Cd application, dry matter weight increased with increasing bentonite application. Increasing bentonite application tended to decrease Cd concentrations in shoot. Increasing bentonite doses significantly affected the reduction of Cd concentration ($P< 0.05$) in shoot.

Increasing soil Cd application without bentonite showed a negative effect on the shoot dry weight. The shoot dry weight in the plants not treated with bentonite was found as 485 mg/plant, but it decreased significantly to 430 mg/plant, with the soil application of 10 mg/kg Cd (Table 1). Dry matter yield increased with increasing bentonite applications. In the control, dry matter yield was determined mean 480 as mg/plant and increased with increasing bentonite doses.

Table 1. The effect of bentonite application on the shoot dry matter in bread wheat

Applications		Shoot dry matter weight, mg $plant^{-1}$			
		0 Cd ppm	5 Cd ppm	10 Cd ppm	Ortalama
Ca Bentonite	0%	485g	526e-g	430g	**481D**
	3%	700cd	669d-f	516fg	**628C**
	6%	845a-c	700cd	673de	**739B**
	12%	1060a	815b-d	946ab	**940A**
Ortalama		**773A**	**678AB**	**641B**	

The highest dry matter yield was determined as 940 mg/plant in 12% bentonite application. These increases and decreases in dry matter yield were found to be statistically significant at the $p<0.05$ level. The present study finding was consistent with, Wafaa and Wagida [33], El-Nagar et al.[34], they explored that the application of bentonite could considerably improved the plant growth and wheat yield.

3.2. Shoot Cadmium Concentration, (mg kg^{-1})

It was determined that there was a decrease in the average Cd concentrations of shoot with the increase of bentonite dose applications. With the increase in Cd doses, the average shoot Cd concentrations increased. These increases and decreases in shoot Cd concentration found to be statistically significant at the $p<0.05$ level. While the shoot Cd concentration in control (Cd0 and bentonite 0%) pots was 2.51 mg kg^{-1}, it became 0.56 mg kg^{-1} with 12% bentonite application and decreased approximately 4.5 fold. It was determined that shoot Cd concentrations decreased as the bentonite doses increased in all applications of Cd (0, 5, 10 mg kg^{-1}) (Table 2).

Table 2. The effect of bentonite application on the shoot cd concantration in bread wheat

Applications		Shoot Cd Concentration, mg kg^{-1}			
		0 ppm	5 ppm	10 ppm	Ortalama
Ca Bentonite	0%	2.51g	18.56c	41.15a	**20.77A**
	3%	1.56g	16.14d	31.16b	**16.28B**
	6%	0.86g	10.53e	14.89d	**8.76C**
	12%	0.56g	5.31f	9.35e	**5.07D**
Ortalama		**1.37C**	**12.63B**	**24.13A**	

Average Cd concentrations decreased with increasing bentonite applications. While the average Cd concentration was 20.74 mg/kg in the control, it was determined as 5.07 in the 12% bentonite application. The present study finding was consistent with, Shirvani et al. [35]. Sirait [36], Yu [37], they stated that bentonite application significantly reduced Cd uptake by plants.
Decrease in Cd uptake by wheat plants might be due to the higher surface area, with high cation exchange and ion adsorption capacity of Cd with Ca-bentonite. Bentonite minerals as one of the inorganic amendments can immobilize Cd by adsorption and precipitation process [26]. Bentonite has strong sorption capacity for soil Cd, which effectively immobilize metals to reduce metal uptake by crops [27]. Our study also showed that bentonite can significantly decreased shoot of Cd uptake. This result showed that Ca-bentonite can effectively decrease the mobility and bio availability of soil Cd. The results indicated that application of Ca-bentonite improved the plant growth by adsorbing the cadmium in the soil and alleviating the cadmium stress to the wheat. This is probably application of Ca-bentonite reduced the bioavailability of Cd and this might be due to the larger surface area as well as the stronger sorptive capacity of bentonite, which decreases the concentration of cations in the soil solution and thereby reduced the uptake by wheat.

4. CONCLUSION

Cadmium is a non-essential heavy metal that is highly toxic even at very low concentrations. Cadmium is pollutants that their discharge to the environment transported from different sources as agricultural and mining waste disposal, manure and phosphate fertilizer application to agricultural soils continuously. Cadmium contamination of agricultural soils is a growing concern which causes uptake by food crops. Wheat is a vital food crop cultivated in the world. Due to its high mobility, Cd can easily reach root uptake in wheat, shoot and grain by displacement. Uptake and accumulation of Cd by wheat may pose a risk to human life. Therefore, various agronomic approaches to reduce Cd uptake by wheat have been increasing rapidly in recent years. Various organic materials are used to reduce Cd uptake by wheat such as biochar, silicon, gyttja and bentonite. One of the most effective when compared to other organic materials is the use of bentonite. Application of bentonite to soils improves pH, CEC, nutrient availability and consequently increases agricultural productivity. According to the results of this research, addition of bentonite increases the chemical sorption of Cd and reduces the mobility of Cd as a consequence of complex formation. So, application of bentonite 12% demonstrated that wheat shoots reduced Cd uptake 4 fold. These results showed that bentonite can be used to reduce heavy metals in plants.

Acknowledgement

This research was supported by Ordu University Scientific Projects Support (BAP) Unit with the project numbered B-2001.

REFERENCES

[1] Özkutlu F, Turan M, Korkmaz K, Huang YM. Assessment of heavy metal accumulation in the soils and hazelnut plant (Corylus avellana L.) from Black Sea coastal region of Turkey. Asian J.of Chemistry. 2009;21(6):4371-4388.

[2] Adrees M, Ali S, Rizwan M, Ibrahim ., Abbas F, Farid M, Rehman MZ, Irshad MK. Bharwana SA. The effect of excess copper on growth and physiology of important food crops: a review. Environ. Sci. Pollut. Res. 2015;22:8148–8162.

[3] Ali S, Bharwana, SA, Rizwan M, Farid M, Kanwal S, Ali Q, Ibrahim M, Gill RA, Khan MD. Fulvic acid mediates chromium (Cr) tolerance in wheat (*Triticum aestivum* L.) through lowering of Cr uptake and improved antioxidant defense system. Environ. Sci. Pollut. Res. 2015;22:10601–10609.

[4] Habiba U, Ali S, Farid M, Shakoor M., Rizwan M, Ibrahim M, Abbasi GH, Hayat T, Al, B. EDTA enhanced plant growth, antioxidant defense system, and phytoextraction of copper by Brassica napus L. Environ. Sci. Pollut. Res. 2015;22:1534–1544.

[5] Rizwan M, Ali S, Abbas T, Zia-ur-Rehman M, Hannan F, Keller C, Ok YS. Cadmium minimization in wheat: a critical review. Ecotoxicology and Environmental Safety. 2016;130:43-53.

[6] Naeem A, Saifullah Rehman, MZ, Akhtar T, Yong SO, Rengel Z. Genetic variation in cadmium accumulation and tolerance among wheat cultivars at the seedling stage. Commun. Soil Sci. Plant Anal. 2016;47(5):554-562.

[7] Singh OV, Labana S, Pandey G, Budhiraja R, Jain, RK. Phytoremediation: an overview of metallic ion decontamination from soil. Appl. Microbiol. Biotechnol. 2003;61(5-6):405-412.
[8] Kılıç R, Korkmaz K. Kimyasal Gübrelerin Tarım Topraklarında Artık Etkileri. Biyoloji Bilimleri Araştırma Dergisi. 2012;5(2):87-90.
[9] Bracher C, Frossard E, Bigalke M, Imseng M, Mayer J, Wiggenhauser M. Tracing the fate of phosphorus fertilizer derived cadmium in soil-fertilizer-wheat systems using enriched stable isotope labeling. Environmental pollution. 2021;287:117314.
[10] Korkmaz, K, Akgün M, Özcan MM, Özkutlu F, Kara ŞM. Interaction effects of phosphorus (P) and zinc (Zn) on dry matter, concentration and uptake of P and Zn in chia. Journal of Plant Nutrition. 2021;44(5):755-764.
[11] Rehman, M. Z., Batool, Z., Ayub, M. A., Hussaini, K. M., Murtaza, G., Usman, M., ... & Ali, S. (2020). Effect of acidified biochar on bioaccumulation of cadmium (Cd) and rice growth in contaminated soil. Environmental Technology & Innovation, 19, 101015.
[12] Özkutlu F, Erdem H. The effect of zinc application doses to bread and durum wheat on cadmium uptake. Turkish Journal of Agriculture-Food Science and Technology. 2018a;6(12):1713-1717.
[13] Özkutlu F, Kara ŞM. The effect of zinc (Zn) fertilization on alleviating cd accumulation in durum wheat grain. Journal of Agricultural Science and Technology B. 2018b;8(2018):203-208.
[14] 14. Korkmaz K, Kara SM, Ozkutlu F, Gul V. Monitoring of heavy metals and selected micronutrients in hempseeds from North-Western Turkey. African Journal of Agricultural Research, 2010;5(6):463-467.
[15] Korkmaz K, Kara SM, Özkutlu F, Akgün M, Şenkal BC. Profile of heavy metal and nutrient elements in some sideritis. species. Indian Journal of Pharmaceutical Education and Research. 2017;51(3):209-212.
[16] Korkmaz K, Ertürk Ö, Ayvaz MC, Özcan MM, Akgün M, Kirli A, Alver DO. Effect of cadmium application on antimicrobial, antioxidant and total phenolic content of basil genotypes. Indian Journal of Pharmaceutical Education and Research, 2018;52(4):108-114.
[17] Huang M, Zhou S, Sun B, Zhao Q. Heavy metals in wheat grain: assessment of potential health risk for inhabitants in Kunshan, China. Sci. Total Environ. 2008;405:54–61.
[18] Dai XP, Feng L, Ma XW, Zhang YM. Concentration level of heavy metals in wheat grains and the health risk assessment to local inhabitants from Baiyin, Gansu, China. Adv. Mater. Res. 2021;518:951–956.
[19] Abedi T, Mojiri, A.. Cadmium uptake by wheat (*Triticum aestivum* L.): An overview. Plants. 2020;9(4):500.
[20] Varrault G, Bermond A. Kinetics as a tool to assess the immobilization of soil trace metals by binding phase amendments for in situ remediation purposes. Journal of Hazardous Materials. 2011;192(2):808-812.
[21] McBride MB, Martinez CE. Copper phytotoxicity in a contaminated soil: Remediation tests with adsorptive materials. Environ. Sci. Tech. 2000;34(43):86-91.
[22] Malandrino M, Abollino O, Buoso S, Giacomino A, Gioia CL, Mentasti E. Accumulation of heavy metals from contaminated soil to plants and evaluation of soil remediation by vermiculite. Chemo. 2011;82:169-78.
[23] Sun Y, Wu QT, Lee CCC, Li BQ, Long XX. Cadmium sorption characteristics of soil amendments and its relationship with the cadmium uptake by hyperaccumulator and normal plants in amended soils. International Journal of Phytoremediation. 2014;16(5):486.
[24] Kumararaja P, Manjaiah KM, Datta SC, Sarkar B. Remediation of metal contaminated soil by aluminium pillared bentonite: synthesis, characterisation, equilibrium study and plant growth experiment. Applied Clay Science. 2017;137:115-122.
[25] Mi J, Gregorich EG, Xu S, McLaughlin NB, Ma B, Liu J. Changes in soil biochemical properties following application of bentonite as a soil amendment. Eur. J. Soil Biol. 2021;251:102-103.
[26] Hamid Y, Tang L, Sohail MI, Cao X, Hussain B, Aziz MZ, Usman M, He Z, Yang X. An explanation of soil amendments to reduce cadmium phytoavailability and transfer to food chain. Sci Total Environ. 2019;660:80–96.
[27] Zhang D, Ding AF. Effects of passivating agents on the availability of Cd and Pb and microbial community function in a contaminated acidic soil. Bull Environ Contam Toxicol. 2019;103(1):98–105.
[28] Sobolewska M, Wenda-Piesik A, Jaroszewska A, Stankowski SE. Habitat and foliar fertilization with K, Zn and Mn on winter wheat grain and baking qualities. Agronomy. 2020;10;276.
[29] Vitale J, Adam B, Vitale P. Economics of wheat breeding strategies: focusing on Oklahoma hard red winter wheat. Agronomy. 2020;10(2):238.
[30] Greger M, Löfstedt M. Comparison of uptake and distribution of cadmium in different cultivars of bread and durum wheat. Crop Sci. 2004;44:501–507.
[31] Jafarnejadi, AR, Homaee M, Sayyad , Bybordi M. Large scale spatial variability of accumulated cadmium in the wheat farm grains. Soil. Sediment Contam. 2011;20:98–113.
[32] Jackson ML. Soil Chemical Analysis, second ed. CRC Press, Baton Rouge, FL. 1958.
[33] Wafaa MTE, Wagida ZH. Effect of potassium humate and bentonite on some soil chemical properties under different rates of nitrogen fertiliztion. J. Soil Sci. and Agric. Eng. 2017;8:539–544.
[34] El-Nagar DA, Sary DH. Synthesis and characterization of nano bentonite and its effect on some properties of sandy soils. Soil and Tillage Research, 2021;208:104872.

[35] Shirvani M, Shariatmadari M, Kalbasi M, Nourbakhsh F, Najafi B. Sorption of cadmium on palygorskite, sepiolite and calcite: equilibria and organic ligand affected kinetics. Colloid. Surf. A. 2006;287(1e3):182-190.

[36] Sirait M, Manalu PD. Preparation nature nano-bentonite as adsorbent heavy metal Cd and Hg. In Journal of Physics: Conference Series. 2018;1120(1):12-23.

[37] Yu K, Xu J, Jiang X, Liu C, McCall W, Lu J. Stabilization of heavy metals in soil using two organo-bentonites. Chemosphere. 2017;184:884-891.

Cilt 11, Sayı 4, Sayfa 55-62, 2022 Volume 11, Issue 4, Page 55-62, 2022

Araştırma Makalesi https://doi.org/10.46810/tdfd.996457 Research Article

Türk Doğa ve Fen Dergisi
Turkish Journal of Nature and Science
www.dergipark.gov.tr/tdfd

Cluster and Must Characteristics of Boğazkere and Kalecik Karası Grape Cultivars Grown on Different Rootstocks

Adem YAĞCI[1*], Abdurrahim BOZKURT[2]

[1]Tokat Gaziosmanpaşa University, Faculty of Agriculture, Department of Horticulture, Tokat, Türkiye
[2]Erzincan Horticultural Research Institute, Erzincan, Türkiye
Adem YAĞCI ORCID No: 0000-0002-3650-4679
Abdurrahim BOZKURT ORCID No: 0000-0001-7315-202X

**Corresponding author: adem.yagci@gop.edu.tr*

(Received: 16.09.2021, Accepted: 09.11.2022, Online Publication: 28.12.2022)

Keywords
Rootstock,
Antochyanin,
Flavonoid,
Total phenolic,
Wine grape

Abstract: The study was carried out in the Kırşehir/Toklumen vineyards of Kavaklıdere Winery Inc. in 2017 and 2018. The changes in bunch, berry, must, pH, total acidity, total phenolic, flavonoid and anthocyanin contents of Boğazkere and Kalecik Karası grape cultivars on 3 different rootstocks (110 Richter, 1103 Paulsen and 140 Ruggeri) from mole to harvest were investigated. An increase in cluster and berry weights of Boğazkere and Kalecik Karası grape cultivars, and softening in berry hardness with maturation, were observed between the veraison and the harvest period. While the must and pH values of the cultivars increased from mole to ripening, the total acidity values decreased. While the total phenolic and flavonoid contents, which were high during the veraison period, decreased towards the harvest period, the anthocyanin contents increased with maturation in both the skin and pulp. The cluster and berry weights of the cultivars on 140 Ru rootstock were lower than the other two rootstocks. During the harvest period, Boğazkere stood out in terms of total phenolic and anthocyanin content, and Kalecik Karası in terms of flavonoid content. Cluster and berry weights, must, pH, total acidity, total phenolic substance, flavonoid and anthocyanin content varied according to cultivar, rootstock and year.

Farklı Anaçlar Üzerinde Yetiştirilen Boğazkere ve Kalecik Karası Üzüm Çeşitlerinin Salkım ve Şıra Özellikleri

Anahtar Kelimeler
Anaç,
Antosiyanin
, Flavonoid,
Toplam fenolik,
Şaraplık üzüm

Öz: Bu çalışma 2017 ve 2018 yıllarında Kavaklıdere Şarapları A.Ş'nin Kırşehir/Toklumen bağlarında gerçekleştirilmiştir. Çalışmada 3 farklı anaç (110 Richter, 1103 Paulsen ve 140 Ruggeri) üzerinde yetiştirilen Boğazkere ve Kalecik Karası üzüm çeşitlerinde ben düşmeden hasat dönemine kadar salkım, tane, şıra, pH, toplam asitlik, toplam fenolik, flavonoid ve antosiyanin içeriklerinin zamana bağlı olarak değişimleri incelenmiştir. Ben düşme ile hasat dönemi arasında her iki yılda Boğazkere ve Kalecik Karası üzüm çeşitlerinin salkım ve tane ağırlığında artış, tane sertliğinde ise olgunlaşma ile birlikte yumuşama görülmüştür. Çeşitlerin şıra ve pH değerleri ben düşmeden olgunlaşmaya doğru artarken, toplam asitlik değerleri azalmıştır. Ben düşme döneminde yüksek olan toplam fenolik ve flavonoid içerikleri hasat dönemine doğru azalırken, antosiyanin içerikleri hem kabukta hem de pulpta olgunlaşma ile birlikte artış göstermiştir. Her iki çeşit 110 R ve 1103 P anaçları bakımından değişkenlik gösterse de 140 Ru anacına göre salkım ve tane ağırlığı bakımından daha yüksek değerler vermiştir. İki yılın hasat döneminde toplam fenolik ve antosiyanin içeriği bakımından Boğazkere üzüm çeşidi, flavonoid içeriği bakımından ise Kalecik Karası üzüm çeşidi ön plana çıkmıştır. Çeşitlerin salkım ve tane ağırlıkları ile şıra, pH, toplam asitlik, toplam fenolik madde, flavonoid ve antosiyanin içerikleri çeşide, anaca ve yıla göre değişkenlik göstermiştir.

1. INTRODUCTION

The main reason for the use of rootstock in vineyards is phylloxera pest [1, 2, 3]. Today, there is still no permanent chemical solution against phylloxera. It has not been successful enough by underwater or disinfecting the vineyard soils. Many rootstocks are used in the world, which can adapt to different soil types, have different resistance to drought, lime, salinity, phylloxera and nematodes, as well as have different compatibility abilities with *Vitis vinifera* L. cultivars. Studies on grape rootstock selection are among the basic studies of modern viticulture [4].

Grape rootstocks can affect the phenological stages, vegetative growing, bud shoot rate, ripening time, quality, cluster weight, must, acidity, leaf area and mineral nutrient content in the leaves of grape cultivars [5, 6, 7, 8, 9, 10, 11, 12, 13]. However, it is not possible to find all the desired characteristics in terms of yield and quality parameters in a single rootstock. It is difficult to clearly determine the interaction effects between rootstock and cultivar. As a matter of fact, vine rootstocks can have a primary or secondary effect on cultivars. It is stated that the primary effect affects the pruning weight (kg / vine) and the secondary effect affects the green parts of the vine[14].

The same grape cultivars can be grafted onto different American vine rootstocks for different reasons (soil, earliness, lateness, resistance to diseases and pests, adaptation, etc.). There are many research results showing that rootstocks affect the yield and quality of the grape cultivar grafted on.

The Central Anatolia region of our country is an important center in terms of viticulture potential. In this region, the provinces of Ankara, Çankırı, Yozgat, Kırıkkale, Kırşehir and Nevşehir come into prominence. While viticulture has an important social and economic place in this region, it has regressed over time due to reasons such as phylloxera damage, migrations, not giving the necessary importance to adaptation studies of new cultivars, and not doing the maintenance and cultural processes applied in viticulture according to the technique [15].

With this work; It was aimed to determine the effects of some wine grape cultivars (Boğazkere and Kalecik Karası) grafted on Berlandieri x Rupestris (110 R, 1103 P, 140 Ru) rootstocks on cluster, must and berry characteristics in Kırşehir (Toklumen) conditions.

2. MATERIAL AND METHOD

Research; It was carried out for two years in a producer's vineyard in Kırşehir in 2017 and 2018. Within the scope of the study, Boğazkere (grafted on 110 R, 1103 P and 140 Ru rootstocks) grape cultivar and Kalecik Karası (140 Ru, 1103 P and own roots) grape cultivar were used. The vines are 11-12 years old, the planting density is 2.0 m x 1.0 m and the training system is wall. After the veraison period, cluster samples were taken and brought to the laboratory in the cold chain environment and the following analyzes were made. Clusters weight; were measured by weighing on a digital scale (0.01 precision). Cluster length and width (cm) were measured with the help of a ruler. In bunch for berry measurement all the berries were plucked and placed in a bowl. Berry width and berry length (mm) were measured with a caliper by taking 25 randomly from this bowl. Berries hardness (Newton) were measured with a 1.54 mm penetrating hardness testing machine (PCE, SLJ-B). Amount of must (%) by refractometer (Atago Master-93H); acidity (g l^{-1}) According to Cemeroğlu [16]; The pH in the must was determined with a ph-measuring equipment (WTW Inolab pH 7310). While determining the phenolic, flavonoid and anthocyanin contents in the berry, sample preparation was done according to Bino et al. [17]. Total amount of phenolic substance Velioğlu et al. [18], the total amount of flavonoids Zhishen et al. [19] and the total amount of anthocyanin was determined according to Di Stefano and Cravero [20].

2.1. Statistical Analyses

Data; The analysis of variance was performed in a randomized block design with 3 replications and 18 vine per replication. Each cultivar was evaluated in itself. LSD ($p \leq 0.05$) test was used to compare the means, and the data of each week were analyzed separately.

3. RESULTS AND DISCUSSION

Two-year cluster and must data of Boğazkere grape cultivar grafted on different rootstocks are given in Table 1 and Table 2.

According to the data obtained, the berry weight and pH values of Boğazkere grape cultivar were found to be statistically significant during the harvest period ($p \leq 0.05$). In terms of cluster weight, some variation was observed between 110 R and 1103 P rootstocks. In the first year of the harvest period, the highest cluster (184.4 g) and berry weight (2.00 g) was 110 R, and the highest pH (3.44) 140 Ru combination. It can be said that the 1103 P combination stands out in terms of cluster weight (375.0 g) in the 2nd year harvest period.

Table 1. Cluster and must characteristics of Boğazkere grape cultivar on different rootstocks (2017)

Sample date	Rootstocks	Cluster weight (g)	Berry weight (g)	Berry hardness (NW)	Must (%)	pH	Acidity (g l^{-1})
August 15	110 R	66.9 a	0.60	1.53	6.5 a	2.72	38.02
	1103 P	51.2 b	0.66	1.77	5.4 b	2.83	38.50
	140 Ru	54.0 b	0.64	1.97	6.2 ab	2.68	42.02
LSD $_{(0.05)}$		11.4	ns	ns	ns	ns	ns
August 22	110 R	60.3 a	0.64	1.06	7.1	2.77	32.36
	1103 P	71.9 a	0.79	1.28	7.0	2.87	35.26
	140 Ru	57.7ab	0.75	1.28	7.5	2.73	29.69
LSD $_{(0.05)}$		9.0	ns	ns	ns	ns	ns
August 29	110 R	68.7 b	0.84 a	0.76	10.5	2.84 b	20.43
	1103 P	110.5 a	0.77 a	1.10	11.2	3.04 a	22.00
	140 Ru	60.6 b	0.59 b	1.14	9.4	2.81 b	20.83
LSD $_{(0.05)}$		36.8	0.10	ns	ns	0.17	ns
September 5	110 R	129.1 ab	1.06	0.55	14.1	2.93	16.47
	1103 P	164.5 a	1.05	0.59	14.5	3.09	17.84
	140 Ru	94.2 b	0.77	0.53	14.5	3.03	17.84
LSD $_{(0.05)}$		67.8	ns	ns	ns	ns	ns
September 12	110 R	141.5	1.40	0.53	16.8 b	3.14	10.61 b
	1103 P	191.1	1.57	0.57	18.2 a	3.19	9.93 b
	140 Ru	136.0	1.26	0.44	14.9 c	3.09	15.05 a
LSD $_{(0.05)}$		ns	ns	ns	ns	ns	2.33
September 18	110 R	167.5	1.52	0.48 b	17.9	3.18	8.41
	1103 P	138.4	1.36	0.55 b	18.7	3.22	8.51
	140 Ru	158.3	1.43	0.91 a	16.2	3.28	7.95
LSD $_{(0.05)}$		ns	ns	0.22	0.22	ns	ns
Harvest	110 R	184.4	2.00 a	0.44	20.7	3.23 c	7.54
	1103 P	182.6	1.67 b	0.52	20.4	3.32 b	7.11
	140 Ru	167.3	1.40 b	0.54	20.7	3.44 a	7.11
LSD $_{(0.05)}$		ns	0,28	ns	ns	0,07	ns

Table 2. Cluster and must characteristics of Boğazkere grape cultivar on different rootstocks (2018)

Sample date	Rootstocks	Cluster weight (g)	Berry weight (g)	Berry hardness (NW)	Must (%)	pH	Acidity (g l^{-1})
August 10	110 R	169.2 a	1.35	0.67 ab	13.2	2.92	13.09 b
	1103 P	104.0 b	1.69	0.48 b	12.6	2.94	20.23 a
	140 Ru	152.7 a	0.89	0.82 a	11.3	2.87	18.70 a
LSD $_{(0.05)}$		ns	ns	0.19	0.19	ns	4.96
August 17	110 R	216.3	1.77	0.36	13.6	3.00	12.02
	1103 P	171.8	1.72	0.42	14.7	2.98	16.28
	140 Ru	158.1	1.48	0.47	12.1	2.93	17.13
LSD $_{(0.05)}$		ns	ns	ns	ns	ns	ns
August 31	110 R	237.2	2.21 a	0.30	17.3	3.05	9.07
	1103 P	278.7	2.23 a	0.34	16.4	3.01	10.71
	140 Ru	228.9	1.70 b	0.31	16.5	3.04	8.33
LSD $_{(0.05)}$		ns	0.32	ns	ns	ns	ns
September 14	110 R	274.3	2.35	0.27	19.6	3.24	7.07
	1103 P	325.5	2.27	0.28	19.3	3.25	6.87
	140 Ru	300.4	1.93	0.23	21.0	3.27	7.24
LSD $_{(0.05)}$		ns	ns	ns	ns	ns	ns
Harvest	110 R	318.3	2.49	0.20	21.8 b	3.32	6.07
	1103 P	375.0	2.42	0.22	21.1 b	3.30	4.84
	140 Ru	314.0	2.72	0.21	23.1 a	3.29	5.88
LSD $_{(0.05)}$		ns	ns	ns	ns	ns	ns

The 2017 and 2018 cluster and must characteristics of Kalecik Karası grape cultivar, which is another combination subject to the study, are given in Table 3 and Table 4. During the harvest period, values total acidity in Kalecik Karası grape cultivar in the 1st year and must in the 2nd year were found to be statistically significant ($p \leq 0.05$). In the harvest period of the first year, 1103 P combinations came to the fore in terms of cluster (236.6 g) and berry weight (1.42 g). In the harvest period of the second year, the combination of Kalecik Karası grape cultivar grown in its own roots stood out in terms of cluster (208.6 g) and berry weight (2.18 g) (Table 3 and Table 4). There are many studies on rootstock and cultivar combinations in viticulture in our country [5, 9, 11, 12, 22, 23, 24, 25, 26, 27]. From these studies; It can be concluded that rootstocks may have different effects on the phenolic stages, vegetative growing, cluster and berry characteristics of the cultivars and chemical parameters (such as must, pH, acidity) and this effect may vary from year to year with climate and cultural practices. 1103 P and Kalecik Karası grape cultivar/own root combinations came into prominence. In terms of cluster and berry weight, 140 Ru rootstock gave lower values in both cultivars compared to other combinations. Considering the data obtained, it is not seen that there is a single rootstock that has all the desired characteristics in terms of quality in viticulture, similar to other fruit species [21].

Table 3. Cluster and must characteristics of Kalecik Karası grape cultivar on different rootstocks (2017)

Sample date	Rootstocks	Cluster weight (g)	Berry weight (g)	Berry hardness (NW)	Must (%)	pH	Acidity (g l^{-1})
August 15	1103 P	121.8	0.99	1.08	14.1	2.84	15.49 b
	140 Ru	91.8	0.76	1.03	14.7	2.84	22.42 a
	Vinifera	135.2	1.08	0.82	14.9	2.99	13.25 b
LSD $_{(0.05)}$		ns	ns	ns	ns	ns	5.93
August 22	1103 P	151.2	1.20	0.62 b	17.1	3.08 b	13.20
	140 Ru	114.9	0.90	0.94 a	15.6	3.03 c	19.23
	Vinifera	134.0	1.13	0.56 b	15.7	3.20 a	12.52
LSD $_{(0.05)}$		ns	ns	0.24	0.24	0.05	ns
August 29	1103 P	181.6 a	1.37	0.60	19.9	3.11	9.23 b
	140 Ru	123.1 b	1.03	0.56	20.0	3.13	10.56 a
	Vinifera	158.0 ab	1.13	0.52	18.9	3.22	8.74 b
LSD $_{(0.05)}$		44.2	ns	ns	ns	ns	1.44
September 5	1103 P	200.3	1.36	0.36	21.3	3.20	8.47
	140 Ru	148.9	1.12	0.47	20.9	3.19	9.99
	Vinifera	166.9	1.16	0.40	22.2	3.35	8.08
LSD $_{(0.05)}$		ns	ns	ns	ns	ns	ns
September 12	1103 P	230.5 a	1.38	0.31	23.7	3.40 b	6.45
	140 Ru	126.7 b	1.13	0.42	23.2	3.46 b	8.16
	Vinifera	165.9 ab	1.20	0.33	23.0	3.58 a	6.96
LSD $_{(0.05)}$		73.3	ns	ns	ns	0.06	ns
Harvest	1103 P	236.6	1.42	0.70	24.3	3.48	6.08 b
	140 Ru	144.2	1.27	0.45	25.7	3.54	7.45 a
	Vinifera	172.1	1.28	0.44	25.9	3.46	7.57 a
LSD $_{(0.05)}$		ns	ns	ns	ns	ns	0.50

Table 4. Cluster and must characteristics of Kalecik Karası grape cultivar on different rootstocks (2018)

Sample date	Rootstocks	Cluster weight (g)	Berry weight (g)	Berry hardness (NW)	Must (%)	pH	Acidity (g l^{-1})
August 10	1103 P	190.0 a	1.84 a	0.28 b	18.4	3.19	8.90
	140 Ru	127.8 b	1.48 b	0.44 a	21.5	3.20	11.08
	Vinifera	155.0 b	1.76 a	0.32 b	17.3	3.39	12.17
LSD $_{(0.05)}$		31.2	0.16	0.08	ns	ns	ns
August 17	1103 P	197.5	1.96 a	0.29	20.9	3.21 b	9.22
	140 Ru	189.7	1.41 b	0.40	19.1	3.28 b	8.64
	Vinifera	170.4	1.88 a	0.26	22.5	3.45 a	8.87
LSD $_{(0.05)}$		ns	0.28	ns	ns	0.08	ns
Harvest	1103 P	198.2	2.17	0.26	23.7 b	3.34	7.60
	140 Ru	196.0	1.70	0.28	25.6 a	3.36	7.07
	Vinifera	208.6	2.18	0.21	26.3 a	3.62	7.33
LSD $_{(0.05)}$		ns	ns	ns	1.8	ns	ns

Other parameters in the study are total phenolic, flavonoid and anthocyanin contents. Data for Boğazkere grape cultivar grafted on different rootstocks are given in Table 5 and Table 6, and data for Kalecik Karası grape cultivar are given in Table 7 and Table 8. In Boğazkere grape cultivar, the highest flavonoid content (3.12 mgQUE g^{-1} in pulp) in the 1st year was detected in the 1103 P combination. The highest total phenolic substance (95.14 mg GAE 100 g^{-1}) and the highest anthocyanin content (17.31 mg g^{-1} bark and 0.83 mg g^{-1} pulp) were determined on 140 Ru rootstock in the same cultivar in the second year. The highest flavonoid content (54.38 mgQUE g^{-1} in the skin) was determined in the 110 R combination (Table 5 and Table 6).

Table 5. Phenolic, flavonoid and anthocyanin contents of Boğazkere grape cultivar grafted on different rootstocks (2017)

Sample date	Rootstocks	Anthocyanin (mg g^{-1})		Flavonoid (mg QUE g^{-1})		Total phenolic (mg GAE 100 g^{-1})
		Pulp	Skin	Pulp	Skin	
August 22	110 R	0.10 a	0.88 a	26.00	384.00 a	760.24 b
	1103 P	0.01 b	0.20 b	20.36	342.81 ab	791.68 ab
	140 Ru	0.08 a	0.71 a	24.93	310.39 b	857.19 a
LSD (0.05)		0.03	0.34	ns	41.4	71.4
August 29	110 R	0.15	1.53	15.92 b	208.21 a	589.78 c
	1103 P	0.12	1.09	17.70 a	186.38 b	697.76 b
	140 Ru	0.18	1.45	18.08 a	157.33 c	748.78 a
LSD (0.05)		ns	ns	1.2	10.7	39.8
September 5	110 R	0.26	3.39	14.37	84.19	362.52
	1103 P	0.20	2.50	15.10	113.74	270.59
	140 Ru	0.26	1.55	16.44	115.73	265.21
LSD (0.05)		ns	ns	ns	ns	ns
September 12	110 R	0.30	3.39	12.57	83.00	223.56
	1103 P	0.25	3.64	13.49	82.50	281.40
	140 Ru	0.32	2.79	13.55	76.50	362.21
LSD (0.05)		ns	ns	ns	ns	ns
September 18	110 R	0.61 a	4.41	7.37 b	55.05 c	285.31 a
	1103 P	0.46 b	4.83	9.54 a	60.74 b	265.94 a
	140 Ru	0.44 b	4.23	9.05 a	72.67 a	234.10 b
LSD (0.05)		0.04	ns	1.20	3.80	28.90
Harvest	110 R	0.81 a	6.50	2.95 b	15.11	161.26
	1103 P	0.52 b	6.07	3.12 a	18.72	188.55
	140 Ru	0.44 b	5.80	3.05 ab	18.13	171.72
LSD (0.05)		0.15	ns	0.11	ns	ns

Table 6. Phenolic, flavonoid and anthocyanin contents of Boğazkere grape cultivar grafted on different rootstocks (2018)

Sample date	Rootstocks	Anthocyanin (mg g^{-1})		Flavonoid (mg QUE g^{-1})		Total phenolic (mg GAE 100 g^{-1})
		Pulp	Skin	Pulp	Skin	
August 10	110 R	0.09	0.56 b	10.82 b	156.40	332.29 b
	1103 P	0.09	0.90 b	10.63 b	157.18	510.21 a
	140 Ru	0.09	1.62 a	11.12 a	153.85	441.79 b
LSD (0.05)		ns	0.69	0.23	ns	76.29
August 17	110 R	0.10 b	0.72 b	7.64	122.44 a	374.07
	1103 P	0.12 b	1.05 b	8.10	122.26 a	346.71
	140 Ru	0.38 a	2.15 a	7.86	117.98 b	315.14
LSD (0.05)		0.22	0.61	ns	2.11	ns
August 31	110 R	0.19 b	5.51	5.40	104.15	253.14
	1103 P	0.14 b	6.27	5.61	101.45	278.21
	140 Ru	0.56 a	5.96	5.69	98.77	276.79
LSD (0.05)		0.06	ns	ns	ns	ns
September 14	110 R	0.30 b	11.79	4.36 a	81.31	305.21
	1103 P	0.49 ab	12.55	4.26 b	80.12	254.79
	140 Ru	0.81 a	12.08	4.43 a	82.93	172.50
LSD (0.05)		0.34	ns	0.11	ns	ns
Harvest	110 R	0.37 b	13.56 b	3.56	54.38 a	79.36 b
	1103 P	0.63 ab	16.78 a	3.53	53.70 ab	75.64 b
	140 Ru	0.83 a	17.31 a	3.47	53.07 b	95.14 a
LSD (0.05)		0.27	2.79	ns	0.77	14.04

In Kalecik Karası grape cultivar, the highest total phenolic substance (202.85 mg GAE 100 g^{-1}) 140 Ru, the highest flavonoid (89.75 mgQUE g^{-1} in skin) and anthocyanin (4.59 mg g^{-1} in skin) in 2017 harvest period contents were determined in the 1103 P combination (Table 7).

Table 7. Phenolic, flavonoid and anthocyanin contents of Kalecik Karası grape cultivar grafted on different rootstocks (2017)

Sample date	Rootstocks	Anthocyanin (mg g^{-1})		Flavonoid (mg QUE g^{-1})		Total phenolic (mg GAE 100 g^{-1})
		Pulp	Skin	Pulp	Skin	
August 22	1103 P	0.13	1.33	33.57	442.50 c	533.21 a
	140 Ru	0.08	1.15	33.72	736.25 a	465.26 b
	Vinifera	0.09	0.95	34.22	508.35 b	392.88 c
LSD (0.05)		ns	ns	ns	32.60	60.30
August 29	1103 P	0.15	1.59 b	18.07 b	261.90	376.83
	140 Ru	0.21	2.19 a	18.93 a	287.49	402.53
	Vinifera	0.15	1.16 b	19.36 a	259.55	379.43
LSD (0.05)		ns	0.58	0.55	ns	ns
September 5	1103 P	0.19	2.15	15.08 c	239.81 a	270.43
	140 Ru	0.32	2.82	16.46 b	222.70 a	323.32
	Vinifera	0.21	3.10	17.01 a	139.82 b	238.53
LSD (0.05)		ns	ns	0.19	26.6	ns
September 12	1103 P	0.29 c	3.22	14.82 a	144.74 a	185.15
	140 Ru	0.50 a	3.33	7.56 b	107.50 b	193.67
	Vinifera	0.35 b	3.46	6.35 c	75.67 c	205.20
LSD (0.05)		0.04	ns	1.16	14.7	ns
Harvest	1103 P	0.61	4.59 a	6.42	89.75 a	161.65 ab
	140 Ru	0.71	3.93 b	6.41	82.25 b	202.85 a
	Vinifera	0.66	3.92 b	6.45	71.75 c	120.10 b
LSD (0.05)		ns	0.16	ns	0.63	41.50

The highest flavonoid content (4.59 mgQUE g-1 in pulp) of the cultivars were determined in the 140 Ru combination in the 2018 harvest period, while other parameters were statistically insignificant ($p \leq 0.05$) during the harvest period (Table 8).

Table 8. Phenolic, flavonoid and anthocyanin contents of Kalecik Karası grape cultivar grafted on different rootstocks (2018)

Sample date	Rootstocks	Anthocyanin (mg g^{-1})		Flavonoid (mg QUE g^{-1})		Total phenolic (mg GAE 100 g^{-1})
		Pulp	Skin	Pulp	Skin	
August 10	1103 P	0.10 b	0.54	9.89 a	155.63	463.71 a
	140 Ru	0.07 c	0.59	9.28 b	154.27	429.14 a
	Vinifera	0.11 a	0.75	9.62 a	156.43	303.93 b
LSD (0.05)		0.01	ns	0.29	ns	114.42
August 17	1103 P	0.14	3.22 a	7.34	125.47 a	251.79
	140 Ru	0.11	2.82 b	7.84	116.64 b	384.14
	Vinifera	0.13	2.46 c	7.75	126.45 a	299.71
LSD (0.05)		ns	0.18	ns	2.15	ns
Harvest	1103 P	0.16	9.04	4.39 c	72.83	55.93
	140 Ru	0.18	8.18	4.59 a	71.64	51.79
	Vinifera	0.11	7.34	4.51 b	74.11	50.79
LSD (0.05)		ns	ns	0.06	ns	ns

According to the harvest period of both years, Boğazkere grape cultivar stands out in total phenolic and anthocyanin content, and Kalecik Karası grape cultivar in flavonoid content. The total phenolic and flavonoid contents, which were high during the veraison period in all combinations, decreased towards the harvest period. The anthocyanin contents of the cultivars, on the other hand, showed an increase towards the harvest from veraison on both the skin and the pulp.

Many researchers stated that the total phenolic content decreases towards maturity and varies on the basis of cultivar and year during the harvest period. [28, 29, 30, 31]. In our study, the amount of phenolic substances of cultivars on the same rootstocks and of the same cultivars on different rootstocks seems to be compatible with the literature. The amount of flavonoids; It decreases towards ripening in grapes and has higher values in black cultivars compared to white cultivars. [32, 33]. The flavonoid content was higher in the skin than in the pulp. Towards ripening, the amount of flavonoids decreased in both the skin and pulp. Cultivars were differend in flavonoid content. Anthocyanins, on the other hand, are generally found in the grape skin and their amount increases from the veraison period. They reach the maximum level during the ripening period and provide the unique color of the grape cultivars [34]. In the study findings, it was determined that anthocyanin content increased towards maturity according to the cultivars and rootstocks. Anthocyanin content in the skin was found to be higher than in the pulp. The anthocyanin content of the cultivars are different from each other. This difference may vary from year to year [35].

4. CONCLUSION

Considering the cluster and berry weights of Kalecik Karası and Boğazkere grape cultivars, it can be said that in general, 1103 P and 110 R rootstocks stand out compared to 140 Ru rootstocks. Although the total phenolic and flavonoid content of the cultivars varied on the basis of rootstocks, 140 Ru combinations came into prominence in general. On the basis of cultivars, Boğazkere grape cultivar in terms of total phenolic and anthocyanin content and Kalecik Karası grape cultivar in terms of flavonoid content came to the fore. In both years, the total phenolic and flavonoid contents of the cultivars, which were high in the veraison period, decreased towards the harvest period. Anthocyanin contents increased towards harvest, from veraison both the skin and pulp. Anthocyanin content in the skin was found to be higher than in the pulp. In the study, cluster and berry weights of the cultivars and must, pH, total acidity, total phenolic substance, flavonoid and anthocyanin contents varied according to cultivar, rootstock and year.

Acknowledgement

This study was supported by Tokat Gaziosmanpaşa University Scientific Research Projects Coordination Unit. Project Number: 2018 / 44. Thank you for your support.

REFERENCES

[1] Oraman M, N. New Viticulture. Ankara University Faculty of Agriculture Publications: 253; Ankara; Textbook: 1965. p.89.
[2] Winkler AJ, Cook JA., Kliewer WM. and Leader LA. General Viticulture. University of California Press. Berkeley, California. (1974). p.710.
[3] Fidan Y. Special viticulture. Ankara Univ. Faculty of Agriculture Publications. 1985. p. 930.
[4] Çelik S. Vine Rootstocks Used in Viticulture and Their Properties. Viticulture (Ampeology), Vol: 1. Avcı Offset Istanbul; 2011.p. 273-308.
[5] Tangolar S. Research on the Effects of Different Rootstocks on Earliness, Yield, Quality Characteristics, Growth and Mineral Substance Uptake and Carbohydrate Levels of Some Early Grape Cultivars. [PhD Thesis]. Adana: Çukurova University. Graduate School of Natural and Applied Sciences;1988.
[6] Altındişli Investigation of the Efficiency of Rootstocks on the Development of Wine Grape Cultivars Grafted on 41B and 5BB Rootstocks. [Master Thesis]. Ankara: Ankara University, Graduate School of Natural and Applied Sciences, Department of Horticulture;1994.
[7] Dardeniz A. Kısmalı İ. A Study on the Determination of Steel Yields and Some Morphological Characteristics of 140 Rugeri and 1103 Poulsen American Vine Rootstocks in Çanakkale-Umurbey Conditions. Journal of Ege University Faculty of Agriculture. 2001; 38(2-3): 1-8.
[8] Ağaoğlu YS. Factors Affecting Berry Growth and Development and Maturation. Scientific and Applied Viticulture, Vol: 2, Vine Physiology: 1, Kavaklıdere Educational Publications No: 5. Ankara; 2002. p. 321-414.
[9] Çelik M. Kısmalı İ. Studies on Grape Yield and Quality and Effects on Vegetative Growth of Some American Vine Rootstocks in Round Seedless Grape Cultivars. Journal of Ege University Faculty of Agriculture; 2003; 40(3).
[10] Güner N. The Relationship of Spreading Performance with Rootstock and Dressing-Pruning in Table and Wine Grape Cultivars. [Master Thesis]. Ankara: Ankara University, Graduate School of Natural and Applied Sciences, Department of Horticulture; 2005.
[11] Çakır A. Şahiner Öylek H. The Effect of Different American Vine Rootstocks on Phenological and Pomological Characteristics of Banaz Black Grape Cultivars. Yüzüncü Yıl University Journal of Agricultural Sciences. 2016; 26(4):569-578.
[12] Çakır A. Şahiner Öylek H. The Effect of American Vine Rootstocks on Some Chemical Quality Traits of 'Banazi Black' Grape Cultivars. Yüzüncü Yıl University Journal of Agricultural Sciences. 2017; 27(3): 416-423.
[13] Bekar T. Cangi R. Determination of Phenological Development Stages and Effective Temperature Sum Requirements of Narince Grape Cultivars Cultivated in Different Ecologies in Tokat. Turkish Journal of Technology and Applied Sciences. 2017; 1(2): 86-90.
[14] Çelik H. Rootstock Use in Viticulture and Its Importance in Cultivation. Journal of Anadolu Aegean Agricultural Research Institute. 1996; 6(2).
[15] Haydaroğlu A. Developments in Modern Viticulture in Ankara, Kırıkkale and Kırşehir Provinces. [Master Thesis]. Ankara: Ankara University, Institute of Science and Technology; 1999.
[16] Cemeroğlu B. Fundamental Analysis Methods in Fruit and Vegetable Processing Industry. Biltav University Books Series, No: 02-2. Ankara. 1992. p. 381.
[17] Bino Rj. De Vos Rch. Lieberman M, Hall Rd. Bovy A Jonker Hh, et al. (2005). The Light-Hyperresponsive High Pigment-2 dg Mutation of Tomato: Alterations in the Fruit Metabolome. New Phytologist166. 2005; 427-438.
[18] Velioğlu YS. Mazza G. Gao L. Oomah, BD. Antioxidant Activity and Total Phenolics in Selected Fruits, Vegetables, and Berry Products. J. Agric. Food Chem.1998; 46(10):4113-4117.
[19] Zhishen J. Mengcheng T. Jianming. The Determination of Flavonoid Contents in Mulberry and Their Scavenging Effects on Superoxide Radicals. Food Chemistry. 1999;(64):555-55.

[20] Di Stefano R. Cravero MC. Metodi per lo studio dei polifenoli dell'uva. Riv. Vitic. Enol. 1991;44(2):37-45.
[21] Çelik H. Rootstock Use in Viticulture and Its Importance in Cultivation. Anatolia, J. of AARI. 1996;6(2):127-148.
[22] Uzun, H. (1996). Studies on Yield and Quality Characteristics of Some Table Grape Cultivars Grafted with Fercal Vine Rootstock. Journal of Akdeniz University Faculty of Agriculture.1996;9 (1):40-60.
[23] Çelik, M, Kısmalı, İ., (2004). Studies on the Effects of Some American Vine Rootstocks on Macro Mineral Nutrients Intake of Round Seedless Grape. Journal of Ege University Faculty of Agriculture. 2004;41(1).
[24] Turhan E. Dardeniz A. Müftüoğlu N. Determination of Salt Stress Tolerance of Some American Vine Rootstocks. Garden. 2005;34(1):11-20.
[25] Çetin E. Toy D. Adar M. Göktürk Baydar N. The Effects of Salt Stress on Shoot Growth and Proline Amounts of Some American Vine Rootstocks in Vitro Conditions. Journal of Suleyman Demirel University Graduate School of Natural and Applied Sciences. 2011;15(1):1-7.
[26] Çakır A. Karaca N. Sidfar M, Baral Ç. Söylemezoğlu G. Determination of Vaccination Rate of Sultani Seedless Grape Cultivars with Different American Vine Rootstocks. Yüzüncü Yıl University Journal of Agricultural Sciences. 2013;23(3):229-235.
[27] Yağcı A. Gökkaynak A. The Effect of Rootstock and Shading Ratio on Sapling Yield and Quality of Sultani Seedless Grape Cultivars. Journal of Ege University Faculty of Agriculture. 2016;53(1):109-116.
[28] Deryaoğlu A. Canbaş A. Physical and Chemical Changes During Ripening in Öküzgözü Grapes of Elazig Region. 2003; Food, 28(2): 131- 140.
[29] Uluocak E. Physical and Chemical Changes During Ripening of Some Wine Grape Cultivars Cultivated in Kazova (Tokat) Region [Master's Thesis]. Tokat: Tokat Gaziosmanpasa University. Graduate School of Natural and Applied Sciences; 2010.
[30] Cangi R. Saraçoğlu O, Uluocak E. Kılıç D. Şen A. Chemical Changes During Ripening of Some Wine Grape Cultivars Cultivated in Kazova (Tokat) Region. Iğdır University, Journal of Science Institute. 2011;1(3):9-14.
[31] Bekar T. Bayram M. Determination of Phytochemical Properties of Wines Produced from Narince Grape Cultivars with and Without the Addition of Commercial Yeast. Gaziosmanpaşa Journal of Scientific Research.2016; 09-24.
[32] Aydın M. Determination of Some Chemical Contents of Grape Cultivars Cultivated in Amasya at Different Maturity Periods [Master's Thesis]. Tokat: Tokat Gaziosmanpaşa University, Institute of Science and Technology, Department of Horticulture; 2015.
[33] Polat A. Determination of Some Phytochemical Profiles of Grape Cultivars Cultivated in Şanlıurfa Province [PhD Thesis]. Urfa: Harran University, Graduate School of Natural and Applied Sciences, Department of Horticulture; 2016.
[34] Kunter B. Cantürk S. Keskin N. Histochemical Structure of Beery Grape. Iğdır University, Journal of Science Institute. 2013; 3(2):17-24.
[35] Ribéreau-Gayon P. Glories Y. Maujean A. & Dubourdieau U. 2000. Handbook of Enology, Volume 2: The Chemistry of Wine and Stabilization and Treatments. John Wiley and Sons Ltd. 2000; p.441.

Araştırma Makalesi https://doi.org/10.46810/tdfd.1186878 Research Article

Türk Doğa ve Fen Dergisi
Turkish Journal of Nature and Science
www.dergipark.gov.tr/tdfd

Wound Healing Potential of Quinic Acid in Human Dermal Fibroblasts by Regulating the Expression of FN1 and COL1α Genes

Sidika GENC[1], Betul CICEK[2], Yesim YENI[3], Ahmet HACIMUFTUOGLU[4]

[1] Bilecik Seyh Edebali University, Faculty of Medicine, Department of Medical Pharmacology, Bilecik, Türkiye
[2] Erzincan Binali Yildirim University, Faculty of Medicine, Department of Physiology, Erzincan, Türkiye
[3] Turgut Ozal University, Faculty of Medicine, Department of Medical Pharmacology, Malatya, Türkiye
[4] Ataturk University, Faculty of Medicine, Department of Medical Pharmacology, Erzurum, Türkiye
Sidika GENC ORCID No: 0000-0003-0000-5103
Betul CICEK ORCID No: 0000-0003-1395-1326
Yesim YENI ORCID No: 0000-0002-6719-7077
Ahmet HACIMUFTUOGLU ORCID No: 0000-0002-9658-3313

**Corresponding author: sidika.genc@bilecik.edu.tr*

(Received: 25.07.2022, Accepted: 14.11.2022, Online Publication: 28.12.2022)

Keywords
FN1A,
COL1A1,
8-OHdG

Abstract: Quinic acid (QA) is an alicyclic organic acid widely found in plants. It accumulates in varying concentrations of plant species and is actively metabolized throughout the plant's life cycle. Wound healing after skin injury involves a complex interaction of many cells, fibroblasts, endothelial cells, and regenerated immune cells and their interrelating extracellular matrix. In this study, it was aimed to investigate the healing effect of QA on scar tissue, changes in oxidative stress parameters, FN1 and COL1A1 gene levels. For this purpose, fibroblast cells were seeded in 24, 96 and well plates for wound healing, MTT analysis and Real-Time PCR testing (respectively). Wells were drawn with a 100 µL pipette tip for wound line. As a conclusion of our study, it was determined that cell viability increased significantly, especially in the QA 20 µg^{-ml} group at the end of 48 hours. Increased cell viability and antioxidant capacity resulted in increased cell proliferation. Both FN1 and COL1A1 gene expression levels were up regulated in the QA groups compared to the control group. Our findings show for the first time that QA promotes migration and/or proliferation of fibroblasts by regulating oxidative stress and the FN1A and COL1A1 genes. This activity may be related to the production of FN1A and COL1A1, which are considered important targets for modulation of the tissue repair process.

Kinik Asit'in FN1 ve COL1A1 Gen Ekspresyonunu Düzenleyerek İnsan Dermal Fibroblastlarında Yara İyileştirme Potansiyeli

Anahtar Kelimeler
FN1A,
COL1A1,
8-OHdG

Öz: Kinik asit (QA), bitkilerde yaygın olarak bulunan bir alisiklik organik asittir. Bitki türlerinin değişen konsantrasyonlarında birikir ve bitkinin yaşam döngüsü boyunca aktif olarak metabolize edilir. Cilt yaralanmasından sonra yara iyileşmesi, başta keratinositler, fibroblastlar, damarların endotel hücreleri ve rejenere bağışıklık hücreleri ve bunlarla ilişkili hücre dışı matris olmak üzere birçok hücrenin karmaşık bir etkileşimini içerir. Bu çalışmada, QA'nın yara dokusu üzerindeki iyileştirici etkisinin oksidatif stres parametreleri, FN1 ve COL1A1 gen düzeylerindeki değişimler incelenmesi amaçlanmıştır. Bu amaçla, fibroblast hücreleri yara iyileşmesi için 24 oyuklu plakalara, MTT analizi için 96 ve Real-Time PCR testi için 6 oyuklu plakalara ekildi. Kuyucuklar, yara hattı için 100 µL pipet ucu ile çizildi. Çalışmamız sonucunda 48 saat sonunda özellikle QA 20 µg^{-ml} grubunda hücre canlılığının önemli ölçüde arttığı belirlendi. Artan hücre canlılığı ve antioksidan kapasitesi, hücre çoğalmasının artmasına neden oldu. Hem FN1 hem de COL1A1 gen ekspresyon seviyeleri, kontrol grubuna kıyasla QA gruplarında yukarı regüle edildi. Bulgularımız ilk kez kinik asidin oksidatif stresi ve FN1A ve COL1A1 genlerini düzenleyerek fibroblastların göçünü ve/veya çoğalmasını desteklediğini göstermektedir. Bu aktivite, doku onarım sürecinin modülasyonu için önemli hedefler olarak kabul edilen FN1A ve COL1A1 üretimi ile ilgili olabilir.

1. INTRODUCTION

Tissue healing process after damage is one of the main characteristics of all organisms due to the preservation of homeostasis of the body [1]. The skin is the body's most important barrier against the harmful effects of external factors. Therefore, complex mechanisms are involved in the self-defense of the tissue and the preservation of the completeness of the skin after damage [2-4]. Wound healing after skin injury contains a complex interaction of many cells, primarily keratinocytes, endothelial cells of vessels, and regenerated immune cells and their extracellular matrix [2, 5]. These processes are regulated by a variety of mediators, including cytokines, growth factors, inflammatory cells, platelets, matrix metalloproteinases [6]. Conversely, some wounds do not heal on time and regularly, therefore it results in chronic non-healing wounds [7]. Since cytokines, growth factors, proteases, and cellular and extracellular elements all play important roles at different stages of the healing process, changes in one or more of these components may explain the impaired healing sighted in chronic wounds [8].

Fibronectin (FN) is an extracellular matrix (ECM) protein that reorganizes the cell's cytoskeleton, facilitating cell movement, dictating cell adhesion, spreading, migration, proliferation, and apoptosis [9]. FN, which has different structures and different roles in wound healing, contributes to the formation of fibrin clots. As a result, they take a role in wound healing by suppressing leukocytes and endothelial cells [10]. Cellular FN is vital for wound sites, like cellular proliferation, fibroblast polarization, cell migration, collagen complex regulation (I/III complex), and regulating neovascularization. A member of the FN family, Fibronectin 1 (FN1) has a critical role in cellular growth and tissue repair and is expressed highly in human dermal fibroblasts (HDFs) [11].

QA is one of the types of organic acids commonly found in plants. This substance, which is found in different concentrations according to the plant species and the developmental stages of the plants, is actively metabolized throughout the life cycle of the plant [12-14]. Some plants have intrinsically high amounts of QA, such as tea, coffee, and some fruits [15, 16]. QA derivatives have many advantageous effects, including antioxidant [17], anti-inflammatory [18], hypoglycemic and hepatoprotective effects, and inhibition of mutagenesis and carcinogenesis.

In this study, the cellular wound repair mechanism was tried to be elucidated by QA and the changes in the FN1 and Collogen1A1 gene levels were considered. In this respect, our study will provide new information to the literature.

2. MATERIAL AND METHOD

2.1. Chemicals & Reagents

QA, Phosphate buffer solution (PBS), Dulbecco Modified Eagles Medium (DMEM), Trypsin (with EDTA), dimethylsulfoxide (DMSO), fetal bovine serum (FBS), and antibiotics were purchased from Sigma (St. Louis, MO, U.S.A).

2.2. Cell Culture

For our study, Primary Dermal Fibroblast Normal; Human, Neonatal (HDFn) was purchased ATCC. The cell was resuspended by fresh medium, 10% FBS, and antibiotic 1% (penicillin, amphotericin B, and streptomycin). The cells were cultured in 6, 24, and 96 well plates and stored at an incubator in optimal condition (5% CO2; 37 °C) [19].

2.3. Wound Assay

With the wound assay, it was evaluated the migration rate of QA in the fibroblast cell line. Fibroblast cells were seeded in a 24-well plate and were incubated until 100% confluency. At the end of day 5, each well was wound with a sterile plastic pipette tip (yellow tip-100 µl). Cell debris was aspirated with PBS. Cells were then exposed to various concentrations of QA (2.5, 5, 10, and 20 μg^{-ml}). Images from the central area of the wound were photographed at 0-48 hours by an invert microscope (Leica Microsystems, Wetzlar, Germany) at ×20 magnification to assess cell migration. All experiments were done in triplicate.

2.4. Drug Administration

After the cells reached 85% confluency, they were seeded into 6 (for Real Time PCR), 24 (for wound healing assay) and 96 well plates (for MTT). Experimental groups were determined as control, wound control, QA (2.5, 5 ,10, and 20 μg^{-ml}) were administered. It was incubated under optimum conditions until the first wound was closed in the experimental groups.

2.5. MTT Tetrazolium Assay Concept

10 µL MTT (5 mg^{-ml} concentration) was added to each well and incubated for 4 hours (5% CO2; 37 °C) to perform the MTT assay. To dissolve formazan crystals, after 4 hours the medium was removed, and 100 µL DMSO was put in. Cell viability was measured by optical density read at 570 nm using the Multiskan™ GO Microplate Spectrophotometer reader (Thermo Scientific, Canada, USA) and the cell viability calculated as a %.
Viability Rate (%) = (O.D of groups/Control O.D) X 100

2.6. Total Antioxidant Capacity (TAC) Assay

The antioxidant capacity was investigated to determine the TAC level. For this purpose, 500 µL reagent 1 (Buffer) solution and 30 µL sample were added to the well, the initial absorbance was measured at 660 nm. 75 µL Reagent 2 (ABTS Radical Cation) solution was added and the second measurement was made at 660 nm. TAC values were calculated as Trolox Equiv/mmol L^{-1}, according to the formula below.

A2-A1= ΔA absorbance (Standard, sample, or H2O)

Result =(H2O ΔA bs-Sample ΔA bs)/(H2O Δbs-standard Δbs)

2.7. Total Oxidant Status (TOS) Assay

500 µL of Reagent1 (Buffer) solution was added to the wells containing 75 µL of a sample, and the initial absorbance value was read at 530nm, for evaluated spectrophotometrically TOS assay. Then 25 µL of Reagent 2 (Pro chromogen) solution was added to the same well. After 10 minutes at room temperature, the second absorbance value was read. TOS values were calculated as H_2O_2 Equiv mmol/L^{-1}, according to the formula below.

A2-A1= Δ Absorbance (Standard or sample)
Results= (Sample Δ Abs)/(Standard ΔAbs) x10

2.8. Lactate Dehydrogenase (LDH) Assay

According to the manufacturer's instructions (Cayman Chemicals, USA), LDH was determined with the LDH detection kit. Cells were seeded in 96 well plates. 6 wells were used for each concentration. Triton X-100 (10%) and 20 µL Assay buffer were added and incubated at room temperature for one hour. The cells were centrifuge 400Xg for five minutes. 100 µL of cell supernatant were transfered to a new 96- well assay plates. LDH reaction solution was added to each well and incubated the plate with gentle shaking on an orbital shaker for 30 minutes at 37 °C. LDH levels was measured the absorbance OD value at 490 nm [20].

((Experimental Value A490)-(Spontaneous Release A490))/((Maximum Release A490)-(Spontaneous Release A490)) X 100

*Maximum release: All cells were killed by adding Triton X-100. Spontaneous release: Control group with nontoxic materials (cell medium) and Experiment value

2.9. Glutathione (GSH) Assay

GSH was investigated with the GSH detection kit (Elabscience, USA). In this method, the principle was based on the formation of a yellow complex due to GSH reaction with dinitrobenzoic acid. The experiment was conducted according to the kit protocol and the results were read at 450 nm wavelength. The obtained results were given as % value.

2.10. 8-hydroxy-2'-deoxyguanosine (8-OHdG) Assay

The Oxidative DNA Damage ELISA kit is an ELISA for the quantitative measurement of 8-OHdG. DNA in each sample was obtained according to the manufacturer's (Cell Biolabs, USA) instructions and the kit protocol was applied according to the manufacturer's instructions.

2.11. Gene Expression

Total RNA was extracted from neuronal cells. Total RNA was used for synthesizing complementary DNA (cDNA) using cDNA Reverse Transcription Kit. The sequences of gene-specific PCR primers are listed below. Results are stated as relative fold compared with the control group. We normalized gene expressions to beta-actin using ΔΔCt method (x) and states as fold change to control.

βactin
Forward: 5'-CCAACCGCGAGAAGATGA-3'
Reverse: 5'-CCAGAGGCGTACAGGGATAG-3'
FN1
Forward:5′-CCAACTACCAGTAGCGAAAA −3′
Reverse: 5′-GCAGGGAAAGGAAAGAAA-3′
COL1A1
Forward: 5′-GACCAGGAATTCGGCTTCGAAGT-3′
Reverse: 5′-CATTGGATCCTGTGTCTTCTGGG-3′

2.12. Statistical Analyses

Statistical analyses were utilized using One-way ANOVA and Tukey HSD method (SPSS 26 software). $P<0.05$ and $P<0.01$ were considered a statistically significant differences in all tests. Results are submitted as mean and standard deviation (mean±SD).

3. RESULTS

3.1.MTT Assay

The wound line closed at the end of 48 hours in the 20 µg-ml group and the experiment was terminated at that hour. Cell viability results of all groups after 48 hours of application were revealed by the MTT test and the cell viability graph is given in Figure 1. Cell viability was considered as 100% in the control group (negative control). In the positive control group (wound), this rate was found to be 66.00% at the end of 48 hours. The viability rate of QA 1 µg-ml was found to be 79.81%. While this rate was QA 2.5 µg-ml 97,65% at the end of 48 hours in the QA 2 µg-ml group, it increased by nearly 45.13% at the QA 20 µg-ml. The cell viability level increased with wound healing. the highest cell viability level was seen in the 20 µg-ml group. When MTT results are examined, it is clearly seen that QA increases cell viability. The results were statistically significant ($P<0.05$, $P<0.01$).

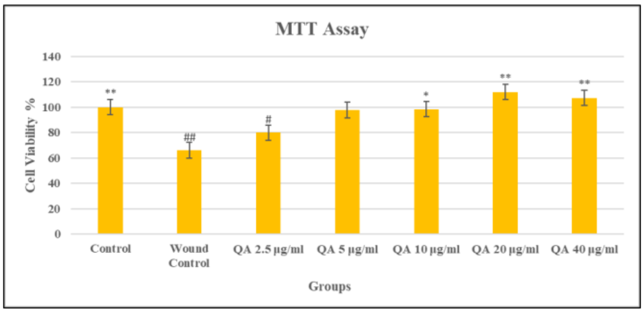

Figure 1. MTT Results of Application Group. # $p<0.05$ values are significant wound group compared to the control * $p<0.05$= significant, ** $P<0.01$= very significant

3.2. Wound Healing

The wound line was created with a 100 µl pipette tip. There was no change at the 12th hour. For this reason, 24-

36- and 48-hours images were used. When our results were examined, it was determined that the wound line was closed from the 36th hour in the QA 20 and 40 μg^{-ml} groups. In the control wound group, the wound line was observed even at the 48th hour. When compared with this group, it was designated that the cell proliferation increased, and the wound line was completely closed in the QA 20 and 40 μg^{-ml} groups (Figure 2).

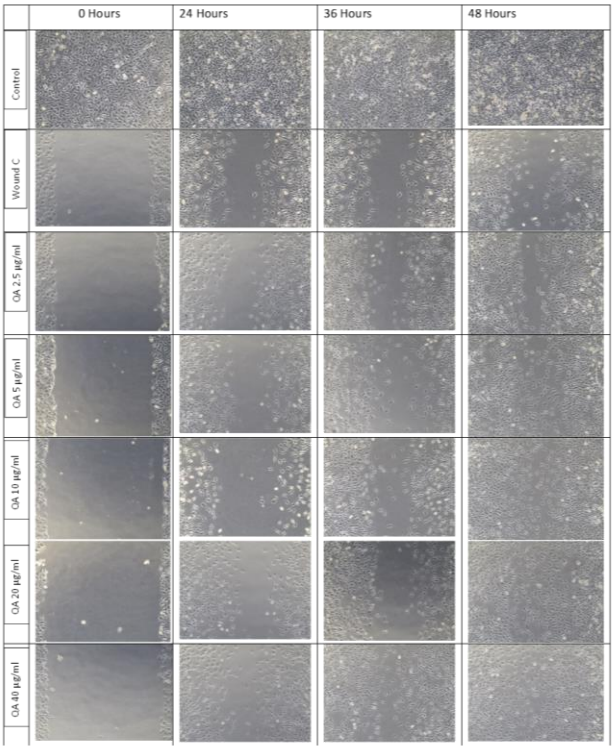

Figure 2. Wound line images of 24, 36 and 48 hours.

3.3. LDH Results

The activity of LDH was rated according to the standard solution (pure-%100) of the commercial kit (Figure 3). The results of the control group were found as 20.61±1.03 % and 10 at the end of 48 hours and the cellular death rate increased as the LDH level increased. The LDH level increased sharply in the wound group (97.96 ± 4.92 %). The wound group was found to be the group with the highest LDH level. Almost 4 times increase was observed compared to the control group. A significant difference was found when compared with the control group. This indicates the extent of cellular damage. However, in the groups treated with QA, there was a decrease in LDH levels at increasing concentrations in parallel with the healing of the scar tissue. The findings were compared with the wound group. Especially in the 20 μg^{-ml} group (42.01 ± 2.11), the LDH level approached the control group. These results correlate with MTT. It was determined that cytotoxicity was eliminated because of QA repairing the scar tissue and contributing to cell proliferation (P<0.05, P<0.01).

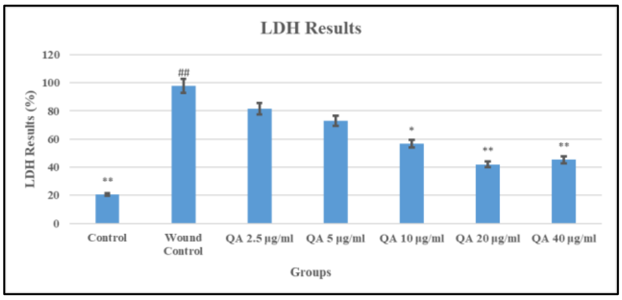

Figure 3. LDH Results of Application Group. # p<0.05 values are significant wound group compared to the control * p<0.05= significant, ** P<0.01= very significant

3.4. Redox State in Fibroblast Cells Treated with QA

TAC level and the findings are given in Figure 4. According to our data, the total antioxidant activity values of the control group were determined as 11.21±1.008 mmol Trolox equivalent/L. When the control group and the wound group were compared, the TAC value of the wound group was determined as 7.73±0.21 mmol Trolox equivalent-L. A significant increase in TAC level occurred in the QA group because it is a molecule with antioxidant activity. The highest increase was observed in the QA group 40 μg^{-ml} (13.15±0.678 mmol Trolox equiv.-L). This value was higher than the control group. We attribute the reason for this to the antioxidant property of the QA molecule. QA caused increased cell proliferation and decreased cellular oxidation (P<0.05, ** P<0.01).

Contrary to the TAC level, the TOS level was the lowest in the control group (5,2±0.08) (Figure 5). TOS level was determined as 20.41±0.234 in the wound group. There was a decrease in the QA group depending on the dose increase. The results were found to be significant when compared with the control group.

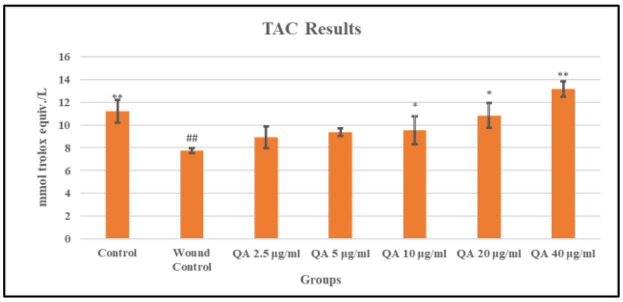

Figure 4. TAC Results of Application Group. # p<0.05 values are significant wound group compared to the control * p<0.05= significant, ** P<0.01= very significant

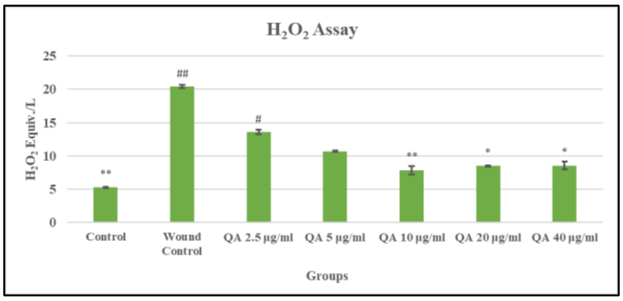

Figure 5. TOS Results of Application Group. # p<0.05 values are significant wound group compared to the control * p<0.05= significant, ** P<0.01= very significant

3.5. GSH Results

Another intracellular enzyme for determining cellular oxidative damage is GSH. GSH activity was measured, and the results were statistically evaluated and presented in Figure 6. The GSH level of the control group was 42.89% after 48 hours. As the GSH level decreases, the cellular death rate increases. After the injury in the wound group, the GSH level was determined as 23.14% and decreased approximately 2 times compared to the control group. In the QA group, the GSH level started to increase gradually, and the results approached the control group in the QA 40 µg^{-ml} group. A significant difference actuarially was observed according to the results obtained (P<0.05 and P<0.001).

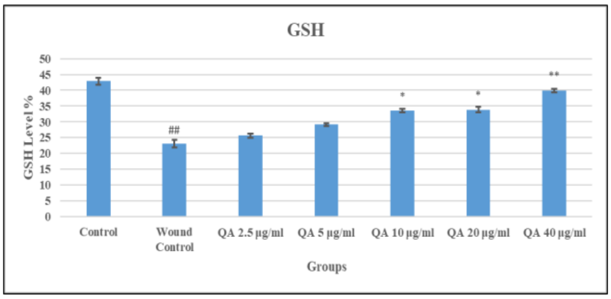

Figure 6. GSH Results of Application Group. # p<0.05 values are significant wound group compared to the control * p<0.05= significant, ** P<0.01= very significant

3.6. 8-OHdG Levels of Fibroblast Cells Treated with QA

Prevalently used as a biomarker for oxidative stress, 8-OHdG is one of the predominant forms of reactive oxygen species (ROS) lesions. In our study, oxidative DNA damage caused by the wound in fibroblast cells was demonstrated using 8-OHdG biomarker. While the 8-OHdG level was found to be 0.289 pg^{-ml} in the control group, cellular damage gradually increased in the wound group. The most significant result was observed in the QA 40 µg^{-ml} group, as in other data. The results were found significant (P<0.05 and P<0.001) (Figure 7).

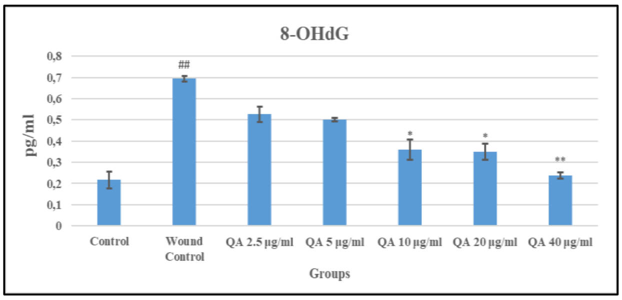

Figure 7. 8-OHdG Results of Application Group. # p<0.05 values are significant wound group compared to the control * p<0.05= significant, ** P<0.01= very significant

3.7. Real- Time PCR Results

There was no change in the COL1A1 gene level in the control and wound groups. With the onset of healing in the wound group, an increase in the regulation of COL1A1 gene expression started in the QA groups. COL1A1 is co-expressed with repair of scar tissue. When the results we obtained were examined, it was determined that there was a 1.6-fold increase in QA 20 and 40 µg^{-ml} concentrations. The control group was accepted as 1, and the other groups were compared to the control group. The data obtained were found to be statistically significant (p<0.05, ** P<0.01) (Figure 8a-b). Similarly, there was no change in the FN1 gene level in the control and wound groups. It was determined that there was a approximately 1.5-fold increase in QA 20 and 40 µg^{-ml} concentrations.

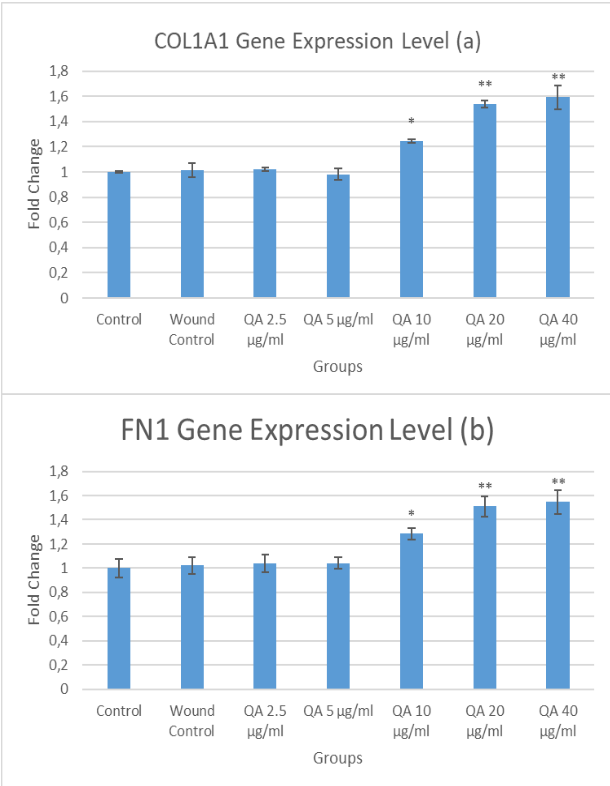

Figure 8. Gene Expression of Application Group. a) COL1A1 gene level; b) FN1 gene level* p<0.05= significant, ** P<0.01= very significant

4. DISCUSSION AND CONCLUSION

In our study, the effect of QA on the healing process of fibroblast cells was investigated. When the findings we obtained were analyzed, it was determined that the increased oxidative stress and cellular cytotoxicity in the wound area were eliminated by QA and the wound line was closed faster than the normal process. Wound healing is a biological process that includes many important stages such as hemostasis, cell proliferation, inflammatory events, and tissue remodeling [1, 21]. Increased oxidative stress at the wound site plays an important role in regulating normal wound healing by inflammation, angiogenesis, facilitating hemostasis, wound closure, granulation tissue formation, and development and maturation of the extracellular matrix [22]. For this reason, the increase in the amount of ROS in that region takes a central place in the wound healing processes. However, various substances with antioxidant activity have been proven to be beneficial in wound healing [23, 24]. However, various substances with antioxidant activity have been proven to be beneficial in wound healing. The antioxidant effect of QA showed a healing effect on the wound. It provided the closure of the wound line in a shorter time compared to the wound group. In addition, the oxidative stress, which increased in the wound group, decreased gradually in the QA group, which triggered the wound area to heal in a shorter time.
During wound healing, FN is one of the first and most abundant ECM components to accumulate at that site [25, 26]. Fibronectin triggers fibril formation with ECM formation. Fibronectin matrix deposition in wounds stimulates collagen and contributes to wound contraction. In addition, fibronectin can link to other cells to further stabilize the ECM [27]. In vitro studies have shown that Fibronectin polymerization leads to the composition and stability of the ECM and cell matrix adhesion [27, 28]. Fibronectin polymerization enables collagen types I and III to be deposited into the ECM and results in stabilization of collagen I matrix fibrils11. A study conducted by Shi and Sottile showed that membrane-type matrix metalloproteinase 1 (MT1-MMP/MMP) promotes ECM fibronectin conversion by regulating the division of large fibronectin fibrils and subsequently regulating endocytosis of $\alpha5\beta1$ integrin [29]. They also showed that inhibiting fibronectin polymerization accelerated myofibroblast migration.

Our findings show for the first time that QA promotes migration and/or proliferation of fibroblasts by regulating oxidative stress and the FN1A and COL1A1 genes. This activity may be related to the production of FN and COL, which are considered important targets for modulation of the tissue repair process and play an important role in the wound healing process. These results are the first evidence to support the traditional use of this substance to treat wounds.

REFERENCES

[1] Guo, S. and L.A. Dipietro, Factors affecting wound healing. J Dent Res, 2010. 89(3): p. 219-29.
[2] Xue, M. and C.J. Jackson, Extracellular Matrix Reorganization During Wound Healing and Its Impact on Abnormal Scarring. Adv Wound Care (New Rochelle), 2015. 4(3): p. 119-136.
[3] Broughton, G., 2nd, J.E. Janis, and C.E. Attinger, Wound healing: an overview. Plast Reconstr Surg, 2006. 117(7 Suppl): p. 1e-S-32e-S.
[4] Gonzalez, A.C., et al., Wound healing - A literature review. An Bras Dermatol, 2016. 91(5): p. 614-620.
[5] Midwood, K.S., L.V. Williams, and J.E. Schwarzbauer, Tissue repair and the dynamics of the extracellular matrix. Int J Biochem Cell Biol, 2004. 36(6): p. 1031-7.
[6] Li, J., J. Chen, and R. Kirsner, Pathophysiology of acute wound healing. Clinics in Dermatology, 2007. 25(1): p. 9-18.
[7] Falanga, V., The chronic wound: impaired healing and solutions in the context of wound bed preparation. Blood Cells Mol Dis, 2004. 32(1): p. 88-94.
[8] Trengove, N.J., et al., Analysis of the acute and chronic wound environments: the role of proteases and their inhibitors. Wound Repair Regen, 1999. 7(6): p. 442-52.
[9] Pankov, R. and K.M. Yamada, Fibronectin at a glance. J Cell Sci, 2002. 115(Pt 20): p. 3861-3.
[10] Grinnell, F., Fibronectin and wound healing. J Cell Biochem, 1984. 26(2): p. 107-16.
[11] Marzotto, M., et al., Arnica montana Stimulates Extracellular Matrix Gene Expression in a Macrophage Cell Line Differentiated to Wound-Healing Phenotype. PLoS One, 2016. 11(11): p. e0166340.
[12] Tarachiwin, L., et al., 1H NMR based metabolic profiling in the evaluation of Japanese green tea quality. J Agric Food Chem, 2007. 55(23): p. 9330-6.
[13] Benali, T., et al., Pharmacological insights into the multifaceted biological properties of quinic acid. Biotechnol Genet Eng Rev, 2022: p. 1-30.
[14] Bahuguna, A., et al., Insights into cyclooxygenase-2 inhibition by isolated bioactive compounds 3-caffeoyl-4-dihydrocaffeoyl quinic acid and isorhamnetin 3-O-beta-D-glucopyranoside from Salicornia herbacea. Phytomedicine, 2021. 90: p. 153638.
[15] Wei, F., et al., Complex mixture analysis of organic compounds in green coffee bean extract by two-dimensional NMR spectroscopy. Magn Reson Chem, 2010. 48(11): p. 857-65.
[16] Naranjo Pinta, M., et al., In Vitro Gut Metabolism of [U-(13) C]-Quinic Acid, The Other Hydrolysis Product of Chlorogenic Acid. Mol Nutr Food Res, 2018. 62(22): p. e1800396.
[17] Liang, N. and D.D. Kitts, Role of Chlorogenic Acids in Controlling Oxidative and Inflammatory Stress Conditions. Nutrients, 2015. 8(1).
[18] Jiang, Y., et al., Induction of cytotoxicity by chlorogenic acid in human oral tumor cell lines. Phytomedicine, 2000. 7(6): p. 483-491.
[19] Altinoz, M.A., et al., Ulipristal-temozolomide-hydroxyurea combination for glioblastoma: in-vitro studies. J Neurosurg Sci, 2022.

[20] Yeni, Y., et al., A Selective Histamine H4 Receptor Antagonist, JNJ7777120, Role on glutamate Transporter Activity in Chronic Depression. J Pers Med, 2022. 12(2).
[21] Janis, J.E. and B. Harrison, Wound Healing: Part I. Basic Science. Plast Reconstr Surg, 2016. 138(3 Suppl): p. 9S-17S.
[22] Sen, C.K. and S. Roy, Redox signals in wound healing. Biochim Biophys Acta, 2008. 1780(11): p. 1348-61.
[23] Fitzmaurice, S.D., R.K. Sivamani, and R.R. Isseroff, Antioxidant therapies for wound healing: a clinical guide to currently commercially available products. Skin Pharmacol Physiol, 2011. 24(3): p. 113-26.
[24] Kunkemoeller, B. and T.R. Kyriakides, Redox Signaling in Diabetic Wound Healing Regulates Extracellular Matrix Deposition. Antioxid Redox Signal, 2017. 27(12): p. 823-838.
[25] Fayet, C., M.P. Bendeck, and A.I. Gotlieb, Cardiac valve interstitial cells secrete fibronectin and form fibrillar adhesions in response to injury. Cardiovasc Pathol, 2007. 16(4): p. 203-11.
[26] Liu, C., et al., Establishment of an In Vitro Scab Model for Investigating Different Phases of Wound Healing. Bioengineering (Basel), 2022. 9(5).
[27] Lenselink, E.A., Role of fibronectin in normal wound healing. Int Wound J, 2015. 12(3): p. 313-6.
[28] Koyuncu, A., et al., Investigation of the synergistic effect of platelet-rich plasma and polychromatic light on human dermal fibroblasts seeded chitosan/gelatin scaffolds for wound healing. J Photochem Photobiol B, 2022. 232: p. 112476.
[29] Shi, F. and J. Sottile, MT1-MMP regulates the turnover and endocytosis of extracellular matrix fibronectin. J Cell Sci, 2011. 124(Pt 23): p. 4039-50.

Araştırma Makalesi https://doi.org/10.46810/tdfd.1180712 Research Article

Türk Doğa ve Fen Dergisi
Turkish Journal of Nature and Science
www.dergipark.gov.tr/tdfd

Investigation of Inhibition Performance of Epdantoin for Mild Steel Protection in HCl Solution: Electrochemical and Quantum Theoretical Approaches

Hüseyin NAZLIGÜL[1], Emre GÜLLÜ[2], Mehmet Erman MERT[3*], Başak DOĞRU MERT[1]

[1]Adana Alparslan Türkeş Science and Technology University, Engineering Faculty, Energy Systems Engineering Department, Adana, Türkiye
[2]Adana Alparslan Türkeş Science and Technology University, Engineering Faculty, Electrical and Electronic Engineering Department, Adana, Türkiye
[3]Adana Alparslan Türkeş Science and Technology University, Advanced Technology Research and Application Center, Adana, Türkiye
Hüseyin NAZLIGÜL ORCID No: 0000-0003-3037-8568
Emre GÜLLÜ ORCID No: 0000-0003-0750-161X
Mehmet Erman MERT ORCID No: 0000-0002-0114-8707
Başak DOĞRU MERT ORCID No: 0000-0002-2270-9032

**Corresponding author: memert@atu.edu.tr*

(Received: 27.09.2022, Accepted: 24.11.2022, Online Publication: 28.12.2022)

Keywords
Corrosion,
Density functional theory,
Mild steel,
Epdantoin

Abstract: In this study, the application potential of the expired "Epdantoin" drug which includes phenytoin (EP) as the corrosion inhibitor was investigated. For this purpose, the electrochemical impedance spectroscopy measurements and polarization curves were obtained for 168 hours immersion period in 0.5 M HCl in the absence and presence of various concentrations of EP. The experimental results were compared with quantum theoretical parameters in order to present adsorption behavior of EP. The adsorption equilibrium constant and Gibbs free energy were calculated as 5000 M^{-1} and -31,05 kj mol^{-1}, respectively. The detected HOMO and LUMO values were -6.67 eV and -0.72 eV, respectively. Results indicated that EP is a convenient candidate of corrosion inhibitor for mild steel (MS) in HCl medium.

Yumuşak Çeliğin HCl Çözeltisinde Korunması için Epdantoin'in İnhibisyon Performansının Araştırılması: Elektrokimyasal ve Kuantum Teorik Yaklaşımlar

Anahtar Kelimeler
Korozyon,
Yoğunluk fonksiyonel teorisi,
Yumuşak çelik,
Epdantoin

Öz: Bu çalışmada, korozyon inhibitörü olarak fenitoin (EP) içeren son kullanma tarihi geçmiş "Epdantoin" ilacının uygulama potansiyeli araştırıldı. Bu amaçla, çeşitli konsantrasyonlarda EP'nin varlığında ve yokluğunda 0,5 M HCl'de 168 saatlik daldırma süresi boyunca elektrokimyasal empedans spektroskopi ölçümleri ve polarizasyon eğrileri elde edildi. EP'nin adsorpsiyon davranışını göstermek için deneysel sonuçlar kuantum teorik parametrelerle karşılaştırıldı. Adsorpsiyon denge sabiti ve Gibbs serbest enerjisi sırasıyla 5000 M^{-1} ve -31,05 kj mol^{-1} olarak hesaplandı. Tespit edilen HOMO ve LUMO değerleri sırasıyla -6,67 eV ve -0,72 eV dir. Sonuçlar, EP'nin HCl ortamındaki yumuşak çelik (MS) için uygun bir korozyon önleyici aday olduğunu gösterdi.

1. INTRODUCTION

Mild steel (MS) is a low-priced material with good machinability that is used in various industries [1]. Although it has a broad range of uses, corrosion is the main issue that restricts usage [2]. The sensitivity of MS to corrosion has been the subject of extensive research up to the present time. The storage of nutrients in a healthy environment, the pipe systems used in the transfer of fluids, construction equipment, vehicles, buildings made of steel construction, coastal structures, production lines, warehouses made of metal and controlling corrosion in many industrial areas are of great importance in terms of reducing operating costs [3]. At the same time, metal poles and transport systems, whose structure is deteriorated due to corrosion, also pose great risks in terms of occupational safety. The simplest method to minimize or slow down the exposure of metals to corrosion is to provide isolation between the metal and the corrosive environment, such as an acidic, basic, or salty environment, in which the metal is present. This is possible by forming a film layer on the metal or by coating the metal [4]. It is impossible to avoid rusting with perfect effectiveness. However, by using corrosion inhibitors, the rate of corrosion to which the steel is exposed can be reduced or the process can be slowed down. As a result, a high financial advantage can be achieved with a low-cost electrochemical process. For this purpose usage of inhibitor chemicals to prevent corrosion is a very efficient strategy [5-7].

Chemicals known as corrosion inhibitors lessen the interaction between the metallic surface and the corrosive environment, hence lowering the vulnerability of metals to corrosion. The inorganic salts such as Arsenic acid and arsenate acids, have been used as inhibitors in the past. Unfortunatelly, they caused environmental damage due to the ecological side effects. But in this century new high-efficiency non-toxic chemicals have been offered which strongly cover the surface, resulting in improved efficiency while also being environmentally safe. The researchers' interest has recently increased to green/non-toxic inhibitor molecules [8-12].

Chemical drugs are increasingly being used as non-toxic organic inhibitors. The inhibitor prices are quite high, which has led researchers to investigate waste drugs applications that have recently expired. In this manner, the harm to the environment caused by disposing of expired medicine is avoided, and a low-cost organic inhibitor is acquired [13-16].

Despite the growing number of studies in the field of organic inhibitor corrosion prevention in scientific world, environmentally friendly corrosion prevention approaches have yet to gain general use in the industry. This demonstrates the need to improve studies on a practical basis [17-19].

In one of the studies [20], the drug with active ingredient Rosuvastatin used in the treatment of cholesterol, its behavior in 0.1 M HCl solution was examined. As a result, corrosion was prevented at 92% efficiency on MS. In another study, it was revealed that the effectiveness of the drug with irbesartan active ingredient in preventing corrosion formation in 1 M HCl solution is 94%. In the study by Zadeh et al. [5], the anti-corrosive activity of the drug with Bupropion active ingredient on carbon steel in HCl and H_2SO_4 solution was examined with the help of Fourier transform infrared (FTIR) Spectroscopy device, and the percent effectiveness was reached 88%. Weigh loss and electrochemical methods were used to investigate the inhibitory effect of an analyzed expired Ambroxol medicine on the corrosion of MS in acid media by Geethamani and Kasthuri. The highest IE observed was 94.03% with a amount of 9.0% inhibitor [21]. Singh et al. [22] modified expired Dapsone drug via chemical reaction with benzaldehyde; salicylaldehyde and they produced new Schiff bases. They researched the corrosion inhibiton performance of the Schiff bases for MS in sulphuric acid solution. Schiff base 1 (Dapsone-benzaldehyde) and Schiff base 2 (Dapsone salicylaldehyde) exhibited 95.67% and 94.23% inhibition efficiency at a concentration of 0.219 mM respectively. Addition of 0.602 mM KI further increased their efficiency up to 99.03% and 97.98% respectively. The corrosion inhibition behavior of carbon steel by three kinds of expired cephalosporins was investigated by Guo et al. [23]. The ceftriaxone sodium (Ceft), cefuroxime sodium (Cefu) and cefotaxime sodium (Cefo) were used for this purpose. The comparison of cephalosporins showed that Ceft was prefable than the others, according to EIS results, the highest inhibition efficiency was detected for 1mM Ceft as 84.4%.

In this study expired Epdantoin drug was investigated as inhibitor against MS corrosion in acidic media. It is a widely available, inexpensive drug made in Turkey and it is distributed with a white prescription. The aim of the study is to get rid of costly destruction processes and to offer an effective inhibitor alternative that does not harm the nature.

2. MATERIAL AND METHOD

The electrochemical measurements were carried out using a CHI 660b electrochemical analyzer. All of the electrochemical tests were carried out in an open atmosphere with three-electrode configuration. The counter electrode was a platinum sheet (2 cm^2), and the reference electrode was Ag/AgCl (3 M KCl). The working electrodes were made of MS alloy with almost 0.5 cm^2 surface area. The chemical composition (in weight percent) was: 0.09645 C, 0.22423 Si, 0.41797 Mn, 0.02095 P, 0.04229 S, 0.02533 Cu, 0.03594 Ni, 0.01396 Cr, 0.00271 Mo, 0.00591 V, 0.00216 Sn, and a Fe balance. Before each experiment, the surface of the MS was polished to 1200 degrees using sandpaper. Epdantoin drug includes 100 mg phenytoin per tablet and excipients are aerosil 200, citric acid, talc. The molecular structure of phenytoin is shown in Figure 1.

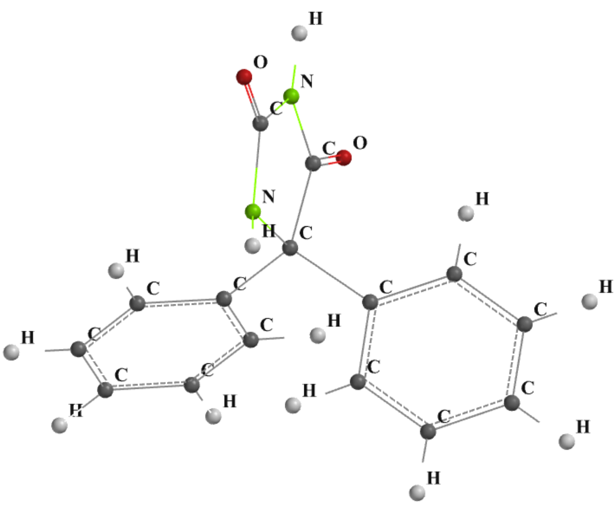

Figure 1. The phenytoin (EP) molecule

For the corrosion tests, MS electrodes were immersed in 0.5 M HCl solutions containing various concentrations (0.5; 1; 3; 5 mM) of EP, and EIS measurements were performed without stirring the electrolyte by applying 5 mV amplitude in the frequency range of 10^5 – $6x10^{-2}$ Hz. The current potential curves were acquired with a scanning speed of 1 mV/s. All of the experiments were conducted at a temperature of 293 K. The potential zero charge (pzc) measurements were done with the help of EIS and graphs were presented as applied potential vs charge transfer resistance. All EIS measurements were fitted via the ZView program. Theoretical calculations were carried out using density functional theory (DFT) with 6-311++G (d,p) basis set for all atoms with the Gaussian 03W program. Some electronic properties such as energy of the highest occupied molecular orbital (E_{HOMO}), energy of the lowest unoccupied molecular orbital (E_{LUMO}), dipole moment, and Mulliken charges were determined.

3. RESULTS

The Nyquist plots of MS were presented in Figures 2, 4 and 5. The equivalent circuits were presented in Figure 3. In Figure 2, the semi-elliptic curves could be seen in the Nyquist diagrams which were started in the high frequency region, continued in the mid-frequency region, and closed in the low-frequency region. It indicated that MS corrosion in 1.0 M HCl solution was under the control of activation [24, 25]. According to obtained results in Figure 2, the resistance of MS decreased with increasing immersion period. MS corroded due to the corrosive acidic environment and specific absorption ability of chloride ions [26, 27].

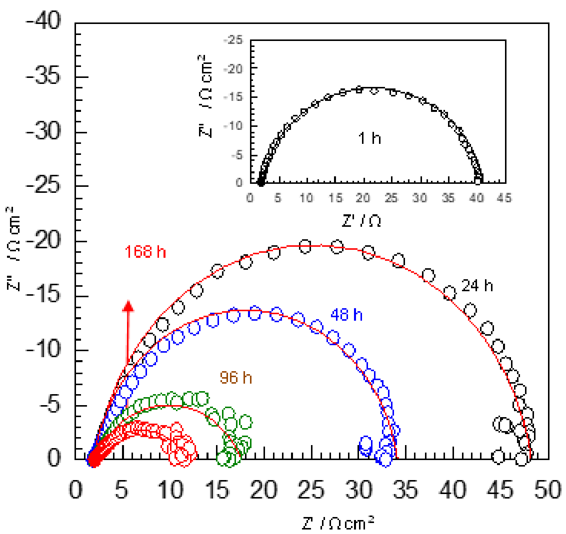

Figure 2. The Nyquist plots of MS in 0.5 M HCl for various exposure times

As seen in Table 1, polarization resistance values of MS were 39 and 9.8 ohm cm^{-2} for 1 and 168 hours immersion period, respectively. The constant phase element values were $690.1x10^{-6}$ and $9973.8x10^{-6}$ sn Ω^{-1} cm^{-2} respectively.

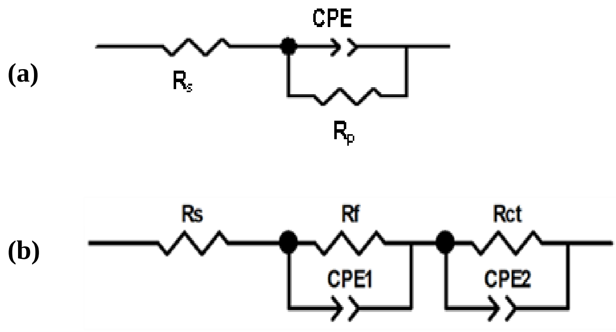

Figure 3. The equivalent circuit models for MSin HCl (a) and EP containing (b) media. The solution resistance R_s; the polarization resistance R_p (includes film resistance; R_f and charge transfer resistance; R_{ct}) and related constant phase elements; CPE1-2.

Table 1. Electrochemical parameters for MS in 0.5 M HCl solution

t (h)	R_p (Ω cm^2)	CPE (10^{-6} sn $\Omega^{-1}cm^{-2}$)
1	39.0	690.1
24	46.1	1084.4
48	32.2	2934.6
96	15.5	7940.3
168	9.8	9973.8

In the presence of inhibitor molecules, the corrosion resistance of MS increased with increasing EP concentration. As seen in Figure 4 and Table 2, polarization resistance values of MS were 928.9 and 1220 Ω cm^{-2} for 3 and 5 mM EP containing HCl, respectively. The constant phase element values were $65.3x10^{-6}$ and $58.3x10^{-6}$ sn Ω^{-1} cm^{-2} respectively. The corrosion protection was noticed almost 97% in the presence of 5 mM EP. This is the comparable value for inhibition efficiency according to literature. The expired Abacavir Sulfate drug was investigated for MS protection against corrosion in 3 M HCl, according to obtained EIS results almost 72.7% inhibition efficiency was detected [28]. The expired salbutamol drug molecule as an emerging anticorrosion additive for MS corrosion in oilfield acidizing fluid was investigated [29]. The maximum inhibition efficiencies of 80 %, 89 % and 84 % were determined from weight loss, potentiodynamics study and EIS at concentration of 0.4 g L^{-1} respectively. Using electrochemical methods and the weight loss method, the antipsychotic drug thioridazine hydrochloride (TH) was assessed for its ability to effectively inhibit corrosion on MS in 1 M HCl [30]. To understand the long-term effect of TH, MS was tested for 7 days in 100 ppm TH containing electrolyte. EIS results showed that the R_p did not change significantly after 24 h exposure as compared to 2 h exposure; whereas the R_p increased by 28% after 7 days exposure. After a 7 days exposure, weight loss assessments showed that TH's remarkable high (98.8%) inhibitory efficiency.

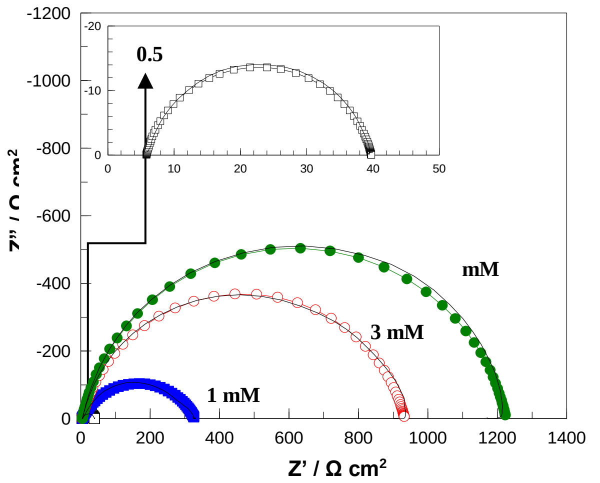

Figure 4. The Nyquist plots of MS in various EP containing 0.5 M HCl for 1h immersion time

Table 2. Electrochemical parameters for MS in various EP containing 0.5 M HCl for 1h immersion time

C (mM)	R_p (Ω cm^2)	CPE (10^{-6} sn $\Omega^{-1}cm^{-2}$)	%η
0.5	33.9	242.7	-
1	324.3	306.0	88
3	928.9	65.3	95.8
5	1220	58.3	96.8

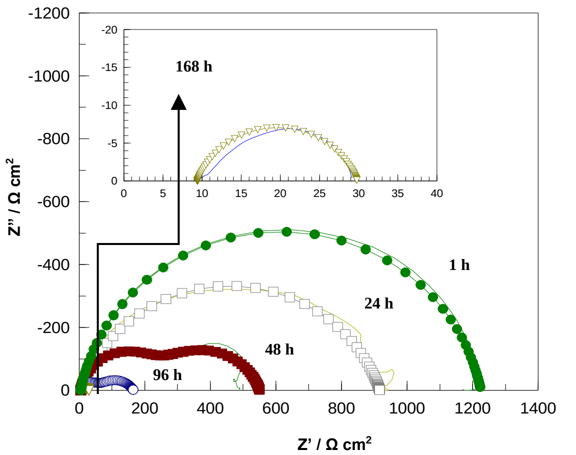

Figure 5. The Nyquist plots of MS in 5mM EP containing 0.5 M HCl for various exposure times

Table 3. Electrochemical parameters for MS in 5mM EP containing 0.5 M HCl for various exposure times

t	R_p		CPE		%η
1	1220		58.3		96.8
24	912.5		78.6		94.9
48	R_f	R_{ct}	CPE_1	CPE_2	94.1
	225	320	56.3	1000	
96	56	102	52	220	90.2
168	20.4		1500		52

The corrosion resistance of MS expanded considerably in the presence of EP molecules. As seen in Figure 5 and Table 3, the polarization resistance values of MS were 912.5 and 20.4 Ω cm^{-2} for 24 and 168 hours immersion periods, respectively. The constant phase element values were 78.6×10^{-6} and 1.5×10^{-3} sn Ω^{-1} cm^{-2} respectively. Despite the fact that resistance values decreased with increasing immersion time, the presence of EP provided improved corrosion prevention.

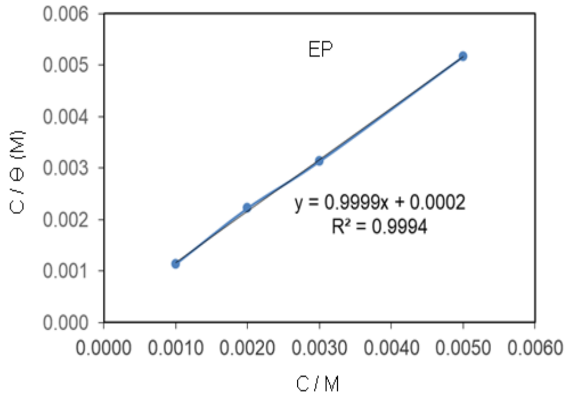

Figure 6. Langmuir adsorption plot for the MS

In order to clarify the adsorption mechanism, several isotherm models were operated but the Langmuir was most convenient for experimental results. In Figure 6, the Langmuir adsorption isotherm was presented and the following equation was used [31];

$$\frac{C_{inh}}{\theta} = \frac{1}{K_{ads}} + C_{inh} \tag{1}$$

where C_{inh} was the concentration of inhibitor, Θ was the degree of surface coverage values for various concentrations of the inhibitors in acidic solution. The Kads was the adsorption equilibrium constant, which was 5×10^3 M^{-1}, and for EP that signed the adherent adsorption ability of inhibitor molecules on the MS surface. The standard free energy of adsorption ΔG°ads value was calculated according to the following equation [32];

$$\Delta G^o{}_{ads} = -RT \ln\left(55.5 K_{ads}\right) \tag{2}$$

where R was universal gas constant and T was the absolute temperature, the calculated value was -31.05 kJ mol^{-1} for EP. The fact that the value of ΔG°ads for EP was less than 40 kJ mol^{-1} indicated both physical and chemical interactions.

In the literature, the study that defined the pharmaceutical thiazofurin as a novel, non-toxic corrosion inhibitor for MS in HCl solution revealed that adsorption corresponded with the Langmuir isotherm [33]. The obtained value of ΔG°ads was almost –29.14 kJ/mol. Pour-Ali and Hejazi declared that tiazofurin adsorbs on the surface of MS in 0.5 M HCl by physiochemisorption mode. Electrochemical behavior for corrosion protection of MS in 1M HCl medium by using lidocaine drug was investigated by Adel et. al [34]. The adsorption of the Lidocaine on MS surface was found to obey Langmuir adsorption isotherm. The calculated ΔG°ads values were –20.6 kJ/mol –20.7 kJ/mol at 298 K and 318 K, respectively. They declared that ΔG^oads values indicated both physical and chemical interactions between MS and Lidocaine.

Further, the potentiodynamic polarization measurements were achieved in the absence and presence of EP and related results were presented in Figure 7.

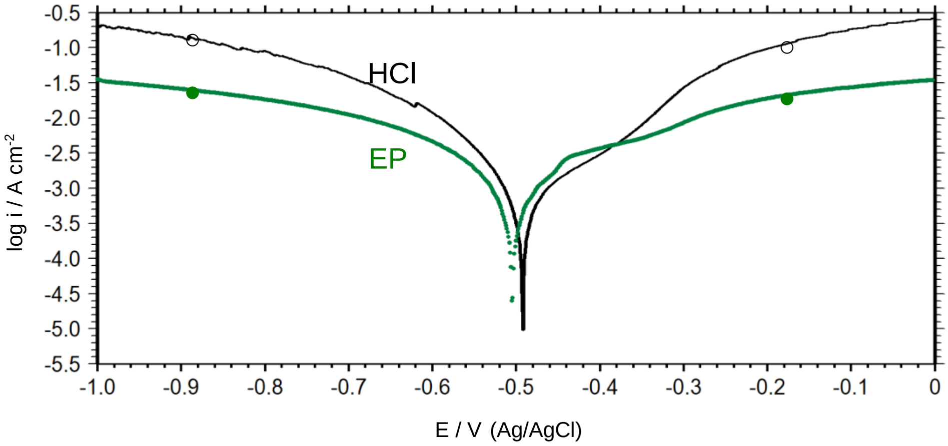

Figure 7. The potentiodynamic polarization curves for the MS electrode in 0.5 M HCl containing 5 mM EP for 168 h exposure time

In the presence of EP, the cathodic and anodic current density values decreased, as shown in Figure 7. The corrosion potential values were almost the same in the presence of EP and they both affected the anodic and cathodic reactions; therefore EP could be identified as the mixed type inhibitor [35, 36].

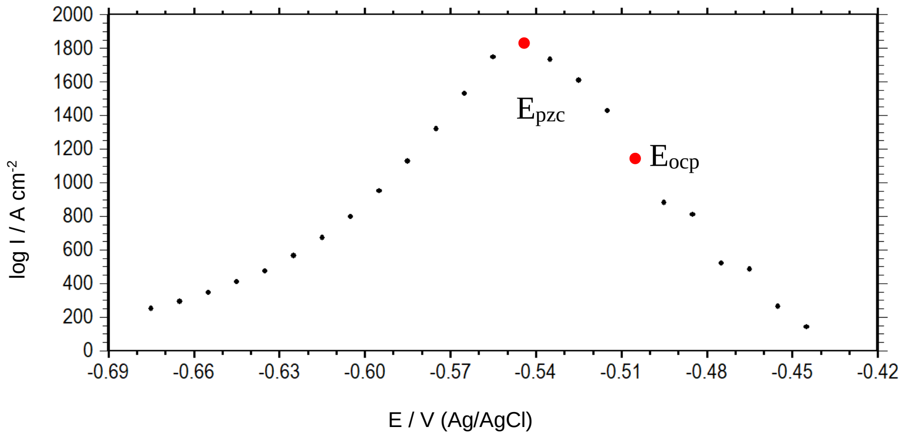

Figure 8. The pzc curve of MS electrode in 0.5 M HCl containing 5 mM EP

As seen in Figure 8, the highest polarization resistance (R_p) was detected at -0.545 V (vs Ag/AgCl; 3 M KCl) as 1824 ohm cm^{-2}. The open circuit potential of MS in this condition was -0.505 V and R_p was 1220 ohm cm^{-2}. According to obtained results, surface charge was positive. As a result, in the acidic solution, negatively charged chloride ions are deposited on the positively charged metal surface and negatively charge it. Following that, protonated (positively charged) EP molecules bond to the metal surface over chloride ions in the acidic environment to form a protective barrier. The obtained all experimental results were compared with quantum chemical methods. For this purpose, the structural analysis of EP was achieved. The highest occupied molecular orbital (E_{HOMO}), energy of the lowest unoccupied molecular orbital (E_{LUMO}), energy gap (ΔE) between LUMO and HOMO and Mulliken charges on the backbone atoms were determined and presented in Figure 9.

(a)

(b)

(c)

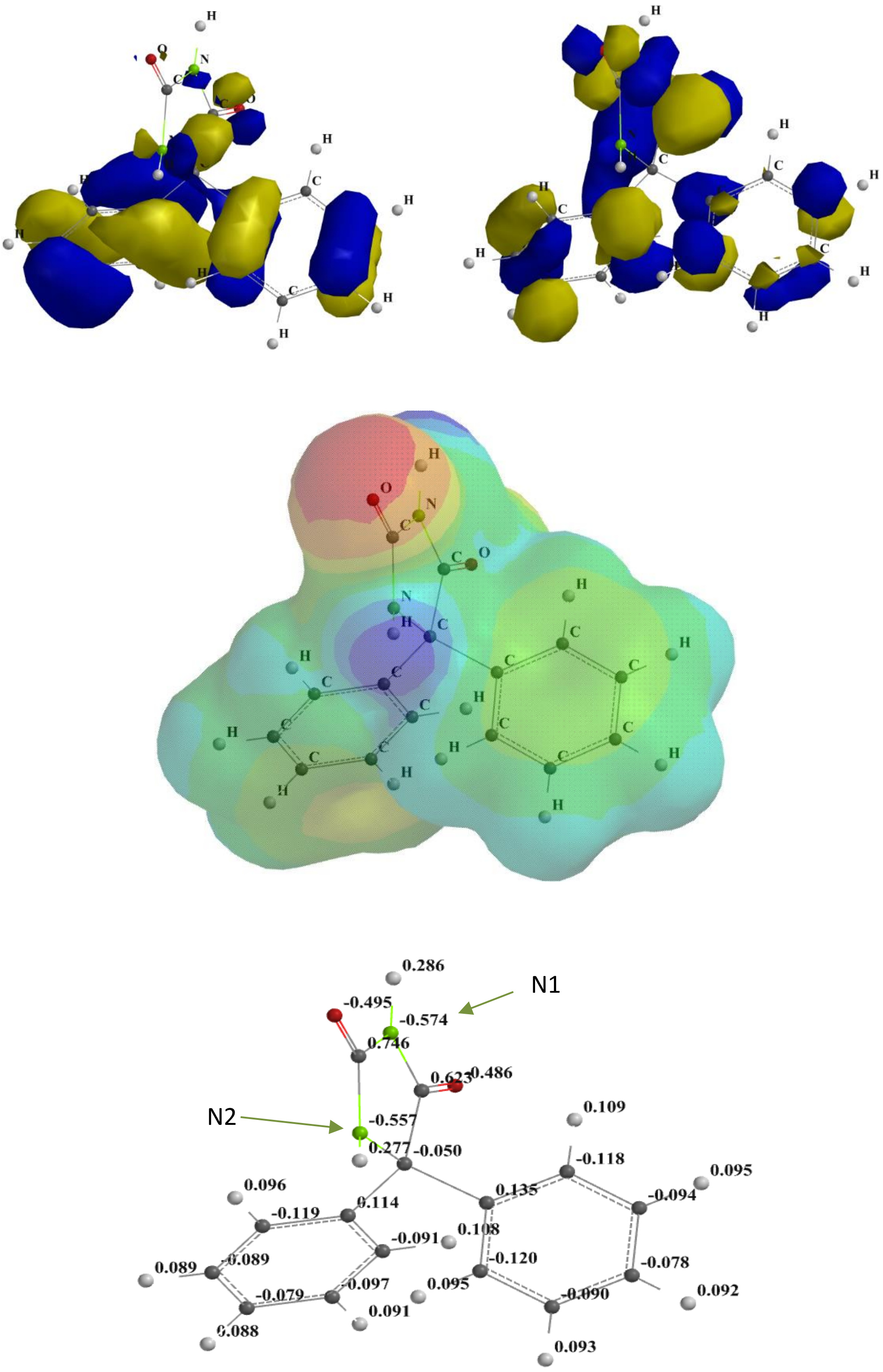

Figure 9. The HOMO and LUMO surfaces of EP **(a)**, electrostatic potential map of EP **(b)** and Mulliken charges of atoms on EP molecule **(c)**

As seen in Figure 9, wide HOMO and LUMO surfaces provide adherent adsorption ability of molecules. The determined HOMO value was -6.67 eV; LUMO value was -0.72 eV. The dipole moment was 2.66 Debye (Table 4). The Mulliken charges of oxygen atoms were -0.495 and -0.486 au and nitrogen atoms were -0.574 au and -0.557 au. In an acidic media, EP could protonate from the N1 and N2 atoms which were assigned in Figure 9c. EP in the protonated forms may adsorb predominantly through electrostatic interactions between such regions and the metal surface. For this purpose the protonated molecular structures (EP-N1 and EP-N2) were analyzed via quantum chemical calculation with the same basis sets and conditions, all data were presented in Table 4.

Tablo 4. The theoretical parameters of EP and protonated EP molecules

Molecules	E_{HOMO} *(eV)*	E_{LUMO} *(eV)*	ΔE (E_{LUMO}-E_{HOMO}) *(eV)*	Dipole Moment *(Debye)*
EP	-6.67	-0.72	5.95	2.66
EP-N1	-10.01	-6.80	3.21	4.10
EP-N2	-10.25	-5.64	4.61	3.19

As seen in Table 4 the more favorable protonated structure was EP-N1. The obtained HOMO, LUMO and dipole moment values were -10.01 eV, - 6.80 eV and 4.10 Debye, respectively. When compared to all molecular forms, EP-N1 had the lowest band gap. The higher dipole moment of EP-N1 may accelerate the adsorption of molecules and may increase the inhibition efficiency, due to dipole–dipole interactions between molecules and electrode surface [35].

4. DISCUSSION AND CONCLUSION

The expired drug that was “Epdantoin” with phenytoin ingredient was investigated as the corrosion inhibitor for MS in HCl medium. The findings of electrochemical methods and quantum chemical computations lead to the following recommendations:

1.According to EIS parameters the inhibition efficiency of EP increased with increasing concentration. During long term immersion, EP could effectively protect MS against corrosion in HCl solution.

2.The adsorption of EP obeyed the Langmuir isotherm. The Kads was $5x10^3$ M^{-1} and the $\Delta G^o ads$ indicated physical adsorption with 31.05 kJ mol^{-1} value.

3.The polarization curves proved that EP was a mixed type inhibitor via suppressed cathodic and anodic polarization reactions.

4.According to pzc results the surface charge was positive in presence of EP. Thus we offered that EP should be in the protonated forms in HCl.

5.The calculated quantum parameters revealed that EP-N1 inhibited more effectively than the other forms due to lower band gap and larger dipole moment values.

All results show that Epdantoin as an expired drug has potential application in the area of corrosion studies, especially MS protection in HCl medium during long term. We offer the usage of expired eco-friendly drugs not only to decrease the corrosion rate of technical metals but also re-gain these drugs for diminishing the carbon footprint all around the world. Because the expired drugs exhibit several advantages such as;

a.protective against corrosion,
b.economic benefits and eliminates the costs of disposal, transportation and storage,
c.lower carbon foot-print etc.

We should emphasize the potential applications.

Acknowledgement

We are greatly thankful to Prof.Dr Gülfeza KARDAŞ.

Conflict of Interest

There are no conflicts of interest declared by any of the writers.

REFERENCES

[1] Akbarzadeh S, Ramezanzadeh M, Ramezanzadeh B, Bahlakeh G. A green assisted route for the fabrication of a high-efficiency self-healing anti-corrosion coating through graphene oxide nanoplatform reduction by Tamarindus indiaca extract. Journal of Hazardous Materials. 2020;390:122147.

[2] Lgaz H, Salghi R, Masroor S, Kim SH, Kwon C, Kim SY, et al. Assessing corrosion inhibition characteristics of hydrazone derivatives on mild steel in HCl: Insights from electronic-scale DFT and atomic-scale molecular dynamics. Journal of Molecular Liquids. 2020;308:112998.

[3] Zhang J, Li W, Zuo X, Chen Y, Luo W, Zhang Y, et al. Combining experiment and theory researches to insight into anti-corrosion nature of a novel thiazole derivatives. Journal of the Taiwan Institute of Chemical Engineers. 2021;122:190–200.

[4] Zhang J, Li W, Zuo X, Chen Y, Luo W, Zhang Y, et al. Combining experiment and theory researches to insight into anti-corrosion nature of a novel thiazole derivatives. Journal of the Taiwan Institute of Chemical Engineers. 2021;122:190–200.

[5] Sorkh Kaman Zadeh A, Shahidi Zandi M, Kazemipour M. Corrosion protection of carbon steel in acidic media by expired bupropion drug; experimental and theoretical study. Journal of the Indian Chemical Society. 2022;99(7):100522.

[6] Azzaoui K, Mejdoubi E, Jodeh S, Lamhamdi A, Rodriguez-Castellón E, Algarra M, et al. Eco friendly green inhibitor Gum Arabic (GA) for the corrosion control of mild steel in hydrochloric acid medium. Corrosion Science. 2017;129:70–81.

[7] Shamnamol GK, Sreelakshmi KP, Ajith G, Jacob JM. Effective utilization of drugs as green corrosion inhibitor – A review. AIP Conference Proceedings. 2020;2225(1):070006.

[8] Nayak P, Kumari P P, Rao SA. Electrochemical approach to interfacial adsorption and inhibitory performance of (2E)-2- [(IH-Imidazole 2yl) methylidene] Hydrazine1-carbothioamide for corrosion mitigation. Chemical Data Collections. 2022;38:100826.

[9] Srivastava M, Tiwari P, Srivastava SK, Prakash R, Ji G. Electrochemical investigation of Irbesartan drug molecules as an inhibitor of mild steel corrosion in 1 M HCl and 0.5 M H 2 SO 4 solutions. Journal of Molecular Liquids. 2017;236:184–97.

[10] Alamry KA, Aslam R, Khan A, Hussein MA, Tashkandi NY. Evaluation of corrosion inhibition performance of thiazolidine-2,4-diones and its

amino derivative: Gravimetric, electrochemical, spectroscopic, and surface morphological studies. Process Safety and Environmental Protection. 2022;159:178–97.

[11] Rodrigues FA de S, Gonçalves YMH, Horta BAC, Santos I da S, Silva BV, D'Elia E. Experimental and theoretical studies of isonitrosoacetanilides derivatives as corrosion inhibitors for mild steel in 1 mol L−1 HCl. Journal of Molecular Structure. 2021;1245:131256.

[12] Salcı A, Yüksel H, Solmaz R. Experimental studies on the corrosion inhibition performance of 2-(2-aminophenyl)benzimidazole for mild steel protection in HCl solution. Journal of the Taiwan Institute of Chemical Engineers. 2022;134:104349.

[13] Haruna K, Saleha TA, Quraishi MA. Expired metformin drug as green corrosion inhibitor for simulated oil/gas well acidizing environment. Journal of Molecular Liquids. 2020;315:113716.

[14] Abdallah M, Al Bahir A, Altass HM, Fawzy A, Guesmi NE, Al-Gorair AS, et al. Anticorrosion and adsorption performance of expired antibacterial drugs on Sabic iron corrosion in HCl solution: Chemical, electrochemical and theoretical approach. Journal of Molecular Liquids. 2021;330:115702.

[15] Chauhan DS, Quraishi MA, Srivastava V, Haque J, ibrahimi BE. Virgin and chemically functionalized amino acids as green corrosion inhibitors: Influence of molecular structure through experimental and in silico studies. Journal of Molecular Structure. 2021;1226:129259.

[16] Kalkhambkar AG, Rajappa SK, Manjanna J, Malimath GH. Effect of expired doxofylline drug on corrosion protection of soft steel in 1 M HCl: Electrochemical, quantum chemical and synergistic effect studies. Journal of the Indian Chemical Society. 2022;99:100639.

[17] Oubaaqa M, Ouakki M, Rbaa M, Abousalem AS, Maatallah M, Benhiba F, et al. Insight into the corrosion inhibition of new amino-acids as efficient inhibitors for mild steel in HCl solution: Experimental studies and theoretical calculations. Journal of Molecular Liquids. 2021;334:116520.

[18] Rahal C, Masmoudi M, Abdelhedi R, Sabot R, Jeannin M, Bouaziz M, et al. Olive leaf extract as natural corrosion inhibitor for pure copper in 0.5 M NaCl solution: A study by voltammetry around OCP. Journal of Electroanalytical Chemistry. 2016;769:53–61.

[19] Sharma S, Kumar A. Recent advances in metallic corrosion inhibition: A review. Journal of Molecular Liquids. 2021;322:114862.

[20] Gholamhosseinzadeh MR, Aghaie H, Zandi MS, Giahi M. Rosuvastatin drug as a green and effective inhibitor for corrosion of mild steel in HCl and H2SO4 solutions. Journal of Materials Research and Technology. 2019;8(6):5314–24.

[21] Geethamani P, Kasthuri PK. Adsorption and corrosion inhibition of mild steel in acidic media by expired pharmaceutical drug. Cogent Chemistry. 2015;1:1091558.

[22]Singh P, Chauhan DS, Chauhan SS, Singh G, Quraishi MA. Chemically modified expired Dapsone drug as environmentally benign corrosion inhibitor for mild steel in sulphuric acid useful for industrial pickling process. Journal of Molecular Liquids. 2019;286:110903.

[23] Guo W, Umar A, Zhao Q, Alsaiari MA, Al-Hadeethi Y, Wang L, et al. Corrosion inhibition of carbon steel by three kinds of expired cephalosporins in 0.1 M H2SO4. Journal of Molecular Liquids. 2020;320:114295.

[24] Altunbaş Şahin E, Tezcan F, Solmaz R, Kardaş G. Inhibitive effect of 4-amino-N-benzylidenebenzamide Schiff base on mild steel corrosion in HCl solution. Journal of Adhesion Science and Technology. 2020; 34:135.

[25] Özkır D, Kayakırılmaz K. The ınhibitor effect of (e)-5-[(4-(benzyl(methyl)amino)phenyl)diazenyl]-1,4-dimethyl-1h-1,2,4-triazol-4-ium zinc(ıı) chloride, an ındustrial cationic azo dye, onto reducing acidic corrosion rate of mild steel. Journal of Electrochemical Science and Technology. 2020;11:257.

[26] Abd El-Lateef HM, Sayed AR, Shalabi K. Studying the effect of two isomer forms thiazole and thiadiazine on the inhibition of acidic chloride-induced steel corrosion: Empirical and Computer simulation explorations. Journal of Molecular Liquids. 2022;356:119044.

[27] Sundaram RG, Vengatesh G, Sundaravadivelu M. Surface morphological and quantum chemical studies of some expired drug molecules as potential corrosion inhibitors for mild steel in chloride medium. Surfaces and Interfaces. 2021;22:100841.

[28] Raghavendra N. Expired abacavir sulfate drug as non-toxic corrosion ınhibitor for mild steel (ms) in 3 M hydrochloric acid system. Gazi University Journal of Science. 2019;32:1113.

[29] Anadebe VC, Nnaji PC, Onukwuli OD, Okafor NA, Abeng FE, Chukwuike VI, et al. Multidimensional insight into the corrosion inhibition of salbutamol drug molecule on mild steel in oilfield acidizing fluid: Experimental and computer aided modeling approach. Journal of Molecular Liquids. 2022;349:118482.

[30] Kannan MB, Rahuma M, Khakbaz H, Melchers R. Antipsychotic drug waste: A potential corrosion inhibitor for mild steel in the oil and gas industry. Waste Management. 2022;145:38.

[31] Wen J, Zhang X, Chen J, Liu T, Zhou Y, Li L. Synthesis of 1, 4, 7-triazaheptane derivative and its corrosion inhibition for mild steel in the hydrochloric medium. Journal of Industrial and Engineering Chemistry. 2022;107:333–45.

[32] Şahin EA, Dursun YA, Tunç M, Geçibesler İH, Solmaz R. Bakırın asidik ortamdaki korozyonuna hurma (Phoenix dactylifera) çekirdeğinin inhibisyon etkisinin incelenmesi. Turkish Journal of Nature Science. 2021;10(2):258-264.

[33] Pour-Ali S, Hejazi S. Tiazofurin drug as a new and non-toxic corrosion inhibitor for mild steel in HCl solution: Experimental and quantum chemical

investigations. Journal of Molecular Liquids. 2022;354:118886.

[34] Ali AH, Fouda AES, Tilp AH. Electrochemical behavior for corrosion protection of mild steel (MS) in 1M HCl medium by using lidocaine drug as an inhibitor. Zastıta Materıjala. 2020;61:286.

[35] Beniken M, Driouch M, Sfaira M, Hammouti B, Touhami ME, Mohsin M. Kinetic–thermodynamic properties of a polyacrylamide on corrosion inhibition for C-Steel in 1.0 M HCl medium: Part 2. Journal of Bio- and Tribo-Corrosion. 2018;4:34.

[36] Arrousse N, Salim R, Kaddouri Y, zarrouk A, Zahri D, Hajjaji FE, et al. The inhibition behavior of two pyrimidine-pyrazole derivatives against corrosion in hydrochloric solution: Experimental, surface analysis and in silico approach studies. Arabian Journal of Chemistry. 2020;13(7):5949–65.

Araştırma Makalesi https://doi.org/10.46810/tdfd.1184982 Research Article

Türk Doğa ve Fen Dergisi
Turkish Journal of Nature and Science
www.dergipark.gov.tr/tdfd

The Use of Macerated Garlic (*Allium Sativum L.*) Oil in Preventing the Postoperative Adhesions in Rats

Gülsüm Ülke ÇALIŞKAN[1*], Nuray EMİN[2]

[1]Kastamonu University Ihsangazi Vocational School, Veterinary Department, 37250, Kastamonu, Türkiye
[2]Kastamonu University Engineering and Architecture Faculty, Biomedical Engineering Department, 37150, Kastamonu, Türkiye
G. Ülke ÇALIŞKAN ORCID No: 0000-0002-4542-315X
Nuray EMİN ORCID No: 0000-0002-0859-2536

Corresponding author: gucaliskan@kastamonu.edu.tr

(Received: 06.10.2022, Accepted: 05.12.2022, Online Publication: 28.12.2022)

Keywords
Garlic,
Histopathology,
Intraabdominal,
Olive Oil,
Surgical
Adhesions

Abstract: In this study, the efficiency in preventing the postoperative adhesions by intra-abdominal use of the macerated oil obtained from Taşköprü Garlic (Kastamonu/Türkiye) was investigated. In the study, the macerated oil prepared using fresh garlic in olive oil at a concentration of 1.2 g/ml was used. Chemical structure of the macerated oil was analyzed by FTIR and GC-MS. Within the scope of in vivo experiments, cecal abrasion were applied to Wistar Albino rats (n=8) under general anesthesia. The physiological saline solution in control group (K) and different doses of macerated oil (0.5-1ml) in study groups (S1-S2) were dropped on the abrasion-zone. On postoperative days 3-28, the adhesions were evaluated during macroscopic observations and classified according to macroscopic adhesion score (MAS) between 0-4. At this stage, tissue samples were taken for histopathological examination from the subjects with adhesions and histopathological adhesion scoring (HAS) was performed between 0-3. The intra abdominal-adhesion was detected in all the subjects on postoperative day 3. On postoperative day 28, adhesions were observed at the MAS-2 level in K subjects, while there was no adhesion in S1-S2 subjects. In addition, histopathological adhesion was determined at the level of HAS-1 in all cases on day 3 and at the HAS-2 level in the K subjects on day 28. In conclusion, the garlic macerated oil, obtained by soaking fresh garlic in olive oil for a while, is an effective anti-adhesion agent which will be easily produced and applied by clinicians at low cost.

Sıçanlarda Postoperatif Adezyonların Önlenmesinde Maserat Sarımsak (*Allium Sativum L.*) Yağı Kullanımı

Anahtar Kelimeler
Cerrahi Adezyonlar,
Histopatoloji,
İntra-abdominal,
Sarımsak,
Zeytinyağı

Öz: Bu çalışmada Taşköprü Sarımsağı'ndan (Kastamonu/Türkiye) elde edilen maserat yağın intra-abdominal kullanımının, ameliyat sonrası yapışıklıkları önlemedeki etkinliği araştırıldı. Çalışmada, zeytinyağında 1.2 g/ml konsantrasyonda taze sarımsakla hazırlanan maserat yağı kullanıldı. Maserat yağın kimyasal yapısı FTIR ve GC-MS yöntemleriyle analiz edildi. İn vivo deneyler kapsamında Wistar Albino cinsi sıçanlara (n=8) genel anestezi altında sekum abrazyonu uygulandı. Kontrol grubunda (K) serum fizyolojik solüsyonu ve çalışma gruplarında (S1-S2) farklı dozlarda (0,5-1ml) sarımsak maserat yağı abrazyon bölgesine damlatıldı. Postoperatif 3. ve 28. günlerde, makroskobik gözlemler sırasında adezyonlar değerlendirildi ve 0-4 arasında makroskobik adezyon skoruna (MAS) göre sınıflandırıldı. Bu aşamada adezyonlu olgulardan histopatolojik inceleme için doku örneği alındı ve 0-3 arasında histopatolojik adezyon skorlaması (HAS) yapıldı. Postoperatif 3. günde, tüm deneklerde intra-abdominal adezyon tespit edildi. Postoperatif 28. günde K deneklerinde MAS-2 seviyesinde adezyonlar görülürken, S1-S2 deneklerinde adezyon olmadığı belirlendi. Ayrıca 3. günde tüm olgularda HAS-1 düzeyinde ve 28. günde K deneklerinde HAS-2 düzeyinde histopatolojik adezyon belirlendi. Sonuç olarak, taze sarımsağın bir süre zeytinyağında bekletilmesiyle elde edilen sarımsak maserat yağı klinisyen hekimler tarafından kolaylıkla üretilip uygulanabilecek, düşük maliyetli ve etkili bir adezyon önleyici ajandır.

1. INTRODUCTION

Intra-abdominal adhesion is a pathological condition, which is observed after various surgical interventions, has a high incidence [1-5], and can cause various complications including stomachache, intestinal obstruction, and female infertility [5, 6]. The incidence rate of postoperative adhesions, which are known to occurs on the 3rd and 5th postoperative days, after abdominal surgery varies between 55 and 94 % [1]. In a prospective study examining 1000 patients who have undergone laparoscopic surgery at least once, adhesion incidence was reported to be 21.1% (n=211) and it was emphasized that the adhesions found in intestines in 28% (n=59) of cases [2]. Various agents and methods were analyzed regarding the prevention of adhesion and/or reducing its incidence [1, 3, 4, 6-9]. In a study using commercial garlic oil, authors reported no positive result [4], whereas several studies showed that garlic oil was successful in preventing adhesion at certain rates [3, 7].

Garlic is a valuable raw material that is included in many pharmacopeias such as African, European, and American pharmacopeia, and used in foods, medications, and dermo-cosmetics [10]. Garlic have been used since the ancient ages [7, 11, 12], the antibacterial effect of garlic oil was proven by Louis Pasteur in the 19th century [11, 13] and, stating that it was as effective as penicillin [11], garlic oil could be used for medical purposes [11, 13]. The antiseptic properties of garlic originates from allicin (di-allyl-thiosulfate), one of the sulfurous essentail oil [11]. Thanks to its organosulfur components [di-allyl sulfide, di-allyl disulfide (DADS), di-allyl trisulfide (DATS), and di-allyl tetrasulfide], garlic was reported to be protective against various diseases [3, 4, 7, 10, 11, 13] and to have hypolipidemic, antihypertensive, antioxidant [10-14], anticarcinogenic [12-15], antimicrobial, antithrombotic, fibrinolytic, and wound-healing effects [3, 4, 7, 10, 11, 13]. It is recommended to use essential oils obtained from fresh garlic as anticarcinogenic and their aqueous solutions as herbal medication [15]. The medicinal importance of garlic emerging as a result of its use as a therapeutic and protective instrument against diseases is much higher than its value as a food [11].

Being one of the most important agricultural products of Kastamonu, “Taşköprü Garlic” was registered with geographical indication by the Turkish Patent and Trademark Office in 2010 [16] and European Union in 2021 [17]. Rich selenium content in agricultural lands of Taşköprü district [10] ensures high selenium content in the composition of Taşköprü Garlic and it is the richest garlic variety grown in Turkey in terms of sulfurous essential oils and their derivatives [11]. Taşköprü Garlic is the richest garlic variety grown in Turkey in terms of sulfurous essential oils and their derivatives [11].

Maceration is a method that is used for extracting essential oils and active compounds from herbs. Offering an extraction time longer than the modern approaches do, maceration is preferred for its lower cost [12, 18]. In macerated oils obtained by keeping garlic cloves in herbal oils, alliin rapidly converts to allicin which is the main thiosulfate in garlic degrading into lipophilic products such as dithiins and ajoen [12, 14]. It was reported that the use of macerated garlic extract products might contribute to wound healing [15].

Considering the bioactive characteristics of garlic (*Allium sativum L.)* accepted as a natural and effective therapeutic agent [12, 13], it was thought that the macerated lipogenic extract to be obtained by macerating it in olive oil [12, 14] having a high level of bioactive properties might be effective in preventing postoperative intra-abdominal adhesion formation, which causes many complications and courses with high morbidity/mortality in veterinary and human medicine. In the present study, the effectiveness of the intra-abdominal use of macerated oil of garlic prepared with olive oil in preventing postoperative adhesions were investigated.

2. MATERIAL AND METHOD

First, the macerated garlic oils were prepared in the study. After chemical analyses were done, the most suitable one was determined. Then, macerated garlic oils were applied to the experimental group subjects at different doses, whereas control group subjects were given routine practice with physiological saline solution. The data were rated using macroscopic and histopathological adhesion scoring and comparatively discussed.

2.1. Ethical Statement

Upon the ethics committee approval [date of 13.05.2019 (26.02.2021-altered) and number of 2019/23 (2021/10-altered)] from the Animal Experiments Local Ethics Committee of Kastamonu University. The present study was carried out in the Experimental Animals Unit in Kastamonu University’s Faculty of Engineering and Architecture.

2.2. Experimental Groups

In the in vivo experiments, a total of 8 (6 female and 2 male), Wistar Albino rats (*Rattus albus*), aged 8-12 weeks and 200-300 g of live weight were included in the study. Rats were housed in conventional cages in pairs under controlled standard laboratory conditions (12 h dark/12 h daylight, 45%-55% of humidity rate, and room temperature at 20-22°C) and were fed ad libitum on filtered tap water and pellet feed approved by Turkish Standards Institute. Subjects were divided into a control group (Group K) (n=4) and an experimental group (n=4). The rats in the experimental group were divided into two subgroups according to received treatmens as 0.5 ml (Group S1) and 1 ml (Group S2) of garlic macerated oil to the lesion experimentally created lesion on the cecum serosa (Table 1). After the postoperative processes, the subjects were followed in individual cages.

Table 1. Study Groups and group numbers

STUDY GROUPS		Total (n)
Control Group The physiological saline solution control group *(0.9% isotonic sodium chloride i.v. infusion solution, Polifarma® Medical, Tekirdağ-Türkiye)*	**Group K** (1 ml)	4
Experimental Groups Macerated oil prepared with olive oil *(Zeo® Extra Virgin Olive Oil, İstanbul-Türkiye)* and 12 g fresh Taşköprü Garlic	**Group S1** (0.5 ml)	2
	Group S2 (1 ml)	2
		8

2.3. Preparation of Macerated Lipogenic Garlic Extract

Before the in vivo experiment phase, the macerated garlic oil was prepared. For this purpose, Taşköprü garlic with medium sized cloves that were acquired from a local farmer with a geographical designation license were used. Commercial olive oil (Zeo® Extra Virgin Olive Oil, İstanbul-Turkey) purchased from the market and determined to be suitable by making use of chromatographic and free fatty acid analyses were used as base oil. Using 0.1 N KOH titration, the free fatty acid concentration of olive oil was found to be 0.8% (oleic acid). Since the amount of free fatty acid was found to be lower than 1% accepted to be the lower threshold for saponification, no additional process was performed before the use [15]. Macerated oils were obtained using garlic having different weights and, considering the potential side effects of garlic, macerated garlic was prepared with olive oil by using 12 g garlic that was the minimum weight providing the most suitable results in Fourier transform infrared spectrophotometer (FTIR) analysis. For this purpose, garlic cloves were peeled and dissected into small pieces. Prepared macerated oil using fresh garlic at a concentration of 1.2 g/ml in olive oil was put into an amber-colored bottle to eliminate the effect of light [12, 14]. The mixture of garlic and olive oil was incubated under darkness and at room temperature for 30 days. At the end of this period, the mixture was filtered using qualitative filter paper and garlic particles were removed. The filtrate was labeled as Z12 and the chemical analyses were performed. Until the in vivo use, the resultant macerated oil was kept at 4°C by sterilizing using a sterile injector filter (0.22 µm, CA). The experiments were conducted in Biomedical Engineering Tissue Culture Laboratory and analyses were performed in Kastamonu University's Central Research Laboratory Center of Application and Research.

2.4. Chemical Analysis of Oil Using FTIR

The structure of chemical components in the Z12 oil sample was analyzed using Bruker® brand Alpha Model ATR-FTIR spectroscopy device (USA). Measurements were performed between 4000 and 400 cm^{-1} at 4 cm^{-1} resolution with 24 scanning parameters.

2.5. Characterization of Oil Composition

The chemical components of macerated oil and their amounts were analyzed using chromatographic methods. First, the essential oil analysis was conducted using gas chromatography-mass spectroscopy (GC-MS) (Shimadzu GCMS-QP2010 ULTRA, Japan). The analysis was conducted for 63 minutes with 3 minutes at 40˚C temperature, 4˚C/min. increase from 40˚C to 240˚C, and 10 minutes at 240˚C. The results were scanned using the device library and components were matched.

Full component analysis of Z12 sample was performed using liquid chromatography-mass spectroscopy/mass spectroscopy (LC MS/MS) (Shimadzu LCMS-8040, Japan) device that can perform more accurate analysis and detect also non-essential oils. During the analysis, measurements were performed using the parameters of the Q3 Scan method, column-free injection, analysis time of 1 minute, injection volume of 0.2 µl, ultrapure water containing 1‰ formic acid (Mobile phase A), and methanol containing 1% formic acid (Mobile phase B). Peaks detected in the chromatogram of the Z12 sample were determined by reviewing and using the literature and PubMed database.

2.6. Creation of Cecal Abrasion

The subjects in all the groups were taken under general anesthesia by the intra-peritoneal implementation of a 2.5% concentration of Tribromoetanol at the dose of 250 mg/kg [20]. The subjects were positioned in a dorsal position. The hairs on the surface of the abdomen were shaved and, after asepsis-antisepsis, laparotomy was performed with an approximately 2 cm median line incision under sterile conditions. After removing the cecum (Figure 1A), cecal abrasion was applied on the upper surface by using a sterile gauze (Figure 1B-1C) [9]. For the subjects in the control group, 1 ml sterile physiological saline solution was dropped on the abrasion zone and the laparotomy incision was closed. Among subjects in the experimental group, two were given 0.5 ml (S1) and the other two were given 1 ml (S2) of sterile macerated oil (Figure 1D) and then the incision line was closed with surgical sutures (Surgicryl® polyglactin 3/0, SMI Steinerberg-Belgium) routinely. To prevent any postoperative complications due to liquid (blood) loss during the postoperative process, all the subjects were received isotonic sodium chloride (0.9%) subcutaneously at the dose of 5 ml/kg as prophylactic liquid support [21]. All the surgical interventions were performed by the same researchers**.**

Figure 1. A. Cecum was taken out of the abdomen, **B.** Application of abrasion on the upper surface of the cecum by using sterile gauze, **C.** The appearance of cecum serosa after abrasion application, **D.** Application of sterile macerated oil (Z12) to cecum serosa

Table 2. Macroscopic and histopathological assessment criteria for intra-abdominal adhesions

Grade/ Score	Macroscopic Assessment Criteria*	Histopathological Assessment Criteria**
0	No adhesion	No fibrosis
1	Very thin and easily separable adhesions	Thin cellular fibrous bundles
2	Thick adhesions limited to a specific region	Wide fibrous areas with decreased vascularization
3	Thick and widespread adhesions	Fibrous areas constituted by thick collagen bundles
4	Thick and widespread adhesions and adhesions observed between abdominal organs and the abdominal wall	-

*Blauer and Collins, 1988, **Yılmaz et al., 2005

2.7. Clinical Assessment

In the postoperative period after the experimental intervention, all the subjects were examined clinically four times a day for the first 3 days and 2 times for the remainder in terms of water consumption, defecation, respiration, mobility, and wound status, and the findings were recorded on the follow-up notebook.

2.8. Macroscopic and Histopathological Adhesion Scoring

Two animals from each group were put down on the 3rd and 28th postoperative days and the adhesions determined during the intra-abdominal exploration were macroscopically assessed/scored using the criteria of Blauer & Collins (1988) (Table 2).

The samples obtained from the subjects were found to have adhesion, staining was performed using hematoxylin-eosin (H&E) for cells, safranine-O (SO) for all the protein content including collagen, and alcian blue (AC) for proteoglycans [22]. Given the staining results, the adhesions were rated between 0 and 3 according to the criteria of Yılmaz et al. (2005) (Table 2).

3. RESULTS and DISCUSSION

3.1. FTIR Analysis

FTIR spectra of the Z12 sample indicated the presence of functional groups such as hydroxyl, carbonyl, carboxylic, and organosulfur compounds. However, the extracts prepared exhibited peaks mainly specific to the olive oil. Besides that, the weak C=S elastic vibrations at 1200-1050 cm^{-1} suggest the presence of C-N stretching of primary amines and organosulfur compounds including allyne, allicin, and diallyl disulfide (Figure 2). The weak peak observed at approximately 1350 cm^{-1} indicates the -SO2- (sulfone) groups. Moreover, the differences in fingerprint zone arise from the garlic extracts put into the olive oil. In this region, the peaks at 630-650 cm^{-1} indicate the C-S bound flexion [24].

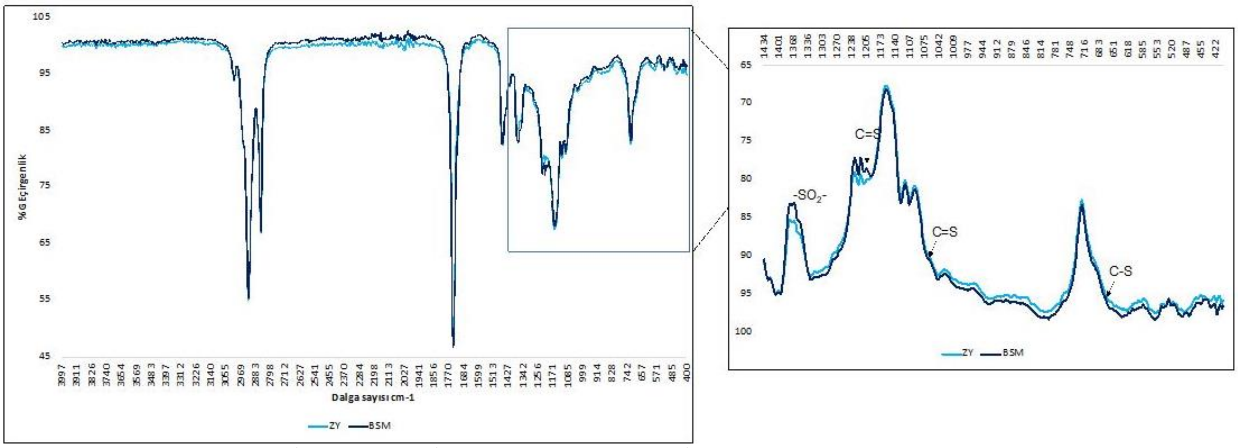

Figure 2. Comparative assessment of FTIR spectra of olive oil (Z) and macerated fresh garlic oil (Z12)

3.2. Component Analysis with LC-MS/MS

Mainly the olive oil components were observed in LC-MS/MS analysis performed for the Z12 sample. In the positive ion scanning, no component that was specific to garlic could be found. However, the chromatogram illustrating the garlic-specific components detected in negative ion scanning [25, 26] is presented in Figure 3.

Through the enzymatic reaction induced by the crush of garlic cells and their exposure to air, the alliinase enzyme interacts with alliin and forms allicin [10, 11,13, 14]. The chemical composition of macerated garlic is related to the possible substrate activity of allinase enzyme within the garlic cell, the use of polar and/or non-polar extraction solvents, and the maceration conditions [14]. Hence, in their study, Ferioli et al. (2020) detected a high amount of lipophilic organosulfur compounds in sunflower oil extracts having an apolar character. In the same study, the analyses conducted with commercially available products suggested that commercially available oil extracts might not contain almost any bioactive compound at all. The presence of various products specified for different purposes makes the standardization of garlic products difficult. Because of the uncertainties in products, it was clearly emphasized that it is important to reveal the sulfurous compounds and their amounts in a commercially available garlic product before the use for potential beneficial effects on health [14]. From this aspect, it is thought that the difference between the results reported in previous studies examining the adhesion-prevention effect of macerated garlic oil [3, 4, 7] arose from the use of commercial macerated oils manufactured by different companies and have different chemical compositions. This thought is also corroborated by the fact that oils used in those studies were not analyzed for suitability. The macerated garlic oil used in the present study was prepared by us by using commercially available olive oil, the suitability of which was confirmed, and locally produced original Taşköprü Garlic.

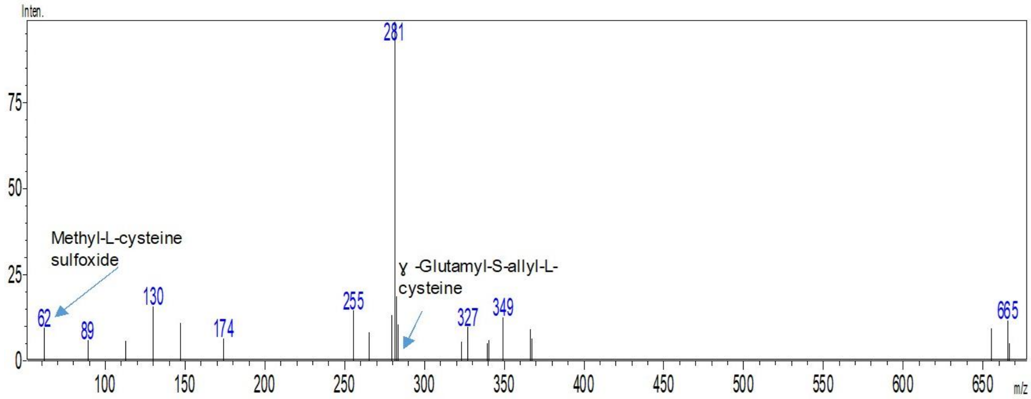

Figure 3. Chromatogram of Z12 sample's LC-MS/MS negative ion

During the preparation phase, various composition ratios were tested (only the data of extract that was used were presented due to a large amount of data) and the macerated oil containing the minimum amount of extract was preferred considering the potential adverse effects of garlic. The chemical structure of the macerated oil, prepared using fresh garlic at a concentration of 1.2 g/ml in olive oil, was analyzed spectrophotometrically using FTIR first. FTIR spectroscopy clearly showed the vibrations, which arise from the shifting movements of links between the atoms constituting functional groups, in mid-infrared range (MIR). The peaks belonging to sulfurous structures that are active compounds specific to garlic were at low levels between 1300 and 1050 cm^{-1} and there was a C-S link flexion in the fingerprint region. These findings confirm the transition of garlic extracts into olive oil. Chromatographic analyses were performed to determine the name and chemical formula of garlic components in the Z12 extract, the suitability of which was determined using FTIR. In the analysis performed using GC-MS, no essential oils were found but the components that were specific to olive oil were detected. Among the components detected during the more precise measurements performed using FTIR, the essential oils were below the detection limits of GC-MS. Thus, LC-MS/MS analysis was performed in order to determine all the components of the macerated mixture. Garlic specific carbohydrates and sulfurous components were detected during the LC-MS/MS analysis and it was determined that macerated oil had bioactive characteristics that were specific to fresh garlic. After these results, the in vivo use of macerated garlic oil was initiated.

3.3. Essential Oil Analysis with GC-MS

The essential oils of Z12 specific to garlic and observed at a low level in the FTIR spectrum couldn't be detected with GC-MS. The components detected were generally those of olive oil (Table 3) and it is thought that garlic extracts were not observed in the chromatogram since they were in trace amounts.

Table 3. Chemical composition of macerated garlic (*Allium sativum L.*) oil as a result of GC-MS analysis

No	Retention time	Compounds	%	ID
1	10.612	Octanoic acid, methyl ester (CAS)	0.845	GC/MS
2	24.744	Tetradecanoic acid, methyl ester (CAS)	1.718	GC/MS
3	28.977	Palmitate <methyl->	310.679	GC/MS
4	30.099	9-Hexadecenoic acid, methyl ester, (Z)-	17.324	GC/MS
5	30.912	Heptadecanoic acid, methyl ester (CAS)	3.300	GC/MS
6	32.801	Methyl stearate	49.978	GC/MS
7	33.760	9-Octadecenoic acid (Z)-, methyl ester (CAS)	2108.934	GC/MS
8	35.147	9,12-Octadecadienoic acid (Z, Z)-, methyl ester	212.660	GC/MS
9	36.232	Eicosanoic acid, methyl ester (CAS)	7.528	GC/MS
10	36.793	9,12,15-Octadecatrienoic acid, methyl ester, (Z,Z)	9.749	GC/MS
11	37.099	cis-11-Eicosenoic acid, methyl ester	5.606	GC/MS
12	37.867	Heneicosanoic acid, methyl ester (CAS)	1.753	GC/MS
13	39.430	Docosanoic acid, methyl ester	3.042	GC/MS
14	42.569	Tetracosanoic acid, methyl ester	2.135	GC/MS

3.4. Clinical Assessment

During the postoperative clinical observations in terms of feed-water consumption, defecation, respiration, mobility, and wound condition after waking up from anesthesia, it was determined that the subjects that turned back to daily activities within six hours approximately, and they were generally in good condition.

3.5. Adhesion Evaluation

3.5.1. Macroscopic adhesion scoring

The distribution of adhesions rated between 0 and 4 according to macroscopic adhesion score (MAS) using the criteria of Blauer & Collins (1988) on postoperative days 3-28 is presented in Table 4, whereas the images related to the MAS assessments are illustrated in Figure 4.

Table 4. MAS and HAS assessments on the 3rd and 28th postoperative days

GROUPS	Day 3		Day 28		*Total (n)*
	MAS	**HAS**	**MAS**	**HAS**	
K *	1 2	1 1	2 0	2 0	4
S1**	1	1	0	0	2
S2***	1	1	0	0	2
Total (n)	4		4		8

* Physiological saline solution group
** Group treated with 0.5 ml dose of macerated oil
*** Group treated with 1 ml dose of macerated oil

Given the macroscopic assessments performed in the present study, all the subjects were found to have an adhesion on the 3rd day. Moreover, it was observed that adhesions reached the level of MAS-2 in the control group but only MAS-1 level adhesions were observed in the experimental group subjects. On the 28th day, no adhesion was observed in the experimental group subjects but the level of adhesions seen in the control group subjects was MAS-2. In all the time points and all experimental group subjects (S1-S2), the abdominal exploration showed that the color of cecum serosa was bright and smooth and turned into dark green (Figure 4). It was thought that the change in the color of cecum serosa in experimental group subjects during the postoperative period was related to the topical sensitivity due to the garlic [14].

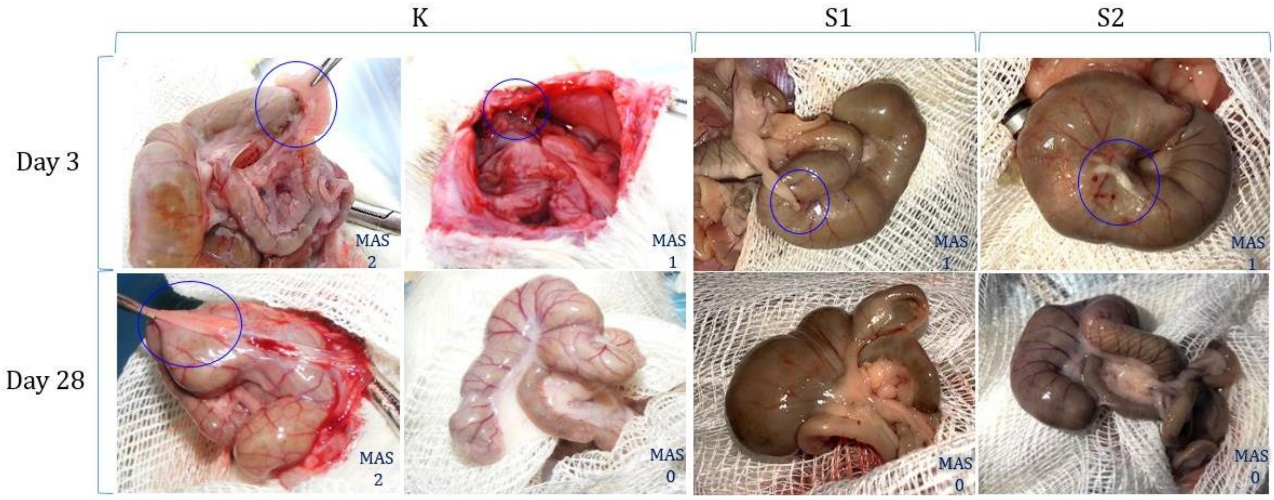

Figure 4. Images and MAS values of control (K) and experimental groups [S1 (0.5 ml)-S2 (1 ml)] on postoperative days 3-28

It was emphasized that the synergetic or antagonistic effect of garlic products on physiology might vary depending on dosage, potential metabolite interactions, and the individual's age and pathology. In humans, excessive consumption of garlic might cause various adverse effects such as allergic reactions, topical sensitivities, prolonged blood coagulation [14], unpleasant odor in breath and on the skin, stomach problems such as indigestion, hypotension [10, 13, 14], tachycardia, headache, sleeplessness, vomiting, and diarrhea. Since it increases the effects of anticoagulant agents (warfarin, coumadin, fluindione, etc.), it is not recommended to use garlic together with these medications [10, 13]. Moreover, it was also reported that consuming a high amount of garlic after surgical interventions increased the risk of postoperative hemorrhage [10]. In studies reporting that intra-peritoneal use of garlic oil reduced the formation of peritoneal adhesion [3, 7], garlic oil was used at the dose of 5 ml/kg. But it was also stated that more experimental studies are needed to determine the best dose of garlic offering the best adhesion prevention [7]. It was aimed to determine the active component content of macerated oil and if it would be effective at that dose because no commercially available preparation was used and because of the presence of bioactive components of garlic detected in laboratory analyses. From this aspect, the macerated oil containing the minimum concentration (1.2 g/ml) of garlic was applied to the cecum serosa of the subjects; the dose was 1 ml (5 ml/kg) for half (n=2) of subjects and 0.5 ml (2.5 ml/kg) for the other half (n=2).

3.5.2. Histopathological adhesion scoring and assessment

The histopathological adhesion scores (HAS) of adhesions rated histopathologically between 0 and 3 using the criteria of Yılmaz et al. (2005) are presented in Table 4.

The distribution of adhesions rated histopathologically between 0 and 3 [23] by HAS is presented in Figure 5 together with the histochemical images. In the control group given physiological saline solution, adhesion formation due to cellular fibrosis was observed on day 3. Given the SO staining in the matrix within adhesion tissue, there were fewer protein structures, whereas AC stating showed that there were more proteoglycan molecules. Especially the glycosaminoglycan (GAG) structures were in form of small aggregates gathering nearby the cells and they were observed to be more in accordance with the cell density. The results obtained from the control group on the 28th day revealed that cellular fibrosis started decreasing but, together with the increased protein level, SO staining indicated the formation of fibrillary collagen bundles. In this parallel, H&E and AC staining procedures showed relative decreases. Moreover, AC staining procedures revealed that, rather than aggregating nearby the cells, proteoglycan-type structures exhibited a fibrillary alignment throughout the matrix. Considering all three histochemical staining processes together, HAS in the control group was rated 1 on day 3 and 2 on day 28.

In the experimental groups (S1-S2), there was cellular fibrosis but at a lower level in comparison to the control group. H&E and AC results corroborated each other and GAG aggregates gathered around the cells. In the S2 sample, proteoglycans were found to shift toward the intercellular area. SO staining procedure stains proteins in the extracellular matrix. SO results in S1 and S2 showed that SO stained the core proteins belonging to proteoglycans concentrated around the cells rather than fibrous proteins (collagen molecules). Considering all three histochemical staining procedures, S1 and S2 samples were found to be HAS-1 on day 3 [23]. Since no adhesion tissue formed on day 28 in the S1 and S2 samples, HAS assessment been considered to be zero.

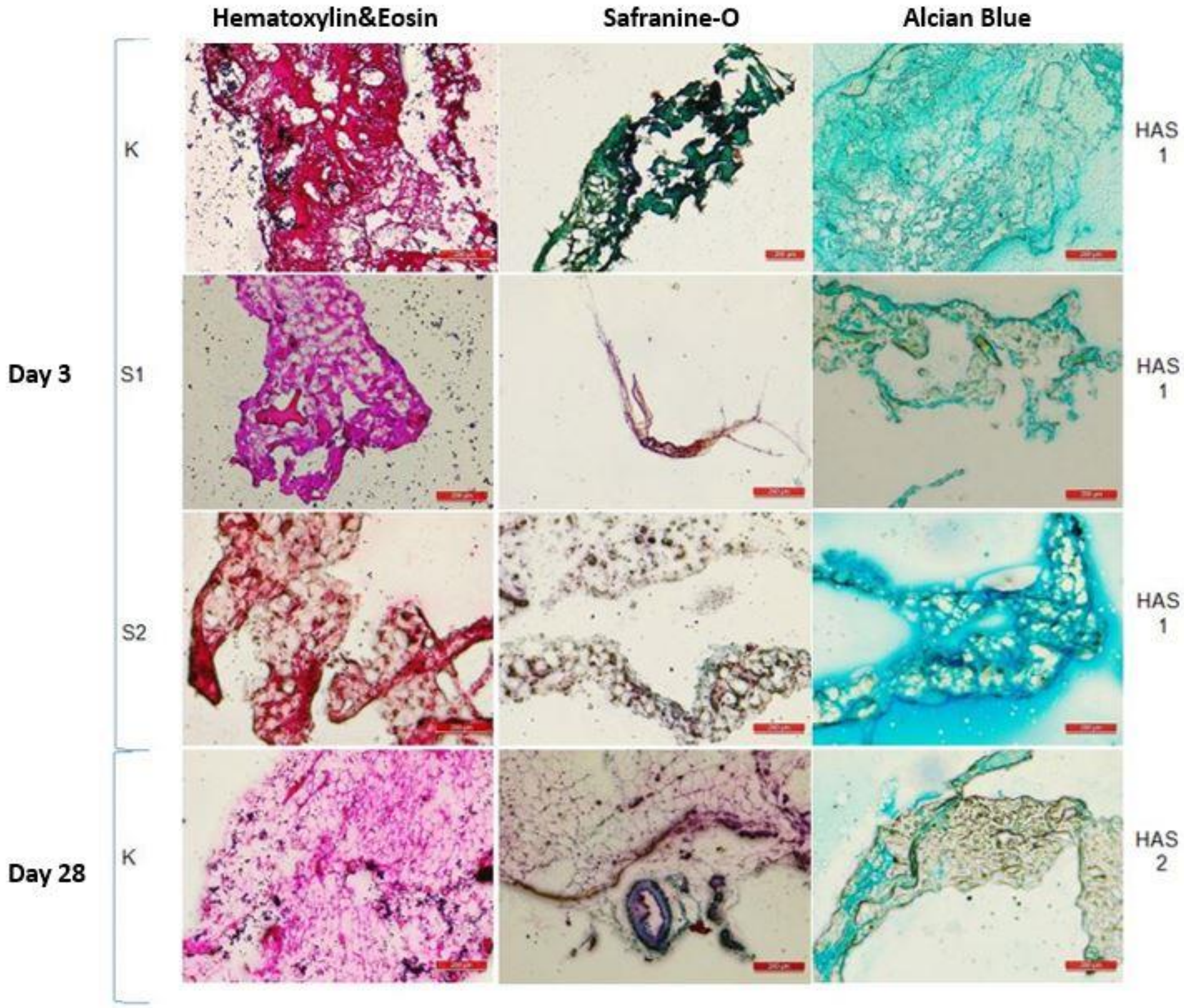

Figure 5. HAS assessment and histopathological examinations were performed using H&E, SO, and AC staining. Since no adhesion tissue formed in S1 and S2 samples on day 28, HAS assessment was considered to be zero (scale = 200 μm)

Ali et al. (2016) reported that intra-peritoneal implementation of garlic oil in diabetic and non-diabetic rats was effective in reducing postoperative adhesions, especially in diabetic subjects. This effect was related to the antimicrobial and anti-inflammatory activity of garlic and the prevention of mechanical contact between surfaces [7]. In a study by Topal et al. (2019), the immunohistochemical analyses conducted to determine the oxidative stress on the cellular surface revealed that garlic didn't reduce the free oxygen radicals. Besides that, in another study [7] analyzing the intra-peritoneal use of garlic oil, immunohistochemical examinations showed that there was no significant increase in D2-40 positive cells in control groups and those given physiological saline solution, whereas positive immune reactions to D2-40 antibodies were found in mesothelium cells in the groups treated with garlic oil. The diabetic rats treated with garlic oil had significantly increased D2-40 expression when compared to those treated with physiological saline solution and the difference was found to be statistically significant ($p<0.001$) [7].

Macerated oil of fresh garlic, which was found to increase the proliferation in human cancer cells and rat bone marrow mesenchymal stem cells (MSCs), was thought to exhibit a nutritive effect on the cells because of the oleic acid content of pure olive oil [7]. During the in vitro cell culture studies carried out in our laboratory, it was determined that pure olive oil increased the proliferation in all the healthy cells and/or those having pathological phenotypes and, thus, promoted tissue formation [15]. The oleic acid content in the pure olive oil used as the base oil in the present study might support the proliferation of fibroblast cells in adhesion structure as in MSCs having a fibroblastic morphology. However, it was observed that the adhesion ratio in the macerated fresh garlic oil group was lower in comparison to the control group. This finding was interpreted as the antiproliferative effect of garlic extracts. Given the MAS values determined on the 3rd and 28th postoperative days, experimental groups (S1-S2) were found to have macroscopically less and lower levels of adhesions in comparison to the control group. Besides that, the histopathological lesion that was at HAS-1 level, which was related to cellular fibrosis, in all the groups on day 3 was found to be at HAS-2 level, which was related to the fibrous tissue-like structures increasing against the decreasing cellular structure, in the control group on day 28. However, no adhesion tissue was observed in S1-S2 subjects on day 28. This result suggested that either no adhesion has formed or the low levels of adhesions observed on day 3 were eliminated by the body with time.

In the present study, the small number of subjects examined at the time points is a limiting factor. For this reason, further studies using garlic, the bioactive components of which were determined, and to be carried out on a higher number of subjects are needed to determine the minimum dose of garlic oil to be applied intra-peritoneally to prevent the adhesion.

4. CONCLUSION

It was thought that the macerated oil of fresh garlic, which was prepared using olive oil having low oleic acid and free fatty acid as base oil and bioactive components which were determined as in the present study, would be more effective in preventing adhesion. Besides that, garlic having a high level of sulfur content, which is known to play role in antioxidant and antimicrobial activity, had a significant contribution to the result obtained. In the present study, it was concluded that the intra-abdominal application of macerated olive oil obtained from fresh fresh garlic was effective in preventing postoperative adhesion. It may be easily performed in veterinary clinic practice. To prevent the formation of intra-abdominal adhesions and to determine the effect mechanism of macerated oil that was applied, there should be further postoperative studies should be carried out on a higher number of subjects and in shorter time points.

Acknowledgement

For their contributions to the laboratory analyses and in vivo process during the present study, the authors would like to thank Havva YAZAR, Omar K. H. ALSHAWI, İpek CEYLAN, and Kıymet NURAL and Salma A. Taher MOHAMED (the postgraduate students in Kastamonu University Institute of Science and Technology), and also Dr. Orçun İŞLER ÖZGÜN (Kastamonu University Ihsangazi Vocational High School Department of Veterinary).

REFERENCES

[1] Pamukçu A. Peritoneal adezyonlardan korunmada gliserinin etkisi. Konya. Selçuk University; 2007.
[2] Dubuisson J, Botchorishvili R, Perrette S, Bourdel N, Jardon K, Rabischong B, et al. Incidence of intraabdominal adhesions in a continuous series of 1000 laparoscopic procedures. Am J Obstet Gynecol. 2010;203:111.e1-3.
[3] Şahbaz A, Işık H, Aynıoğlu Ö, Güngördük K, Gün BD. Effect of intraabdominal administration of *Allium Sativum* (garlic) oil on postoperative peritoneal adhesion. Eur J Obstet Gyn R B. 2014; 177:44–47.
[4] Topal U, Göret NE, Göret CC, Özkan ÖF. The effect of *Allium sativum* in experimental peritoneal adhesion model in rats. Acta Cir Bras. 2019; 34(10);e201901002.
[5] Tang J, Xiang Z, Bernards MT, Chen S. Peritoneal adhesions: Occurrence, prevention and experimental models. Acta Biomat. 2020:116;84-104.
[6] Blauer KL, Collins RL. The effect of intraperitoneal progesteron on postoperative adhesion formation in rabbit. Fertil Steril. 1988;49:144–8.
[7] Ali SN, Al Badawi MH, Galhom RA, Badr FM. Macroscopic and microscopic study of *Allium Sativum* (garlic) oil effects on post-operative intra-abdominal adhesion in diabetic and non diabetic male rats. J Cell Sci Ther. 2016;7(2):240-6.
[8] Tabibian N, Swehli E, Boyd A, Umbreen A, Tabibian JH. Abdominal adhesions: A practical review of an often overlooked entity. Ann. Med. Surg. 2017;15: 9-13.
[9] Kıvçak B. Sarımsağın ilaç endüstrisinde değerlendirilmesi. Taşköprü Sarımsak Paneli, Kastamonu: North Anatolian Development Agency (Document Number 2012-RP-29/31); 2012. p. 59-67.
[10] Koyuncu M. Sarımsağın Tarihçesi, Kullanım Alanları, Sarımsağın Faydaları, Taşköprü Sarımsak Paneli, Kastamonu: North Anatolian Development Agency (Document Number 2012-RP-29/31); 2012. p. 11-20.
[11] Ferioli F, Giambanelli E, D'Alessandro V, D'Antuono LF. Comparison of two extraction methods (high pressure extraction vs. maceration) for the total and relative amount of hydrophilic and lipophilic organosulfur compounds in garlic cloves and stems. An application to the Italian ecotype “Aglio Rosso di Sulmona” (Sulmona Red Garlic). Food Chem. 2020;312:126086 (9 pages).
[12] Kızılaslan N, Tokatlı K. Sarımsağın İnsan Sağlığı Üzerine Etkileri (Effects of garlic on human health). J Togu Heal Sci. 2021;1(2):62 71.
[13] Staba EJ, Lash L, Staba JE. A commentary on the effects of garlic extraction and formulation on product composition. J Nutr. 2001;131(3):1118-19.
[14] Alshawi OKH. İnsan kolorektal kanser hücrelerine farklı sarımsak (*Allium Sativum L.*) ekstraktlarının

antikarsinojenik etkisinin araştırılması (Investigation of the anticarcinogenic effects of different garlic (*Allium Sativum L.*) extracts on human colorectal cancer cells). Kastamonu: Kastamonu University; 2021.

[15] Turkish Patent and Trademark Institution [Internet]. Taşköprü Sarımsağı; 2010 [cited 2022 May 01]. Available from https://ci.turkpatent.gov.tr/cografi-isaretler/detay/38009.

[16] Turkish Ministry of Foreign Affairs [Internet]. Taşköprü Garlic and Bayramiç White Registered as Geographical Indications in the European Union; 2021 [cited 2022 May 01]. Available from https://www.ab.gov.tr/taskopru-sarimsagi-ve-bayramic-beyazi-avrupa-birliginde-cografi-isaret-olarak-tescil-edildi_52527.html.

[17] Srivastava N, Singh A, Kumari P, Nishad JH, Gautam VS, Yadav M, et al. Advances in extraction technologies: isolation and purification of bioactive compounds from biological materials. In: Sinha R, Häder DP, editors. Natural Bioactive Compounds. Natural Bioactive Compounds. India: Academic Press; 2021. p.409–433.

[18] Armutçu F, Namuslu M, Yüksel R, Kaya M. Zeytinyağı ve sağlık: biyoaktif bileşenleri, antioksidan özellikleri ve klinik etkileri. Konuralp Tıp Derg. 2013; 5(1):60-68.

[19] Institutional Animal Care and Use Committee (IACUC) [Internet]. Use of Tribromoethanol (Avertin); 2019 [cited 2020 Apr 04]. Available from https://iacuc.wsu.edu/documents/2016/06/32_avertin_policy_final.pdf/.

[20] Diehl KH, Hull R, Morton D, Pfister R, Rabemampianina Y, Smith D, et al. A good practice guide to the administration of substances and removal of blood, including routes and volumes. J Appl Toxicol. 2001;21:15–23.

[21] Emin N, Koç A, Durkut S, Elçin AE, Elçin YM. Engineering of rat articular cartilage on porous sponges: Effects of TGF-β 1 and microgravity bioreactor culture. Artif Cell Blood Sub. 2008;36 (2):123-137.

[22] Yılmaz HG, Taçyıldız IH, Keles C, Gedik E, Kılınç N. Micronized purified flavonoid fraction may prevent formation of intraperitoneal adhesions in rats. Fertil Steril. 2005;84(2):1083-8.

[23] Gündüz T. İnstrumental analiz. Ankara University Science Faculty Publishing; 1988.

[24] Fellner M, Kneifel W, Gregorits D, Leonhardt W. Identification and antibiotic sensitivity of microbial contaminants from callus cultures of garlic *Allium sativum L.* and *Allium longicuspis Regei*. Plant Sci. 1996;113(2):193-201.

[25] Ham JS, Lee SG, Kim MK, Oh MH, Jeong SG, Kim DH, et al. Inhibitory activity of garlic fermented by Pediococcus pentosaceus KACC 91419 against antibiotic-resistant pathogens. Asian Austral J Anim. 2010; 23(9):1236-1243.

Cilt 11, Sayı 4, Sayfa 88-97, 2022
Volume 11, Issue 4, Page 88-97, 2022

Araştırma Makalesi https://doi.org/10.46810/tdfd.1172011 Research Article

Türk Doğa ve Fen Dergisi
Turkish Journal of Nature and Science
www.dergipark.gov.tr/tdfd

Hydrated C_{60} Fullerene Enhances Parthanatos and Induces Autophagy-Related Biomarkers in Glioblastoma Cell Line

Aryan M. FARAJ[1,2], Victor S. NEDZVETSKY[1,3], Artem A. TYKHOMYROV[4], Giyasettin BAYDAS[5], Abdullah ASLAN[6], Can Ali AGCA[1*]

[1]Department of Molecular Biology and Genetics, Bingol University, 12000, Bingöl, Türkiye
[2]Department of Medical Laboratory Science, Sulaimani Polytechnic University, Sulaymaniyah, Iraq
[3]Department of Physiology, Biochemistry of Animals and Lab Diagnostics, Dnipro State Agrarian and Economic University, 49600, Dnipro, Ukraine
[4]Department of Enzyme Chemistry and Biochemistry, Palladin Institute of Biochemistry of the National Academy of Sciences of Ukraine, Kyiv, Ukraine
[5]Department of Enzyme Chemistry and Biochemistry, Altinbash University, 34218 İstanbul, Türkiye
[6]Faculty of Science, Department of Biology-Molecular Biology and Genetics Program, Firat University, Elazig, Türkiye
Aryan M. FARAJ ORCID No: 0000-0002-7229-3717
Victor S. NEDZVETSKY ORCID No: 0000-0001-7352-441X
Artem A. TYKHOMYROV ORCID No: 0000-0003-2063-4636
Giyasettin BAYDAS ORCID No: 0000-0002-9206-3177
Abdullah ASLAN ORCID No: 0000-0002-6243-4221
Can Ali AGCA ORCID No: 0000-0002-0244-3767

**Corresponding author: caagca@bingol.edu.tr*

(Received: 09.09.2022, Accepted: 05.12.2022, Online Publication: 28.12.2022)

Keywords
Glioblastoma, C_{60} hydrated fullerene, Autophagy, Parthanatos

Abstract: Glioblastoma is one of the most aggressive type of brain cancers, which is resistant to chemo- and radio-therapy. Nanoparticles of C_{60} fullerene derivates develop anticancer activity in various models. Therefore, we investigated the effect of water soluble hydrated C_{60} fullerene (HyC_{60}Fn) on the expression of PARP, Beclin1, LC3, and GFAP in human glioblastoma U373 cell. Cell viability and migration were detected by MTT and wound healing-scratch assay, respectively. The expression of PARP, Beclin1, and LC3 were analyzed by western blotting and GFAP was detected by immunocytochemistry. HyC_{60}Fn in a range of doses 0.5 – 2.0 µM decreased cell viability. Furthermore, the doses of HyC_{60}Fn 1.0 and 2.0 µM noticeably suppressed glioblastoma cell migration. Mechanistically, we defined that HyC_{60}Fn markedly up-regulated Beclin-1 and ratio of LC3-II/LC3-I expression as autophagy markers. Furthermore, water soluble HyC_{60}Fn activated cleaved PARP fragment and consequently parthanatos in glioblastoma U373 cancer cell. Present results demonstrate that HyC_{60}Fn could initiate anti-tumor effect via the combination of severe autophagy flux and parthanatos in glioblastoma cells. Thus, HyC_{60}Fn affects the cancer cell death machinery, at least partially, through modulating glioblastoma cells reactivity and programmed cell death. Our findings suggest that pristine hydrated C_{60} fullerene could be a promising anti-cancer therapeutics and further study is required.

Hydrated C_{60} Fullerene, Glioblastoma Hücre Hattında Parthanatosu Arttırır ve Otofaji İle İlgili Biyobelirteçleri İndükler

Anahtar Kelimeler
Glioblastoma, C_{60} hydrated fullerene, Otofaji,

Öz: Glioblastoma, kemo ve radyoterapiye karşı dirençli, en agresif beyin kanseri tiplerinden biridir. C_{60} fulleren türevi nanopartiküller, çeşitli modellerde antikanser aktivite amacı ile geliştirilmektedir. Bu nedenle, suda çözünür hydrated C_{60} fullerene'in (HyC_{60}Fn) insan glioblastoma U373 hücresinde PARP, Beclin1, LC3 ve GFAP ekspresyonu üzerindeki etkileri araştırılmıştır. Hücre canlılığı ve göçü, sırasıyla MTT ve yara iyileşmesi testi ile belirlendi. PARP, Beclin1 ve LC3 ekspresyonu western blot ile ve GFAP ise immünositokimya ile tespit edildi. 0.5

Parthanatos – 2.0 µM doz aralığındaki HyC_{60}Fn, hücre canlılığını azalttığı belirlendi. Ayrıca, HyC_{60}Fn 1.0 ve 2.0 µM dozları, glioblastoma hücre göçünü belirgin şekilde bastırmıştır. Mekanizma olarak, HyC_{60}Fn'nin otofaji belirteçleri olarak Beclin-1'i ve LC3-II/LC3-I ekspresyon oranını belirgin şekilde yukarı regüle ettiği belirlendi. Ayrıca, suda çözünür HyC60Fn'nin PARP fragmanı ve bu durumun doğal sonuç olarak glioblastoma U373 hücrelerinde parthanatos aktive ettiği belirlendi. Mevcut sonuçlar, HyC60Fn'nin, glioblastoma hücrelerinde şiddetli otofaji akışı ve parthanatos kombinasyonu yoluyla anti-tümör etkisini başlatabildiğini göstermektedir. Bu nedenle HyC_{60}Fn, glioblastoma hücrelerinin reaktivitesini ve programlanmış hücre ölümünü modüle ederek en azından kısmen hücre ölüm mekanizmasını etkiler. Bulgularımız, HyC_{60}Fn 'in umut verici bir kanser karşıtı terapötik olabileceğini ve bu konuda daha fazla çalışmanın gerekli olduğunu göstermektedir.

1. INTRODUCTION

Glioblastoma is one of the most aggressive types of primary brain tumors, a highly combative brain tumor in adults, and among the most lethal cancer in humans. Despite advances in the surgical and radio chemotherapy approach of glioblastoma, it is insufficient in preventing recurrence due to its important side effects and only limited effectiveness [1,2] and the mortality rate of patients remains high. Thus, more effective chemotherapy agents with fewer side effects are urgently needed. Several types of fullerene nanoparticles act as neuron protector and antioxidant [3]. On the other hand, small-size C_{60} fullerene has higher toxicity potency and leads to inhibition of DNA polymerase [4]. It should be noted that fullerene C_{60} and its derivatives may also have a toxic effect in some circumstances, whereas C_{60} can also protect the cells from the condition of oxidative damage or pathological statesThe most of reported data on fullerene bioactivity in respect to brain tissue cells were obtained with functionalized C_{60} derivates in both *in vivo* and *in vitro* studies [5–7]. C_{60} fullerene develops extremely wide range of bioactivity in dependence of a dose and the state of surface [8–10] Cytotoxic effect of several functionalized C_{60} fullerene is recognized as a function of its prooxidant effect [6, 11, 12]. Various anticancer effects of several fullerene forms were established including DNA methylation [13], cell cycle arrest [14], anti-angiogenic effect [15] and stress-induced apoptosis [16]. Besides, neuroprotective effect of pristine C_{60} fullerene on autophagy flux and apoptosis was demonstrated in rat brain stressed with hyperglycemia [17]. One of the hallmarks of malignation is the overproduction of reactive oxygen and nitrogen species (ROS/RNS) that play an importante role in cancer process [18–20]. Previous studies have emphasized that ROS/RNS, as two-faced molecules, play a dual role as a tumor promoting agent depending on the intracellular level or tumor-suppressing due to their implication in triggering cell death [20–22]. However, redox abnormality is not specific for tumor cells. There is a rising evidence that prevaling number, if not all, of various cellular disturbances are accompanied by increased free radicals generation. Despite wide studied pro-oxidant effects of functionalized fullerene, pristine C_{60} fullerene could inhibit tumor progress via modulation of regulatory pathways and gene expression [17, 23]. Glioblastoma cells progress depends on multiple mutations and abnormal regulation of cell death pathways, including resistance to programmed cell death initiation [24]. Programmed cell death, particularly apoptosis and autophagy, plays a fundamental role in the cellular strategy to maintain the balance in surviving and elimination of damaged cell [25]. However, the modulation of programmed cell death is promising therapeutic development to suppress cancer growth too, including the autophagy lysosomal pathway in gliomas [26]. Autophagy is described as a self-cannibalism that is a highly conserved dynamic cellular process occurring as a cellular response to starvation or pathogen infection that degrades macromolecules or organelles [27]. The formation of the self-cannibalism mechanism is initiated with encapsulating of macromolecule or organelles into double-membrane intracellular vesicles and then fused with lysosomes to be recycled [28, 29]. Previous studies have indicated that autophagy, which is characterized by the presence of auto-phagosome, plays a dual role as a lysosomal degradation pathway and autophagy depend-cell death, inhibiting cancer growth depending on the intracellular stress of cells [29, 30]. Previous studies have emphasized that C_{60} fullerene, as two-faced molecules, could induce accumulation of ROS [31] or in contrast, serves reduce oxidative damage and ROS level [32]. Autophagy-related proteins (Atg), Beclin-1, and microtubule-associated protein 1A/1B-light chain 3 (LC3) are central regulatory proteins in autophagy. Beclin-1 is an important regulator involved in the initiation of autophagy [33]. In the autophagy pathway, Beclin-1 and LC3 which is called Atg8, have non-negligible function in the autophagosome membrane. [29, 34]. Besides, autophagy-dependent cell death, non-apoptotic cell death signaling pathways including parthanatos have recently gained great interest [35]. Parthanatos, other cell death pathway, is a poly(ADP-ribose) synthetase 1 (PARP1)- dependent cell death that initiated by overactivation of PARP1 accompanied by depletion of NAD and ATP [35, 36]. Parthanatos is tightly associated with various macromolecular damages and mitochondrial dysfunction as well as other types of programmed cell death [35]. Despite many factors contribute to parthanatos, it does not require caspases participation [36]. Overexpression of PARP1, which in turn leads to a number of biological consequences, induces apoptosis-inducing factor (AIF), release into the cytoplasm, and then is translocated into the nucleus where it triggers chromatin condensation and DNA fragmentation [36, 37]. The effect of fullerene on parthanatos initiation remains unknown. Besides, there are limited data in respect with the suppression of glioblastoma progress by fullerene exposure [7, 38]. GFAP is a glial specific intermediate filaments protein and its overexpression is the main marker of astrogliosis [39]. Furthermore, there was reported that expression of GFAP isoforms involved in glial cell motility and proliferation where dynamic rearrangement of intermediate filaments network is accompanied by the modulation of focal adhesion [40]. However, the role of glial intermediate filaments in cell motility remains enigmatic. Thus, the aim of the present study was to elucidate the effect of C_{60} fullerene on Beclin1, LC3 and PARP expression, and migratory activity in human glioblastoma U373 cell line.

2. MATERIAL AND METHOD

2.1. Cell Line and Culture Condition

The human glioblastoma cell line (U373 MG) was purchased from the American Type Culture Collection (ATCC, American Type Culture Collection; Rockville, MD, USA). The cells were grown in culture dishes in DMEM medium supplemented with 10% fetal bovine serum. The medium was also supplemented with 64 µg/ml penicillin (cat. No. A1837.0010) + 0.1 mg/ml streptomycin (cat. No. A1852.0025; both VWR, USA) antibiotic solution. The cells were incubated in 5% CO_2 at 37 °C and 80–90% confluence, cells were carefully removed with trypsin/EDTA and washed with phosphate buffered saline (PBS).

2.2. Determination of Cell Viability

The cell viability was determined as previously described [41] by the MTT assay. Briefly, to determine the C_{60} fullerene inhibitory potency on growth, 6,000 cells were seeded into each well of 96-multiwell cell culture plates in culture medium containing 10% FBS. The cells were treated with various concentrations of C_{60} (0.5, 1.0 and 2.0 µM) allowed to grow for 24 h. After that, 10 µl of MTT labelling reagent, 3-(4, 5- dimethylthiazolyl-2)-2, 5-diphenyltetrazolium bromide (MTT) stock solution (0.5 mg/ml) was added to each well and incubated for 4 h at far from light. The purple-coloured formazan pellets were dissolved in 100 µl DMSO, incubated for 15 min and read using a microplate reader (Molecular devices LLC, USA) at 550-600 nm (the reference wavelength 650 nm).

2.3. Migration Test

The day before treatment, U373 cells (5×10^4 cells/dish) were seeded into 12 wells plate for attachment. A mechanical scratch was made with the help of a sterile 200 µl pipette tip, and the plates were then washed with PBS to remove detached cells. The cells were treated with 1 and 2 µM of C_{60} for 24 h. The wells were photographed at different time points. Cell migration pictures were monitored using an invert microscope (Olympus, CKX41, Tokyo, Japan) at 40× magnification.

2.4. Western Blotting

U373 cells (1×10 6 cells/dish) were maintained on a 10-cm dish with DMEM medium containing 10% FBS for 24 h and were incubated with 24 h of C_{60} fullerene for 0, 0.5, 1, and 2 µM. After treatment, cells were collected by scratching without trypsinization and suspended in a fresh lysis buffer (RIPA) plus 1 mM PMSF (phenyl methane sulfonyl fluoride) and a proteinase and phosphatase inhibitor cocktail as described previously [41]. Protein concentrations were measured and re-suspended in a loading buffer. A total 30 µg from each sample was electrophoresed by 10 or 12% SDS-polyacrylamide gel electrophoresis (SDS-PAGE) and transferred to polyvinylidene difluoride membranes (PVDF, Millipore, Germany/USA; cat. No. IPVH00010). 5% non-fat milk was used for blocking the membrane, which was then incubated with primary antibodies (Beclin1, LC3 and PARP diluted 1:1,000, β-actin – 1:3,000, Santa Cruz, CA, USA) at 4◦ C overnight. The membranes were then incubated with secondary antibody (anti-mouse IgG-HRP and anti-rabbit IgG-HRP-1:5,000, Advansta, California, USA) that conjugated with horseradish peroxidase for 1 h at room temperature with gentle agitation. The signal was developed by an enhanced chemiluminescence method with the use of X-ray films (Carestream, USA). Densitometry analysis was performed using the ImageJ software (USA) and normalized against its respective loading control.

2.5. Immunofluorescence

GFAP immunocytochemistry (ICC) was performed in U373 cells according to the immunofluorescence assay protocol as described earlier [42]. Briefly, fixed and permeabilized cells were washed with cold PBS and then cells were blocked with 5% BSA by 60 min at 37°C. Cells were then incubated with primary anti-GFAP antibody (1:200 dilutions in PBS-Tween, Santa Cruz, CA, USA) overnight at 4°C. Cells were washed with PBS-Tween for 15 min. Secondary anti-rabbit antibodies (Sigma-Aldrich, USA) conjugated with green fluorophore fluorescein isothiocyanate (FITC) in 1:400 dilution were added and incubated for 60 min at 37 °C. After that, the cells were washed again three times with PBS-Tween for 15 min, nuclei were counterstained with blue fluorescent dye Hoechst-33342 (1 µg/ml). Fluorescent images captured using the Zeiss LSM510 Meta confocal microscope were converted to gray-scale and normalized to background staining. Specific signal of GFAP immunofluorescence from the at least nine regions of interest (ROI) of each group of cells was evaluated using the ITCN plugin for ImageJ (https://imagej.nih.gov/ij/). Quantification of GFAP-positive U373 cells was measured as the percentage of area occupied by fluorescent-labeling in each ROI and then correlated with the number of nuclei located in each ROI. GFAP-positive signal intensities were expressed as % from the control level.

2.6. Statistical Analyses

Cell viability, western blot, and values of GFAP immunofluorescence results were evaluated by analysis in Graph Pad Prism 5.01 program. The result were analysed by one-way ANOVA followed by post-hoc Tukey test and the analysis were carried out for three replications. P level less than 0.05 was considered statistically significant.

3. RESULTS

3.1.Effects of C_{60} Fullerene on U373 Cell Viability

First, we examined the effect of C_{60} fullerene on cell viability in U373 cell line with different concentration of C_{60} fullerenes (0, 0.1, 0.25, 0.5, 1.0 and 2.0 µM) for 24 h. The cell viability was assessed by MTT assay measurements. As shown in Figure 1, after 24 h treatment of C_{60} fullerene, it was observed that C_{60} fullerene inhibited cell growth. The U373 cell viability was almost unchanged at a low dose as compared with the control group, whereas, it was reduced at the high dose of 1 and 2 µM, indicating the most effective concentration.

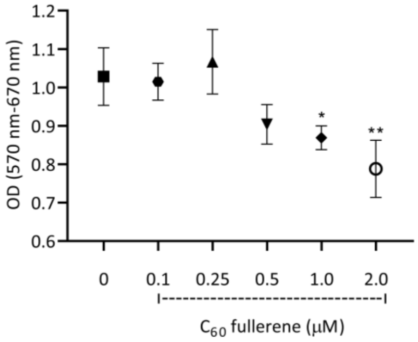

Figure 1. Effects of C_{60} fullerene on cell viability in U373 cell line. Concentrations of C_{60} fullerene, µM, are shown below the diagrams. *P < 0.05 and **P <0.01 vs. the control group.

3.2.Effects of C_{60} Fullerene on U373 Cell Migration

Next, we explored whether C_{60} could suppress cell migration in U373 cell line. The U373 migrative activity was detected as one of the features of tumorigenicity as well as invasive and metastasis index. Present wound healing assay results have shown that the doses of C_{60} 1.0 and 2.0 µM were able to inhibit the migration of U373 glioblastoma cells (Figure 2).

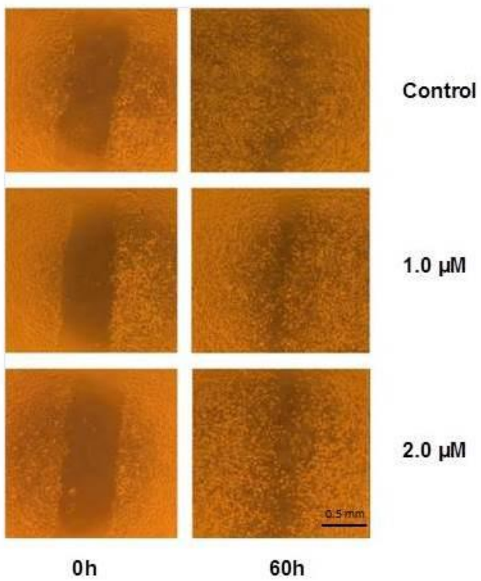

Figure 2. Effects of C_{60} fullerene on the cell migration in U373 cell line. Wound healing-scratch assays were performed to evaluate cell migration. The images were acquired at 0 h and 60 h.

3.3.Effects of C_{60} Fullerene on Beclin1, LC3 and PARP Expression

Given the above results, we further examined the protein expression of Beclin1, LC3 and PARP. It is reported that various anti-cancer agents increase ROS production and induce the activation of autophagy-mediated cell death in malignant glioma [43, 44]. Western blot results demonstrated that C_{60} treatment increased Beclin 1 protein expression in U373 cell line (Figure 3). Moreover, as quantified accordingly western blot results, while the cells treated with 2 µM markedly upregulated the levels of Beclin1 compared to the control group, treatment with 0.5 or 1.0 µM C_{60} did not reach statistical significance. Furthermore, LC3-II significantly increased in U373 cells subjected to 1.0 µM C_{60} treatment compared to at low dose and the untreated cells. To further confirm the roles of C_{60} treatment on U373 cells, western blotting analysis was carried out after treating with C_{60} treatment for 24 h. PARP protein expression was significantly upregulated in the high dose treatment group when compared to the control group. Nevertheless, treatment with 0.5 µM C_{60} did not reach statistical significance.

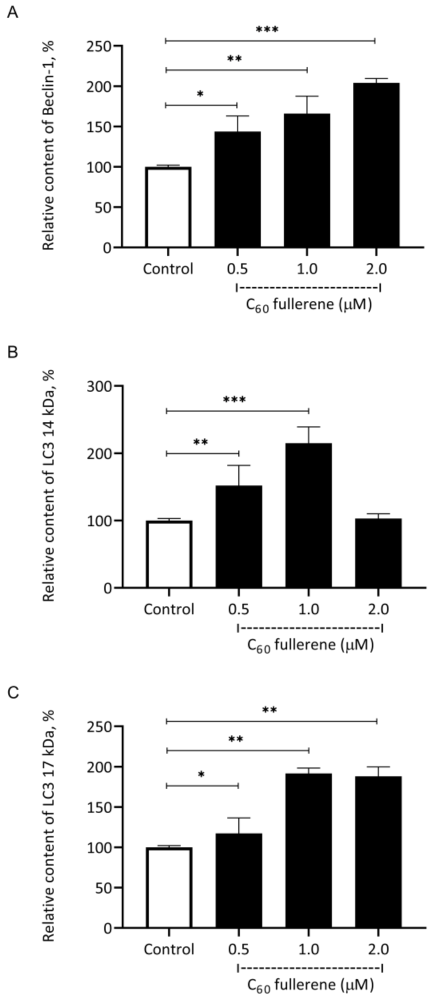

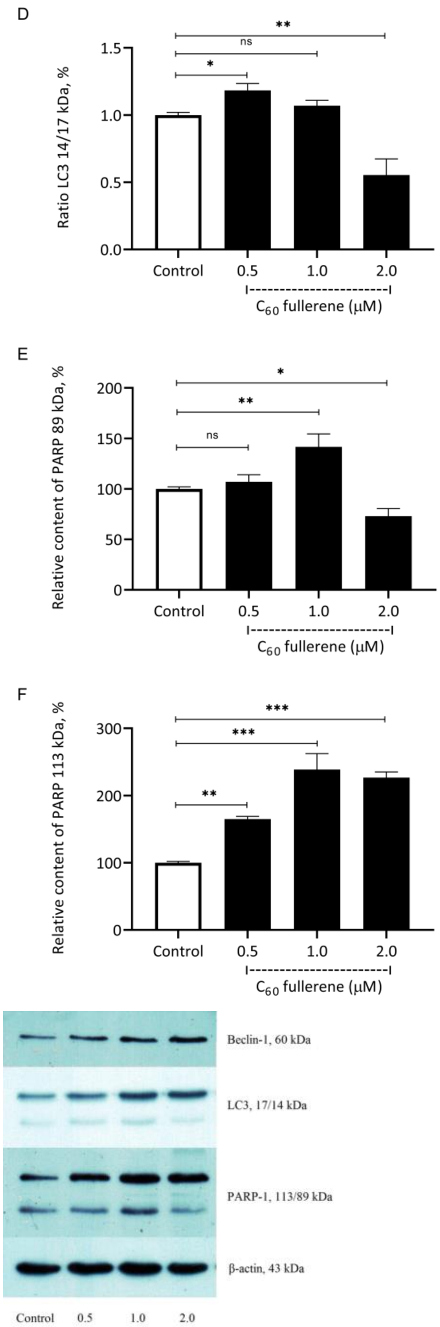

Figure 3. Effects of C_{60} fullerene on Beclin1, LC3 and PARP expression in U373 cell line.Western blot results of Beclin1 (A), LC3-14kDa (B), LC3-17kDa (C), LC3-14/17kDa (D), PARP-89kDa (E), PARP-113kDa (F) proteins in U373 cells treated with C_{60}. The results were normalized using protein expression rates of β-actin. Compared with the control group, *: P<0.05, **: P<0.01, *** P<0.001.

3.4.Effects of C_{60} Fullerene on GFAP

To further establish the effect of C_{60} fullerenes on U373 glioma cell reactivity, GFAP expression was investigated by immunocytochemistry as a marker of glial reactivity. As shown by immunocytochemistry imaging, C_{60} fullerene suppressed GFAP expression in U373 cells as compared to control non-treated cells (Figure 4.). The obtained result means that C_{60} fullerene is able to modulate important determinants of tumor invasiveness such as cell migration and adhesion by modulating expression of intermediate filament protein of astrocytic cytoskeleton, and thus may diminish tumor infiltration.

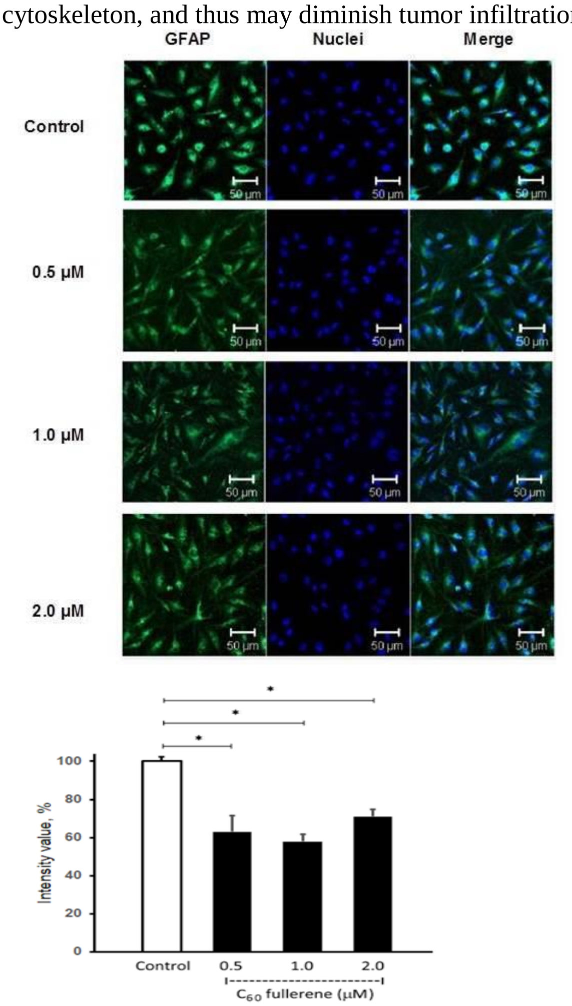

Figure 4. Immunocytochemical staining of GFAP in C_{60} fullerene treated U373 cells. Concentrations of C_{60} fullerene, μM, are shown on the diagrams. *P < 0.05 vs. the control group.

4. DISCUSSION AND CONCLUSION

Biomedical potential to apply C_{60} fullerene as an anticancer tool is based on its capability to initiate the switching programmed cell death to apoptosis, necrosis or both of them. Well studied manner to initiate apoptosis is ROS-dependent pathways which is reported as the most prospective to suppress tumor growth [12]. Contrary, the effects of C_{60} fullerene via modulating programmed cell death remain unknown. However, research data on the impact of hydrated water-soluble C_{60} fullerene in GBM cells are absent in literature. There is extremely limited number of the reports in regards with pristine water-soluble C_{60} fullerene types and water suspensions in glioma cells where cytotoxic effect was detected in a wide range of concentrations [5, 38]. The results obtained in our study showed that U373 cells exposure to $HyC_{60}Fn$ exerts cytotoxity as well as the modulation of autophagy flux in a dose dependent manner. Thus, our results are consistent with literature data presented in respect to various water soluble C_{60} fullerene types [5, 7, 38] On other hand, cytotoxic effect of water soluble $HyC_{60}Fn$ in glioblastoma cells is presented for the first time. It deserves to be mentioned that meaningful cytotoxicity of C_{60} is observed in a large concentrations range, but as a rule these doses most high then 1 μM [38, 45, 46]. The measurement of autophagy markers Beclin1 and LC3 in our study have shown a significant increase in both of them. Especially, high $HyC_{60}Fn$ doses 1-2 μM have induced significant up-regulation in Beclin1 and LC3 expression (Figure 2 A and B). Thus, $HyC_{60}Fn$ could regulate autophagy flux in U373GM cells. There was demonstrated that mild autophagy enhancement can maintain cell viability in a course of starvation or exposure to other detrimental factors [47]. Despite of this phenomenon, severe autophagy flux can induce cell death via total cleaving of macromolecules [48]. Data presented in our study indicate that $HyC_{60}Fn$ doses 1- 2 μM can initiate extensive autophagy flux in U373GM cells and limit cell viabilty at least partialy by this type of programmed cell death. Beclin1 cannot inhibit anti-apoptotic function of Bcl-2, when it absorbed on the mitochondrial membrane surface. Despite of this fact, anti-apoptotic Bcl-2 proteins Bcl-2 or Bcl-XL that forms the complex with Beclin1 can reduce its pro-autophagy activity [49]. Recently, there was demonstrated that C_{60} fullerene can modulate autophagy flux via Bcl-2/Beclin-1 reciprocal expression in rat brain [17]. Thus, obtained results are adjust with the effect of pristine C60 fullerene on Bcl-2/Beclin-1 pathway in glial tumor cells. Taking into account that malignation is tightly linked to impaired mitochondrial function and the state of mitochondrial membrane affect on interaction of autophagy-regulating proteins, including Bcl-2 and Beclin1, observed in study C60 fullerene effect on glioblastoma suppression could be mediated with modulation of mitochondrial functions [50, 51]. Harhaji and coauthors demonstrated the role of autophagy in C_{60} fullerene-dependent cell death where inhibition of acidification of intracellular vesicles initiated cell death in glioma exposed to relatively low C_{60} fullerene dose [38]. Actualy, the observed modulation of Beclin1 and LC3 expression by pristine C_{60} fullerene can reflect only one of multifaceted effects of tumor suppression in the present study. PARP overexpression can lead to cell death pathway called parthanatos [52]. The impact of PARP modulation in glioblastoma cells was reported in several studies [53, 54]. However, there are no data on the modulation of parthanatos flux with pristine fullerene nanoparticles. Our results on the up-regulation of PARP in U373GM cells provide evidence that $HyC_{60}Fn$ could up-regulate other PARP-dependent cell death pathway called parthanatos. Observed increase in both PARP expression and cleaved PARP fragments let us to presume $HyC_{60}Fn$-induced parthanatos in gliobastoma cells. To the best of our knowledge, the data on C_{60}-induced parthanatos in gliobastoma cells are presented firstly. During the last decades, several methods were proposed to produce water soluble C_{60} nanoparticles based on solvent-exchange manner, water suspension and chemical functionalization with various groups including hydroxilation and carbonylation [5, 55]. However, prevaling number of these methods generate extremely various nanoparticles with different biology activity without any principle standards. Similar great vary of cytoprotective and cyto-toxic effects C_{60} nanomaterials are presented in literature. Therefore, the distinct effect of C_{60} fullerene solubilized with various manner could be explaned individual features of carbon cage surface. The state of the fullerene surface is a critic for exhibiting both cytoprotective and antitumor effects. Several water-soluble C_{60} fullerene derivatives were demonstrated as the prospective agents to inhibit glioblastoma in vitro [5]. On other hand, various cancer cell types have a unique complex of mutations and are susceptible to specific manner of anti-cancer strategy. Therefore, multiple features of various water soluble C_{60} fullerene types are requested to be identified in brain tumor cells. In respect with neural tissue cells, the effect of C_{60} fullerene has been described in several reports including neuroprotection against amyloid peptide [56], hypoxic insult [57] and glutamate toxicity via modulating cytoskeleton-associated proteins [57]. Hydrated C_{60} fullerene was detected to be capable of reducing serum homocysteine level and TRPM2 gene expression in vivo [23]. Enhancing effect of the water-soluble C_{60} fullerene derivatives has been shown on the neurite outgrowth of NGF-stimulated cultured PC12 cells in vitro [58]. Dugan and coauthors reported that polyhydroxylated C_{60} derivatives possess the potential to reduce excitotoxic and apoptotic injuries in cortical cell cultures due to its anti-oxidant features [55]. Thus, pristine C_{60} fullerene is capable of modulating various pathways in neural tissue cells that could recognized as an argument to apply it as anti-glioma agent. There are numerous contraversial reports on anti-oxidant and/or pro-oxidant activity of pristine C_{60} fullerene in both normal and malignated cells [5, 7]. However, normal cells in common have much higher resistance to pro-oxidant C_{60} fullerene effect than their cancerous counterparts [10, 38, 59]. Furthermore, pristine fullerene is recognized as nontoxic compound up to 2 mg/kg [60] The most important property of pristine of the C_{60} fullerene is low toxicity in respect with normal cells. The absent of abnormalities in the rats were observed in both acute and chronic exposure to 2,000 mg/kg and 1,000 mg/kg, respectively [60, 61]. Besides, no histopathological changes were detected in liver, kidney and spleen in the end of 28 days administration period as well as the accumulation of fullerene C_{60} were not detected in all of aforementioned organs [61]. Contrary, there are several reports on neurotoxicity and cytotoxicity of various C_{60} fullerene types. For instance, pristine unfunctionalized C60 fullerene in high concentration (100 μg/mL) have been detected to be able to induce cytotoxicity in both undifferentiated and differentiated by growth factor exposure PC-12 cells [8]. Comparative analyses of cytotoxicity among water-soluble fullerene species, nano-C_{60}, a fullerene aggregate, have showed that C_{60} colloidal suspension is potent to induce various cellular damages [62]. However, there were no detected DNA and mitochondrial disturbances in fibroblasts, liver carcinoma cells (HepG2), and astrocytes in aforementioned study. Anti-cancer effect of C_{60} fullerene water suspension was demonstrated in gioma cells where fullerene suppressed tumor cell proliferation [38]. Astrocytes transition into reactive state is a process that is characterized by morphological and biochemical changes by loosing the original properties of cells and increased vimentin expression as one of the intermediate filament protein [63]. The results of ICC assay obtained in our study demonsrated the mild suppression of GFAP staining in glioma cells exposed to all applied doses of C_{60} fullerene. Taking into account the present results and the fact that GFAP is involved in astrocyte reactivity, C_{60} fullerene exposure could inhibit the rearrangement of glioma cytoskeleton via reprograming parthanatos and autophagy fluxes. Firstly, hydrated C_{60} fullerene has been shown to markedly ameliorate astroglial reactivity and modulate GFAP expression in vivo in brain tissue of rats chronically exposed to ethyl alcohol [64]. The down-regulation of GFAP caused by C_{60} treatment is agreed with early explored effect of pristine fullerene on glial intermediate filaments in brain and retina of rats with experimental diabetes mellitus [65, 66]. The current study provides the first evidence that the C_{60} fullerene can regulate expression of intermediate filament protein of the astrocytic cytoskeleton that is accompanied by enhanced parthantos and up-regulation in Beclin1 and LC3 autophagic markers in the glioma U373 cells. Cell migration activity plays a key role in the invasion and metastasis of GBM. We used cell migration/wound healing test to determine the effect of C_{60} fullerene on GBM cells migration activity. The present results (Fig. 2) demonstrated that C_{60} fullerene doses 1 and 2 µM inhibited migration capability of GBM during 60 h-period of observation. Obtained data indicate that these doses of hydrated C_{60} fullerene can suppress GBM migration through massive programmed cell death and reactivity of GBM cells. The various cellular disturbances were observed glioma cells exposed to high dose (≥1 µg/ml) and lower concentration (0.25 µg/ml) including stimulation of extracellular signalregulated kinase (ERK), growth of acidified intracytoplasmic vesicles indicative of autophagy and ROS-mediated necrotic cell damage. Furthermore, the exposure to high dose predominantly induced cell death by necroic pathway. On the other hand, the low dose of C_{60} fullerene water suspension had no effect on glioma necrosis, but this low C_{60} concetration could provoke the increment in cancer cells accumulation in G2/M phase that is an index of the cell cycle arrest. The authors showed that cytostatic effect of low-dose C_{60} was only less significant in primary astrocytes then in transformed glial cell, but it has no absent [38]. Distinct cytotoxic mechanisms were observed in respect with anticancer effect of pristine C_{60} fullerene and water-soluble polyhydroxylated fullerene. Despite necrotic effect of pristine C_{60} nanocrystals, hydroxylated fullerene C_{60} may induce various apoptotic events, including DNA fragmentation, ROS-independent cell death with characteristics of apoptosis and loss of the specific shape of cellular membrane [6]. Therefore, C_{60} nanoparticles exhibit extremely various bioactivity depending on the dose, the manners for solubilization and the rate of hydratation of C_{60} nanoparticles, which are critic for cytotoxic and cytoprotective features of C_{60} fullerene and its derivates. Correlation between autophagy flux and parthanatos observed in our study uncovers the part of antiglioma effect of pristine hydrated C_{60} fullerene. Taking into account that hydrated fullerene is able to interact with proteins [67], we can presume hypotetic mechanism in which direct effect of C_{60} on cell death machinery could be involved, at least partialy, in the modulation of autophagy and parthanatos. Presented results demonstrate dose-dependent cytotoxicity of water-soluble HyC_{60}Fn in U373GM cells. Furthermore, the doses of 1.0 and 2.0 µM HyC_{60}Fn could initiate anti-tumor effect via the combination of severe autophagy flux and parthanatos in glioblastoma cells. Therefore, pristine hydrated C_{60} fullerene displays potent anti-cancer features and further study is required.

Acknowledgement
This research was funded by the Scientific Research Projects Coordination Unit of Bingol University, grant number BAP-5-317-2015 and BAP-FEF.2016.00.010.

REFERENCES

[1] Sanai N, Polley MY, McDermott MW, Parsa AT, Berger MS. An extent of resection threshold for newly diagnosed glioblastomas: Clinical article. J Neurosurg. 2011 Jul;115(1):3–8.
[2] Louis DN, Perry A, Reifenberger G, von Deimling A, Figarella-Branger D, Cavenee WK, et al. The 2016 World Health Organization Classification of Tumors of the Central Nervous System: a summary. Vol. 131, Acta Neuropathologica. Springer Verlag; 2016. p. 803–20.
[3] Baldrighi M, Trusel M, Tonini R, Giordani S. Carbon nanomaterials interfacing with neurons: An in vivo perspective. Vol. 10, Frontiers in Neuroscience. Frontiers Media S.A.; 2016. p. 1–27.
[4] Song M, Yuan S, Yin J, Wang X, Meng Z, Wang H, et al. Size-dependent toxicity of nano-C60 aggregates: More sensitive indication by apoptosis-related bax translocation in cultured human cells. Environ Sci Technol [Internet]. 2012 Mar 20 [cited 2020 Jul 21];46(6):3457–64.
[5] Hsieh FY, Zhilenkov A V., Voronov II, Khakina EA, Mischenko D V., Troshin PA, et al. Water-Soluble Fullerene Derivatives as Brain Medicine: Surface Chemistry Determines if They Are Neuroprotective and Antitumor. ACS Appl Mater Interfaces. 2017;9(13):11482–92.
[6] Isakovic A, Markovic Z, Todorovic-Marcovic B, Nikolic N, Vranjes-Djuric S, Mirkovic M, et al. Distinct cytotoxic mechanisms of pristine versus hydroxylated fullerene. Toxicol Sci. 2006;91(1):173–83.
[7] Jou MJ. Pathophysiological and pharmacological implications of mitochondria-targeted reactive oxygen species generation in astrocytes. Adv Drug Deliv Rev; 2008 p. 1512–26.
[8] Larner SF, Wang J, Goodman J, O'Donoghue Altman MB, Xin M, Wang KKW. In vitro neurotoxicity resulting from exposure of cultured neural cells to several types of nanoparticles. Journal of Cell Death. Libertas Academica Ltd.; 2017
[9] Biby TE, Prajitha N, Ashtami J, Sakthikumar D, Maekawa T, Mohanan P V. Toxicity of dextran stabilized fullerene C60 against C6 Glial cells. Brain Res Bull. 2020 Feb 1;155:191–201.
[10] Johnston HJ, Hutchison GR, Christensen FM, Aschberger K, Stone V. The Biological Mechanisms and Physicochemical Characteristics Responsible for Driving Fullerene Toxicity. Toxicol Sci. 2010;9;114(2):162–82.

[11] Trpkovic A, Todorovic-Markovic B, Trajkovic V. Toxicity of pristine versus functionalized fullerenes: Mechanisms of cell damage and the role of oxidative stress. Archives of Toxicology. Arch Toxicol; 2012 p. 1809–27.

[12] Markovic Z, Trajkovic V. Biomedical potential of the reactive oxygen species generation and quenching by fullerenes (C60). Biomaterials. Biomaterials; 2008 p. 3561–73.

[13] Li J, Tian M, Cui L, Dwyer J, Fullwood NJ, Shen H, et al. Low-dose carbon-based nanoparticle-induced effects in A549 lung cells determined by biospectroscopy are associated with increases in genomic methylation. Sci Rep. 2016 2;6(1):1–11.

[14] Sosnowska M, Kutwin M, Jaworski S, Strojny B, Wierzbicki M, Szczepaniak J, et al. <p>Mechano-signalling, induced by fullerene C60 nanofilms, arrests the cell cycle in the G2/M phase and decreases proliferation of liver cancer cells</p>. Int J Nanomedicine. 2019, 6 14:6197–215.

[15] Wierzbicki M, Sawosz E, Grodzik M, Prasek M, Jaworski S, Chwalibog A. Comparison of anti-angiogenic properties of pristine carbon nanoparticles. Nanoscale Res Lett. 2013;8(1):1–8.

[16] Ye S, Chen M, Jiang Y, Chen M, Zhou T, Wang Y, et al. Polyhydroxylated fullerene attenuates oxidative stress-induced apoptosis via a fortifying Nrf2-regulated cellular antioxidant defence system. Int J Nanomedicine. 2014 29;9(1):2073–87.

[17] Demir E, Nedzvetsky VS, Ağca CA, Kirici M. Pristine C60 Fullerene Nanoparticles Ameliorate Hyperglycemia-Induced Disturbances via Modulation of Apoptosis and Autophagy Flux. Neurochem Res. 2020;1;45(10):2385–97.

[18] Kumari S, Badana AK, Murali Mohan G, Shailender G, Malla RR. Reactive Oxygen Species: A Key Constituent in Cancer Survival. Biomarker Insights. SAGE Publications Ltd; 2018.

[19] Yang H, Villani RM, Wang H, Simpson MJ, Roberts MS, Tang M, et al. The role of cellular reactive oxygen species in cancer chemotherapy. Journal of Experimental and Clinical Cancer Research. BioMed Central Ltd.; 2018 p. 266.

[20] Mijatović S, Savić-Radojević A, Plješa-Ercegovac M, Simić T, Nicoletti F, Maksimović-Ivanić D. The Double-Faced Role of Nitric Oxide and Reactive Oxygen Species in Solid Tumors. Antioxidants. 2020; 30;9(5):374.

[21] Moloney JN, Cotter TG. ROS signalling in the biology of cancer. Seminars in Cell and Developmental Biology. Elsevier Ltd; 2018. p. 50–64.

[22] Galadari S, Rahman A, Pallichankandy S, Thayyullathil F. Reactive oxygen species and cancer paradox: To promote or to suppress? Free Radical Biology and Medicine. Elsevier Inc.; 2017. p. 144–64.

[23] Etem EO, Bal R, Akağaç AE, Kuloglu T, Tuzcu M, Andrievsky G V., et al. The effects of hydrated C(60) fullerene on gene expression profile of TRPM2 and TRPM7 in hyperhomocysteinemic mice. J Recept Signal Transduct. 2014;34(4):317–24.

[24] Eisele G, Weller M. Targeting apoptosis pathways in glioblastoma [Internet]. Vol. 332, Cancer Letters. Elsevier Ireland Ltd; 2013. p. 335–45.

[25] Wong RSY. Apoptosis in cancer: From pathogenesis to treatment [Internet]. Vol. 30, Journal of Experimental and Clinical Cancer Research. BioMed Central; 2011. p. 87.

[26] Kaza N, Kohli L, Roth KA. Autophagy in brain tumors: A new target for therapeutic intervention. In: Brain Pathology. 2012. p. 89–98.

[27] Yang K, Niu L, Bai Y, Le W. Glioblastoma: Targeting the autophagy in tumorigenesis. Vol. 153, Brain Research Bulletin. Elsevier Inc.; 2019. p. 334–40.

[28] Levine B, Kroemer G. Autophagy in the Pathogenesis of Disease. Vol. 132, Cell. 2008. p. 27–42.

[29] Feng F, Zhang M, Yang C, Heng X, Wu X. The dual roles of autophagy in gliomagenesis and clinical therapy strategies based on autophagic regulation mechanisms. Biomedicine and Pharmacotherapy. 2019.

[30] Mizushima N, Levine B. Autophagy in mammalian development and differentiation. Vol. 12, Nature Cell Biology. Nature Publishing Group; 2010. p. 823–30.

[31] Wang F, Jin C, Liang H, Tang Y, Zhang H, Yang Y. Effects of fullerene C60 nanoparticles on A549 cells. Environ Toxicol Pharmacol. 2014;1;37(2):656–61.

[32] Hu Z, Guan W, Wang W, Zhu Z, Wang Y. Folacin C60 derivative exerts a protective activity against oxidative stress-induced apoptosis in rat pheochromocytoma cells. Bioorganic Med Chem Lett. 2010;15;20(14):4159–62.

[33] Zhou YY, Li Y, Jiang WQ, Zhou LF. MAPK/JNK signalling: A potential autophagy regulation pathway. Biosci Rep. 2015;35(3):1–10.

[34] Lee CM, Huang ST, Huang SH, Lin HW, Tsai HP, Wu JY, et al. C60 fullerene-pentoxifylline dyad nanoparticles enhance autophagy to avoid cytotoxic effects caused by the β-amyloid peptide. Nanomedicine Nanotechnology, Biol Med. 2011;1;7(1):107–14.

[35] Hartman ML. Non-Apoptotic Cell Death Signaling Pathways in Melanoma. Int J Mol Sci. 2020; 23;21(8):2980.

[36] Fatokun A. Parthanatos: Poly adp ribose polymerase (parp)-mediated cell death. In: Apoptosis and Beyond: The Many Ways Cells Die. 2018. p. 535–58.

[37] Liu SY, Song JY, Fan B, Wang Y, Pan YR, Che L, et al. Resveratrol protects photoreceptors by blocking caspase- and PARP-dependent cell death pathways. Free Radic Biol Med. 2018 Dec 1;129:569–81.

[38] Harhaji L, Isakovic A, Raicevic N, Markovic Z, Todorovic-Markovic B, Nikolic N, et al. Multiple mechanisms underlying the anticancer action of nanocrystalline fullerene. Eur J Pharmacol. 2007 Jul 30;568(1–3):89–98.

[39] Pan Y, Jing R, Pitre A, Williams BJ, Skalli O. Intermediate filament protein synemin contributes to

the migratory properties of astrocytoma cells by influencing the dynamics of the actin cytoskeleton. FASEB J. 2008;22(9):3196–206.

[40] Moeton M, Stassen OMJA, Sluijs JA, van der Meer VWN, Kluivers LJ, van Hoorn H, et al. GFAP isoforms control intermediate filament network dynamics, cell morphology, and focal adhesions. Cell Mol Life Sci. 2016;3; 73(21):4101–20.

[41] Agca CA, Tykhomyrov AA, Baydas G, Nedzvetsky VS. Effects of a Propolis Extract on the Viability of and Levels of Cytoskeletal and Regulatory Proteins in Rat Brain Astrocytes: an In Vitro Study. Neurophysiology. 2017 Aug 1;49(4):261–71.

[42] Tykhomyrov A, Nedzvetsky V, Shemet S, Ağca CA. Production and characterization of polyclonal antibodies to human recombinant domain B-free antihemophilic factor VIII. Turkish J Biol. 2017;41(6):857–67.

[43] Thayyullathil F, Rahman A, Pallichankandy S, Patel M, Galadari S. ROS-dependent prostate apoptosis response-4 (Par-4) up-regulation and ceramide generation are the prime signaling events associated with curcumin-induced autophagic cell death in human malignant glioma. FEBS Open Bio. 2014;1;4:763–76.

[44] Gong K, Chen C, Zhan Y, Chen Y, Huang Z, Li W. Autophagy-related gene 7 (ATG7) and reactive oxygen species/extracellular signal-regulated kinase regulate tetrandrine-induced autophagy in human hepatocellular carcinoma. J Biol Chem. 2012 Oct 12;287(42):35576–88.

[45] Dal Forno GO, Kist LW, De Azevedo MB, Fritsch RS, Pereira TCB, Britto RS, et al. Intraperitoneal exposure to nano/microparticles of fullerene (C 60) increases acetylcholinesterase activity and lipid peroxidation in adult zebrafish (danio rerio) Brain. Biomed Res Int. 2013.

[46] Peng Y, Yang D, Lu W, Hu X, Hong H, Cai T. Positron emission tomography (PET) guided glioblastoma targeting by a fullerene-based nanoplatform with fast renal clearance. Acta Biomater. 2017; 1; 61:193–203.

[47] Butler D, Bahr BA. Oxidative stress and lysosomes: CNS-related consequences and implications for lysosomal enhancement strategies and induction of autophagy. Antioxidants and Redox Signaling. Antioxid Redox Signal; 2006 p. 185–96.

[48] Gonzalez CD, Lee MS, Marchetti P, Pietropaolo M, Towns R, Vaccaro MI, et al. The emerging role of autophagy in the pathophysiology of diabetes mellitus. Autophagy. Taylor and Francis Inc.; 2011. p. 2–11.

[49] Maiuri MC, Le Toumelin G, Criollo A, Rain JC, Gautier F, Juin P, et al. Functional and physical interaction between Bcl-XL and a BH3-like domain in Beclin-1. EMBO J. 2007 ;16;26(10):2527–39.

[50] Seyfried TN, Shelton LM. Cancer as a metabolic disease [Internet]. Vol. 7, Nutrition and Metabolism. 2010. p. 1–22.

[51] Decuypere J-P, Parys JB, Bultynck G. Regulation of the Autophagic Bcl-2/Beclin 1 Interaction. Cells. 2012; 6;1(3):284–312.

[52] Fatokun AA, Dawson VL, Dawson TM. Parthanatos: Mitochondrial-linked mechanisms and therapeutic opportunities [Internet]. Vol. 171, British Journal of Pharmacology. Nature Publishing Group; 2014; p. 2000–16.

[53] Jannetti SA, Carlucci G, Carney B, Kossatz S, Shenker L, Carter LM, et al. PARP-1-targeted radiotherapy in mouse models of glioblastoma. J Nucl Med. 2018;1;59(8):1225–33.

[54] Majuelos-Melguizo J, Rodríguez MI, López-Jiménez L, Rodríguez-Vargas JM, Martín-Consuegra JMM, Serrano-Sáenz S, et al. PARP targeting counteracts gliomagenesis through induction of mitotic catastrophe and aggravation of deficiency in homologous recombination in PTEN-mutant glioma. Oncotarget. 2015;6(7):4790–803.

[55] Dugan LL, Gabrielsen JK, Yu SP, Lin TS, Choi DW. Buckminsterfullerenol free radical scavengers reduce excitotoxic and apoptotic death of cultured cortical neurons. Neurobiol Dis. 1996;3(2):129–35.

[56] Makarova EG, Gordon RY, Podolski IY. Fullerene C 60 prevents neurotoxicity induced by intrahippocampal microinjection of amyloid-β peptide. In: Journal of Nanoscience and Nanotechnology. J Nanosci Nanotechnol; 2012. p. 119–26.

[57] Giust D, Da Ros T, Martín M, Albasanz JL. [C60]Fullerene derivative modulates adenosine and metabotropic glutamate receptors gene expression: A possible protective effect against hypoxia. J Nanobiotechnology. 2014 14;12(1):27.

[58] Tsumoto H, Kawahara S, Fujisawa Y, Suzuki T, Nakagawa H, Kohda K, et al. Syntheses of water-soluble [60]fullerene derivatives and their enhancing effect on neurite outgrowth in NGF-treated PC12 cells. Bioorganic Med Chem Lett. 2010;15;20(6):1948–52.

[59] Kraemer ÂB, Parfitt GM, Acosta D da S, Bruch GE, Cordeiro MF, Marins LF, et al. Fullerene (C60) particle size implications in neurotoxicity following infusion into the hippocampi of Wistar rats. Toxicol Appl Pharmacol. 2018; 1;338:197–203.

[60] Mori T, Takada H, Ito S, Matsubayashi K, Miwa N, Sawaguchi T. Preclinical studies on safety of fullerene upon acute oral administration and evaluation for no mutagenesis. Toxicology. 2006; 1;225(1):48–54.

[61] Takahashi M, Kato H, Doi Y, Hagiwara A, Hirata-Koizumi M, Ono A, et al. Sub-acute oral toxicity study with fullerene C60 in rats. J Toxicol Sci. 2012;37(2):353–61.

[62] Sayes CM, Gobin AM, Ausman KD, Mendez J, West JL, Colvin VL. Nano-C60 cytotoxicity is due to lipid peroxidation. Biomaterials. 2005;26(36):7587–95.

[63] Lagos-Cabré R, Alvarez A, Kong M, Burgos-Bravo F, Cárdenas A, Rojas-Mancilla E, et al. αVβ3 Integrin regulates astrocyte reactivity. J Neuroinflammation. 2017;14(1).

[64] Tykhomyrov AA, Nedzvetsky VS, Klochkov VK, Andrievsky G V. Nanostructures of hydrated C60 fullerene (C60HyFn) protect rat brain against alcohol impact and attenuate behavioral

impairments of alcoholized animals. Toxicology. 2008 Apr 18;246(2–3):158–65.
[65] Nedzvetsky V, Andrievsky G. Differences in Antioxidant/Protective Efficacy of Hydrated C60 Fullerene Nanostructures in Liver and Brain of Rats with Streptozotocin-Induced Diabetes. J Diabetes Metab. 2012;03(08).
[66] Nedzvetskii VS, Pryshchepa I V., Tykhomyrov AA, Baydas G. Inhibition of Reactive Gliosis in the Retina of Rats with Streptozotocin-Induced Diabetes under the Action of Hydrated C60 Fullerene. Neurophysiology. 2016 1;48(2):130–40.
[67] [Rozhkov SP, Goryunov AS, Sukhanova GA, Borisova AG, Rozhkova NN, Andrievsky G V. Protein interaction with hydrated C60 fullerene in aqueous solutions. Biochem Biophys Res Commun. 2003 4;303(2):562–6.

Cilt 11, Sayı 4, Sayfa 98-103, 2022 Volume 11, Issue 4, Page 98-103, 2022

Araştırma Makalesi https://doi.org/10.46810/tdfd.109743 Research Article

Türk Doğa ve Fen Dergisi
Turkish Journal of Nature and Science
www.dergipark.gov.tr/tdfd

siRNA Mediated Gene Silencing in the Pancreatic Cancer Capan-1 Cell Line

Fatma Azize BUDAK YILDIRAN[1*]

[1] Kırıkkale University Vocational High School of Health Care Services, Department of Medical Services and Techniques, Kırıkkale, Türkiye
F. Azize BUDAK YILDIRAN ORCID No: 0000-0001-7031-6834

**Corresponding author: azizebudak@kku.edu.tr*

(Received: 02.04.2022, Accepted: 05.12.2022, Online Publication: 28.12.2022)

Keywords
Gene therapy, c-Myc, siRNA, Capan-1, Real-Time PCR, Pancreatic cancer

Abstract: İngilizce Today, cancer is the second leading among the causes of death. Especially pancreatic cancer which is an aggressive type progressing without giving too many symptoms. In addition, non-response to traditional treatments cause a low survival rate in this type of cancer. Therefore, many target-oriented studies are carried out to develop alternative diagnosis and treatment methods such as gene therapy method. Small non-coding RNA (siRNA) are used in studies as a therapeutic agent by its delivery to the target gene by various mechanisms.
This study aimed to silence the c-Myc gene using gold nanoparticle (AuNP)-siRNA in the Capan-1 cell line. We performed Real-Time PCR analysis, WST-1 *assay* in the *cytotoxicity* analysis, Double Staining method and Agarose gel electrophoresis using gold nanoparticles (2X, 4X, 8X) and siRNA (25 nM) at concentrations determined in the Capan-1 cell line. The data obtained by Real Time PCR were evaluated as relative (Efficiency 2). $2^{\Delta Ct}$ values were calculated. The $2^{\Delta Ct}$ value was 0.352 for the control, and these values were found to be between 0.210-0.027 in AuNP / siRNA applications. Considering these values, it was observed that the gene expression decreased the most for 8XAuNP/siRNA.
The averages of the OD values (438 nm) read in the WST-1 analysis were calculated. These values were calculated as 0.180 for the control group, 0.194 for 2XAuNP/siRNA, 0.293 for 4XAuNP/siRNA, and 0.277 for 8XAuNP/siRNA.
The data obtained from the analysis suggested that the nanoparticle siRNA complex could be used effectively in silencing the target gene. Nevertheless, more knowledge is needed on this subject.

Pankreas Kanseri Capan-1 Hücre Hattında siRNA Aracılı Gen Susturulması

Anahtar Kelimeler
Gen terapi, c-Myc, siRNA, Capan-1, Real-Time PCR, Pancreas kanseri

Öz: Günümüzde kanser ölüm nedenleri arasında ikinci sırada yer almaktadır. Özellikle agresif bir tip olan Pankreas kanseri çok fazla belirti vermeden ilerlemektedir. Ayrıca geleneksel tedavilere yanıt alınamaması bu kanser türünde düşük sağkalım oranına neden olmaktadır. Bu nedenle gen tedavisi gibi hedef odaklı alternatif tanı ve tedavi yöntemleri geliştirmeye yönelik çalışmalar yapılmaktadır. Küçük kodlayıcı olmayan RNA (siRNA), çeşitli mekanizmalarla hedef gene ulaştırılmasıyla çalışmalarda terapötik ajan olarak kullanılmaktadır.
Küçük kodlayıcı olmayan RNA (siRNA), çeşitli mekanizmalarla hedef gene ulaştırılmasıyla çalışmalarda terapötik ajan olarak kullanılmaktadır.
Bu çalışmada; Capan-1 hücre hattında, altın nanopartikül (AuNP)- siRNA kullanılarak c-Myc geninin susturulması amaçlandı. Capan-1 hücre hattında belirlenen konsantrasyonlarda altın nanopartiküller (2X, 4X, 8X) ve siRNA (25 nM) kullanılarak Real-Time PCR analizi, sitotoksisite analizinde WST-1 testi, Double Staining yöntemi ve Agaroz jel elektroforezi gerçekleştirdik. Real-Time PCR ile elde edilen veriler göreceli olarak değerlendirildi (Verimlilik 2). $2\Delta Ct$ değerleri hesaplandı. Kontrol için $2\Delta Ct$ değeri 0,352 olup, AuNP/siRNA uygulamalarında bu değerler 0,210-0,027 arasında bulunmuştur. Bu değerlere bakıldığında gen ekspresyonunun en çok 8XAuNP/siRNA için azaldığı gözlendi. WST-1 analizinde OD değerlerinin (438 nm) ortalamaları

hesaplandı. Bu değerler kontrol grubu için 0,192, 2XAuNP/siRNA için 0,194, 4XAuNP/siRNA için 0,293 ve 8XAuNP/siRNA için 0,277 olarak hesaplandı.
Analizlerden elde edilen verilere göre; Nanopartikül siRNA kompleksinin hedef genin susturulmasında etkili bir şekilde kullanılabileceği düşünülmektedir. Ancak bu konuda daha fazla bilgi birikimine ihtiyaç vardır.

1. INTRODUCTION

Ana başlıklar büyük harf ile yazılmalıdır. Bu alandaki Cancer is among the most important causes of morbidity and mortality worldwide. According to GLOBOCAN, a subsidiary of the World Health Organization (WHO), 19.3 million new cases and 10 million deaths were detected in 2020. 233 thousand new cancer cases and 126 thousand cancer-related deaths were reported in 2020 in Turkey. The number of cancer-related deaths worldwide in 2020 reported that pancreatic cancer ranked seventh in the overall rating of the highest percentile. [1] Furthermore, this type of cancer is among the most aggressive. The five-year survival rate is less than 5%, which is due to its progress without symptoms, difficulty in early diagnosis, and traditional treatment methods being not as effective as desired. [2, 3]

Primarily the mutations that inhibit DNA repair mechanisms, mutations in tumor suppressor genes, disorders in RNA function and faults in the control mechanism of the cell cycle are effective in cancer formation. [4-6]

The MYC proto-oncogene is involved in the expression of genes normally involved in cell proliferation. In many types of cancer, it turns into an oncogene with the formation of multiple copies of the MYC gene due to faults in DNA replication. Since the increase in cell proliferation by transcriptional activation of MYC oncogene increases the malignant potential of tumor cells, it is considered to be effective in ovarian, breast, colon, pancreatic, stomach and uterine cancers. Buchholz et al. [7] reported that ectopic activation of NFATc1 and Ca2+/calcineurin signaling pathway is an important mechanism of oncogenic c-Myc activation in pancreatic cancer. [8, 9]

Apoptosis and necrosis mechanisms are vital in cancer. It is a common knowledge that cancer develops due to an increase in cell proliferation and a decrease in apoptosis. [10] Apoptosis is programmed cell death where the nucleus is affected, and changes begin at this stage; the nucleus shrinks, and the chromatin condenses. Necrosis, on the other hand, is characterized by disruption of cell integrity and leakage of its contents. [11, 12] One of the methods used to detect apoptotic and necrotic cells is the HO/PI staining method. It is a method that allows the observation and counting of viable, apoptotic and necrotic cells in a single preparation by staining cells with two fluorescent dyes (Hoechst 33258 and propidium iodide). While Hoechst 33258 stains the nuclei of all cells, propidium iodide cannot pass through the membrane and stains late apoptotic and necrotic cells with impaired membrane integrity. [13, 14]

Today, studies on new therapeutic methods have increased, especially due to the inefficacy of traditional ones. The most prominent among these new methods is the gene therapy method. Gene therapy can be performed by increasing or inhibiting the expression of defective genes responsible for the formation and development of the disease. [15] It has two types: germline and somatic gene therapies. The most crucial factor in gene therapy depends on the effective delivery and expression of the nucleic acid-based molecule to the target cell. However, when these molecules are administered, they attach to many biological barriers in the bloodstream. [16] In gene therapy, gene transfer systems have been developed for nucleic acids to cross barriers and modulate their expression in the target tissue. These systems, called gene transfer vectors, are recognized by the specific receptors of the cells in the target tissue and pass through the cell membrane and reach the nucleus and provide a therapeutic effect. [17, 18]

The gene silencing approach, which occurs at the transcription or translation stage, includes Antisense, RNA interference (RNAi), and aptamer and ribozyme technologies. RNA interference (RNAi) pathway is the pathway where RNA inhibition is achieved by microRNA (microRNA; miRNA) and small interfering RNA (small interfering RNA; siRNA). siRNA contains 20-24 nt long sequence. In the siRNA-mediated pathway, the double-stranded RNA molecule (dsRNA) released into the cytoplasm is cut by the Dicer enzyme, and double-stranded siRNA is formed. The guide sequence, which directs the RNAi mechanism with the base pairing of siRNA, is included in the structure of the RNA-induced silencing complex (RISC). The RISC complex binds to the target mRNA, causing it to be destroyed, resulting in the reduction of proteins and specific mRNA. Although RNA interference is a natural mechanism, the expression of endogenous genes can be suppressed by using siRNAs synthesized in vitro. Therefore, siRNA has a wide application in gene therapy. [19-22]

In gene therapy, carrier molecules called vectors are used to transport the gene to the targeted cell. These are classified into two categories as biological and physical/chemical vectors. The biological vectors are plasmid or viral ones. Physical/chemical vectors, which are non-viral, are transferred to the cell by physical or chemical means. Molecules such as lipid-DNA complex or nanoparticles can also be used. Of these, nanoparticles are colloidal particles ranging from 10-100 nm, which release the absorbed active substance in a controlled manner. These particles are advantageous as they are targeted by ligands, encapsulated and stored in a lyophilized form. [23, 24] Nanoparticles are prevalently preferred in the release of targeted drugs in medicine and biotechnology, such as biosensors, and in gene therapy, especially in the diagnosis and treatment of cancer.[25-27]

Gold nanoparticles (AuNP) are effective inorganic structures for gene therapy and drug delivery applications. Their biocompatibility, stability, physical size and low cytotoxicity are their most significant advantages, but their low DNA binding capacity reduces transfection efficiency. Gold nanoparticles can be visualized by techniques such as dark field microscopy and transmission electron microscopy, and their uptake into the cell can be observed. [28]

In this study, it was aimed to silence the c-Myc gene using gold nanoparticle (AuNP)-siRNA. Using gold nanoparticles-siRNA complex in the Capan-1 cell line. Real-Time PCR, Dual Staining and gel electrophoresis were performed for this aim. According to the data obtained from the analysis; it is thought that the nanoparticle siRNA complex can be used effectively in silencing the target gene. However, it is thought that effective results can be obtained with more knowledge on this subject.

2. MATERIAL AND METHOD

2.1. Cell Line, Chemicals and Devices Used

Human pancreatic cancer cell line Capan-1, RPMI-1640 medium (Roswell Park Memorial Institute-1640), Fetal Bovine Serum (FBS; Biological Industries), ethanol, PBS (Biological Industries) with Trypsin-EDTA Solution C) and trypan blue dye was used for analysis.

The siRNA (c-Myc) Human siRNA Oligo Duplex (Locus ID 4609) used for the target c-Myc gene was obtained from ABM. Polyethylene imine-coated gold nanoparticle, a polymeric nanoparticle, to provide controlled delivery of silencing siRNA to the target gene.

WST-1 analysis kit (Biovision), which is applied as a standard for cytotoxicity tests, Ribonuclease A (Serva), Hoechst 33342 (Serva), Propidium Iodide (Serva) in the preparation of the dual dye solution.

High Pure RNA Isolation Kit (Roche) for RNA isolation; Transcriptor High Fidelity cDNA Synthesis Kit (Roche) for cDNA synthesis from the obtained RNAs and LightCycler® 480 system (Roche) to investigate the expression of the c-Myc gene. Housekeeping GADPH and c-MYC R5'-CAACATCGATTTCTTCCTCATCTT-3', c-MYC F5'-TGAGGAGACACCGCCCAC-3' primers (Sybrgreen, Roche) in RT-PCR analysis; High Pure RNA Isolation Kit (Roche) for RNA isolation; Transcriptor High Fidelity cDNA Synthesis Kit (Roche) for cDNA synthesis from the obtained RNAs; LightCycler® 480 system (Roche) to investigate the expression of the c-Myc gene.

Cell culture study was performed in culture dishes and multi-well plates (Corning, USA) using 6-well plate, 48-well plate, 25 cm² cell culture flask, cryo tube 1 ml (BD), 15 ml centrifuge tube (Nunc), 0.2 µm filter (Sartorius), 96 e-plate (RTCA Resistor) plate 96, (Roche) disposable pipettes (2ml, 5ml, 10ml), micropipette (20µm-100µm-1000µm; Scaltec) and various glassware.

Laminar Flow Cabinet (ESCO class ll BSC Laminar Flow Cabinet, Labor Ildam, Turkey), refrigerated centrifuge (ROTINA 380R Hettich), inverted microscope (Leica DM6000B), vortex, Elisa plate reader (BIOTEK GEN5 Elisa Reader PowerWave XS2), carbon dioxide oven (Binder CB150) and LightCycler® 480 system (Roche, Germany) device used were.

2.2. Real Time PCR Assay and Cytotoxicity Analysis

Cell culture by culturing CAPAN-1 pancreatic cancer cells frozen in liquidnitrogen was prepared by culturing. c-Myc-siRNA at 25 nM in 2X, 4X and 8X concentrations from 50% polyethylene coated gold nanoparticle (AU-PEI) solution provided for use in the studies. The resulting solutions were sterilized by keeping them under UV light for 15 minutes. siRNA-Au nanoparticles were incubated at room temperature for 30 minutes for Capan-1 cell interaction; then performed WST-1 test for cytotoxicity analysis of the specified doses; and examined the effect of combined applications on cells.

In order to examine whether siRNA increases or maintains its single and double effects on cells by double staining an inverted microscope (Leica DM6000, Sweden) was used to morphologically determine which death pathway the cells chose; and evaluated the data obtained.

In the last part, RT-PCR was applied to demonstrate the expression level of the c-Myc gene suppressed by siRNA and performed mRNA isolation for different Au nanoparticle and siRNA applications. Then, we conducted cDNA synthesis from the isolated RNA. After applying different concentrations prepared with Au nanoparticle and siRNA to the cells, the expression levels of the c-Myc gene was analyzed with the LightCycler 480® instrument. In addition, PCR products were run on 1.7% agarose gel electrophoresis and determined band profiles by Gel Imaging.

3. RESULTS

3.1. Necrotic Index Results Obtained by Double Staining

We specified the irradiance obtained with the PI fluorescent dye used in the double staining method under fluorescent light (with FITC filter) at a 480-520 nm wavelength in Capan-1 necrotic cells of siRNA-nanoparticle applications. It was observed that the applied nanoparticle siRNA complex increased cell death in a necrotic pathway. Some of the obtained necrosis microscope images are given in Figure 1.

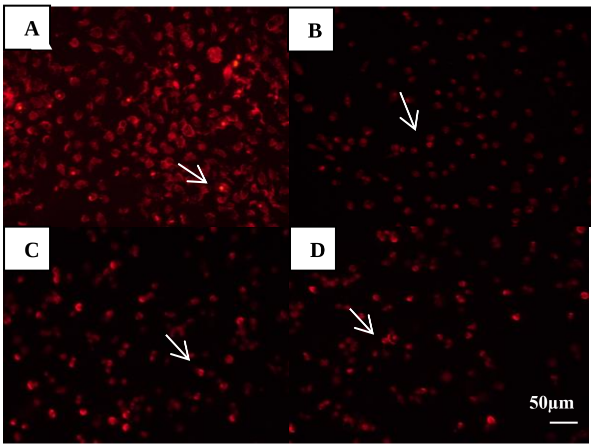

Figure 1. Photographs of necrotic cells using PI fluorescent dye (Leica DM6000, Sweden; 200X magnification) **A:** Control group **B:** Capan-1 cells interacting with 2X PEI-coated AuNP-siRNA **C:** Capan-1 cells interacting with 4X PEI-coated AuNP-siRNA **D:** Capan-1 cells interacting with 8X PEI coated AuNP-siRNA. (BAR= 50µm)

3.2. Real Time PCR (RT-PCR) Results and Agarose Gel Electrophoresis Evaluation

First of all, we performed mRNA isolation from Capan-1 cells, then cDNA synthesis from the isolated RNA samples. We oxidized these cDNA samples with the synthetic primer sequences synthesized for the c-Myc gene with the LightCycler480® analyzer. The data obtained by Real Time PCR were evaluated as relative. Furthermore, we ran PCR products in agarose gel electrophoresis (1.7%) and assessed band profiles. Figure 2 shows the obtained band profile.

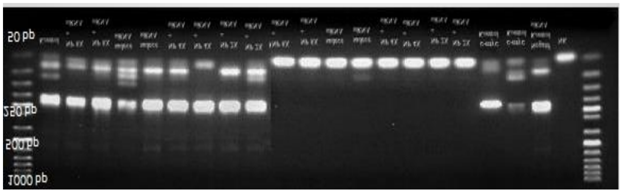

Figure 2. Agarose gel image of the products obtained in RT-PCR analysis (1.7%) (1 and 23 lined 50 bp DNA ladder)

In addition, in WST-1 analysis, it was observed that the viability values in % were higher than the control group. The data of OD values (438 nm) are given Table 3.1. The averages of the OD values (438 nm) read in the WST-1 analysis were calculated. These values were calculated as 0.192 for the control group, 0.194 for 2XAuNP/siRNA, 0.293 for 4XAuNP/siRNA, and 0.277 for 8XAuNP/siRNA. WST-1 analysis results are shown in Figure 3.

Table 1. OD values (438 nm) for WST-1 analysis

Groups/ OD values	1	2	3	Average
Control	0,24	0,162	0,175	0,192
siRNA	0,193	0,136	0,113	0,147
Np 2X	0,29	0,266	0,211	0,256
Np 4X	0,324	0,296	0,198	0,272
Np 8X	0,336	0,357	0,357	0,350
NP2X+siRNA	0,212	0,184	0,186	0,194
NP4X+siRNA	0,366	0,265	0,249	0,293
Np8X+siRNA	0,273	0,261	0,297	0,277

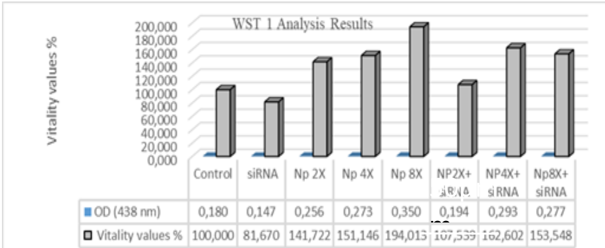

Figure 3. The results of WST 1 analysis

4. DISCUSSION AND CONCLUSION

Today, the importance of new therapeutic methods such as gene therapy is increasing. Gene therapy enables a targeted approach to the disease process. It is a mechanism frequently used in RNAi gene silencing studies. In such studies, it is important to effectively transport the gene to the target cell. Among the vectors used for this, gold nanoparticles have been demonstrated to be effective. According to the study, it is thought that the AuNp-siRNA complex is effective in silencing the target gene. Dykman et al. [29] reported that AuNPs enabled the efficient transport of siRNA, at organismal and cellular levels, and this facilitated the clinical application of siRNA treatments for genetic diseases. In another study, Daniels et al. [30] demonstrated that PEG-AuNP was effective in siRNA-mediated gene silencing in the MCF-7 cell line. Ku et al. [31] suggested that nanoparticles affected the transport of siRNA to the target tissue in cancer therapy, while we observed in this study that AuNPs did the same. Shaat et al. [32] used gold AuNPs (siRNA/bPEI/AuNP) modified with cationic polyethyleneimine (bPEI) to ensure efficient and reliable intracellular delivery of siRNA targeting the c-Myc gene in human hepatocellular carcinoma cells. They used comparative semi-quantitative and quantitative real-time PCR to quantify c-Myc gene expression, reported successful c-Myc protein translation in transfected HuH7 cells with pure siRNA and achieved siRNA/bPEI/AuNPs. Similar results were obtained in this study, necrosis was observed in Capan-1 cells interacting with siRNA and siRNA-PEI-AuNP, and a decrease in cell proliferation was detected.

While obtaining DNA band in the expected range for the GAPDH housekeeping gene used in the study, we observed no amplification for the targeted region for siRNA, AuNP-siRNA and NK.

In addition, it was observed that the vitality values in % in WST-1 analysis were higher than the control. It is considered that the reason for this may be due to the increase in values by affecting the absorbance of the residues remaining on the surface during the application of Au nanoparticle particles.
The fact that the viability values were higher in the WST-1 analysis compared to the control is thought to be due to the fact that the residues on the surface of AuNPs increase the values by affecting the absorbance.

This study evinced that AuNP-siRNA could be effectively used therapeutically to silence the target gene. As a consequence of the increase of similar studies, it is vital to develop target-oriented methods alternative to traditional ones which cause several adverse effects. However, further knowledge is needed for the effective application of such methods.

REFERENCES

[1] http://gco.iarc.fr/today (Date Accessed: 08.12.2021).
[2] Siegel RL, Miller KD, and Jemal A.. Cancer statistics, 2015. CA Cancer J. Clin. 2015; 65: 5–29. doi: 10.3322/caac.21254.
[3] Schottenfeld D. and Fraumeni JR. Cancer epidemiology and prevention: Oxford University Press; 2006.
[4] Zhou L, Sawaguchi S, Twining SS, Sugar J, Feder RS, Yue BY.. Expression of degradative enzymes and protease inhibitors in corneas with keratoconus. Invest Ophthalmol Vis Sci. 1998; 39 (7): 1117-24.
[5] Kenney MC, Chwa M, Lin B, Huang GH, Ljubimov AV, Brown DJ. Identification of cell types in human diseased corneas. Cornea. 2001; 20 (3): 309-16.
[6] Parkin BT, Smith VA, Easty DL. The control of matrix metalloproteinase-2 expression normal and keratoconic corneal keratocyte cultures. Eur J Ophthalmol. 2000; 10(4): 276-85.
[7] Buchholz M, SchatzMartin A, Wagner M, Michl P, Linhart T, Adler G, Gress TM, Ellenrieder V. Overexpression of c-myc in pancreatic cancer caused by ectopic activation of NFATc1 and the Ca2+/calcineurin signaling pathway, EMBO J. 2006; 25: 3714–3724.
[8] Buchholz M, SchatzMartin A, Wagner M, Michl P, Linhart T, Adler G, Gress TM, Ellenrieder V. Overexpression of c-myc in pancreatic cancer caused by ectopic activation of NFATc1 and the Ca2+/calcineurin signaling pathway, EMBO J. 2006; 25: 3714–3724.
[9] Miller DM, Thomas SD, Islam A, Muench D, Sedoris K. c-Myc and cancer metabolism. Clin. Cancer Res. 2012; 18: 5546–5553.
[10] Meng XW, Lee SH, Kaufmann SH. Apoptosis In The Treatment Of Cancer: A Promise Kept?. Curr Opin Cell Biol, 2006; 18: 668-76.
[11] Kim WJ, Shah S, Wilson SE. Differences in keratocyte apoptosis following transepithelial and laser - scrape photorefractive keratectomy in rabbits. J Refract Surg. 1998; 14(5):526-33.
[12] Wilson SE. Role of apoptosis in wound healing in the cornea. Cornea. 2000; 19:7-12.
[13] Grusch M, Fritzer-Szekeres M, Fuhrmann G, Rosenberger G, Luxbacher C, Elford HL, Smid K, Peters GJ, Szekeres T, Krupitza G. Activation of caspases and induction of apoptosis by novel ribonucleotide reductase inhibitors amidox and didox. Experimental Hematology. 2001; 29(5): 623-632.
[14] Fahrig R, Heinrich JC, Nickel B, Wilfert F, Leisser C, Krupitza G, Praha C, Sonntag D, Fiedler B, Scherthan H, Ernst H. Inhibition of induced chemoresistance by cotreatment with (E)-5-(2-bromovinyl)-2'- deoxyuridine (RP101). Cancer Research.2003; 63(18): 5745-5753.
[15] Gad SC. Handbook of pharmaceutical biotechnology. Vol. 2: John Wiley & Sons. 2007.
[16] Giacca M, Zacchigna S. Virus-mediated gene delivery for human gene therapy. Journal of Controlled Release. 2012; 161: 377–388.
[17] Gad, SC, Handbook of pharmaceutical biotechnology. John Wiley & Sons. 2007, Vol. 2.
[18] Daniel S. Advanced textbook on gene transfer, gene therapy and genetic pharmacology: principles, delivery and pharmacological and biomedical applications of nucleotide-based therapies. 2013, World Scientific: Vol. 1.
[19] Hosseinkhani H, Domb AJ. Biodegradable polymers in gene-silencing technology. Polym Adv Technol. 2019; 30:2647–2655.
[20] Hosseinkhani H, Chen YR, He W, Hong PD, Yu DS, Domb AJ. Engineering of magnetic DNA nanoparticles for tumor-targeted therapy. J Nanopart Res. 2013; 15(1):1345-1355.
[21] Gündoğdu R, Çelik V. RNA İnterferans (RNAi). Erciyes Üniversitesi Fen Bilimleri Enstitüsü Fen Bilimleri Dergisi, 2009; 25(1): 34-47.
[22] Aagaard L, Rossi JJ. RNAi therapeutics: Principles, prospects and challenges. Adv Drug Deliv Rev. 2007; 59: 75–86.
[23] Attar A. Gen terapisi yöntemleri: fiziksel ve kimyasal metotlar. Turkish Bulletin of Hygiene & Experimental Biology/Türk Hijyen ve Deneysel Biyoloji. 2017; 74(1):103-112.
[24] Sayıner Ö, Çomoğlu T. Nanotaşıyıcı sistemlerde hedeflendirme. Ankara Üniversitesi Eczacılık Fakültesi Dergisi. 2016; 40(3): 62-79.
[25] Adijanto J., Naash M.I. 2015. Nanoparticle-based technologies for retinal gene therapy. Eur J Pharm Biopharm, 95: 353-67.
[26] Alexis F. Nanoparticle technologies for cancer therapy, in Drug delivery. Springer. 2010; 197: 55-86.
[27] Bhattacharya R, Mukherjee P. Biological properties of "naked" metal nanoparticles. Adv Drug Deliv Rev. 2008; 60(11): 1289-306.
[28] Urie R, Rege K. Nanoscale inorganic scaffolds as therapeutics and delivery vehicles. Current Opinion in Chemical Engineering. 2015; 7: 120-128.
[29] Dykman L. Khlebtsov NGold nanoparticles in biomedical applications: recent advances and perspectives. Chemical Society Reviews. 2012; 41(6):2256-2282.

[30] Daniels AN, Singh M. Sterically stabilized siRNA:gold nanocomplexes enhance c-MYC silencing in a breast cancer cell model. Nanomedicine. 2019; 14: 1387-1401.
[31] Ku SH, Kim K, Choi K, Kim SH, Kwon I.C. Tumor-Targeting Multifunctional Nanoparticles for siRNA Delivery: Recent Advances in Cancer Therapy. Adv. Healthcare Mater. 2014; 3: 1182–1193.
[32] Shaat H., Mostafa A, Moustafa M, Gamal-Eldeen A, Emam A, El-Hussieny E, Elhefnawi M. Modified gold nanoparticles for intracellular delivery of anti-liver cancer siRNA. International journal of pharmaceutics. 2016; 504: 125-133.

Cilt 11, Sayı 4, Sayfa 104-110, 2022

Volume 11, Issue 4, Page 104-110, 2022

Araştırma Makalesi https://doi.org/10.46810/tdfd.1199583 Research Article

Türk Doğa ve Fen Dergisi
Turkish Journal of Nature and Science
www.dergipark.gov.tr/tdfd

$Wb\bar{b}$ QCD Predictions in Proton Proton Collisions for the LHC and FCC

Kamuran DİLSİZ[1*]

[1]Bingol University, Art and Science Faculty, Physics Department, Bingöl, Türkiye
Kamuran DİLSİZ ORCID No: 0000-0003-0138-3368

*Corresponding author: kdilsiz@bingol.edu.tr

(Received: 04.11.2022, Accepted: 05.12.2022, Online Publication: 28.12.2022)

Keywords
QCD,
LHC,
FCC,
W Boson,
b quark.

Abstract: This study presents leading order (LO) and next-to-leading order (NLO) QCD cross sections for inclusive $Wb\bar{b}$ production channel at 14, 27 and 100 TeV center-of-mass energies for the Large Hadron Collider (LHC) and Future Circular Collider (FCC). To obtain the numerical results, five modern parton distribution functions (PDFs) were used and the PDF errors were obtained by the MCFM Monte Carlo program. In addition, a scale uncertainty calculation was performed for different values of renormalization and factorization scales. Contrary to the single W channel scale uncertainty results, the scale uncertainties in NLO QCD were found to be higher than the scale uncertainties in LO QCD for all energies considered in this calculation. To show the effect of the increasing energy on the uncertainties, a comparison of the scale, PDF and α_S uncertainties with the increasing energy were performed. To confirm the consistency of the code used in the current study, a comparison of the Monte Carlo results at $\sqrt{s}$ =7 TeV were performed with the available CMS data at the same energy. Then, LO and NLO QCD cross sections of $Wb\bar{b}$ production channel at $\sqrt{s}$ =14, 27 and 100 TeV were calculated. Using these results, the required amount of data that reach the same statistics with $\sqrt{s}$ =7 TeV energy were calculated for $\sqrt{s}$ = 14, 27 and 100 TeV energies.

Proton Proton Çarpışması Sonucu Oluşan $Wb\bar{b}$ Üretim Kanalının LHC ve FCC İçin Kuantum Renk Dinamiği Tahminleri

Anahtar Kelimeler
QCD,
LHC,
FCC,
W Boson,
b quark.

Öz: Bu çalışma, Büyük Hadron Çarpıştırıcısı (BHÇ) ve Gelecekteki Dairesel Çarpıştırıcı (FCC) için 14, 27 ve 100 TeV kütle merkez enerjilerinde $Wb\bar{b}$ üretim kanalının leading order (LO) ve next-to-leading order (NLO) kuantum renk dinamiği (KRD) tesir kesitlerini sunmaktadır. Sayısal sonuçları elde etmek için beş farklı parton dağılım fonksiyonu (PDF) kullanılmış ve PDF hataları MCFM Monte Carlo programı ile elde edilmiştir. Ayrıca renormalizasyon ve faktörizasyon ölçeklerinin farklı değerleri için scale hata payı hesaplaması yapılmıştır. W üretim kanalında elde edilen scale hata paylarının aksine $Wb\bar{b}$ üretim kanalında NLO QCD'deki scale hata payları LO QCD'deki scale hata paylarından daha yüksek bulunmuştur. Artan enerjinin hata payları üzerindeki etkisini test etmek için, artan enerji ile scale, PDF ve α_S belirsizliklerinin karşılaştırılması yapılmıştır. Ayrıca, bu çalışmada kullanılan simülasyon kodunun doğruluğunu onaylamak için $\sqrt{s}$ =7 TeV enerji değerinde elde edilen sonuçlar ile aynı enerjideki CMS verileri karşılaştırılmıştır. Yazılmış olan kodların doğruluğunun onaylanmasından sonra, $Wb\bar{b}$ üretim kanalının $\sqrt{s}$ = 14, 27 ve 100 TeV'deki LO ve NLO QCD tesir kesitleri hesaplanmıştır. Daha sonra $\sqrt{s}$ = 7 TeV enerjisindeki veri ile aynı istatistiğe sahip verinin elde edilmesi için $\sqrt{s}$ = 14, 27 ve 100 TeV enerjilerinde ihtiyaç duyulan veri miktarı hesaplanmıştır.

1. INTRODUCTION

Particle accelerators are huge colliders that play significant roles in search of new particles in high energy and particle physics. Particularly, the necessity of testing various predicted theories in the Standard Model (SM) and beyond it has increased the necessity for particle accelerators. The Large Hadron Collider (LHC) [1], the current largest accelerator in the world, focuses on new discoveries and searches for new physics. The LHC was initially operated at 7 TeV center-of-mass energy ($\sqrt{s}$) in

2009 and the energy was increased to 8 TeV in 2012. It is currently operating at 13.8 TeV and the energy will reach its desired collision energy of 14 TeV in the near future. Luminosity, the number of collisions per centimeter square per second, that occur in particle colliders, is an important parameter that shows the accelerator's performance. Higher luminosity provides more data to observe rare processes. To increase the performance of the LHC with a luminosity increase, High-Luminosity LHC (HL-LHC) has been planned to operate at 14 TeV with 10 times higher luminosity than that of the current run [2].

The likelihood high energy colliders that are planned to build in the future will contribute to search new physics. Comparing to the current colliders, they will provide the opportunity of testing theoretical predictions that cannot be estimated at low energies because of their high energies. The Future Circular Collider (FCC), which is planned to be built at CERN with a maximum 100 TeV collision energy, is projected to have three accelerators according to its conceptual design report. These are FCC-ee (electron-positron), High-Energy LHC (HE-LHC) and FCC-hh collider (proton-proton, ion-ion) [3]. The beams of electron and positron at several center-of-mass energies will be collided at FCC-ee [4]. After HL-LHC has successfully finished its operation, the beams of protons at $\sqrt{s}$= 27 TeV will be collided at HE-LHC [5] which will be located in the same tunnel with the LHC. The proton beams at $\sqrt{s}$= 100 TeV will be collided at FCC-hh collider [6] and this energy will be the maximum planned energy of the collider.

Understanding of the detectors and their response to the particles produced is required for the measurement of the proposed signals of the processes that provide access to new physics. A precise software calibration depends on accurate calculation of the cross-section processes of particles whose properties are well known. QCD predictions, that are very important in determining the cross section of a particle, is calculated by the monte carlo production tools. MCFM [7] monte carlo program is one of these tools and it produces the QCD results of many physics processes. In this context, we have calculated LO and NLO QCD cross sections of $Wb\bar{b}$ production channel using MCFM program. Parton distribution functions (PDFs), which give the probability to find partons in a hadron, are important parameters to calculate the cross sections of the physics processes produced by the hadron colliders. Therefore, we used LHAPDF6 [8] library to select different PDFs for calculation.

The total and differential cross sections of $Wb\bar{b}$ at 10 TeV and 14 TeV center-of-mass energies were previously calculated [9]. However, our purpose in this study is not to follow the same steps that were provided in Ref [9]. In current study, $Wb\bar{b}$ LO and NLO QCD predictions were obtained at $\sqrt{s}$ = 27 TeV and 100 TeV in addition to $\sqrt{s}$ = 14 TeV. Additionally; scale, PDF and α_S uncertainties were calculated and the effect of increasing energy on the uncertainties were provided. Particularly, using two different methods in the selection of renormalization (μ_R) and factorization (μ_F) scales, the scale uncertainties were calculated (section 3.1). All results were produced by the MCFM monte carlo program [7] and five modern PDFs were used to confirm the selection of the reference PDF (NNPDF3.1). In the last step, the necessary amount of data at $\sqrt{s}$ = 14, 27 and 100 TeV energies were calculated to show the amount of data to reach the same statistic with the data at $\sqrt{s}$ = 7 TeV (section 3.2).

2. GENERAL SETUP

In this study, the results of $Wb\bar{b}$ production channel were obtained both for the next LHC run and FCC pp collider runs. The production energies have been set to 14 TeV and 27 TeV (100 TeV) center-of-mass energy for the LHC and the HE-LHC (FCC-hh), respectively. The focus of the study was the leptonic decay of the W boson. The mass of the b quark was taken as m_b = 4.62 GeV. Because of the geometry in the detectors of the LHC (CMS and ATLAS), the selection criteria were set on the lepton transverse momentum (p_T^l) and lepton pseudorapidity (η). For this channel, a p_T^l greater than 25 GeV was preferred and η value of leptons and b jets smaller than 2.5 were selected. Having the pseudocone size (R) equal to 0.7, the $k_T$algorithm [10, 11] was implemented for the b jets. μ_R and μ_F scales were selected as μ_R= μ_F=$M_W + 2M_b$ where M_W and M_b are the masses of the W and b quarks, respectively . The scale uncertainty was calculated taking the differences between the cross section values of twice and half of the default μ_R and μ_F. More details about the calculation of the scale uncertainty implemented in this study is given in our previous study [12]. Following the confirmation of the NNPDF3.1 PDF through the comparison of five different PDF sets, both the LO and NLO predictions were obtained with the NNPDF3.1 PDF set [13]. The strong coupling factor, α_S (M_Z), was set to 0.118 both for LO and NLO QCD corrections.

3. RESULTS AND DISCUSSIONS

3.1. Uncertainties

The uncertainties calculated in this study were obtained based on the chosen reference PDF, NNPDF3.1.To search the effect of increasing collision energy on the rank of the uncertainties; PDF, scale and α_S uncertainties were computed at $\sqrt{s}$ = 14, 27 and 100 TeV energies respectively by taking the LO and NLO accuracies of the cross sections into account. PDF uncertainties were calculated following the steps defined at ref. [20]. Varying the values of μ_R and μ_F, two different scale uncertainties were calculated. Initially, the masses of the W boson and b quarks were taken into account and the μ_R and μ_F were simultaneously varied as $\frac{M_{W+2b}}{2} \leq \mu_R \leq 2M_{W+2b}$ and $\frac{M_{W+2b}}{2} \leq \mu_F \leq 2M_{W+2b}$ (scale 1), where M_{W+2b} is the sum of W boson and b quarks masses. Then, the mass of W boson was taken into account and the μ_R and μ_F simultaneously varied as $\frac{M_W}{2} \leq \mu_R \leq 2\, M_W$ and $\frac{M_W}{2} \leq \mu_F \leq 2M_W$ (scale 2), where M_W is the mass of W boson.

The default values of μ_R and μ_F were set to M_{W+2b} and M_W for scale 1 and scale 2, respectively. Then, the variations were assigned as up and down errors. In order to calculate α_S error, α_S was varied by 0.002 and the difference with the default value was taken as α_S error. The numerical results of the calculated LO (NLO) uncertainties are given in Table 1 (Table 2). A comparison of the scale 1, scale 2, PDF and α_S errors are shown in Figure 1. NLO QCD suffers from scale uncertainty even though the scale uncertainty shows low systematic error at LO QCD. In addition, all uncertainties increase with the increasing energy at LO and NLO QCD except of the scale uncertainty at $\sqrt{s}$ = 100 TeV at LO QCD. These results show that the scale uncertainty at next runs (14, 27 and 100 TeV) will suffer with high systematic errors. In order to reduce the uncertainty, higher order calculations would be necessary.

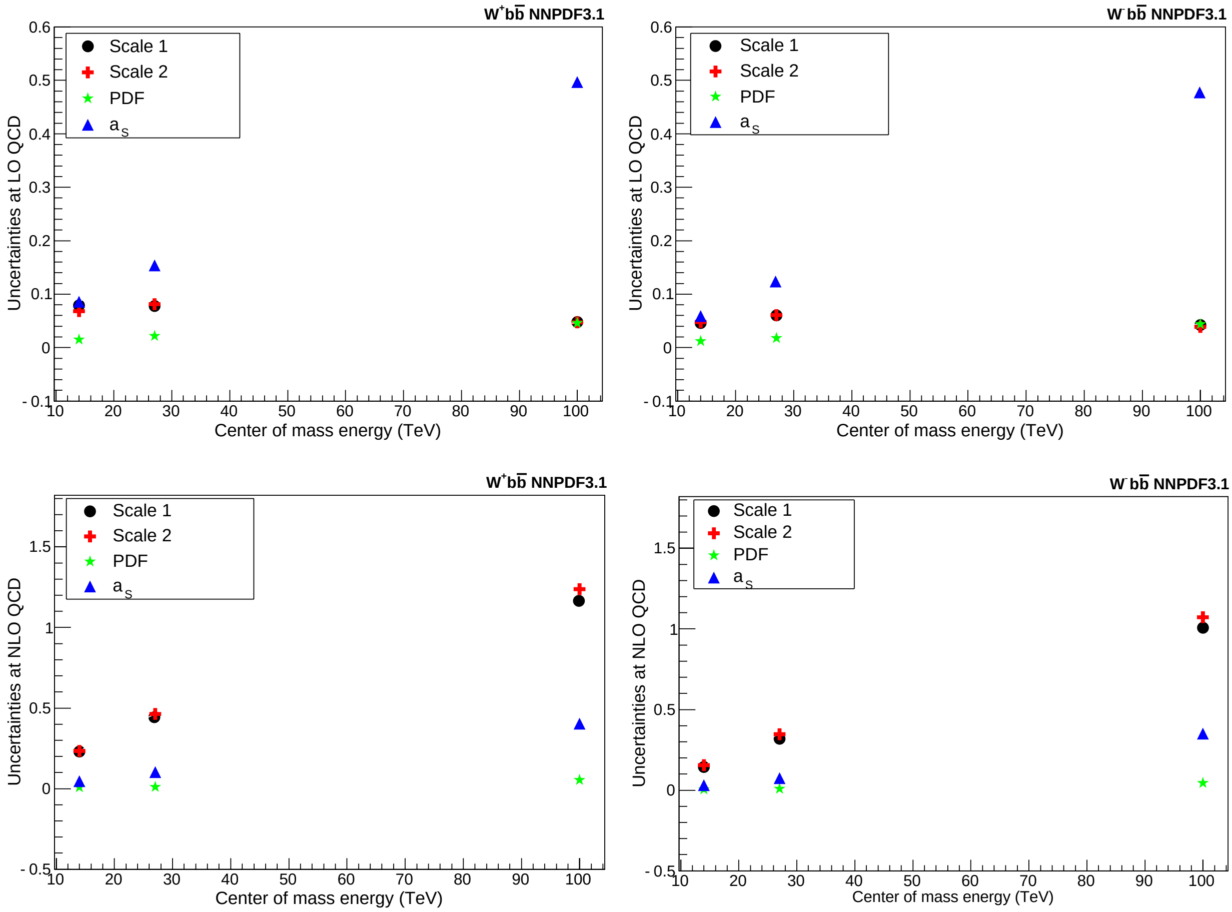

Figure 1. Scale, PDF and α_S uncertainties at LO and NLO QCD for $W^+b\bar{b}$ (left) and $W^-b\bar{b}$ (right) production channel.

Table 1. The numerical results of the uncertainties calculated at LO QCD for different energies. All results are in the units of pb.

Production Channel	Uncertainty	14 Tev	27 TeV	100 TeV
$W^+b\bar{b}$	Scale 1	+0.079 −0.053	+0.078 −0.067	+0.033 −0.048
	Scale 2	+0.068 −0.056	+0.081 −0.070	+0.037 −0.047
	PDF	+0.015 −0.015	+0.022 −0.022	+0.046 −0.046
	α_S	+0.086 −0.086	+0.154 −0.154	+0.497 −0.497
$W^-b\bar{b}$	Scale 1	+0.046 −0.037	+0.060 −0.053	+0.024 −0.042
	Scale 2	+0.048 −0.038	+0.061 −0.054	+0.025 −0.039
	PDF	+0.012 −0.012	+0.018 −0.018	+0.044 −0.044
	α_S	+0.059 −0.059	+0.123 −0.123	+0.476 −0.476

Table 2. The numerical results of the uncertainties calculated at NLO QCD for different energies. All results are in the units of pb.

Production Channel	Uncertainty	14 Tev	27 TeV	100 TeV
$W^+b\bar{b}$	Scale 1	+0.226 −0.163	+0.441 −0.321	+1.162 −0.950
	Scale 2	+0.234 −0.170	+0.463 −0.335	+1.238 −0.953
	PDF	+0.008 −0.008	+0.011 −0.011	+0.053 −0.053
	α_S	+0.046 −0.047	+0.102 −0.094	+0.404 −0.367
$W^+b\bar{b}$	Scale 1	+0.144 −0.105	+0.318 −0.235	+1.006 −0.837
	Scale 2	+0.155 −0.112	+0.347 −0.240	+1.073 −0.850
	PDF	+0.005 −0.005	+0.008 −0.008	+0.045 −0.045
	α_S	+0.032 −0.031	+0.075 −0.073	+0.351 −0.345

3.2. QCD Predictions at $\sqrt{s}$ = 14, 27 and 100 TeV

CMS collaboration previously measured inclusive $Wb\bar{b}$ fiducial cross section with the data taken by the CMS detector at 7 TeV center-of-mass energy [14]. Since we make the predictions for the future experiments and have no available experimental data at $\sqrt{s}$ = 14, 27 and 100 TeV, the confirmation of the codes used in the MCFM program are crucial in terms of obtaining the accurate results for the future experiments. These were verified through comparison of the fiducial QCD predictions of $Wb\bar{b}$ at $\sqrt{s}$= 7 TeV with the results obtained by the CMS collaboration at the same energy. Using the selection criteria explained in section 2, LO and NLO QCD predictions were obtained by the MCFM and the predicted results are given in Table 3. The comparison of the LO and NLO QCD predictions with the experimental CMS results are illustrated in Figure 2. NLO prediction is consistent with the data while the LO prediction does not agree with the experimental results. Since the NLO accuracy has one loop matrix element, it provides more accurate calculations in comparison to the LO correction. Due to this, NLO QCD results show a better agreement with the experimental data. This confirmation shows the validation of the codes in the MCFM for the next runs at higher energies ($\sqrt{s}$ = 14, 27 and 100 TeV). However, selection of an appropriate PDF among the most modern ones are needed as there are differences among the PDF groups. This study has compared the NLO QCD predictions obtained by NNPDF3.1 with the NLO corrections obtained by CT14 [15], MSTW2008 [16, 17], MMHT2014 [18] and HERA [19] PDFs (Fig. 3). This comparison shows that the results obtained by NNPDF3.1 are consistent with the outcomes of the other PDFs. This confirmed the reliability of NNPDF3.1 comparing its results with the results obtained by the other PDFs (Fig. 3). The numerical results of NLO QCD predictions obtained with different PDFs for $W^+b\bar{b}$ and $W^-b\bar{b}$ production channels at $\sqrt{s}$ = 14, 27 and 100 TeV are given in Table 4. According to the results given in table 4, NNPDF3.1 results at $\sqrt{s}$ =14 TeV in $W^+b\bar{b}$ ($W^-b\bar{b}$) channel are respectively 1.61% (0.75%), 2.45% (4.42%), 2.83% (3.32%) and 1.00% (1.47%) different than CT14, MSTW2008, MMHT2014 and HERA PDF results. In addition, NNPDF3.1 results at $\sqrt{s}$ =27 TeV in $W^+b\bar{b}$ ($W^-b\bar{b}$) channel are respectively 1.65% (1.64%), 2.19% (4.30%), 2.83% (3.60%) and 1.77% (3.00%) different than CT14, MSTW2008, MMHT2014 and HERA PDF results. Moreover, NNPDF3.1 results at $\sqrt{s}$ =100 TeV in $W^+b\bar{b}$ ($W^-b\bar{b}$) channel are respectively 1.82% (1.91%), 2.49% (3.38%), 2.92% (3.03%) and 4.72% (4.74%) different than CT14, MSTW2008, MMHT2014 and HERA PDF results.

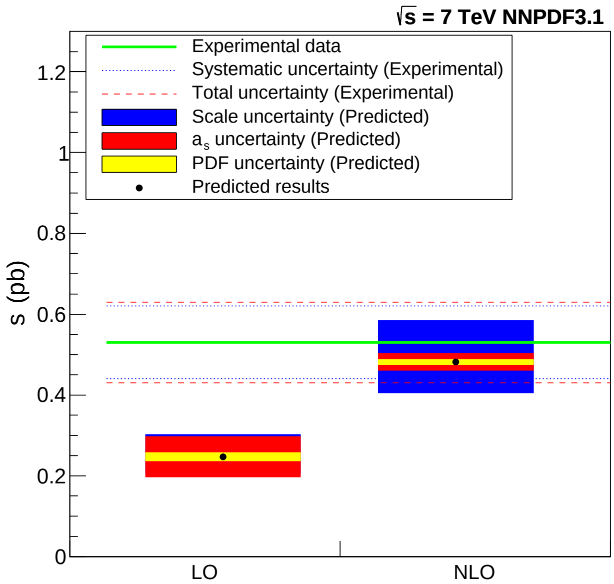

Figure 2. A comparison of LO and NLO QCD results obtained by NNPDF3.1 PDF with the data taken by the CMS detector at $\sqrt{s}$ = 7 TeV.

Table 3. LO and NLO QCD predictions for $Wb\bar{b}$ production channel at $\sqrt{s}$ = 7 TeV. The uncertainties are respectively scale, α_S, and PDF errors. All results are in the units of pb.

Production Channel	LO	NLO
$W^+b\bar{b}$	$0.213^{+0.047+0.044+0.008}_{-0.036-0.044-0.008}$	$0.419^{+0.089+0.019+0.005}_{-0.067-0.018-0.005}$
$W^-b\bar{b}$	$0.126^{+0.028+0.024+0.006}_{-0.021-0.024-0.006}$	$0.239^{+0.049+0.010+0.003}_{-0.037-0.011-0.003}$
Total $Wb\bar{b}$	$0.247^{+0.055+0.050+0.010}_{-0.042-0.050-0.010}$	$0.482^{+0.102+0.021+0.006}_{-0.077-0.021-0.006}$

107

Table 4. NLO QCD predictions that are obtained with different PDFs for $W^+b\bar{b}$ *and* $W^-b\bar{b}$ production channels at $\sqrt{s}$ = 14, 27 and 100 TeV. All results are in the units of pb.

Production Channel	Energy (TeV)	NNPDF3.1PDF	CT14 PDF	MSTW2008 PDF	MMHT2014 PDF	HERA PDF
$W^+b\bar{b}$	14	0.996	0.980	1.021	1.025	0.986
	27	2.059	2.025	2.105	2.119	2.096
	100	7.676	7.536	7.872	7.907	8.056
$W^-b\bar{b}$	14	0.670	0.655	0.701	0.693	0.680
	27	1.582	1.556	1.653	1.641	1.631
	100	6.972	6.839	7.216	7.190	7.319

Table 5. LO and NLO QCD predictions at $\sqrt{s}$ = 14, 27 and 100 TeV for $W^+b\bar{b}$ *and* $W^-b\bar{b}$ production channels. The uncertainties are respectively scale, α_S, and PDF errors. All results are in the units of pb.

Production Channel	Energy (TeV)	LO	NLO
$W^+b\bar{b}$	14	$0.392^{+0.079+0.086+0.015}_{-0.053-0.086-0.015}$	$0.996^{+0.226+0.046+0.008}_{-0.163-0.047-0.008}$
	27	$0.650^{+0.078+0.154+0.022}_{-0.067-0.154-0.022}$	$2.059^{+0.441+0.102+0.011}_{-0.321-0.094-0.011}$
	100	$1.713^{+0.033+0.497+0.046}_{-0.048-0.497-0.046}$	$7.676^{+1.162+0.404+0.053}_{-0.950-0.367-0.053}$
$W^-b\bar{b}$	14	$0.276^{+0.046+0.059+0.012}_{-0.037-0.059-0.012}$	$0.670^{+0.144+0.032+0.005}_{-0.105-0.031-0.005}$
	27	$0.520^{+0.060+0.123+0.018}_{-0.053-0.123-0.018}$	$1.582^{+0.318+0.075+0.008}_{-0.235-0.073-0.008}$
	100	$1.589^{+0.024+0.476+0.044}_{-0.042-0.476-0.044}$	$6.972^{+1.006+0.351+0.045}_{-0.837-0.345-0.045}$

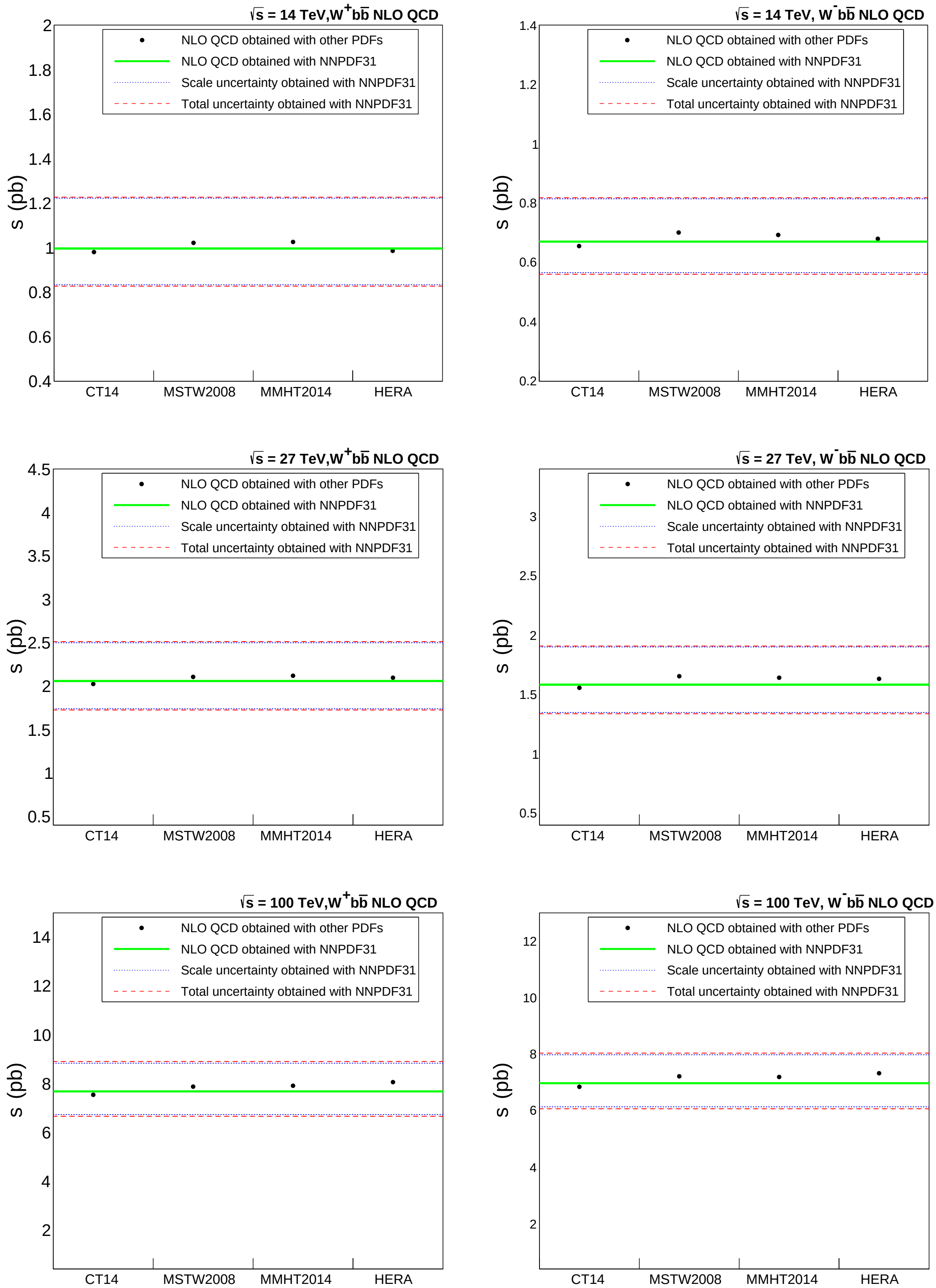

Figure 3. A comparison of NLO QCD results obtained by NNPDF3.1 with the NLO QCD results obtained by CT14, MSTW2008, MMHT2014 and HERA PDFs.

After the confirmation of the codes and the PDF set, LO and NLO QCD corrections at $\sqrt{s}$ = 14, 27 and 100 TeV have been calculated. During the calculation, LO corrections have been calculated with the LO PDF and NLO corrections have been calculated with NLO PDF. Table 5 shows the numerical results of these corrections. NLO QCD has more yield than the LO QCD for all selected energies shown in the table. For $\sqrt{s}$ = 14, 27 and 100 TeV energies of $W^+b\bar{b}$ ($W^-b\bar{b}$) channel, NLO results are respectively 2.541, 3.168 and 4.481 (2.428, 3.042 and 4.388) times higher than the LO results. Figure 4 shows this difference between LO and NLO corrections. The difference between LO and NLO QCD results increases while the energy increases. However, this increase is not identical for both channels ($W^+b\bar{b}$ and $W^-b\bar{b}$). When the energy ranges from 14 TeV to 100 TeV, the gap between LO and NLO corrections in $W^+b\bar{b}$ channel becomes larger than the gap between LO and NLO corrections in $W^-b\bar{b}$ channel. Due to the proportionality of the cross-section and the number of events, the results in the table also show that there will be more $W^+b\bar{b}$ events than $W^-b\bar{b}$ events in the future experiments. However, the number of $W^-b\bar{b}$ events will be close to $W^+b\bar{b}$ events while the energy is increased. This is because the asymmetry between W^+ and W^- events decreases with the increasing energy.

In a collision, the number of events is proportional to the cross section and the relationship between them is given with the following equation:

$$N = \sigma \times L \quad (1)$$

where N is the number of events, σ is the cross section and L is the luminosity. This equation shows that equal amount of data at different energies provides more signal events at the highest energy. If the same number of events are taken at different energies, the highest energy will provide less amount of data to reach the same statistic with the lower energies. Based on this consideration, the following equation can be written:

$$\sigma_1 L_1 = \sigma_2 L_2 \Rightarrow L_2 = \frac{\sigma_1 L_1}{\sigma_2} \quad (2)$$

Using this equation, the following statistics are calculated at $\sqrt{s}$ = 14, 27 and 100 TeV for the required data to reach the same statistics at $\sqrt{s}$ = 7 TeV. The recorded CMS data at $\sqrt{s}$ = 7 TeV is equal to 5.55 fb^{-1}.

$$L_{14TeV} = \frac{\sigma_{7TeV} L_{7TeV}}{\sigma_{14TeV}} = \frac{0.482x5.55}{1.200} = 2.230\ fb^{-1} \quad (3)$$

$$L_{27TeV} = \frac{\sigma_{7TeV} L_{7TeV}}{\sigma_{27TeV}} = \frac{0.482x5.55}{2.597} = 1.030\ fb^{-1} \quad (4)$$

$$L_{100TeV} = \frac{\sigma_{7TeV} L_{7TeV}}{\sigma_{100TeV}} = \frac{0.482x5.55}{10.370} = 0.260\ fb^{-1} \quad (5)$$

The results in equations 3, 4 and 5 show that the required data at $\sqrt{s}$ = 14, 27 and 100 TeV are 60%, 81% and 95% less than the data at $\sqrt{s}$ = 7 TeV. Figure 5 shows the amount of data taken at different energies to reach the same statistic with the lowest energy of the LHC (7 TeV). For the future pp collision runs, the collisions at $\sqrt{s}$ = 14, 27 and 100 TeV will need less data to reach the same statistic with $\sqrt{s}$ = 7 TeV pp collision energy.

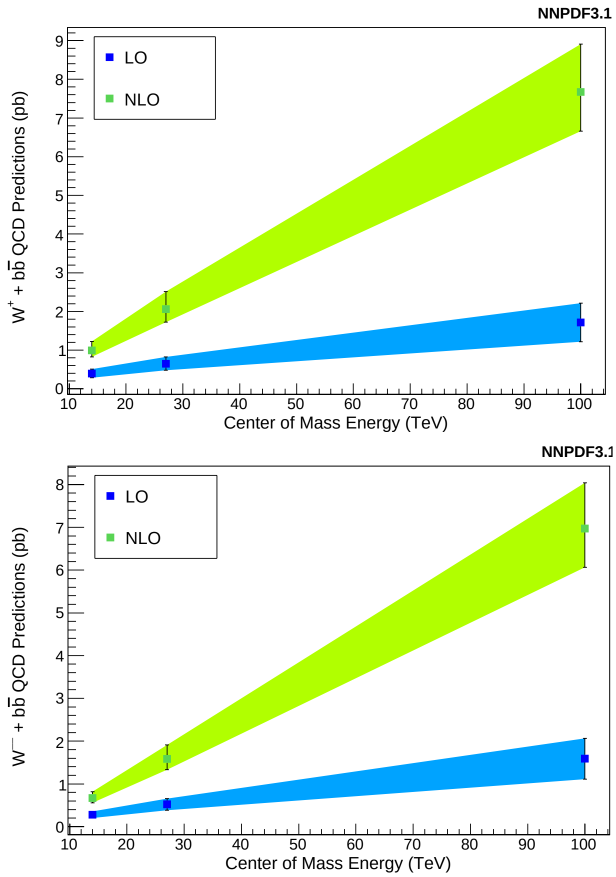

Figure 4. LO and NLO QCD predictions at $\sqrt{s}$ = 14, 27 and 100 TeV for $W^+b\bar{b}$ (top) and $W^-b\bar{b}$ (bottom).

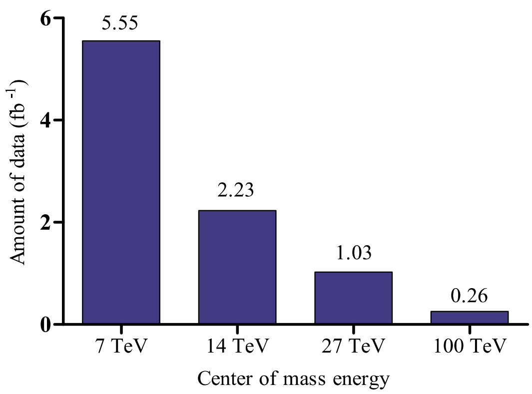

Figure 5. The required data at $\sqrt{s}$ = 14, 27 and 100 TeV to reach the same statistics with $\sqrt{s}$ = 7 TeV energy.

4. CONCLUSION

LO and NLO QCD cross sections of $W^+b\bar{b}$ and $W^-b\bar{b}$ channels at $\sqrt{s}$ = 14, 27 and 100 TeV were presented in this study. Both LO and NLO predictions were obtained by the most modern PDF, NNPDF3.1. During the calculation, the consistency of the results was confirmed by the comparison of the results with the available CMS results and the consistency of the NNPDF3.1 was confirmed via comparing with the results obtained by other PDFs. The scale uncertainties were calculated by two different methods in which different μ_R and μ_F values were specified. On the first method (scale

1), the default values of μ_R and μ_F were taken as sum of W and b quarks masses and the μ_R and μ_F values were changed as half and twice of this default value. On the second method (scale 2), the default values of μ_R and μ_F were set to W boson mass; then, the μ_R and μ_F values were changed as half and twice of this default value. Following that, the scale uncertainties for both methods were calculated taking the difference between the default and changed values. The results of scale 1 were partially found to be lower than that of the scale 2. Therefore, scale 1 results were taken into account at the uncertainty results of the final LO and NLO QCD results at $\sqrt{s}$ = 14, 27 and 100 TeV. In addition to the scale uncertainty, the effect of the increasing energy on the uncertainties was analyzed by comparing energy with the scale, PDF and α_S uncertainties. Finally, using NNPDF3.1 as a reference PDF model, LO and NLO QCD predictions were obtained for the next run of the LHC (14 TeV), HE-LHC (27 TeV) and FCC-hh (100 TeV). According to the obtained results, LO and NLO QCD predictions increase as the collision energy increases. This showed that there would be more amount of data at the next LHC run and FCC runs and the necessary amount of data to reach same statistics with the data at $\sqrt{s}$ = 7 TeV would respectively reduce while the collision energy was increased to $\sqrt{s}$ = 14, 27 and 100 TeV.

Acknowledgement

The numerical calculations reported in this paper were fully/partially performed at TUBITAK ULAKBIM, High Performance and Grid Computing Center (TRUBA resources).

REFERENCES

[1] Evans L, Bryant P. LHC Machine. Journal of Instrumentation 2008; 3: S08001.
[2] Kuehn S. Impact of the HL-LHC detector upgrades on the physics program. International Workshop on Future Linear Colliders. LCWS2021. Zurich, 15-18 March 2021.
[3] Future Circular Collider Conceptual Design Report, The European Organization for Nuclear Research, (2019), URL:https://fcc-cdr.web.cern.ch/
[4] The FCC Collaboration, Eur. Phys. J Spec. Top. 2019;228:261-623.
[5] Abada A, Abrescia M, Abdussalam S, Abdyukhanov I, Fernandez J, Abramov A, et al. HE-LHC: The High Energy Large Hadron Collider. Eur. Phys. J. Spec. Top. 2019; 228:1109–1382.
[6] The FCC Collaboration. FCC-hh: The Hadron Collider: Future Circular Collider Conceptual Design Report Volume 3. Eur. Phys. J. Spec. Top. 2019; 228:755–1107.
[7] Campbell J, Ellis K, Neumann T, Williams C. MCFM Monte Carlo for FeMtobarn processes. [2022 November 3] Available from: https://mcfm.fnal.gov/
[8] Buckley A, Ferrando J, Lloyd S, Nordstrom K, Page B, Ruefenacht M, et al. LHAPDF6: parton density access in the LHC precision era. Eur. Phys. J. C. 2015; 75(132): 1-20.
[9] Cordero F, Reina L, Wackeroth D. W and Z boson production with a massive bottom quark pair at the Large Hadron Collider. Phys. Rev. D 2009; 80: 034015.
[10] Catani S, Dokshitzer YL, Webber BR. The k_T clustering algorithm for jets in deep inelastic scattering and hadron collisions. Phys. Lett. B. 1992; 285 (3): 291-299.
[11] Kilgore B, Giele T. Next-to-leading order gluonic three-jet production at hadron colliders. Phys. Rev. D. 1997; 55:7183.
[12] Dilsiz K, Tiras E. Inclusive W boson QCD predictions and lepton charge asymmetry in proton-proton collisions at $\sqrt{s}$ = 14 TeV. Canadian J. of Phys. 2018; 96(9):1029-1033.
[13] Ball R, Bertone V, Carrazza S, Debbio L, Forte S, Groth-Merrild P, et al. Parton distributions from high-precision collider data. Eur. Phys. J. C. 2017; 77(10): 663.
[14] Chatrchyan S, Khachatryan V, Sirunyan A, Tumasyan A, Adam W, Bergauer W, et al. Measurement of the production cross section for a W boson and two b jets in pp collisions at $\sqrt{s}$ = 7 TeV. Phys. Lett. B. 2014; 735: 204–225.
[15] Dulat S, Hou T, Gao J, Guzzi M, Huston J, Nadolsky P, et al. New parton distribution functions from a global analysis of quantum chromodynamics. Phys. Rev. D. 2016; 93(3): 033006.
[16] Martin A, Stirling S, Throne RS, Watt G. Parton distributions for the LHC. Eur. Phys. J. C. 2009; 63:189–285.
[17] Martin A, Stirling S, Thorne RS, Watt G. Heavy-quark mass dependence in global PDF analyses and 3 and 4 flavour parton distributions. Eur. Phys. J. C. 2010; 70: 51–72.
[18] Harland-Lang L.A, Martin A.D, Motylinski P, Throne R.S. Parton distributions in the LHC era:MMHT 2014 PDFs. Eur. Phys. J. C. 2015;75(5): 204.
[19] Abramowicz H, Abt I, Adamczyk L, Adamus M, Andreev V, Antonelli S, et al. Combination of measurements of inclusive deep inelastic $e^{\pm}$ p scattering cross section and QCD analysis of HERA data. Eur. Phys. J. C. 2015; 75:580.
[20] Butterworth J, Carrazza S, Cooper-Sarkar A, Roeck A, Feltesse J, Forte S, et al. PDF4LHC recommendations for LHC Run II. J. Phys. G. 2016; 43: 023001.

Cilt 11, Sayı 4, Sayfa 111-116, 2022 Volume 11, Issue 4, Page 111-116, 2022

Araştırma Makalesi https://doi.org/10.46810/tdfd.1092040 Research Article

Türk Doğa ve Fen Dergisi
Turkish Journal of Nature and Science
www.dergipark.gov.tr/tdfd

The Relationship of Blood Asprosin Levels and Biochemical Parameters in Pregnant Cows

Mehmet Akif KILINÇ [1*], Ali RİŞVANLI [2], Tarık ŞAFAK [3], Öznur YILMAZ [4], Burak Fatih YÜKSEL [5], İbrahim ŞEKER[6]

[1] Department of Obstetrics and Gynecology, Faculty of Veterinary Medicine, University of Bingol, Bingöl, Türkiye,
[2] Department of Obstetrics and Gynecology, Faculty of Veterinary Medicine, University of Turkish Manas University, Kyrgyzstan,
[3] Department of Obstetrics and Gynecology, Faculty of Veterinary Medicine, University of Kastamonu, Kastamonu, Türkiye,
[4]Department of Obstetrics and Gynecology, Faculty of Veterinary Medicine, University of Siirt, Siirt, Türkiye,
[5]Department of Obstetrics and Gynecology, Faculty of Veterinary Medicine, University of Firat, Elaziğ, Türkiye,
6Department of Zootechny, Faculty of Veterinary Medicine, University of Firat, Elaziğ, Türkiye.
Mehmet Akif KILINÇ ORCID No: 0000-0003-1577-1556
Ali RİŞVANLI ORCID No: 0000-0001-5653-0025
Tarık ŞAFAK ORCID No: 0000-0002-6178-4641
Öznur YILMAZ ORCID No: 0000-0003-0424-9471
Burak Fatih YÜKSEL ORCID No: 0000-0002-7256-9189
İbrahim ŞEKER ORCID No: 0000-0002-8135-6142

**Corresponding author: makilinc@bingol.edu.tr*

(Received: 24.03.2022, Accepted: 11.12.2022, Online Publication: 28.12.2022)

Keywords
Cow,
Asprosin,
Biochemical parameters,
Pregnancy,
Simmental.

Abstract: In this study, it was aimed to determine asprosin levels in pregnant and non-pregnant cows and to determine the relationship between some biochemical parameters and asprosin levels. For this purpose, 60 Simmental cows were divided into two groups as pregnant (n=30) and non-pregnant cows on the postpartum 15th day (n=30), and asprosin levels and biochemical parameters were measured by taking blood from the cows once. Measured biochemical parameters were Alkaline phosphatase (ALP), Amylase, Creatine kinase myocardial band (CK-MB), Creatine kinase N-acetyl cysteine (CK-NAC), Gamma glutamyl transferase (GGT), Aspartate Aminotransferase (AST), Alanine aminotransferase (ALT)), Direct bilirubin, Total bilirubin , Calcium (Ca), Choline (CHO), Creatine, Glucose, Total protein, Urea, Albumin, Iron, Phosphorus, Lactate dehydrogenase (LDH-P), High-density lipoprotein cholesterol (HDL-C)), Low-density lipoprotein (LDL), Triglyceride, Magnesium (Mg) and Unsaturated iron binding capacity (UIBC). Asprosin levels were measured using commercial ELISA kits and biochemical parameters were measured in an autoanalyzer. Asprosin levels and biochemical parameters were compared both within and between groups and the results were evaluated. As a result of the data obtained, the amount of direct bilirubin and total bilirubin in non-pregnant cows was found to be higher than that of pregnant cows, while the amounts of CHO, HDL-C, LDL and asprosin were found to be lower. When asprosin and biochemical parameters of pregnant cows were compared, a positive correlation was found between asprosin and albumin, direct bilirubin, total bilirubin and creatinine levels. In non-pregnant cows, there was a negative correlation between asprosin and amylase and phosphorus, and a positive correlation between asprosin and creatine and glucose. As a result, it was concluded that asprosin levels are higher in pregnant cows and there may be negative or positive correlations between this hormone and biochemical parameters. However, it would be beneficial to carry out more comprehensive studies on the subject in order to reach more definite conclusions.

Gebe İneklerde Kan Asprosin Düzeylerinin Biyokimyasal Parametrelerle İlişkisi

Anahtar Kelimeler
İnek,

Öz: Bu çalışmada, gebe ve gebe olmayan ineklerde asprosin düzeylerinin tespit edilmesi, bazı biyokimyasal parametreler ile asprosin düzeyleri arasındaki ilişkinin belirlenmesi amaçlanmıştır. Bu amaçla 60 adet Simental ırkı inek, gebe olan (n=30) ve postpartum 15. günde (n=30) gebe

Asprosin, Biyokimyasal parametreler, Gebelik, Simental.

olmayan inekler olmak üzere iki gruba ayrıldı ve ineklerden bir kez kan alınarak asprosin düzeyleri ve biyokimyasal parametreler ölçüldü. Ölçülen biyokimyasal parametreler Alkalen fosfataz (ALP), Amilaz, Kreatin kinaz miyokardial band (CK-MB), Kreatin kinaz N-asetil sistein (CK-NAC), Gama glutamil transferaz (GGT), Aspartat Aminotransferaz (AST), Alanin aminotransferaz (ALT), Direkt bilirubin, Total bilirubin, Kalsiyum (Ca), Kolin (CHO), Kreatin, Glikoz, Total protein, Üre, Albümin, Demir, Fosfor, Laktat dehidrogenaz (LDH-P), Yüksek yoğunluklu lipoprotein kolesterol (HDL-C), Düşük yoğunluklu lipoprotein (LDL), Trigliserit, Magnezyum (Mg) ve Doymamış demir bağlama kapasitesi (UIBC)'dir. Asprosin düzeyleri ticari ELİSA kitleri kullanılarak, biyokimyasal parametreler ise otoanalizörde ölçüldü. Asprosin düzeyleri ve biyokimyasal parametreler hem grup içi hem de gruplar arası karşılaştırılarak sonuçlar değerlendirildi. Elde edilen veriler ışığında gebe olmayan ineklerin direkt biluribin ve total biluribin miktarı gebe ineklerden yüksek, CHO, HDL-C, LDL ve asprosin miktarları ise düşük bulundu. Gebe ineklerin asprosin ile biyokimyasal parametreleri karşılaştırıldığında ise asprosin ile albümin, direkt biluribin, total biluribin ve kreatin miktarları arasında pozitif yönde korelasyon bulundu. Gebe olmayan ineklerde ise asprosin ile amilaz ve fosfor arasında negatif korelasyon, asprosin ile kreatin ve glikoz arasında pozitif yönde korelasyon gözlendi. Sonuç olarak, gebe ineklerde asprosin düzeylerinin daha yüksek olduğu ve bu hormonla biyokimyasal parametreler arasında negatif veya pozitif yönde korelasyonlar olabileceği kanaatine varıldı. Ancak daha kesin sonuçlara varılabilmesi için konu ile ilgili daha kapsamlı çalışmaların yapılması faydalı olacaktır.

1. INTRODUCTION

Evaluation of blood parameters in cows refers to the analysis of blood biochemical components helpful in diagnosing and preventing metabolic and nutritional problems [1]. Monitoring the metabolic profile is more important when animals are sensitive to metabolic changes, such as in early lactation, considering the herd characteristics, geographical location and physiological condition of the animals [2].

Asprosin is a new peptide hormone released from white adipose tissue. Asprosin, encoded by two exons (exon 65 and exon 66) of the fibrillin 1 (FBN1) gene, was first described by Romere et al. [3] in a study on neonatal progeroid syndrome (NPS) patients. Asprosin, which release during periods of fasting, activates the G protein-cAMP-PKA pathway and increases glucose secretion in the liver [4-6]. Studies on humans and mice prove that recombinant asprosin injection is associated with insulin resistance due to elevation of blood glucose and insulin [4]. Therefore, many studies have focused on the association of asprosin with obesity and reported that asprosin concentrations increase in obese humans and mice [7-9]. Recent studies have reported that asprosin plays an essential role in metabolism and metabolic diseases [6]. In studies conducted with subjects with type 2 diabetes (T2DM), it has been reported that asprosin levels are higher than the control group and asprosin levels are positively correlated with insulin resistance in subjects with T2DM [10-12]. Polycystic ovary syndrome (PCOS) is a common metabolic and reproductive disorder associated with insulin resistance [4]. According to studies conducted on subjects with polycystic ovary syndrome, it has been reported that asprosin levels are higher than in the control group, and it is a candidate molecule for the determination of this disease in the future [4-13]. In addition to performing a glucogenic function, asprosin has been reported as a potential appetite stimulating hormone in the treatment of both obesity and diabetes [6]. Excessive weight gain and gestational diabetes during pregnancy cause pregnancy pathologies. Insulin resistance (IR), high blood glucose levels and hormonal disorders cause incorrect programming of the infant's energy metabolism [14]. When the asprosin level is examined in pathological pregnancies such as gestational diabetes, preeclampsia, severe preeclampsia, intrauterine growth retardation and fetal macrosomia, it is reported that there is a statistically significant increase compared to the control group, and a significant decrease is observed in those with intrauterine growth retardation [15]. As a result of these studies, asprosin is thought to be not only a potential biomarker for early diagnosis of type 2 diabetes mellitus and other metabolic disorders, but also a new therapeutic agent to counter the perinatal programming of childhood obesity [16].

There are not many publications in ruminants about Asprosin, which has been frequently examined in human medicine, especially in diabetes-related publications recently. It is thought that it will be useful to follow the data of this hormone, especially in monitoring the parameters related to the metabolic status of pregnant cows. Therefore in this study, it was aimed to determine the relationship between asprosin and biochemical parameters in pregnant and non-pregnant cows both within themselves and between groups, and to determine the relationship between them in the postpartum and pregnancy period. At the same time, it is aimed to evaluate the possibility of asprosin being a marker in the problems that may occur by determining the relationship with the changes in biochemical parameters in these processes.

2. MATERIAL AND METHOD

In this study, 60 simmental breed 2 and 4 years old cows in a farm located in Bingöl province in the eastern part of Turkey. The animals were fed year-round in semi-open pastures and a free-roaming barn with concentrate feed containing barley and a ration containing dry meadow grass, corn silage, alfalfa and hay. The age, lactation number, lactation period, daily milk yield, and previous disease information of the cows used as material were obtained.

The cows included in the study were divided into two groups as the cows that were pregnant in the 2nd and 4th months of pregnancy (n=30) Group I and the cows that completed the normal gestation period (n=30) as Group II. Cows in Group II were selected from clinically healthy cows with body condition scores varying from 3.5 to 3.8 and on the 15th postpartum day. Group 2 was formed as a control group by selecting clinically healthy animals on the 15th postnatal day. Blood samples were taken from the cows once in 10 ml tubes, then their serums were removed and the serums were kept at -80 ˚C.

Biochemical parameters and asprosin levels were measured in the collected blood serum.

Approval for the research was obtained from Bingöl University Experimental Animals Ethics Committee (Date and Number: 15/03/2022-E.54083).

2.1. Biochemical Analyzes

ALP, CK-MB, CK-NAC, GGT, AST, ALT, Direct bilirubin, Total bilirubin, Ca, CHO, Creatine, Glucose, Total protein, Urea, Albumin, Iron, Phosphorus, LDH-P, HDL-C, LDL , Triglyceride, Mg and UIBC analyzes were performed using an autoanalyzer (SIEMENS, ADVIA 2400, USA) [17]. These analyzes were performed in Fırat University Veterinary Faculty Animal Hospital Diagnostic Laboratory.

2.2. Measuring Asprosin Levels

Asprosin levels in the blood serum were determined using a commercial enzyme-linked immunosorbent assay (ELISA) kit (Sunred Bovine Asprosin Kit, Shanghai) and reading the levels on an ELISA reader (Bio Tek Instruments, USA) as described [7].

2.3. Statistical Analysis

First of all, descriptive statistics of the data obtained at the end of the research were calculated. It was analyzed and evaluated whether the data were normally distributed and whether they met the parametric test assumptions for all the examined features. Then, the independent student t test was used for comparisons between groups for all parameters. The Pearson method was used to calculate the correlation coefficients between Asprosin and other parameters within each group and overall [18]. SPSS program was used in all statistical analyzes [19].

3. RESULTS

As a result of the comparison of the biochemical parameters of the cows in group I and group II (ALP, amylase, CK-MB, CK-NAC, GGT, AST, ALT, albumin) between the groups, no statistically significant difference was found (P>0.05), (Table 1).

Table 1. Comparison of biochemical parameters between groups I.

	Group I			Group II			
	n	**Mean**	**Std. Error of Mean**	**n**	**Mean**	**Std. Error of Mean**	**P**
ALP (U/L)	30	61.17	7.33	30	47.93	4.20	-
Amylase (U/L)	30	136.93	11.71	30	131.73	9.37	-
CK-MB (U/L)	30	125.47	10.85	30	129.37	10.57	-
CK-NAC (U/L)	30	207.07	13.38	30	667.45	322.91	-
GGT (U/L)	30	23.80	1.01	30	24.37	.89	-
AST (U/L)	30	77.89	5.78	30	132.04	29.81	-
ALT (U/L)	30	24.47	2.27	30	27.77	3.46	-
Albumin (g/dl)	30	3.09	.084	30	2.95	.046	-

P, independent student t test

As a result of the comparison of other biochemical parameters (direct bilirubin, total bilirubin, Ca, CHO, creatine, glucose, total protein, urea, iron, phosphorus, LDH-P, HDL-C, LDL, triglyceride, magnesium, UIBC, asprosin) between the groups, the amount of direct bilirubin (0.1119 mg/dl) and total bilirubin (0.2787 mg/dl) of cows in Group II was higher than Group I, the amount of CHO (93.300 mg/dl), HDL-C (49.7333 mg/dl), LDL (29.6333 mg/dl) and asprosin (0.887 mg/dl) amounts were found to be lower than Group I (P<0.005), (Table 2).

Table 2. Comparison of biochemical parameters between groups.

	Group I (n=30)	**Group II (n=30)**	**P**
Iron (ug/dl)	94.0690	84.0333	-
Phosphorus (mg/dl)	4.2818	4.5843	-
LDH-P (U/L)	2828.0667	3263.4667	-
HDL-C (mg/dl)	60.8667	49.7333	.022
LDL (mg/dl)	54.7667	29.6333	.000
Triglyceride (mg/dl)	15.0667	11.4333	-
Mg (mg/dl)	2.4333	5.5500	-
UIBC (ug/dl)	203.2000	193.2000	-
Asprosin (mg/dl)	2.1783	.8887	.000
Direct Bilirubin (mg/dl)	.0713	.1119	.028
Total bilirubin (mg/dl)	.1253	.2787	.010
Ca (mg/dl)	10.0500	10.2967	-
CHO (mg/dl)	118.4000	93.3000	.002
Creatine (mg/dl)	1.3313	1.1633	-
Glucose (mg/dl)	54.1000	45.6552	-
Total protein (g/dl)	6.5833	6.9800	-
Urea (mg/dl)	36.6333	38.5172	-

P, independent student t test

When the asprosin values and biochemical parameters of the animals in Group I were compared, a positive correlation was found between asprosin and albumin

(0.398), direct bilirubin (0.367), total bilirubin (0.459) and creatine (0.522) (P<0.05), (Table 3).

Table 3. Correlation of asprosin with other biochemical parameters in pregnant animals.

Asprosin	1
UIBC	-,061
MG	-,050
Triglyceride	-,094
LDL	,160
HDLC	,195
LDHP	,029
Phosphorus	-,183
Iron	,085
Urea	,220
Total protein	,224
Glucose	-,099
Creatine	,522(**)
CHO	,245
CA	,249
T biluribin	,459(*)
D biluribin	,367(*)
Albumin	,398(*)
ALT	,012
AST	,351
GGT	,018
CKNAC	-,157
CKBM	-,036
Amylase	-,044
ALP	,005
	Asprosin

P < 0.05* significant positive correlation
P < 0.01** significant positive correlation

When the asprosin values and biochemical parameters of the animals in Group II were compared, weak negative correlation (P<0.05) between asprosin and amylase, weak positive correlation (P<0.05) between asprosin and creatine and glucose, moderate negative correlation between asprosin and phosphorus was determined (P<0.01), (Table 4).

Table 4. Correlation of asprosin with other biochemical parameters in non-pregnant animals.

Asprosin	
-,260	**ALP**
-,395(*)	**Amylase**
,123	**CKBM**
,140	**CKNAC**
-.225	**GGT**
,148	**AST**
,155	**ALT**
-,115	**Albumin**
,091	**D biluribin**
,131	**T biluribin**
,285	**CA**
-,161	**CHO**
,444(*)	**Creatine**
,444(*)	**Glucose**
-,108	**Total protein**
-,116	**Urea**
,070	**Iron**
-,629(**)	**Phosphorus**
,118	**LDHP**
,009	**HDLC**
,239	**LDL**
-,280	**Triglyceride**
,190	**MG**
-,150	**UIBC**
1	**Asprosin**

P < 0.05* significant positive correlation
P < 0.01** significant positive correlation

4. DISCUSSION AND CONCLUSION

Determination of the blood biochemical profile in cows is widely used to reveal the causes of diseases or low productivity [20]. It has been reported that blood biochemical parameters are important in the evaluation of the health status of animals, and the determination of these parameters is a standard rule for diagnosing various pathophysiological and metabolic disorders in cattle [21]. Tainturier et al. [22], it is stated that while the activities of AST and GGT show irregular and small changes from time to time during pregnancy and early lactation, ALT activity decreases significantly in the seventh and eighth months of pregnancy and at the beginning of lactation. Stojević et al. [23] reported that there are significant differences in AST, ALT and GGT activities in dairy cows in lactation and dry period according to the lactation stage. In a different study, a significant negative correlation was found between daily milk yield and blood ALT concentration [24]. Prodanovic et al. [25] reported that there was a significant positive correlation between urea nitrogen and lipid content in the liver ten days after calving, and that total protein and albumin concentrations were significantly lower than in the dry period. In a study conducted in sheep, it was stated that serum urea, total bilirubin, direct bilirubin, total protein, albumin, ALT and CK concentrations increased significantly during pregnancy, and serum glucose, creatinine, Ca, ALP and phosphorus concentrations were higher after birth than before lambing [26]. In the study of Sevinç et al. [27], total protein, albumin, glucose, creatinine, inorganic phosphorus, magnesium, AST, ALT, calcium, total and direct bilirubin and urea values were statistically significantly higher in cows followed from the seventh month of pregnancy to the second month of lactation significant differences are reported. In the present study, there was no statistically significant difference as a result of the comparison of ALP, amylase, CK-MB, CK-NAC, GGT, AST, ALT, and albumin between cows in the 2nd and 4th months of pregnancy and the cows on the 15th day after calving. The direct bilirubin and total bilirubin amounts of the cows in Group II were higher than the pregnant cows, and the CHO, HDL-C and LDL amounts were lower than the pregnant cows. It was seen that the obtained findings were mostly in agreement with our source literature. It was concluded that some of the differences were due to factors such as feeding, race and lactation period.

Asprosin is a recently discovered hormone that is released from white adipose tissue during fasting and stimulates hepatic glucose and insulin release by stimulating the feeling of starvation after crossing the blood-brain barrier. In humans, a genetic deficiency in asprosin causes a syndrome characterized by anorexia and extreme weakness. Asprosin rises with fasting and falls acutely with food intake. In the case of intravenous administration of asprosin, it has been reported that it activates the hunger center in the hypothalamus and causes appetite stimulation [3]. It has been reported that the serum asprosin level is increased in obese humans and mice, and neutralization of asprosin through antibody treatment regulates food intake, reduces body weight, and increases insulin sensitivity in mice [5]. Studies have shown that asprosin levels are significantly higher in women with T2DM and positively correlated with insulin resistance in women with polycystic ovary syndrome (PCOS) [4-28]. In other studies with results similar to this study, it is stated that asprosin level is relatively high in patients with T2DM [10-29]. There are not many publications on the levels of the hormone asprosin in cattle. In a study conducted to determine the relationship between asprosin and PCOS [30] heifer ovaries collected from the slaughterhouse were used as material and it was shown that asprosin receptors were expressed in the follicles of the collected ovaries. In another study, it was found that the hormone asprosin is present in the blood serum of cows at a measurable level and is higher in cows with postpartum disease than in healthy cows [31]. In the present study, asprosin level was found to be higher in pregnant cows compared to cows on postpartum 15th day as a result of comparison between groups. As a result of the comparison of the groups within themselves, there was a positive correlation between asprosin and albumin, direct bilirubin, total bilirubin, and creatinine in pregnant cows, a weak negative correlation between asprosin and amylase, a weak positive correlation between asprosin and creatine and glucose, a moderate negative correlation between asprosin and phosphorus in cows on the postpartum 15th day was found.

As a result, when the levels of asprosin and biochemical parameters in pregnant and non-pregnant cows were compared both within themselves and between the groups, it was found that asprosin levels were higher in pregnant cows and there might be negative or positive correlations between this hormone and biochemical parameters. However, it was concluded that it would be beneficial to carry out more comprehensive studies to evaluate the possibility of asprosin being a marker in the problems that may occur by determining the relationship between changes in biochemical parameters.

REFERENCES

[1] Rossato W, Gonzalez F, Dias M, Ricco D, Valle S F, Rosa V, et al. Number of lactations affects metabolic profile of dairy cows. Arch Vet Sci. 2001; 6(2): 83-8.

[2] Payne J, Dew SM, Manston R, Faulks M. The use of a metabolic profile test in dairy herds. Vet Rec. 1970; 87: 150-8.

[3] Romere C, Duerrschmid C, Bournat J, Constable P, Jain M, Xia F, et al. Asprosin, a fasting-induced glucogenic protein hormone. Cell 2016; 165(3): 566-79.

[4] Alan M, Gurlek B, Yilmaz A, Aksit M, Aslanipour B, Gulhan I, et al. Asprosin: a novel peptide hormone related to insulin resistance in women with polycystic ovary syndrome. Gynecol Endocrinol. 2019; 35(3); 220-3.

[5] Duerrschmid C, He Y, Wang C, Li C, Bournat J C, Romero C, et al. Asprosin is a centrally acting orexigenic hormone. Nat Med. 2017; 23(12): 1444-53.

[6] Yuan M, Li W, Zhu Y, Yu B, Wu J. Asprosin: a novel player in metabolic diseases. Front Endocrinol. 2020; 11: 1-7.

[7] Ugur K, Aydin S. Saliva and blood asprosin hormone concentration associated with obesity. Int J Endocrinol. 2019; 2019.

[8] Sünnetçi Silistre E, Hatipoğlu HU. Increased serum circulating asprosin levels in children with obesity. Pediat Int. 2020; 62(4); 467-76.

[9] Wang M, Yin C, Wang L, Liu Y, Li H, Li M, et al. Serum asprosin concentrations are increased and associated with insulin resistance in children with obesity. Ann Nutr Metab. 2019; 75(4); 205-212.

[10] Zhang L, Chen C, Zhou N, Fu Y, Cheng X. Circulating asprosin concentrations are increased in type 2 diabetes mellitus and independently associated with fasting glucose and triglyceride. Clin Chim Acta. 2019; 489; 183-8.

[11] Wang Y, Qu H, Xiong X, Qui Y, Liao Y, Chen Y, et al. Plasma asprosin concentrations are increased in individuals with glucose dysregulation and correlated with insulin resistance and first-phase insulin secretion. Mediators Inflamm. 2018; 2018.

[12] Gozel N, Kilinc F. Investigation of plasma asprosin and saliva levels in newly diagnosed type 2 diabetes mellitus patients treated with metformin. Endokrynol Pol. 2021; 72(1): 37-43.

[13] Deniz R, Yavuzkir S, Ugur K, Ustebay D U, Baykus Y, Ustebay S, et al. Subfatin and asprosin, two new metabolic players of polycystic ovary syndrome. J Obstet Gynaecol. 2021; 41(2): 279-84.

[14] Ruth J, Thorben H, Tawfik MYA, Gerhard S, Jörg D, Eva H R, et al. Asprosin in pregnancy and childhood. Mol Cell Pediatr. 2020; 7(18).

[15] Baykus Y, Yavuzkir S, Ustebay S, Ugur K, Deniz R, Aydin S. Asprosin in umbilical cord of newborns and maternal blood of gestational diabetes, preeclampsia, severe preeclampsia, intrauterine growth retardation and macrosemic fetus. Peptides. 2019; 120: 170132.

[16] Janoschek R, Hoffmann T, Morcos YAT, Sengle G, Dötsch J, Hucklenbruch-Rother E. Asprosin in pregnancy and childhood. Mol Cell Pediatr. 2020; 7(1): 1-5.

[17] Mamun M, Hassan MM, Shaikat A H, Islam S A, Hoque M A, Uddin M, et al. Biochemical analysis of blood of native cattle in the hilly area of Bangladesh. Bangladesh J Vet Med. 2013; 11(1): 51-6.

[18] Akgul A. Statistical analysis techniques in medical researches “SPSS applications. 3rd ed. Emek Ofset Ltd Sti, Ankara, Turkey; 2005.

[19] Anonim. SPSS 22.0 Statistical Package in Social Sciences for Windows. Chicago, USA; 2016.

[20] Lee A, Twardock A, Bubar R, Hall J, Davis C. Blood metabolic profiles: their use and relation to nutritional status of dairy cows. J Dairy Sci. 1978; 61(11): 1652-70.

[21] Hagawane S, Shinde S, Rajguru D. Haematological and blood biochemical profile in lactating buffaloes in and around Parbhani city. Vet World. 2009; 2(12): 467-9.

[22] Tainturier D, Braun J, Rico A, Thouvenot J. Variations in blood composition in dairy cows during pregnancy and after calving. Res Vet Sci. 1984; 37(2): 129-31.
[23] Stojević Z, Piršljin J, Milinković-Tur S, Zdelar-Tuk M, Ljubić BB. Activities of AST, ALT and GGT in clinically healthy dairy cows during lactation and in the dry period. Vet Arh. 2005; 75(1): 67-73.
[24] Sakowski T, Kuczyńska B, Puppel K, Metera E, Sloniewski K, Barszczewski J. Relationships between physiological indicators in blood, and their yield, as well as chemical composition of milk obtained from organic dairy cows. J Sci Food Agric. 2012; 92(14): 2905-12.
[25] Prodanović R, Sladojević Ž, Kirovski D, Vujanac I, Ivetic V, Savic B, et al. Use of metabolic profiles and body condition scoring for the assessment of energy status of dairy cows. Prodanović R, Sladojević Ž, Kirovski D, et al. Use of metabolic profiles and body condition scoring for the assessment of energy status of dairy cows. Biotechnol Anim Husb. 2012; 28(1): 25-32.
[26] Gürgöze S Y, Zonturlu A K, Özyurtlu N, Icen H. Investigation of some biochemical parameters and mineral substance during pregnancy and postpartum period in Awasi ewes. Kafkas Üni Vet Fak Derg. 2009; 15(6): 957-63.
[27] Sevinç M, Başoğlu A, Birdane F, Gökçen M, Küçükfındık M. The changes of metabolic profile in dairy cows during dry period and after. Turk J Vet Anim Sci.1999; 23(EK3): 475-8.
[28] Li X, Liao M, Shen R, Zhang L, Hu H, Wu J, et al. Plasma asprosin levels are associated with glucose metabolism, lipid, and sex hormone profiles in females with metabolic-related diseases. Mediat Inflamm. 2018; 2018.
[29] Zhang X, Jiang H, Ma X, Wu H. Increased serum level and impaired response to glucose fluctuation of asprosin is associated with type 2 diabetes mellitus. J Diabetes Investig. 2020; 11(2): 349-55.
[30] Maylem E R S, Spicer L J, Batalha I, Schutz LF. Discovery of a possible role of asprosin in ovarian follicular function. J Mol Endocrinol 2021; 66(1): 35-44.
[31] Kilinc M A, Risvanli A. The relationship of asprosin with β-hydroxybutyric acid and postpartum disorders in cows. Acta Vet Hung 2022 ; 70(1), 58-63.

Cilt 11, Sayı 4, Sayfa 117-125, 2022 Volume 11, Issue 4, Page 117-125, 2022

Araştırma Makalesi https://doi.org/10.46810/tdfd.1201248 Research Article

Türk Doğa ve Fen Dergisi
Turkish Journal of Nature and Science
www.dergipark.gov.tr/tdfd

Optimization of Software Vulnerability with the Meta-Heuristic Algorithms

Canan BATUR ŞAHİN[1*]

[1] Malatya Turgut Özal University, Faculty of Engineering and Natural Sciences, Software Engineering Department, Malatya, Türkiye
Canan BATUR ŞAHİN ORCID No: 0000-0002-2131-6368

**Corresponding author: canan.batur@ozal.edu.tr*

(Received: 08.11.2022, Accepted: 13.12.2022, Online Publication: 28.12.2022)

Keywords
Meta-heuristic algorithm,
Optimization,
Clock-work mechanism,
Software vulnerability

Abstract: In order to ensure the development of secure software, it is essential to predict software vulnerabilities. Nevertheless, there can be considerable losses in case of an attack on an information system. Detecting a dangerous code, which can lead to severe unknown consequences, requires great effort. There is a strong need to devise meta-heuristic-based approaches to provide effective security and prevent vulnerabilities or mitigate them. The primary focus of studies on software vulnerability prediction models is to specify the best set of predictors that are related to the presence of vulnerabilities. However, the existing vulnerability detection methods suffer from coarse detection granularity and a bias toward global features or local features. The framework proposed in the present work improves optimization algorithms for the best set of optimized vulnerability patterns correlated for software vulnerabilities based on a clock-work memory mechanism. Using the proposed framework, we found vulnerable optimized patterns based on clock-work memory mechanism feature representation learning that directly. The effectiveness of the developed algorithm was further improved with the clock-work memory mechanism based on 6 open-source projects, such as LibTIFF, Pidgin, FFmpeg, LibPNG, Asteriks, and VLC media player datasets.

Meta-Sezgisel Algoritmalar ile Yazılım Güvenlik Açıklarının Optimize Edilmesi

Anahtar Kelimeler
Meta-sezgisel algoritmalar,
Optimizasyon
, Saat-hafıza mekanizması,
Yazılım güvenlik açığı

Öz: Yazılım güvenlik açığının tahmini, güvenli yazılım geliştirmek için önemli bir husustur. Ancak, bir bilgi sistemine saldırı yapıldığında büyük kayıplara neden olabilir. Tehlikeli kodun tespiti büyük çaba gerektirir ve bu da bilinmeyen ciddi sonuçlara yol açabilir. Etkili güvenlik sağlamak ve güvenlik açıklarının oluşmasını önlemek veya güvenlik açıklarını azaltmak için meta-sezgisel tabanlı yaklaşımlar geliştirmeye güçlü bir ihtiyaç vardır. Yazılım güvenlik açığı tahmin modelleri üzerine yapılan araştırmalar, temel olarak, güvenlik açıklarının varlığı ile ilişkili en iyi tahmin ediciler kümesini belirlemeye odaklanmıştır. Buna rağmen, mevcut güvenlik açığı algılama yöntemleri, genel özelliklere veya yerel özelliklere yönelik önyargı ve kaba algılama ayrıntı düzeyine sahiptir. Bu yazıda, önerilen çerçeve, bir saat-çalışma belleği mekanizmasına dayalı yazılım güvenlik açıkları ile ilişkili en iyi optimize edilmiş güvenlik açığı kalıpları kümesi için optimizasyon algoritmalarını geliştirmektedir. Geliştirilen algoritmanın etkinliği, LibTIFF, Pidgin, FFmpeg, LibPNG, Asteriks ve VLC medya oynatıcı veri kümeleri gibi 6 açık kaynak projesine dayanan saatli çalışan bellek mekanizması ile daha da artırılmıştır.

1. INTRODUCTION

Exploitable vulnerabilities in software considerably weaken computer systems' security and pose a threat to the information technology infrastructure of numerous government organizations and sectors. Software vulnerabilities represent exploitable weak points in a source code with the objective of causing harm or loss. Software vulnerabilities are also the root cause of cyberattacks. Detecting vulnerabilities means revealing code snippets that induce errors in particular cases in large code chunks. It is still difficult and requires a lot of time to detect vulnerabilities to date.

A number of techniques are available for detecting software vulnerabilities. It is possible to identify them at design time (without executing the source code) or at run time (while executing the software). Static code analysis (SCA) takes place among the most common design-time techniques and involves code analysis without executing the program for the purpose of identifying possible problems (alerts). It is possible that a part of the above-mentioned alerts are software vulnerabilities. The said process is realized using static analysis tools (SATs), which are either open-source or commercial.

The major branch of detection approaches is the discovery of possible vulnerabilities in the source code. Nevertheless, they have weaknesses, such as high false-positive rates and low efficiency. Whereas the vulnerability detection method that employs machine learning technology has advanced considerably in accuracy and automation, the problems specified below create obstacles to its performance: (1) Long-term dependency between code elements. There is valuable information for detecting vulnerabilities in the dependencies between elements. Nevertheless, elements that are related in semantic terms can be located far from each other. Hence, we suggest an automated software vulnerability framework based on clock-work memory mechanism recurrent neural networks for a representation method. We believe that deep learning algorithms have the capability to capture complex vulnerability patterns.

The need for optimization techniques with higher reliability, particularly meta-heuristic optimization algorithms, has recently arisen because of the constantly increasing complex nature and difficulty of real-world problems. The said techniques are mainly stochastic and perform the estimation of optimal solutions for various optimization problems. Reasoning about processes at multiple time scales is facilitated by Clock-Work RNN (CW-RNN) models. The hidden layer in a CW-RNN is separated into various modules. Each of these modules processes inputs at its temporal granularity, making calculations solely at the prescribed clock rate. Forward connections are present in the CW-RNN, from the input to the hidden layer and from the hidden to the output layer. CWRNN models primarily contribute to discussing long-term dependencies. The architecture of the CW-RNN is similar to that of a simple RNN with an input, output, and hidden layer. There are g modules in the hidden layer, and each of these modules has its clock rate. The neurons within each module are completely interconnected, meaning that the connectivity among neurons of various modules is set on the basis of the modules' clock periods.

The current work makes the following main contributions:

1. The study creates the metaheuristic algorithm-based vulnerability detection system with metaheuristic optimization algorithms,
2. A framework is proposed, improving the detection capability of heuristic approaches based on a clock-work memory for learning optimized patterns to extract the optimized features for detecting software vulnerable codes.
3. Our framework's design is validated by conducting experiments, and the usage of clock-work memory is shown as optimized-feature representations.

The rest of the paper is organized as follows: Section 2 describes the Material and Method Section 3 describes the the proposed Model used in the study. Section 4 describes the Results and Discussion. Section 5 describes the conclusion.

2. MATERIAL AND METHOD

The current part contains the background of the most frequently employed techniques in the literature.   .

2.1. Meta-Heuristic Algorithms

In this part, the bio-inspired metaheuristic algorithms used are given as follows.

2.1.1. Whale optimization algorithm (WOA)

The Whale Optimization Algorithm (WOA) has been newly developed, and its basis is whales' hunting behavior. The mentioned algorithm includes the following three stages: circling hunting, bubble-net attacking, and prey hunting.

In circling hunting, whales first circle the prey and thus set the trap. Afterward, a search agent is selected according to the distance of an individual whale from the prey. After identifying the search agent, the positions of all whales in the group are updated according to the search agent's position, which can be expressed in mathematical terms, as shown below:

$$\vec{D} = [\vec{C}.\ \vec{X} * (t) - \vec{X}(t)] \quad (1)$$

Where $C = 2 * r$, r denotes a random number in the range of 0-1; $\vec{X}$ refers to the local optimal position; $\vec{X}(t)$ current denotes the current position; refers to the iteration number; and represents the distance between every whale and the search agent.

Afterward, whales perform bubble-net attacking by utilizing the spiral around and spiral update methods [15]. They move in the prey's direction spirally according to the search agent. It is possible to determine the updated position of other search agents moving toward the best agent by Equations 2-3 :

$$\vec{X}(t+1) = \vec{X} * (t) - \vec{A}.\vec{D} \quad (2)$$

$$\vec{A} = 2.\vec{a}\ \vec{r} - \vec{a} \quad (3)$$

Eqs. (4) and (5) are used to find the search agent's random position:

$$\vec{D} = [\vec{C}.\ \vec{X}_{rand} - \vec{X}] \quad (4)$$

$$\vec{X}(t+1) = \vec{X}_{rand} - \vec{A}.\vec{D} \quad (5)$$

The shrink position in the movement with a helix shape toward the prey is updated by the whale, as shown in Equation 6:

$$\vec{X}\,(t+1) = \vec{D}\,.\,e^{bL}\ .cos(2\,\pi\,L)\ + \vec{X}\ *\ t \qquad (6)$$

Where $\vec{X}(t+1)$ Updated denotes the whales' updated position; b refers to a constant representing the logarithmic spiral's shape; l represents the distance between the whale and the food. L = −1 denotes the minimum distance to the food, and L = +1 refers to the maximum distance to the food. It was assumed that the possibility of selecting a method for a certain case was 50%, and Equation 7 expresses the chance of choosing the path:

$$\vec{X}\,(t+1) = \begin{cases} \vec{X}*\,(t) - \vec{A}\,.\vec{D} & p < 0.5 \\ \vec{D}\,.\,e^{bL}\ .cos(2\,\pi\,L)\ + \vec{X}\ *\ t & p > 0.5 \end{cases} \qquad (7)$$

Here, p refers to a number chosen in a random way between 0 and 1.

2.1.2. Multi-verse optimizer (MVO) algorithm

The Multi-Verse Optimizer (MVO) takes place among the new swarm intelligence algorithms. Its source of inspiration is the multiverse theory discussing how the big bangs generate multiple universes and the interaction of the said universes with each other via various hole types. In the MVO algorithm, the "white hole" and "black hole" concepts with the objective of exploring the wormholes to utilize the search spaces for formulating a population-based algorithm and considered that every solution was a universe and every variable/attribute in the solution denoted an object in the said universe. Furthermore, there is a fitness value (inflation rate) in every solution, reflecting the solution quality, which is computed by the corresponding objective function.

A solution receives a good objective value in case white holes appear, whereas the solution receives a worse objective value in case black holes appear. With a higher number of interactions between white holes and black holes, the movement of the variable values of the good solutions to poor solutions occurs.

2.1.3. Grey Wolf Optimizer (GWO)

The Grey Wolf Optimizer (GWO) represents a meta-heuristic optimization algorithm. Grey wolves' hunting strategy and leadership hierarchy are mimicked in the GWO. The leadership hierarchy comprises four wolf types, including alpha (the fittest solution), beta (the second-best solution), delta (the third-best solution), and omega (the remaining part of the candidate solutions). In practice, the prey is encircled by grey wolves, who march during the hunt, which is expressed with the equations below:

$$\vec{D} = \left|\vec{C}.\ \vec{X}_p\ (t) - \vec{X}\,(t)\right| \qquad (8)$$

$$\vec{X}\,|(t+1) = \vec{X}_p\ (t)\ - \vec{A}.\,\vec{D} \qquad (9)$$

Here, t represents the current iteration, D displays the movement vector, $\vec{X}_p$ denotes the prey's position vector, A and C refer to the coefficient vectors, and $\vec{X}$ displays a grey wolf's position vector. The calculation of the coefficient vectors (A and C) is performed by means of the equations below:

$$\vec{A} = 2.\vec{a}\ \vec{r}_1\ - \vec{a} \qquad (10)$$

$$\vec{C} = 2.\ \vec{r}_2 \qquad (11)$$

where r1 and r2 are selected in a random manner in the normal range from zero to unity. During iterations, the components of a decrease in a linear way from 2 to 0. By utilizing Equations (10-11), a grey wolf is capable of getting closer to the prey by altering its position around the prey in a random manner.

3. THE PROPOSED METHOD

3.1. Methodology

The objective of the current work is to enhance the effectiveness of meta-heuristic algorithms with the clock-work memory mechanism for predicting software vulnerabilities. The optimized software patterns that were the most appropriate for vulnerability prediction in software systems were obtained. Reasoning about processes at multiple time scales is facilitated by Clock-Work RNN (CW-RNN) models, making calculations solely at the prescribed clock rate. Neurons of various modules are connected on the basis of the modules' clock periods [14].

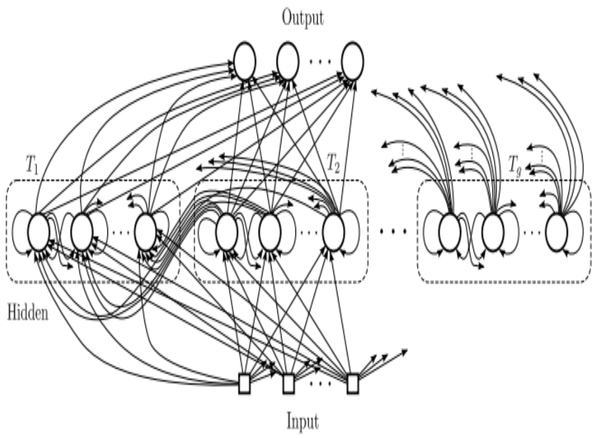

In the CW-RNN, the speed of the clocks is the same all the time, but sometimes they run at a slower speed and sometimes at a faster one. At each CW-RNN time step *t*, just the outputs of module *i*, satisfying(t MOD T_i) = 0, are active. It is arbitrary to choose the set of periods {T_1, . . . , T_g}. In the present work, the exponential series of periods is utilized; the ith module has a clock period of T_i = 2_i−1. In the proposed framework, each metaheuristic algorithm's metadynamics uses the clock-work memory mechanism as a logging function for the optimized best candidate patterns. For each heuristic algorithm, the information is aggregated from generations using a clock-work memory logged mechanism based on time scales.

Algorithm 1. Pseudo-code of the proposed Clock-Work Memory Mechanism

Input : *Set of vectors of vulnerable code :* $X= [X_1, X_2, . . . , X_N]$

Output : *Set of optimized best patterns:* $S_{best}=\{S_1, S_2, ..., S_N\}$;

BEGIN

Step 1: *{Initialize Metaheuristic Algorithms' parameters}*

Step 2: *[1,2,...N] Initialize the solutions' positions randomly.*

Step 3: *Calculate the fitness of each search agent*

Step 4: For *each iteration,* ***do****:*

Step 4.1: *[Train Clock-Work Network]*

Step 4.1.1: For *each search agent* ***do****:*

Step 4.1.2: *update the position of each current search agent*

Step 4.1.3: *Hidden dimensions are updated in groups at time period clock rates.*

Step 4.1.4: *create the clock-work memory based on time scales* $\{T_1, . . . ,T_g\}$ *for each optimized search agents (candidate solutions)*

Step 4.1.5:*Calculate the fitness of each search agents*

Step 4.1.6:END For

Step 4.1.7: *[END Train Clock-Work Network]*

Step 5: END For

Step 6: *Add List optimized best search agents stored in clock-work memory*

Step 7: END For

Step 8:END

CW-RNN separates the hidden recurrent units into 10 g modules, each runs their own computation at specific, hidden layer units as 32, 64 and 128 rates.The explanation of the general experimental methodology is presented in Algorithm 1, designed based on the each baseline metaheuristic algorithms.

Binary encoding is employed for the purpose of representing feature selection or exclusion in the solution set. Every candidate solution is expressed as a bit string having a length *n*, where n refers to the total feature number. Feature *j* was retained in case of the j^{th} bit being equal to 1, whereas it was removed in case of the jthbit being equal to 0.

The fitness function is employed with the objective of showing the quality of each candidate optimized pattern. The fitness of a candidate solution of each nature-inspired algorithm is proportional to the classification error rate of the model.

4. DISCUSSION AND CONCLUSION

The data source includes vulnerable and non-vulnerable functions from the six open-source projects, such as LibTIFF, Pidgin, FFmpeg, LibPNG, VLC media player, and Asterisk. The vulnerability labels were acquired from the National Vulnerability Database (NVD) [11] and the Common Vulnerability and Exposures (CVE) [12] websites. The algorithms are designed for the collective extraction of beneficial information from real-world vulnerability datasets in order to enhance vulnerability detection performance. The Word2vec [1] model is employed in the embedding layer of the Clock-Work Recurrent Neural network in order to convert an input sequence to meaningful embeddings.

Table 1. Dataset

Data source	**Datasource/Collection**	**#of functions used/Collected**	
Real-world Open Sources	FFmpeg	**Vulnerable**	**Non-Vulnerable**
	LibTIFF	213	5701
	LibPNG	96	731
	Pidgin	43	577
	VLC Media Player	29	8,050
	Asteriks	42	3,636

4.1. Results

In Tables 2-7, we compared the performances of the improved heuristic algorithms for detecting vulnerabilities based on the FFmpeg, LibTIFF, LibPNG, Pidgin, Asterisk, and VLC media Player datasets. EvoloPy toolbox contains twenty three benchmarks (F1-F23). In the optimizer.py you can setup your experiment by selecting the test sets. In this study on five test modules (F1-F5). The results demonstrate that the Asterisk dataset displayed the best performance with a 0.029643 error rate for hidden layer unit 128 and test F4, based on the CW-MVO algorithm, compared to the other vulnerability datasets. Nevertheless, according to the results, the worst error rate was found in the LibTIFF dataset with a 0.063467 error rate for hidden layer units 32 and test F5 based on the WOA algorithm. Generally, the FFpmeg, LibTIFF and Pidgin datasets exhibited close error rate performances, except for MVO algorithm. Concerning the other datasets, it was observed that the improved algorithm achieved the highest performance results in the Asteriks, VLC media player, Pidgin, LibPNG, LibTIFF, and FFpmeg datasets, respectively.

Table 2. Error Rate of compared Algorithms for FFpmeg Dataset

Test Benchmark	Hidden Layer units	Algorithms					
		WOA	CW-WOA	GWO	CW-GWO	MVO	CW-MVO
Test F1	32	0.054853	0.052401	0.0575321	0.04920	0.050653	0.05096
	64	0.053425	0.04912	0.0445252	0.04612	0.049034	0.04742
	128	0.047965	0.041231	0.0453258	0.041875	0.047532	0.040094
Test F2	32	0.046744	0.045536	0.0564363	0.050919	0.0553286	0.057168
	64	0.0478532	0.044321	0.0516742	0.047903	0.057754	0.054721
	128	0.0435731	0.04132	0.050584	0.04566	0.053522	0.053663
Test F3	32	0.0606471	0.056726	0.0534211	0.050791	0.0543457	0.049463
	64	0.057854	0.0541267	0.0543245	0.048925	0.056732	0.045412
	128	0.050765	0.052288	0.0513856	0.047164	0.0483878	0.0432609
Test F4	32	0.0564325	0.0517321	0.0564356	0.052452	0.056057	0.056463
	64	0.055736	0.0498425	0.05345673	0.049756	0.055743	0.052557
	128	0.049732	0.045733	0.0494565	0.047654	0.0564537	0.0534435
Test F5	32	0.0614543	0.057841	0.055843	0.054876	0.052345	0.05086
	64	0.0553561	0.059625	0.055372	0.05321	0.049872	0.04773
	128	0.0542423	0.051097	0.0508490	0.047535	0.0415678	0.042195

Table 3. Error Rate of compared Algorithms for LibTIFF Dataset

Test Benchmark	Hidden Layer units	Algorithms					
		WOA	CW-WOA	GWO	CW-GWO	MVO	CW-MVO
Test F1	32	0.0576353	0.050203	0.054352	0.04964	0.0575353	0.050649
	64	0.0512432	0.04734	0.050543	0.04682	0.055356	0.052134
	128	0.048676	0.043651	0.045684	0.043636	0.0523907	0.050036
Test F2	32	0.049756	0.044792	0.053453	0.048659	0.0598543	0.055804
	64	0.046532	0.042143	0.0504221	0.0440867	0.0558641	0.052178
	128	0.041344	0.040974	0.0478942	0.039435	0.052578	0.050932
Test F3	32	0.055632	0.052367	0.05673221	0.049543	0.0578975	0.050754
	64	0.057437	0.0521358	0.0523624	0.0485867	0.0545789	0.052468
	128	0.054633	0.051579	0.0485784	0.0443234	0.0534218	0.050732
Test F4	32	0.052459	0.050952	0.0597428	0.0546573	0.0575432	0.053494
	64	0.0513493	0.0470328	0.0534647	0.050535	0.0538098	0.049053
	128	0.049064	0.044573	0.050432	0.045867	0.0498752	0.046256
Test F5	32	0.063467	0.0597538	0.0545789	0.0519754	0.0508124	0.04572
	64	0.060342	0.0557321	0.05458445	0.05296365	0.048753	0.043723
	128	0.056313	0.0501735	0.0513461	0.04642805	0.0445809	0.0414695

Table 4. Error Rate of compared Algorithms for LibPNG Dataset

Test Benchmark	Hidden Layer units	Algorithms					
		WOA	CW-WOA	GWO	CW-GWO	MVO	CW-MVO
Test F1	32	0.044853	0.03772	0.0475732	0.0366264	0.0456772	0.039963
	64	0.037833	0.034085	0.0413855	0.0347854	0.0406432	0.0383445
	128	0.035356	0.0327045	0.0408253	0.0335466	0.03784214	0.0368952
Test F2	32	0.0495321	0.040558	0.0512345	0.0456779	0.0586328	0.0536874
	64	0.045364	0.041589	0.0509427	0.0437643	0.05743462	0.0527895
	128	0.039752	0.039753	0.0424525	0.039034	0.0528474	0.050643
Test F3	32	0.0543527	0.052356	0.0583252	0.0518514	0.0464632	0.0436784
	64	0.054523	0.0507543	0.0534653	0.0507432	0.0445639	0.0427895
	128	0.049792	0.047059	0.0519478	0.0457322	0.0413563	0.0403468
Test F4	32	0.0567943	0.049743	0.060642	0.049732	0.0584636	0.0516733
	64	0.0512428	0.0469325	0.0574736	0.046457	0.0556473	0.050634
	128	0.0465374	0.043582	0.0508321	0.0413468	0.053452	0.0498368
Test F5	32	0.056975	0.053623	0.054996	0.0506435	0.0595736	0.0458537
	64	0.054245	0.0525672	0.051847	0.0524632	0.0524573	0.0432466
	128	0.049802	0.039953	0.048735	0.0376784	0.0486352	0.035653

Table 5. Error Rate of compared Algorithms for Pidgin Dataset

Test Benchmark	Hidden Layer units	Algorithms					
		WOA	CW-WOA	GWO	CW-GWO	MVO	CW-MVO
Test F1	32	0.0598224	0.0526843	0.0535784	0.047535	0.0574531	0.054566
	64	0.05465893	0.051246	0.0524462	0.043567	0.0534625	0.051457
	128	0.0513750	0.05074	0.0467848	0.0424653	0.0507436	0.048965
Test F2	32	0.0512463	0.046445	0.0575743	0.053546	0.0619357	0.055684
	64	0.0508396	0.0434562	0.0547362	0.050434	0.0587485	0.052356
	128	0.0447497	0.042567	0.0534639	0.051467	0.0553568	0.050754
Test F3	32	0.0587942	0.052435	0.0567387	0.0497543	0.0596492	0.0445663
	64	0.0553683	0.050476	0.05432842	0.046543	0.0535783	0.0421455
	128	0.0507354	0.051389	0.0532424	0.0434656	0.04784281	0.040754
Test F4	32	0.0587639	0.050643	0.0565743	0.0507546	0.0556437	0.053784
	64	0.0528436	0.045345	0.0534564	0.045726	0.05547326	0.0507643
	128	0.04576932	0.042566	0.0475832	0.0416434	0.0497432	0.045878
Test F5	32	0.0609643	0.055743	0.058473	0.052455	0.0565493	0.053561
	64	0.0612485	0.053465	0.0513452	0.0506754	0.05178458	0.0496433
	128	0.0508467	0.048954	0.0487638	0.0464667	0.0478353	0.044527

Table 6. Error Rate of compared Algorithms for VLC Media PlayerDataset

Test Benchmark	Hidden Layer units	Improved Algorithms					
		WOA	CW-WOA	GWO	CW-GWO	MVO	CW-MVO
Test F1	32	0.0456352	0.395433	0.0498532	0.042456	0.0479425	0.041673
	64	0.0425739	0.040754	0.0453694	0.040643	0.043689	0.0398573
	128	0.0389431	0.037955	0.04052783	0.038954	0.0375392	0.03589
Test F2	32	0.0475378	0.0408753	0.0475489	0.042453	0.0497875	0.045643
	64	0.0439625	0.039855	0.0432563	0.0408674	0.0476542	0.0425824
	128	0.0356382	0.0348457	0.0387426	0.035353	0.0343637	0.0398756
Test F3	32	0.0538032	0.0499484	0.0568324	0.048873	0.0537509	0.043673
	64	0.0514587	0.047745	0.0553572	0.045635	0.0446982	0.041566
	128	0.0468743	0.040937	0.0445638	0.042546	0.0408532	0.040753
Test F4	32	0.0538721	0.0468476	0.0486379	0.040742	0.0546848	0.0464095
	64	0.0517939	0.0473456	0.0465395	0.04287567	0.0534743	0.0459372
	128	0.0459372	0.0428457	0.0443761	0.0413456	0.05075298	0.043524
Test F5	32	0.0578463	0.0513674	0.0597463	0.051456	0.0489573	0.044355
	64	0.0548790	0.0478473	0.0565302	0.0508474	0.04574712	0.042466
	128	0.0516840	0.048763	0.0535726	0.045245	0.0423524	0.040837

Table 7. Error Rate of compared Algorithms for Asteriks Dataset

Test Benchmark	Hidden Layer units	Algorithms					
		WOA	CW-WOA	GWO	CW-GWO	MVO	CW-MVO
Test F1	32	0.0457943	0.040536	0.04336456	0.0356466	0.04795821	0.040633
	64	0.0424672	0.037899	0.04074351	0.0367847	0.0445793	0.039745
	128	0.0409201	0.035854	0.03854974	0.0335366	0.0409536	0.0346783
Test F2	32	0.0425565	0.0316783	0.0409732	0.038646	0.04357893	0.0368476
	64	0.0389532	0.0390624	0.0397327	0.0375673	0.0416897	0.03357221
	128	0.0307432	0.031735	0.0335912	0.032573	0.0479434	0.0314742
Test F3	32	0.0407245	0.0375467	0.03356362	0.0324567	0.0485892	0.030635
	64	0.0375372	0.031455	0.0306361	0.0308422	0.043680	0.039654
	128	0.0386847	0.0396325	0.0237975	0.039644	0.04168361	0.035689
Test F4	32	0.0376893	0.0324578	0.0398526	0.03254673	0.04876483	0.033567
	64	0,03482562	0.313657	0.0346938	0.0397455	0.0436789	0.036642
	128	0.03047314	0.306773	0.0297476	0.0345632	0.0456834	0.029643
Test F5	32	0.0384630	0.0346746	0.0386953	0.0339572	0.0435893	0.0377593
	64	0.0335693	0.0345664 3	0.0326891	0.0397455	0.4075256	0.0324567
	128	0.0313574	0.0335736	0.02975327	0.0300484	0.0426894	0.031546

The improved CW-WOA model achieved the best results as a 0.306773 error rate based on test F4 and a 0.0327045 error rate based on test F1 for the Asteriks and LibPNG datasets, respectively, using 128 hidden layer units. Moreover, it was observed that the CW-GWO model achieved the best performance results, such as a 0.0300484 error rate based on test F5 and a 0.0335466 error rate based on test F1 for the Asteriks and LibPNG datasets, respectively, using 128 hidden layer units. The improved CW-MVO model obtained a 0.029643 error rate in test F4 and a 0.035653 error rate in test F5 for the Asteriks and LibPNG datasets, respectively, using 128 hidden layer units. The obtained results indicate that the Asteriks and Pidgin datasets achieved the highest performance for Test-F3 benchmark. However, the findings demonstrate that the best classification error rate performance exhibited for FFmpeg and VLC Media Player datasets based on the Test-F2 benchmark. Furthermore, the best results showed for LibPng and LibTIFF datasets based on Test-F1 benchmark.

All experimental results show that low hidden layers process, retain, and output high error rates. Meanwhile, high hidden layers generally concentrate on the local, high-frequency information with low error-rate performances.

5. CONCLUSION

The application of nature-inspired metaheuristic optimization algorithms for vulnerability detection is an immature area of research having numerous problems waiting for a solution. The representation learning capability of nature-inspired algorithms to optimize patterns of software vulnerabilities and their customizable structure are promising for the automated learning of complex vulnerable patterns, which will motivate and attract a higher number of researchers to ensure a contribution to the said field with high potential. According to the findings acquired, the proposed framework leverages the detection rate of the optimized patterns well, which ensures that vulnerable programming patterns learned from software source projects facilitate the representation generation on a target project to predict vulnerabilities better.

Future studies may include effectively optimized representations with the updated vulnerability dataset to achieve recently improved vulnerability detection performance.

Acknowledgement

The present paper does not include any research with human participants conducted by any of the authors.

REFERENCES

[1] Mikolov, T., Chen, K., Corrado, G., & Dean, J. Efficient Estimation of Word Representations in Vector Space.doi.org/10.48550/arXiv.1301.3781, 2013.

[2] Shi, Y., Wang, Y., & Zheng, H. Wind Speed Prediction for Offshore Sites Using a Clockwork Recurrent Network. Energies, 2022, 15(3), 751.

[3] Koutník, J., Greff, K., Gomez, F., & Schmidhuber, J. A Clock-Work RNN, doi.org/10.48550/arXiv.1402.3511. 2014.

[4] Khurma, R.A., Aljarah, I., Sharieh, A., Mirjalili, S. EvoloPy-FS: An Open-Source Nature-Inspired Optimization Framework in Python for Feature Selection. In: Mirjalili, S., Faris, H., Aljarah, I. (eds) Evolutionary Machine Learning Techniques. Algorithms for Intelligent Systems. Springer, Singapore.https://doi.org/10.1007/978-981-32-9990-0_8, 2020.

[5] Özlem B. D., Canan B. Ş., Prediction of phishing websites with deep learning using WEKA environment, Avrupa Bilim ve Teknoloji Dergisi, vol. 24, pp. 35-41, doi:10.31590/ejosat.901465, 2021.

[6] Guha, R., Chatterjee, B., Khalid Hassan, S.K., Ahmed, S., Bhattacharyya, T., Sarkar, R. Py_FS: A Python Package for Feature Selection Using Meta-Heuristic Optimization Algorithms. In: Das, A.K., Nayak, J., Naik, B., Dutta, S., Pelusi, D. (eds) Computational Intelligence in Pattern Recognition . Advances in Intelligent Systems and Computing, vol 1349. Springer, Singapore. https://doi.org/10.1007/978-981-16-2543-5_42, 2022.

[7] Riyahi, M, Rafsanjani, MK, Gupta, BB, Alhalabi, W. Multiobjective whale optimization algorithm based feature selection for intelligent systems. Int J Intell Syst. 37: 9037- 9054. doi:10.1002/int.22979, 2022.

[8] Abu Khurma, R.; Aljarah, I.; Sharieh, A.; Abd Elaziz, M.; Damaševičius, R.; Krilavičius, T. A Review of the Modification Strategies of the Nature Inspired Algorithms for Feature Selection Problem. Mathematics,10,464.https://doi.org/10.3390/math10030464. 2022.

[9] Rohlfs, C. Generalization in Neural Networks: A Broad Survey. 2022, arXiv. https://doi.org/10.48550/arXiv.2209.01610.

[10] Zhang, G, Ding, Z, Xu, J, Zhong, G, Jiang, N, Zhang, Y. Reasoning and tracing of information security events in the expressway networking system based on deep learning. Int J Intell Syst., 37: 8988- 9012. 2022, doi:10.1002/int.22977.

[11] [Internet]. [cited 2022 November 27]. Available from: https://nvd.nist.gov/

[12] [Internet]. [cited 2022 October 13]. Available from: https://cve.mitre.org/

[13] Batur Şahin, C., Learning Optimized Patterns of Software Vulnerabilities with the Clock-Work Memory Mechanism. Avrupa Bilim ve Teknoloji Dergisi,156-165.2022, https://doi.org/10.31590/ejosat.1159875.

[14] C. B. Şahin, DCW-RNN: Improving Class Level Metrics for Software Vulnerability Detection Using Artificial Immune System with Clock-Work Recurrent Neural Network, 2021 International Conference on INnovations in Intelligent SysTems

and Applications (INISTA), pp. 1-8, 2021, doi: 10.1109/INISTA52262.2021.9548609.
[15] Tansel D., Ayça D. and Hakan K. A Comprehensive Survey on Recent Metaheuristics for Feature Selection. , Neurocomputing, 494, 269-296, 2022.
[16] Abd Elaziz, M., Dahou, A., Abualigah, L. et al. Advanced metaheuristic optimization techniques in applications of deep neural networks: a review. Neural Comput & Applic 33, 14079–14099, 2021, https://doi.org/10.1007/s00521-021-05960-5.
[17] Şahin, C.B., Dinler, Ö.B. & Abualigah, L. Prediction of software vulnerability based deep symbiotic genetic algorithms: Phenotyping of dominant-features. Appl Intell 51, 8271–8287. https://doi.org/10.1007/s10489-021-02324-3. 2021.
[18] Singh, S.K., Chaturvedi, A. Applying Deep Learning for Discovery and Analysis of Software Vulnerabilities: A Brief Survey. In: Pant, M., Kumar Sharma, T., Arya, R., Sahana, B., Zolfagharinia, H. (eds) Soft Computing: Theories and Applications. Advances in Intelligent Systems and Computing, vol 1154. Springer, Singapore. 2020, https://doi.org/10.1007/978-981-15-4032-5_59.
[19] Dinler, Ö.B., Nizamettin A. An Optimal Feature Parameter Set Based on Gated Recurrent Unit Recurrent Neural Networks for Speech Segment Detection. Appl. Sci., 10, 1273. 2020, https://doi.org/10.3390/app10041273.
[20] Ullah, A., Aznaoui, H., Sahin, C. B, Sadie, M., Ozlem Dinler, Ö.B, Imane, L, Cloud computing and 5G challenges and open issues,11-3, 2022, http://doi.org/10.11591/ijaas.v11.i3.pp187193.
[21] Batur Şahin C. , Batur Dinler Ö. , Abualigah L. Analysis of Risk Factors in the Scope of Distributed Software Team Structure. EJOSAT. (28): 417-424, 2021.
[22] Batur Şahin, C., Abualigah, L. A novel deep learning-based feature selection model for improving the static analysis of vulnerability detection. Neural Comput & Applic 33, 14049–14067, 2021. https://doi.org/10.1007/s00521-021-06047-x.
[23] Batur Dinler Ö. , Batur Şahin C. Prediction of Phishing Web Sites with Deep Learning Using WEKA Environment. EJOSAT. 2021; (24): 35-41.
[24] Batur Şahin C. , Diri B. Sequential Feature Maps with LSTM Recurrent Neural Networks for Robust Tumor Classification. Balkan Journal of Electrical and Computer Engineering. 2021; 9(1): 23-32.
[25] Ullah A. , Batur Dinler Ö. , Batur Şahin C. The Effect of Technology and Service on Learning Systems During the COVID-19 Pandemic. EJOSAT. 2021; (28): 106-114.
[26] Ullah A. , Aznaoui H., Batur Şahin C. , Batur, Daanoune I., Dinler Ö. ,CloudIoT paradigm acceptance for e-learning: analysis and future challenges. Jurnal Informatika. 2022; 16(3): 154-168.ISSN 1978-0524.

Cilt 11, Sayı 4, Sayfa 126-134, 2022 Volume 11, Issue 4, Page 126-134, 2022

Araştırma Makalesi https://doi.org/10.46810/tdfd.1201415 Research Article

Türk Doğa ve Fen Dergisi
Turkish Journal of Nature and Science
www.dergipark.gov.tr/tdfd

Deep Learning Based Air Quality Prediction: A Case Study for London

Anıl UTKU[1], Umit CAN[1*]

[1] Munzur University, Engineering Faculty, Computer Engineering Department, Tunceli, Türkiye
Anıl UTKU ORCID No: 0000-0002-7240-8713
Umit CAN ORCID No: 0000-0002-8832-6317

**Corresponding author: ucan@munzur.edu.tr*

(Received: 8.11.2022, Accepted: 13.12.2022, Online Publication: 28.12.2022)

Keywords
Deep learning, London, $PM_{2.5}$ prediction, Machine learning, Air quality prediction

Abstract: Although states take various measures to prevent air pollution, air pollutants continue to exist as an important problem in the world. One air pollutant that seriously affects human health is called $PM_{2.5}$ (particles smaller than 2.5 micrometers in diameter). These particles pose a serious threat to human health. For example, it can penetrate deep into the lung, irritate and erode the alveolar wall and consequently impair lung function. From this, the event $PM_{2.5}$ prediction is very important. In this study, $PM_{2.5}$ the prediction was made using 12 models, namely, Decision Tree (DT), Extra Tree (ET), k-Nearest Neighbourhood (k-NN), Linear Regression (LR), Random Forest (RF), Support Vector Machine (SVM), Extreme Gradient Boosting (XGBoost), Multi-Layer Perceptron (MLP), Convolutional Neural Network (CNN), Recurrent Neural Network (RNN), Gated Recurrent Unit (GRU), and Long Short-Term Memory (LSTM) models. The LSTM model developed according to the results obtained achieved the best result in terms of MSE, RMSE, MAE, and R^2 metrics.

Derin Öğrenme Tabanlı Hava Kalitesi Tahmini: Londra İçin Bir Vaka Çalışması

Anahtar Kelimeler
Derin öğrenme, Londra, $PM_{2.5}$ tahmini, Makine öğrenmesi, Hava kalitesi

Öz: Hava kirliliğini önlemek için her ne kadar devletler çeşitli önlemler alsada dünyada hava kirleticileri önemli bir problem olarak varlığını sürdürmektedir. İnsan sağlığına ciddi etkileri bulunan hava kirleticilerinden biri ise $PM_{2.5}$ (çapı 2,5 mikrometreden küçük partiküller) olarak adlandırılır. Bu patiküller insan sağlığını ciddi tehdit etmektedir. Örneğin akciğere derinlemesine nüfuz edebilir, alveol duvarını tahriş edebilir ve aşındırabilir ve sonuç olarak akciğer fonksiyonunu bozabilir. Bundan olayı $PM_{2.5}$ tahmini çok önemlidir. Bu çalışmada Decision Tree (DT), Extra Tree (ET), k-Nearest Neighbourhood (k-NN), Linear Regression (LR), Random Forest (RF), Support Vector Machine (SVM), Extreme Gradient Boosting (XGBoost), Multi-Layer Perceptron (MLP), Convolutional Neural Network (CNN), Recurrent Neural Network (RNN), Gated Recurrent Unit (GRU) ve Long Short-Term Memory (LSTM) modelleri olmak üzere toplam 12 model kullanılarak $PM_{2.5}$ tahmini yapılmıştır. Elde edilen sonuçlara göre geliştirilen LSTM modeli MSE, RMSE, MAE ve R^2 metrikleri cinsinden en iyi sonucu elde etmiştir.

1. INTRODUCTION

As a result of the high population density and increasing rapid industrialization throughout the world, an increase in the emission of air pollutants has inevitably occurred. Gaseous pollutants and particulate matter, which are very small particles, form air pollutants. The different properties of these tiny particles (PM), including their size, determine the impact power of PM. Defined as a PM group, $PM_{2.5}$, despite its small diameter length, has a large surface area and therefore can transport various toxic substances, pass through the filtration of the nasal hairs, reach the end of the respiratory tract with the airflow, and accumulate there. Thus, it can damage other parts of the body through air exchange in the lungs [1]. It has also been shown that long-term exposure to $PM_{2.5}$, is associated with fatal outcomes by increasing the incidence of diseases such as heart disease (16% increase) and stroke (14% increase) [2].

Increasing urbanization plays a vital role in public health exposure to deadly problems. As a result of industrial activities, intense air pollution occurs. Since people are exposed to $PM_{2.5}$ for a long time, lung cancer, heart disease, and mortality rates increase. Air pollution prediction become a popular area of research. Besides $PM_{2.5}$, the primary air pollutants in urban areas are carbon dioxide (CO2), carbon monoxide (CO), nitrogen dioxide (NO2) and nitrogen monoxide (NO), and PM10 particulate matter. Numerous control measures can be taken to reduce $PM_{2.5}$ emissions. For example, industrial production vehicles equipped with new technologies that reduce the emission of air pollutants can be used. In cities, individual heating technologies can be updated instantly. By reducing the use of lump coal, the use of coal with low gas emission rates can be encouraged or incentives can be applied to switch to cleaner fuels such as natural gas. Steps are also needed to reduce dust from construction sites, including promoting more green spaces [3].

Accurate prediction of $PM_{2.5}$ concentration has an important place in determining air quality and taking necessary precautions in this regard. Accurate and effective predictions can guide policymakers in this regard. In the literature, statistical models, deterministic, and machine learning-based methods are used as the basis for $PM_{2.5}$ prediction. Machine learning methods achieve very successful results because they can successfully use complex linear and non-linear relationships. For example, Ma et al. [4] achieved better results on daily $PM_{2.5}$ prediction with the XGBoost method than the WRF-Chem model, which is a deterministic model.

Effective planning is needed to control the emission levels of air pollutants to keep air quality at a high level. From this point of view, it is essential for the success of these plans to make an accurate prediction of $PM_{2.5}$ concentration for the future. For example, a study conducted in Delhi by Masood and Ahmad [5] tried to predict $PM_{2.5}$ by using air quality values covering two years. Two different models, SVM and Artificial Neural Network (ANN) were used for this prediction. According to the results obtained, the prediction performance of ANN is higher than that of SVM. Danesh Yazdi et al. [6] used an ensemble machine learning method to predict $PM_{2.5}$ intensity in the Greater London area. The ensemble method included RF, k-NN, and Gradient Boosting Machine (GBM) methods, and successful results were obtained. The sparseness of meteorological vertical observations has resulted in limitations in the forward prediction of air and air pollution. $PM_{2.5}$ estimation was made using photographic data from the Beijing region of China. Feng et al. [7] used a common camera to automatically photograph day and night lights in an urban area in Beijing between 2019 and 2020. The photographs they obtained can show the processes of cloud, fog, and precipitation by characterizing the scattering effect of $PM_{2.5}$ on visible sunlight or lamps. By using these features, estimation was done with machine learning methods. Successful results were obtained with DT and MLP among these methods. Lv et al. [8] applied three machine learning algorithms to correct deviations in their study to improve numerical prediction accuracy. Their results showed that the RF and SVM models offer much better prediction performance. Enebish et al. [9] compared the performance of six different machine learning algorithms to predict $PM_{2.5}$ concentrations using data between 2010 and 2018 in Ulaanbaatar, Mongolia. Results on the advantage and applicability of machine learning approach in predicting $PM_{2.5}$ levels in an environment with limited resources and extreme levels of air pollution are discussed. In another study, Multiple Additive Regression Trees, Deep Feedforward Neural Network methods, and LSTM based models were used by Karimian et al. [10] to predict $PM_{2.5}$ concentrations effectively at different time intervals. According to the results obtained, the LSTM-based model gave better results. Pak et al. [11] presented a study on the $PM_{2.5}$ prediction for Beijing, China. The hybrid model, developed using CNN and LSTM models, was used to predict the next day's average $PM_{2.5}$. Xiao et al. [12] proposed an ensemble machine learning-based approach. In this study, in which satellite data is used, first of all, missing satellite data is filled with multiple assignments. Then, for the modelling area, China, seven regions were obtained using a spatial clustering method to control for unobserved spatial heterogeneity. Machine learning models such as RF, Generalized Additive Model (GAM), and XGBoost are trained separately for each region. A generalized ensemble model is proposed to incorporate predictions from the models. Kleine Deters et al. [13] developed a machine-learning model that makes effective $PM_{2.5}$ predictions for Quito, Ecuador, a medium-sized city at high altitudes. In this study, weather data obtained from the city of Quito was used. This method aims to categorize different levels of $PM_{2.5}$, has yielded very effective results.

This study, it is aimed to predict the short-term $PM_{2.5}$ values using the measurement data obtained from the Eltham measurement station in London between January 1, 2019 and May 1, 2019. DT, ET, k-NN, LR, RF, SVM, XGBoost, MLP, CNN, RNN, GRU, and LSTM models compared for $PM_{2.5}$ prediction. According to the results obtained, RF gave better results than other machine learning methods. This study emerges as an important study both in terms of the results it has achieved and by comparing a total of twelve successful machine learning and deep learning methods in this field.

2. DEEP LEARNING BASED AIR QUALITY PREDICTION

In this section, the general developmental stages of machine learning models developed for the effective prediction of $PM_{2.5}$, a hazardous air pollutant, were explained. These stages were shown in Figure 1.

2.1. Dataset

In this study, a dataset consisting of hourly $PM_{2.5}$ measurement values taken from 7 different stations in London was used. The dataset consists of hourly measurement values for a total of 120 days between January 1, 2019, and May 1, 2019. The dataset consists of utc, location, parameter, unit, and value attributes. Utc represents time and date information. Location refers to the station name. Parameter refers to $PM_{2.5}$ measurements. The unit stands for µg/m3 measurement unit. The value represents the measured $PM_{2.5}$ value. In this study, the data obtained at the London Eltham measuring station were used. The dataset is available on Kaggle [14]. Figure 2 shows $PM_{2.5}$ concentrations over time for the London dataset.

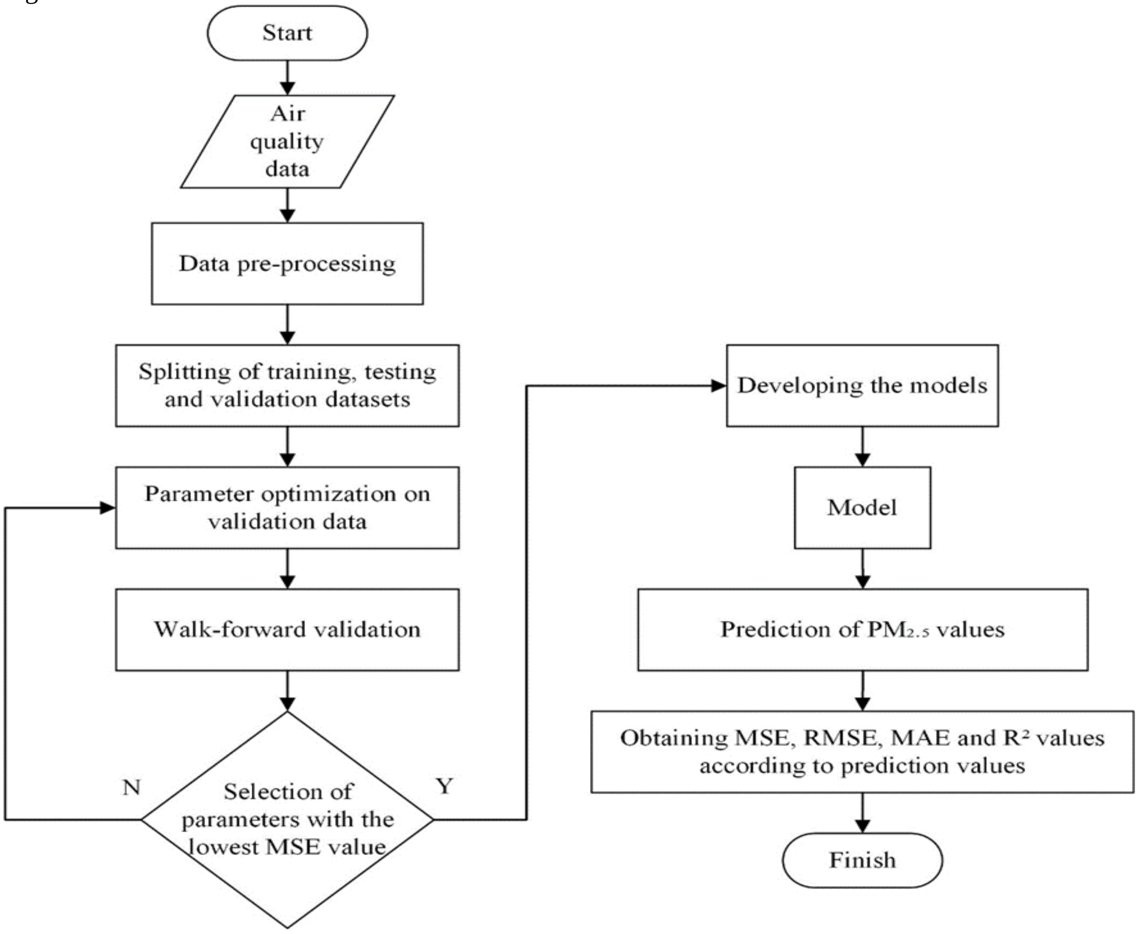

Figure 1. Flow chart of developed machine learning based prediction models

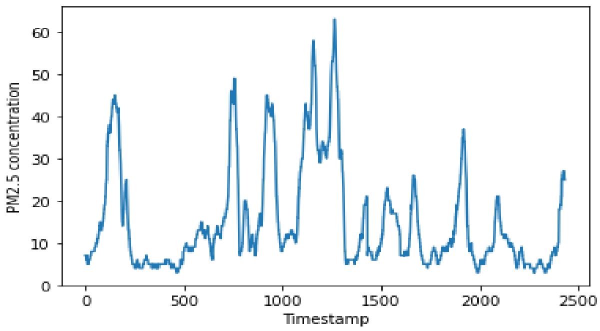

Figure 2. Variation of $PM_{2.5}$ concentrations over time

2.2. Data Pre-processing

In the data pre-processing stage, empty and incorrect fields in the dataset were checked. The dataset used in this study is a time series dataset. Time series data refers to data ordered according to a certain time index. In order to apply machine learning methods to time series data, it is necessary to transform the dataset into a supervised learning problem structure. The sliding window method is used to transform the time series data into a supervised learning problem structure. In the sliding window method, observation data as much as the specified window size is taken as input. The value to be predicted at the next time step is the output. For example, considering the sliding window in 3 dimensions, it is aimed to predict a value at time t_4 using the observation values at time steps t_1, t_2, and t_3. The sliding window shifts one unit to the right after each prediction is made. It is aimed to predict the value in the next time step by using the inputs in the window size determined in this way.

As seen in Figure 3, the dataset is structured as a supervised learning problem in which the pollution value at a certain time can be predicted using the $PM_{2.5}$ values from the past time steps, using the sliding window method.

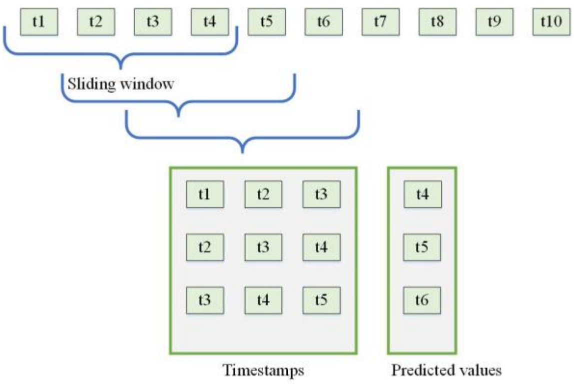

Figure 3. Sliding window method

After transforming the data into a supervised learning problem structure, the measurement values were normalized in the range of 0-1 using MinMaxScaler. The purpose of normalization is to change the values of the numeric columns in the dataset to a common scale without breaking the differences in the range of values. Normalization affects the performance of the developed model and the stability of the training. After the normalization step, the data was split into 80% training and 20% testing. 10% of the training data was split for validation. The dataset was split into training/test sets with 1945 rows of training data and 487 rows of test data. Validation data was used for the optimization of model parameters. In order for the compared machine learning algorithms to give the best results, parameter optimization was made using the GridSearchCV library. In the GridSearch method, a model is built separately with all combinations for the hyperparameters to be tested in the model and their values, and the most successful hyperparameter set is determined. With parameter optimization, the parameters with the lowest MSE values were determined and models were created.

In time series modelling, predictions over time become less and less accurate. Therefore, it is important to retrain the model with real observation data in order to obtain more accurate predictions. Walk forward validation method, as seen in Figure 4, refers to the inclusion of test data in the training process with actual observation values after prediction.

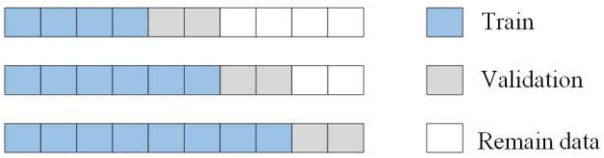

Figure 4. Walk forward validation method

2.2. Prediction Models

In this study, popular machine learning and deep learning methods are used for air quality prediction. These methods are briefly described in this section.

DT: It is a sequential model that efficiently and harmoniously combines a set of core tests in which a numerical feature is compared with a threshold value in each test [15]. DT is an important method in solving classification and regression problems. DT is one of the powerful methods widely used in application areas such as machine learning, image processing, and pattern recognition. For example, it is widely used in marketing, fraud detection, and scientific discovery tasks. The ID3, C4.5, and C5.0 algorithms, which are the classical algorithms of the decision tree, have advantages such as high classification speed, strong learning ability, and simple use [16].

ET: This method is a new tree-based ensemble method for supervised classification and regression problems [17]. It is an effective method used to overcome the disadvantages of traditional DTs and basically consists of strongly randomizing both the feature and the choice of breakpoint when splitting a tree node. Because of the randomization feature for numeric inputs, the ET method is useful for problems involving a large number of numeric features. In such cases, it often contributes to increased accuracy [18].

k-NN: In this method, determining the class of an element in the sample space is determined according to the class of k elements close to it. This method was proposed by T. M. Cover and P. E. Hart [19]. kNN is a classification algorithm based on measuring the distance between sample data. In kNN, the proximity between test samples and training samples is calculated by various distance-measuring methods [20]. k-NN is used for classification, clustering, and regression in various research areas such as financial modelling, image interpolation, and visual category recognition [21].

LR: This model proposed by Vapnik [22] is a statistical model and plays a dominant role in the field of statistical modelling. The LR model aims to develop a regression function to make accurate predictions. Since LR, which is the basis of current methods, has a linear structure, its parameters are easier to interpret. In addition, LR offers successful solutions when the sample space size is small [23].

RF: This method is an ensemble method that makes predictions based on its results from a collection of DTs and was introduced by Ho [24]. In this method, the predictions obtained by combining the DTs are collected. If the number of variables is more than the number of observations in a problem, RF shows high performance in these problems. It has easy adaptability [25].

SVM: It was proposed by Vapnik for solving classification and regression problems [26]. The decision function of the SVM is an optimal "hyperplane" for classifying observations of one class from another based on patterns of knowledge about those observations. This hyperplane can then be used to identify the most likely label for the invisible data [27]. The strength of an SVM comes from its ability to learn data classification models with balanced accuracy and repeatability. Also, SVM is one of the classic machine learning techniques that can help solve big data classification problems. It is especially successful in applications in big data environments [28].

XGBoost: The XGBoost algorithm based on the gradient boosting algorithm was proposed by Chen and Guestrin [29]. XGBoost is one of the best-performing algorithms in supervised learning tasks. It can be used for both regression and classification problems. Apart from basic computing, Xgboost is preferred by data scientists due to its high execution speed [30]. The key innovation of XGBoost is that it adds an edit component to the loss function. Thus, the complexity of the resulting community is taken into account along with predictability in each compartment. In addition, XGBoost allows its users to reduce model overfitting by adjusting multiple hyper-parameters such as forest complexity, learning rate, regularization terms, and column subdomains. XGBoost offers additional innovations such as processing missing data with nodes [31].

MLP: This model, which consists of input, output, and hidden layer, is a feed-forward neural network. The input layer transmits the incoming signal to other layers for processing, and the output layer gives the predictions or classification results. It uses a back propagation technique for learning [32]. A random number of hidden layers placed between the input and output layers is the true computation engine of MLP [33].

CNN: It was first proposed by Fukushima [34] in 1988. It is one of the most widely used and popular deep learning networks. The main advantage of CNN over its predecessors which makes it the most used feature is that it automatically detects important features without any human supervision [35]. CNN gives very good results in pattern recognition applications. It has been successfully used in different application areas by extracting automatic features in areas such as speech recognition and computer vision [36].

RNN: This model is a simple adaptation of a standard feedforward neural network to model sequential data. Text, video, and audio data are sequential data and this model has been used frequently in the processing of this data [37]. At each time step, the RNN receives an input, updates its latent state, and makes a prediction. In the traditional RNN architecture, the RNN can refresh the current state based on past state connections and input states. This is done in a circular structure. The high-dimensional latent state and non-linear nature of RNN are great advantages [38].

GRU: It is a version of RNNs. GRU is similar to LSTM in terms of its internal structure and RNN method with its organization of input and output structures [39]. GRUs are popular methods; the main reason for this is the computational cost and simplicity of the model. GRUs are simpler RNN approaches than standard LSTM in terms of topology, computational cost, and complexity. This technique combines forgetting and entry gates into a single update gate and can combine cell state and hidden state with some other modifications [40].

LSTM: It was suggested by Hochreiter and Schmidhuber [41]. LSTM has an RNN structure and also has a multilayer cell structure. Further LSTM includes state memory. LSTM neural networks gave successful results in pattern recognition and classification tasks, and categorizing audio and images. It is used in many fields, from medicine to statistics, because its sequential data processing features are strong [42].

2.2. Evaluation Metrics

MSE, RMSE, MAE, and R^2 metrics are metrics used to measure prediction accuracy in regression problems. The MSE is calculated using Equation 1 by averaging the squares of the differences between the actual observation values and the predicted values.

$$MSE = \frac{1}{n}\sum_{i=1}^{n}(y-\hat{y})^2 \tag{1}$$

y is the actual values, $\hat{y}$ predicted values and n is the number of samples.

The RMSE is calculated by taking the square root of the MSE and measuring the standard deviation of errors. The RMSE is calculated using Equation 2.

$$RMSE = \sqrt{\frac{1}{n}\sum_{i=1}^{n}(|y-\hat{y}|)^2} \tag{2}$$

MAE expresses the mean of the absolute values of the differences between the actual observation values and the predicted values. Calculates the mean of errors. MAE is calculated using Equation 3.

$$MAE = \frac{1}{n}\sum_{i=1}^{n}|y-\hat{y}\,| \tag{3}$$

R^2 is a measure of the fit of the applied models to the dataset. R^2 evaluates the distribution of data points around the regression line. Higher R^2 values for the same dataset indicate lower errors between actual and predicted values. R^2 is calculated using Equation 4.

$$R^2 = \frac{\sum(y-\hat{y})^2}{(y-\bar{y})^2} \tag{4}$$

$\hat{y}$ is the predicted y values, and $\bar{y}$ is the average of the y values.

3. EXPERIMENTAL RESULTS

In this study, a comparative analysis of DT, ET, k-NN, LR, RF, SVM, XGBoost, MLP, CNN, RNN, GRU, and LSTM models for $PM_{2.5}$ predictions is presented. The results obtained according to MSE, RMSE, MAE, and R^2 metrics for each applied algorithm were analysed comparatively.

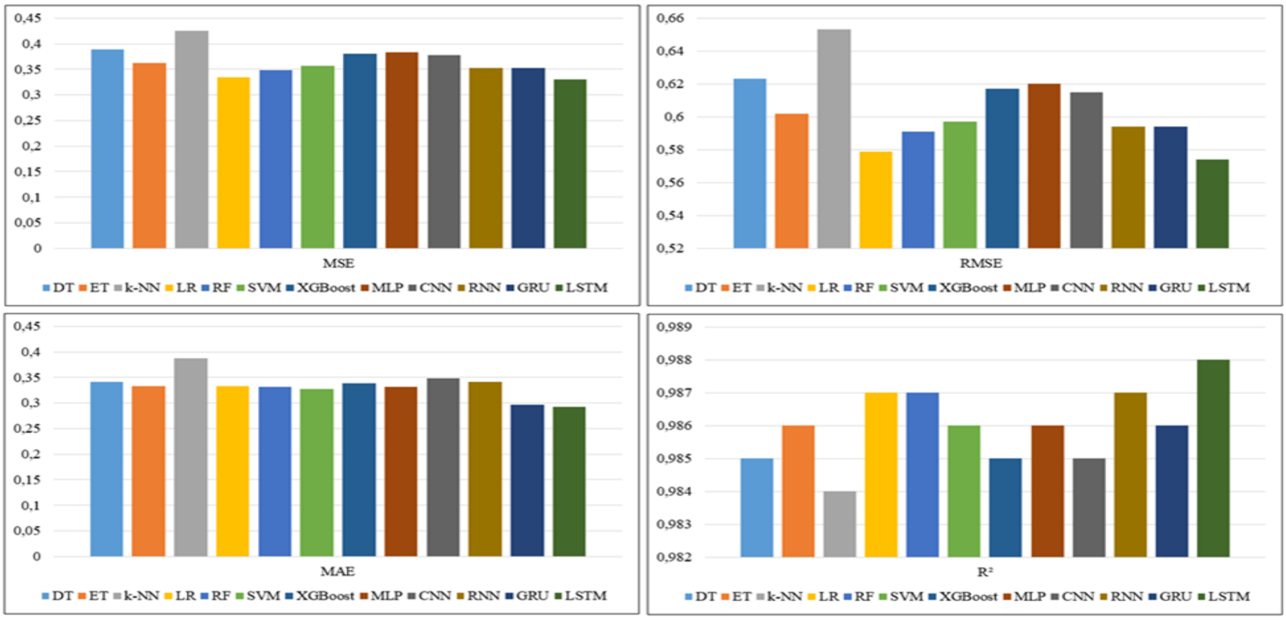

Figure 5. Comparative experimental results

In this study, the sliding window size was tested using values between 2 and 20 to determine the sliding window size. Table 1 shows an example of the test results according to the MAE metric of the models applied to express w different sliding window sizes.

Table 1. Test results for determining the sliding window size

Model	*w*=3	*w*=4	*w*=5	*w*=10	*w*=15	*w*=20
DT	0.341	0.360	0.362	0.521	0.522	0.525
ET	0.333	0.356	0.357	0.437	0.441	0.459
k-NN	0.388	0.414	0.443	0.546	0.600	0.701
LR	0.333	0.334	0.334	0.335	0.335	0.338
RF	0.331	0.348	0.354	0.422	0.429	0.432
SVM	0.328	0.326	0.335	0.343	0.351	0.352
XGBoost	0.339	0.357	0.363	0.445	0.449	0.452
MLP	0.342	0.325	0.331	0.351	0.360	0.367
CNN	0.349	0.327	0.332	0.414	0.424	0.435
RNN	0.331	0.325	0.328	0.346	0.360	0.365
GRU	0.297	0.323	0.327	0.343	0.347	0.354
LSTM	0.292	0.315	0.319	0.319	0.320	0.322

As seen in Table 1, as a result of the experimental studies, when the sliding window size is 3, the lowest error rate was obtained for all models applied. Comparative experimental results are shown in Table 2 and Figure 5.

Table 2. Comparative experimental results

Model	MSE	RMSE	MAE	R^2
DT	0.389	0.623	0.345	0.985
ET	0.363	0.602	0.333	0.986
k-NN	0.426	0.653	0.388	0.984
LR	0.335	0.579	0.333	0.987
RF	0.349	0.591	0.331	0.987
SVM	0.357	0.597	0.328	0.986
XGBoost	0.380	0.617	0.345	0.985
MLP	0.384	0.620	0.331	0.986
CNN	0.378	0.615	0.349	0.985
RNN	0.353	0.594	0.342	0.987
GRU	0.353	0.594	0.297	0.986
LSTM	**0.330**	**0.574**	**0.292**	**0.988**

In Table 1 and Figure 5, it is seen that all the models applied can be used successfully in $PM_{2.5}$ predictions. All compared algorithms have very low MSE, RMSE, and MAE values. Also, R^2 values are high for all models.

Experimental results showed that LSTM had better results than other models compared. After LSTM, GRU, SVM, MLP, RF, LR, ET, RNN, XGBoost, DT, CNN, and k-NN algorithms were successful, respectively. Figure 5 shows the prediction results of LSTM on the test data.

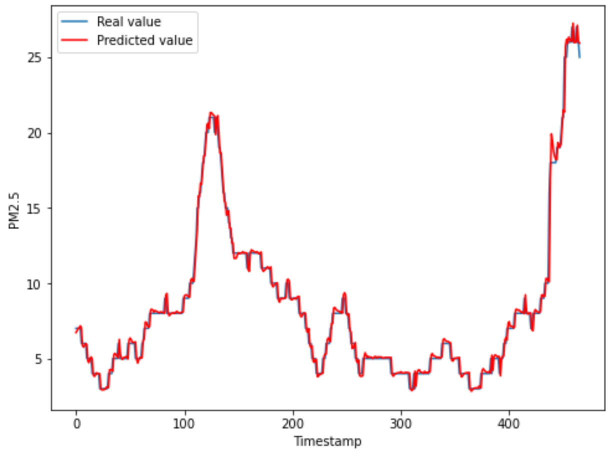

Figure 4. Prediction results of LSTM on test data

As can be seen in Figure 4, the LSTM successfully predicted the fluctuations in the dataset and outperformed the other models compared.

4. CONCLUSION

This study, it is aimed to estimate the short-term $PM_{2.5}$ values using the data obtained from the Eltham measuring station in London between January 1, 2019, and May 1, 2019. DT, ET, k-NN, LR, RF, SVM, XGBoost, MLP, CNN, RNN, GRU, and LSTM models were compared practically according to MSE, RMSE, MAE, and R^2 metrics. Experimental results have shown that LSTM gives more successful results than other models. After LSTM, GRU, SVM, MLP, RF, LR, ET, RNN, XGBoost, DT, CNN, and k-NN algorithms were successful, respectively.

The reason why RF gives better results than k-NN is the values of the features in the dataset. RF basically assumes local similarities and very similar samples are classified in the same way. k-NN can select only the most similar samples based on distance.

The fact that RF has better experimental results than LR can be interpreted as generally that LR performs better when the number of noise variables is less than or equal to the number of explanatory variables. SVM supports both linear and non-linear solutions using kernel trickery. SVM handles outliers better than LR when training data is scarce. In this study, SVM and LR had a close performance.

The fact that LR has better experimental results than k-NN can be interpreted as k-NN is a non-parametric model and LR is a parametric model. The fact that SVM has better performance than k-NN can be interpreted as SVM being more sensitive to outliers. If the training data is much larger than the number of features, k-NN may be more successful than SVM. However, SVM outperforms k-NN when there are lots of features and less training data.

The fact that RF outperforms DT and ET can be interpreted as DT and ET placing high emphasis on a certain set of features. RF randomly selects features during the training process. As such, it is not heavily dependent on any particular feature set. RF can generalize better data. This random selection of features makes RF much more accurate than DTs.

The better performance of RF than XGBoost can be explained by the concept of bias in tree structures. XGBoost relies on weak learners (high bias, low variance) i.e. shallow trees. But RF uses fully grown DTs (low bias, high variance). It performs the error reduction task by reducing the variance.

The fact that RNN is more successful than CNN can be interpreted with the architectures of these models. CNN is a feed-forward neural network. RNN is a feedback neural network. In CNN the size of the input is fixed whereas in RNN the size of the input is variable. The feedback structure in the RNN architecture enabled the past observations to be remembered and presented to the network as input again.

The fact that GRU is more successful than RNN can be interpreted with the structure of GRU that allows long-term dependencies to be remembered. RNN is not successful enough when long-term dependencies need to be learned because of the disappearing gradient problem. The fact that LSTM is more successful than other models compared is that LSTM's architecture includes special units in addition to other iterative neural network architectures. LSTM contains cells that can hold information in memory for long periods. In addition, there are doors used for remembering and forgetting information. This makes it easier to learn about long-term dependencies.

Air pollution forecasting has individual, national, and global implications. Accurate estimation of air pollution is important in terms of people who are sensitive to polluted air, determining public policies, and taking measures to reduce air pollution. The experimental results obtained in this study have shown that air pollution values can be successfully predicted by artificial intelligence methods. By using artificial intelligence-supported air pollution prediction models, it is possible to predict future pollution values and thus take measures to reduce pollution at the national and global levels. In future studies, more successful predictions can be made by using hybrid versions of traditional machine learning models and deep learning models. In addition, these studies can be expanded by using more data sets.

REFERENCES

[1] Xing YF, Xu YH, Shi MH, The impact of PM2. 5 on the human respiratory system. J. Thorac. Dis. 2016;8(1), E69. https://doi.org/ 10.3978/j.issn.2072-1439.2016.01.19Lian YX.

[2] Hayes RB, Lim C, Zhang Y, Cromar K, Shao Y, Reynolds HR, et al. PM2. 5 air pollution and cause-specific cardiovascular disease mortality. Int. J. Epidemiol. 2020;49(1), 25-35.

[3] He K, Yang F, Ma Y, Zhang Q, Yao X, Chan CK, et al. The characteristics of PM2. 5 in Beijing, China. Atmos. Environ. 2001; 35(29), 4959-4970. https://doi.org/10.1016/S1352-2310(01)00301-6

[4] Ma J, Yu Z, Qu Y, Xu J, Cao Y. Application of the XGBoost machine learning method in PM2. 5 prediction: A case study of Shanghai. Aerosol Air Qual. Res. 2020; 20(1), 128-138. https://doi.org/10.4209/aaqr.2019.08.0408

[5] Masood A, Ahmad K. A model for particulate matter (PM2. 5) prediction for Delhi based on machine learning approaches. Procedia Comput. Sci. 2020; 167, 2101-2110. https://doi.org/10.1016/j.procs.2020.03.258

[6] Danesh Yazdi M, Kuang Z, Dimakopoulou K, Barratt B, Suel E, Amini H, et al. Predicting fine particulate matter (PM2. 5) in the greater London area: an ensemble approach using machine learning methods. Remote Sens. 2020; 12(6), 914. https://doi.org/10.3390/rs12060914

[7] Feng L, Yang T, Wang Z. Performance evaluation of photographic measurement in the machine-learning prediction of ground PM2. 5 concentrations. Atmos. Environ. 2021;262, 118623. https://doi.org/10.1016/j.atmosenv.2021.118623

[8] Lv L, Wei P, Li J, Hu J. Application of machine learning algorithms to improve numerical simulation prediction of PM2. 5 and chemical components. Atmos. Pollut. Res. 2021; 12(11), 101211. https://doi.org/10.1016/j.apr.2021.101211

[9] Enebish T, Chau K, Jadamba B, Franklin M. Predicting ambient PM2. 5 concentrations in Ulaanbaatar, Mongolia with machine learning approaches. J. Exposure Sci. Environ. Epidemiol. 2021; 31(4), 699-708. https://doi.org/10.1038/s41370-020-0257-8

[10] Karimian H, Li Q, Wu C, Qi Y, Mo Y, Chen G, et al. Evaluation of different machine learning approaches to forecasting PM2. 5 mass concentrations. Aerosol Air Qual. Res. 2019; 19(6), 1400-1410. https://doi.org/10.4209/aaqr.2018.12.0450
[11] Pak U, Ma J, Ryu U, Ryom K, Juhyok U, Pak K, et al. Deep learning-based PM2. 5 prediction considering the spatiotemporal correlations: A case study of Beijing, China. Sci. Total Environ. 2020;699, 133561. https://doi.org/10.1016/j.scitotenv.2019.07.367
[12] Xiao Q, Chang HH, Geng G, Liu Y. An ensemble machine-learning model to predict historical PM2. 5 concentrations in China from satellite data. Environ. Sci. Technol. 2018;52(22), 13260-13269. https://doi.org/10.1021/acs.est.8b0291
[13] Kleine Deters J, Zalakeviciute R, Gonzalez M, Rybarczyk Y. Modeling PM2. 5 urban pollution using machine learning and selected meteorological parameters. J. Electr. Comput. Eng. 2017: 5106045. https://doi.org/10.1155/2017/5106045
[14] Pollution PM2.5 data London 2019 Jan to Apr. Access time: 10 September 2022. https://www.kaggle.com/siddharthnobell/pollution-pm25-data-london-2019-jan-to-apr
[15] Charbuty B, Abdulazeez A. Classification based on decision tree algorithm for machine learning. J. Appl. Sci. Technol. Trends. 2021; 2(01), 20-28. https://doi.org/10.38094/jastt20165
[16] Brijain M, Patel R, Kushik MR, Rana K. A survey on decision tree algorithm for classification. Int. J. Eng. Dev. Res. 2014;2(1).
[17] Geurts P, Ernst D, Wehenkel L. Extremely randomized trees. Mach. Learn. 2006;63(1), 3-42. https://doi.org/10.1007/s10994-006-6226-1
[18] Sharaff A, Gupta H. Extra-tree classifier with metaheuristics approach for email classification. In Advances in computer communication and computational sciences. 2019. https://doi.org/189-197. 10.1007/978-981-13-6861-5_17
[19] Cover T, Hart P. Nearest neighbor pattern classification. IEEE Trans. Inf. Theory, 1967;13(1), 21-27. https://doi.org/10.1109/TIT.1967.1053964
[20] Ali N, Neagu D, Trundle P. Evaluation of k-nearest neighbour classifier performance for heterogeneous data sets. SN Appl. Sci. 2019; 1(12), 1-15. https://doi.org/10.1007/s42452-019-1356-9
[21] Ertuğrul ÖF, Tağluk ME. A novel version of k nearest neighbor: Dependent nearest neighbor. Appl. Soft Comput, 2017;55,480-490. https://doi.org/10.1016/j.asoc.2017.02.020
[22] Vapnik VN. Statistical learning theory. Wiley;1998.
[23] Su X, Yan X, Tsai CL. Linear regression. Wiley Interdiscip. Rev. Comput Stat. 2012;4(3), 275-294. https://doi.org/10.1002/wics.1198
[24] Ho TK. Random decision forests. Proceedings of the International Conference on Document Analysis and Recognition, ICDAR, Montreal, Canada, 1995. pp. 278–282.
[25] Biau G, Scornet E. A random forest guided tour. Test. 2016;25(2), 197-227. https://doi.org/10.1007/s11749-016-0481-7
[26] Drucker H, Burges CJ, Kaufman L, Smola A, Vapnik V. Support vector regression machines. Adv. Neural Inf. Process. Syst. 1997; 9, 155-161.
[27] Pisner DA, Schnyer DM. Support vector machine. Mach. Learn. 2020. https://doi.org/10.1016/b978-0-12-815739-8.00006-7
[28] Suthaharan S. Support vector machine. Machine learning models and algorithms for big data classification, Springer, Boston, MA, 2016. pp. 207-235.
[29] Chen T, Guestrin C. XGBoost. In Proceedings of the 22nd ACM SIGKDD International Conference on Knowledge Discovery and Data Mining, San Francisco, CA, USA, 2016. pp. 785–794.
[30] Osman AIA, Ahmed AN, Chow MF, Huang YF, El-Shafie A. Extreme gradient boosting (Xgboost) model to predict the groundwater levels in Selangor Malaysia. Ain Shams Eng. J. 2021; 12(2), 1545-1556. https://doi.org/10.1016/j.asej.2020.11.011
[31] Sagi O, Rokach L. Approximating XGBoost with an interpretable decision tree. Inf. Sci. 2021;572, 522-542. https://doi.org/10.1016/j.ins.2021.05.055
[32] Desai M, Shah M. An anatomization on breast cancer detection and diagnosis employing multi-layer perceptron neural network (MLP) and Convolutional neural network (CNN). Clin. eHealth. 2021; 4, 1-11. https://doi.org/10.1016/j.ceh.2020.11.002
[33] Abirami S, Chitra P. Energy-efficient edge based real-time healthcare support system. In Advances in computers. Elsevier; 2020, Vol. 117, No. 1, pp. 339-368. https://doi.org/10.1016/bs.adcom.2019.09.007
[34] Fukushima K. Neocognitron: A hierarchical neural network capable of visual pattern recognition. Neural Netw. 1988; 1, 119–130.
[35] Alzubaidi L, Zhang J, Humaidi AJ, Al-Dujaili A, Duan Y, Al-Shamma O, et al. Review of deep learning: Concepts, CNN architectures, challenges, applications, future directions. J. Big Data. 2021;8(1), 1-74. https://doi.org/10.1186/s40537-021-00444-8
[36] Botalb A, Moinuddin M, Al-Saggaf UM, Ali SS. Contrasting convolutional neural network (CNN) with multi-layer perceptron (MLP) for big data analysis. In 2018 International conference on intelligent and advanced system (ICIAS), Kuala Lumpur, Malaysia: IEEE; 2018. pp. 1-5. https://doi.org/10.1109/ICIAS.2018.8540626
[37] Sutskever I, Martens J, Hinton GE. Generating text with recurrent neural networks. In ICML. 2011.
[38] Yu Y, Si X, Hu C, Zhang J. A review of recurrent neural networks: LSTM cells and network architectures. Neural Comput. 2019;31(7), 1235-1270. https://doi.org/10.1162/neco_a_01199
[39] Yang S, Yu X, Zhou Y. Lstm and gru neural network performance comparison study: Taking yelp review dataset as an example. In 2020 International workshop on electronic communication and artificial intelligence (IWECAI). Shanghai, China: IEEE; 2020. pp. 98-101. https://doi.org/ 10.3978/10.1109/IWECAI50956.2020.00027

[40] Alom MZ, Taha TM, Yakopcic C, Westberg S, Sidike P, Nasrin MS, et al. A state-of-the-art survey on deep learning theory and architectures. Electron. 2019;8(3), 292. https://doi.org/10.3390/electronics8030292
[41] Hochreiter S, Schmidhuber J. Long short-term memory. Neural Comput. 1997;9(8), 1735-1780. https://doi.org/10.1162/neco.1997.9.8.1735
[42] Smagulova K, James AP. A survey on LSTM memristive neural network architectures and applications. Eur. Phys. J. Spec. Top. 2019;228(10), 2313-2324.

Cilt 11, Sayı 4, Sayfa 135-141, 2022 Volume 11, Issue 4, Page 135-141, 2022

Araştırma Makalesi https://doi.org/10.46810/tdfd.1208075 Research Article

Türk Doğa ve Fen Dergisi
Turkish Journal of Nature and Science
www.dergipark.gov.tr/tdfd

Behavioral Steganography in Social Networks

Muharrem Tuncay GENÇOĞLU*

[1] Fırat University, Vocational School of Technical Sciences, Elazığ, Türkiye
Muharrem Tuncay GENÇOĞLU ORCID No: 0000-0002-8784-9634

**Corresponding author: mt.gencoglu@firat.edu.tr*

(Received: 21.11.2022, Accepted: 13.12.2022, Online Publication: 28.12.2022)

Keywords
Steganography, behavior Steganography, hide the existence of the information, Knapsack algorithm, Social network

Abstract: Recently, using human behavior to hide the existence of information has been at the center of steganography research. In this study, a behavioral steganography algorithm using CMI (Coded Signal Inversion) coding is proposed to minimize the high bit error rate that occurs when transmitting a large number of continuous and identical confidential information in the knapsack algorithm, which is used to improve information transmission efficiency and flexibility of transmission mode in social networks. In the proposed algorithm; Data redundancy is reduced by reducing the number of mutual friends of the sender and each receiver. Then, the proposed algorithm was applied and the results were analyzed. Experimental analysis shows that this scheme improves the practical value of behavioral steganography in social networks and has high security.

Sosyal Ağlarda Davranışsal Steganografi

Anahtar Kelimeler
Steganografi, davranış Steganografisi, bilginin varlığını gizleme, Sırt çantası algoritması, Sosyal ağ

Öz: Son zamanlarda bilginin varlığını gizlemek için insan davranışlarının kullanılması steganografi araştırmalarının merkezinde yer almaktadır. Bu çalışmada, sosyal ağlarda iletim modunun verimliliği ve esnekliğini iyileştirmede kullanılan knapsack algoritmasında çok sayıda sürekli ve özdeş gizli bilgi iletilirken oluşan yüksek bit hata oranını en aza indirmek için CMI (Coded Signal Inversion) kodlaması kullanan bir davranışsal steganografi algoritması önerilmiştir. Önerilen algoritmada; Göndericinin ve her alıcının ortak arkadaşlarının sayısı azaltılarak veri fazlalığı azaltıımıştır. Daha sonra önerilen algoritma uygulanmış ve sonuçlar analiz edilmiştir. Deneysel analiz, bu şemanın sosyal ağlarda davranışsal steganografinin pratik değerini geliştirdiğini ve yüksek güvenliğe sahip olduğunu göstermektedir.

1. INTRODUCTION

Steganography [2,6], known as hiding the existence of data, can be defined as the technology of using information embedding algorithms to hide confidential information on non-secret networks. Continuous improvements in steganalysis techniques reduce the reliability of traditional steganography day by day. The decrease in the reliability of steganography emerges as a serious problem in this field. To eliminate this problem, steganography methods applied against steganalysis have emerged. Recently, using human behavior to hide the existence of information has been at the center of steganography research. Social networks have become an integral part of life today. Especially services such as Facebook, Instagram, Google, and LinkedIn have had an important place in interaction and communication in recent years.

The most important communication features in social networks are time and interaction. Based on these features; Pantic and Husain proposed a social network behavior steganography using the length of Twitter information to convey confidential information [11]. Li et al. used selected social networks and online accounts to hide the existence of information [9] Zhang suggested a similar behavior technique using behaviors in social media [16]. However, this method is very difficult to implement due to the high bit error rate in the transmission of confidential information containing many consecutive identical bits. Zhao et al. proposed an FPGA-based CMI (Coded Mark Inversion) design [17]). Subramanian et al.

proposed a channel-based binary coding technique for secure data transmission in wireless networks [12]. This method is not very useful as it proposes a distributed methodology with a high compression ratio. Çıtlak et al. analyzed the existing methods for detecting spam accounts in the Twitter network and compared the strengths and weaknesses of the methods for distinguishing real users and fake users [1]. Hu et al. proposed a behavioral correlation-based stenographic method for social networks [6]. Kantartopoulos et al. analyzed hostile attacks based on AdaBoost on fake Twitter accounts using machine learning and suggested the use of K-NN for defense [7]. Li et al. proposed a data hiding technique that transforms a secret message directly into a hologram-based fingerprint image obtained from the secret message [8].

The motivation for this study is to reduce the bit error rate mentioned above. For this, a 0-1 knapsack algorithm based on the probabilistic solution finding algorithm [5] proposed by Hu for solving the 0-1 knapsack problem will be proposed.

Firstly, the 0-1 knapsack problem will be introduced in this context. Then, behavioral steganography algorithm flow based on the 0-1 knapsack algorithm will be given. Then, the experimental results of the feasibility analysis will be given. Finally, the findings of the study will be evaluated.

2. 0-1 KNAPSACK PROBLEM

Wang at all. the genetic algorithm is used to solve the 0-1 knapsack problem and the principles and implementation process of the two methods are analyzed [13,14]. Han and Li applied a chaotic transformation with chaotic map image encryption [3,4]. Hu et al. proposed behavioral steganography based on the 0-1 knapsack algorithm. They used CMI coding to solve the high bit error rate when transmitting a large number of continuous and identical confidential information [6].

The Knapsack problem simply aims to fit the most items in a bag. In the 0-1 knapsack problem; All items are either bought or left. It is not possible to take part in the item to be purchased. Therefore, if we indicate with X_i whether an item is bought or not, the problem can be modeled as follows:

$$\sum_{i=1}^{n} p_i x_i$$

to be as large as possible and $x_i \in \{0,1\}$

$$\sum_{i=1}^{n} a_i x_i \leq c_i.$$

In this model, the value of X_i can be 0 or 1. If it is 0, it is not taken from the i element, and when it is 1, the whole element i is taken.

2.1. Coded Mark Inversion (CMI)

"CMI encoding doubles the data rate. A zero is sent as a low to high [01] transition, while a one is sent as either a one (1) or zero (0) depending on the previous state. If it was low the one is sent as a one (1)" [18].

2.2. Arithmetic Coding (AC)

"The basic idea of arithmetic coding is to use a range of numbers between 0 and 1 to represent each possible series of n messages" [10].

3. Behavior Steganography Based on the Proposed Knapsack Algorithm

The detailed process of the proposed behavioral steganography method based on the 0-1 knapsack algorithm between sender and receiver is as follows:

3.1. Sender

To be represented by the Sender S;

Step 1.
$M = [m_1, m_2, \dots, m_l]^T$ binary secret
N = Number of friends of the sender
H_i = similarity matrix that records friend's likes on the sender's posts
In the H matrix, liking is recorded as 1, and dislike as 0.

$$\begin{bmatrix} v(1,1) & v(1,2) & \cdots & v(1,l) \\ \vdots & & \ddots & \vdots \\ v(n,1) & v(n,2) & \cdots & v(n,l) \end{bmatrix}_{nxl} \qquad (1)$$

Step 2.
i: Friend, j: Like status;
The sender sends a secret M message R_i (i= 1,2,…,r_1) to the r_1 receivers. CMI coding is done on M to get rid of consecutive similar bits in M and to obtain the N column [17].

Step 3.
By multiplying H and N, the D post sequence is obtained. G matrix is obtained by encoding the D post matrix with inverse arithmetic coding. Thus, decimal numbers between 0 and 1 with probability p are represented as information strings [12]. The probability P is derived from the H matrix. 1 ratio in rows of H; A probability of 1 gives a probability of 0, a probability of 0. Multiply D by a coefficient b, such as 10^{-1} or 10^{-2}, to get all probabilistic decimals.

$$D = \begin{bmatrix} v(1,1) & v(1,2) & \cdots & v(1,l) \\ \vdots & & \ddots & \vdots \\ v(n,1) & v(n,2) & \cdots & v(n,l) \end{bmatrix}_{nxl} X \begin{bmatrix} 1 \\ 2 \\ \vdots \\ l \end{bmatrix}_{lx1} = [1 \quad 2 \quad \dots \quad n]_{nx1} \qquad (2)$$

Step 4.

The sender marks the tracking movements of n friends according to the G matrix. That is if the element in G is 1, he likes it, if it is 0, he does not like it.

3.2. Receiver

Recipients R_i (i=1,2,…,r_1) and r_1 are the number of recipients, and non-recipients are N_j (j=1,2,..,r_2) and r_2 are the number of non-recipients;
R_i and N_j make possible contacts. well
$K=r_1+r_2$ (3)
All persons are expressed with p_λ $(\lambda = 1,2,\ldots,k)$.

Step 1.
R_i's are selected in p_λ. R_i; It reconstructs the G matrix according to the likes, creating the G_i matrix corresponding to the mutual friends of S and R_i. R_i scans the G_i for rows, removes the same rows, and represents the final matrix with A.

Step 2.
The matrix B is obtained by coding the arithmetic according to the probability P of A. The matrix B is multiplied by b^{-1}. A is a submatrix of G. Since each row of G corresponds to H, R_i observes H to form the matrix corresponding to A and denotes it by C. So C becomes the submatrix of H. N columns are obtained by reconstructing the data, and *M* message is decoded by performing CMI decoding on N. If the receiver's status is represented by a y value, the sender can check the receiver's status based on that y value.
w_λ , is to show the weight of p_λ;
if p_λ is the receiver w_λ>0
If p_λ is not a receiver, let w_λ=y.

$$\sum_{\lambda=1}^{r_1+r_2} w_\lambda = y \quad (4)$$

y will reflect the state of p_λ.

The sender sets a threshold value of $a > y$ and changes the value of a to check the status of p_λ. The relationship between a and y is denoted by

$$\text{argmin(a-y)} = \text{y} \quad (5)$$

When $x_\lambda = 1 p_\lambda$ is a receiver,

When $x_\lambda = 0$, p_λ is not a receiver. This relationship is mathematically

$$\sum_{\lambda=1}^{r_1+r_2} w_\lambda x_\lambda \leq a \quad (6)$$

is expressed by the correlate. That is, the sender selects a threshold to check the p_λ state and uses the minimum difference between a and y for the optimal state of p_λ. Each of p_λ weights of w_λ and a value of v_λ.
The receiver chooses 〖$r_1 p_\lambda$ randomly among $k p_\lambda$ and values for $v_{k\varphi}(\varphi = 1,2,\ldots,r_1)$

$$\sum_{\varphi=1}^{r_1} v_{k\varphi} = v_{[k][c]} \quad (7)$$

checks whether the formula is met. Here $v_{[k][c]}$ is the maximum value of the knapsack problem. If equation (7) is satisfied, all $r_1 p_\lambda$ are receivers, otherwise, the 0-1 knapsack assignment protocol is repeated. The 0-1 knapsack assignment protocol is shown in figure 1.

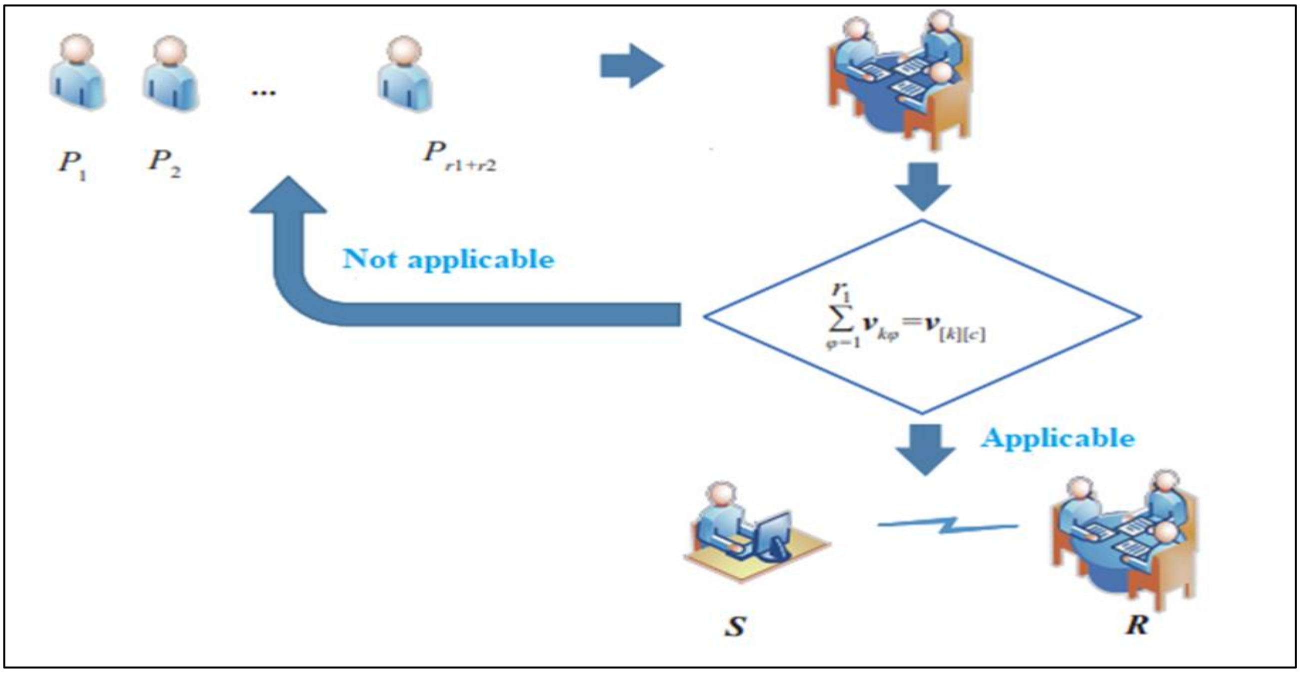

Figure 1. Knapsack personnel assignment protocol

2.3. Algorithm Flow

The detailed process of behavioral steganography based on the proposed 0-1 knapsack algorithm is as follows:

Behavioral steganography algorithm
Input: Secret information *M*, like matrix H, like probability P, knapsack capacity C, value information $V=[v_1,v_2,\ldots,v_k]$, weight information $W=[w_1,w_2,\ldots,w_k]$, $V_{[0][\ ]}=0$, $V_{[\ ][0\ ]}=0$ Output: Secret message *M* 1. Begin CMI encoding on *M* to obtain N; 2. D ← H*N 3. calculate the inverse arithmetic coding of b.D according to P to obtain G; 4. randomly select k sub-matrices of G as the common friends of the sender and k receivers; 5. for i ←1 to k 6. do for j ←1 To c 7. v[i][j] ← v[i - 1][j] ; 8. If (j ≥ wi) 9. v[i][j] ← Max (v[i][j], v[i - 1][j - w_i]+ v_i) ; 10. return v [k][c] ; 11. randomly select r_1 elements in $V=[v_1,v_2,\ldots,v_k]$ (7) is satisfied 12. connect the matrix G_i in turn, and remove the same row of G_i to get the matrix A; 13. find the C corresponding to A in H; 14. calculate the arithmetic code of A according to P, and multiply the result by b^{-1} to get B; 15. reconstruct the solution N according to the data; 16. decode N with CMI to get *M* 17. end

The sender corresponds to lines 1-4 in the pseudocode, the receiver corresponds to lines 5-16 in the ps4.

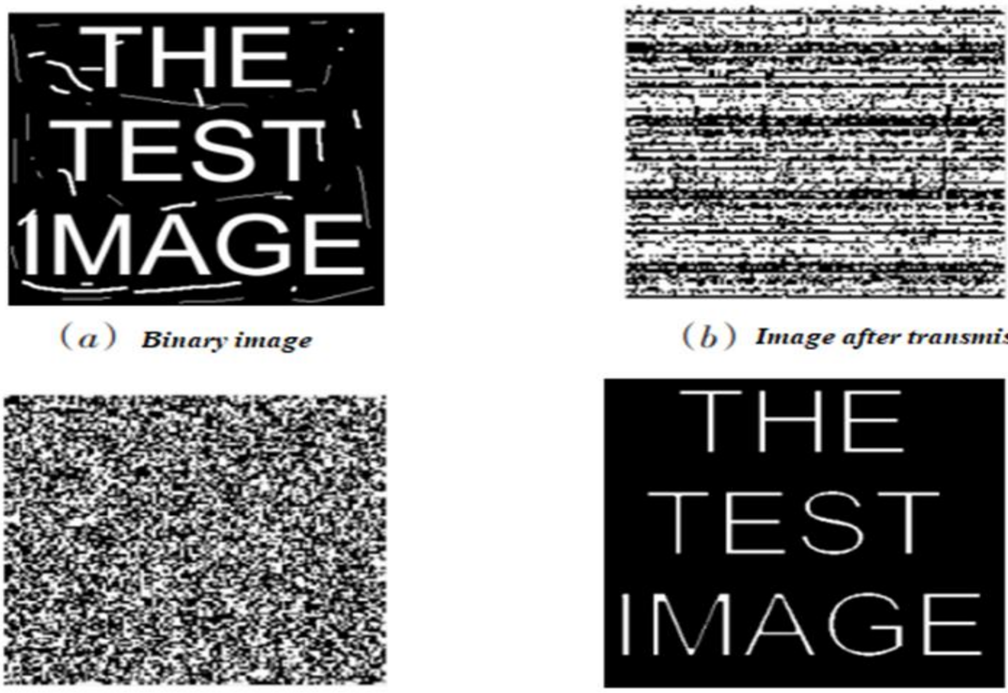

(*a*) *Binary image* (*b*) *Image after transmission* (*c*) *Image after chaotic transformation* (*d*) *CMI coded image*

Figure 2. Feasibility Analysis of Binary Image Transfer

3. EXPERIMENTAL RESULTS

In this section, a user on LinkedIn is selected as a sender, and his friends who meet the conditions are selected as recipients. Tests and analyzes were carried out on these.

3.1. Feasibility Analysis

The 8 friends of S are designated as possible recipients, the bit number of *M* is 16 and the bit number of CMI is 8. First, in a 128x128 binary image transmission examination, 16 pixels are selected as secret information, and 6 bits with at least 8 common friends with S are selected as possible recipients. The sender selects 4 receivers and 2 non-receivers according to the 0-1 knapsack protocol. It splits the 256x256 grayscale image into 8 binary images and performs cross processing. The receiver synthesizes the 8 restored binary images into a grayscale image for bit error rate analysis.

3.2. Feasibility Analysis of Binary Image Transfer

The binary image to be transmitted is given in figure 2(a). The image after the transmission is shown in figure 2(b). Here, the bit error rate is calculated as 48.78%, which is quite high. In this binary image, the arithmetic coding has a greater error rate as there are many consecutive identical bits.

The image as a result of the chaotic transformation is given in figure 2(c). The bit error rate in this image was 51.23 percent. This rate is quite high. The CMI-coded image is shown in figure 2(d). The bit error rate in this image is calculated as 0.03%. Therefore, it is clear that the image obtained with the added CMI code gives better results since it has a low bit error rate.

3.3. Feasibility Analysis of Transferring Grayscale Image

The Lena grayscale image is shown in figure 3(a). The 8 bitmaps separated from the grayscale image are shown in Figure 3(b) and Figure 3(i), respectively. The image separated from the grayscale image after the receiver correction is seen in figure 3(j). The total bit error rate of 8 bitmaps was calculated as 0.46% and the bit error rate of grayscale images was calculated as 2.99%. These experimental results revealed that the proposed method has a low bit error rate and high applicability.

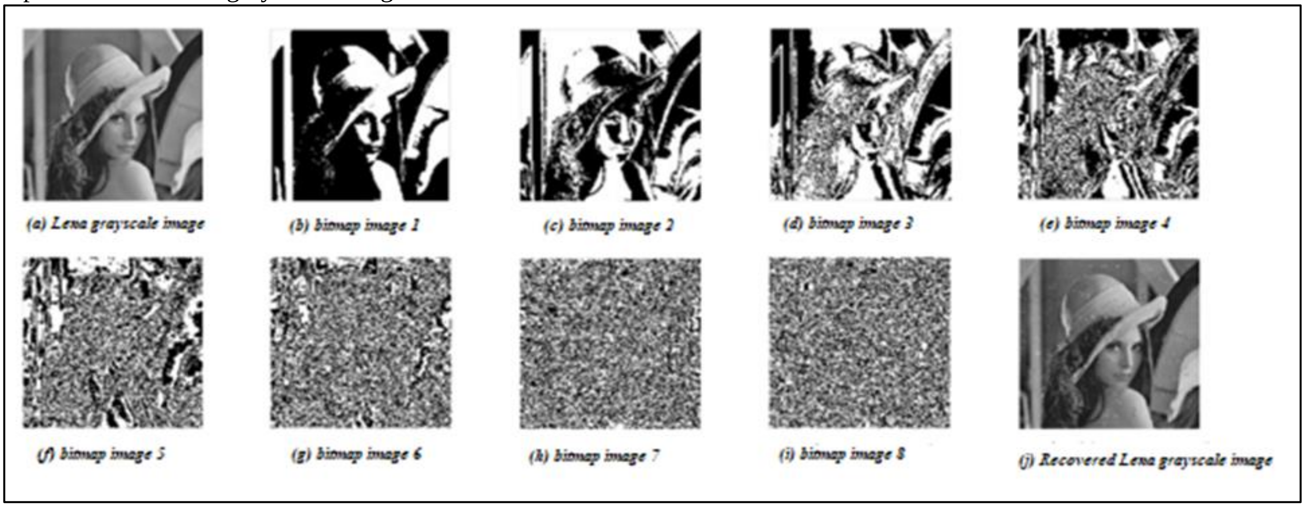

Figure 3. Feasibility Analysis of Grayscale Image Transfer

4. SECURITY ANALYSIS

4.1. Security Analysis Under Brute-Force Attacks

Brute-Force attacks [15] are successful code-breaking attacks that usually target limited capacity password dictionaries and encryption schemes. Although behavioral steganography on social networks has a limited capacity password dictionary, they are resistant to Brute-Force attacks. Therefore, the proposed behavioral steganography is theoretically absolutely safe against Brute Force attacks. The steganalysis algorithm [6] used to detect anomalous similar behaviors using behavioral correlation ranks the actions in the social network according to the increasing number of likes. The difference between d_1 making up less than one-third of the likes, d_2 making up more than two-thirds of the likes, and d_1^l and d_2^l the number of likes made by the two suspects, respectively, and the difference is; It is denoted by $d = \frac{d_1^l}{d_1} - \frac{d_2^l}{d_2}$. If $d < 0.25$, similar behavior is abnormal; otherwise, it is normal. Brute-Force attack and steganalysis methods were used to attack and break the proposed behavioral steganography under different test sets. The statistics of the data set used are shown in Table 1.

Table 1. Sample Statistics of Data Set

Sample Number in the Data Set	Number of Common Friends
50	10
60	12
70	13
80	15
90	17

It is known in the literature that the number of mutual friends between the sender and the receiver increases with the increase in the data set, which will lead to an increase in the total brute force cracking attack [16]. With this data set, in the brute-force attack performed under the 0-1

knapsack algorithm; It was seen that the total capacity of the brute-force dictionary did not change because the mutual friends of the sender and the receiver did not change.

t; To observe the improvement of the security of the 0-1 knapsack algorithm, provided that it shows the capacity of the brute force dictionary, a security analysis was made with different data and the results of this analysis are given in Table 2.

Table 2. Security Analysis with Different Data Sets

Sample Number in the Data Set	h	T
50	3	6545
60	4	124830
70	5	1110785
80	6	4947125
90	7	23853520
100	8	69606485

As a result, with the increase of h, it is seen that the capacity of the brute force dictionary has increased significantly and its security has increased accordingly.

4.2. Feasibility Analysis according to Receivers

For the receiver to correctly extract the confidential information M_{lX1}, the combination of transmission matrices received by other receivers must be less than $2l$ rows.

R_i (i=1,2,…,r_1) receiver and S sender's mutual friends number n_i (i=1,2,…,r_1);

h; It is the arithmetic mean of the number of mutual friends between R_i and S.

$$h = \sum_{i=1}^{r_1} \frac{n_i}{r_1} \quad (8)$$

Taking the data set samples given in Table 1, 4 confidential messages were sent by the sender to 5 friends, provided that the receiver was 3 mutual friends. This process was repeated 1000 times and the results were tested. The results of some of these tests are given in Table 3.

Table 3. Analysis of Receiver ($l = 5, r_1 = 4$)

S	h	h.S	Sonuç ($> 2l$)
2	3	6	<
	4	8	<
	5	10	=
	6	12	>
	7	14	>
	8	16	>
3	3	9	<
	4	12	>
	5	15	>
	6	18	>
	7	21	>
	8	24	>

In this test, it was observed whether the key point about whether the confidential information was transmitted successfully was h.S>2l, not the number of receivers. Therefore, in practice, h must be increased to achieve a high rate of successful transmission of confidential information.

4.3. Security Analysis under Impersonation Attacks

The resistance of the proposed method against impersonation attacks [7] has been tested.
In an impersonation attack; The non-recipient receives the recipient's information and acts as the recipient. Since the process of selecting r1 potential buyers is random in the protocol, there is a probability that the fraudster has successfully impersonated a certain identity.
However, for the proposed protocol, even if the attacker is successful, since he cannot be involved in the communication process, he cannot receive and destroy confidential information. Because this attack has nothing to do with the sample size of the dataset, the attacker hijacks the send matrix. This messes up the matrix and can destroy confidential information.

The analysis process is as follows;

Since the impersonation attack has nothing to do with the sample size of the dataset, the effect of the sample size of the dataset is not taken into account.

r_3 : Number of attackers among non-recipients
p_1 : the probability of success of r1 buyers
p_2 : the probability of the attacker being destroyed
p_3 : the probability of detection of the attacker and interruption of communication

Each event is tested 1000 times, and each time the recipients and non-recipients are randomly selected.

There are three conditions in each experiment:

1. Buyer succeeds
2. The attacker is destroyed
3. During the execution of the protocol, if there are two or more potential recipients with the same knapsack information, the attacker is detected and communication is interrupted.

If one of these three conditions is not met, the protocol is repeated. When the number of attackers is two, the attacker can have two situations;

1. Different receiver
2. Same recipient

These two situations are shown in Table 4 on the right and left of the cells, respectively.

Table 4. Security Testing under Impersonation Attacks

r1	r2	r3	P1 (%)	P2 (%)	P3 (%)
3	2	1	23.4	21.1	63.7
3	2	2	2.5 / 7.0	6.8 / 22.3	25.3 / 41.2
4	2	1	17.5	17.8	74.7
4	2	2	1.2 / 4.9	2.8 / 16.0	21.8 / 57.7

These tests show that the resistance of the proposed protocol against impersonation attacks is quite weak.

5. RESULT

In this study, the social steganography model of the social network 0-1 knapsack algorithm is proposed. While the proposed protocol has good performance against brute force attacks, its security against impersonation attacks is quite low. The capacity to transmit confidential information should be improved.

Acknowledgments

Muharrem Tuncay Gencoglu has been supported by TUBİTAK (121E323) also a member of the working group COST Action CA18232 Mathematical models for interacting dynamics on networks, Belgium.

REFERENCES

[1] Çıtlak O, Dörtler M. and Doğru, İ. A. A survey on detecting spam accounts on Twitter network. Soc.Netw. Anal. Min. 2019, 9:35.
[2] Dutta H, Das R K, Nandi S, An overview of digital audio steganography. IETE Technical Review, 2020, 37(6): 632 - 650.
[3] Evsutin O, Melman S, Meshcheryakov R, V. Digital steganography and watermarking for digital images: a review of current research directions. IEEE Access, 2020, 8: 166589 - 166611.
[4] Han X, Li G. Dynamic cat transformation and chaotic mapping image encryption algorithm.

Computer Engineering and Design, 2020, 41(08): 2381 - 2387.
[5] Hu F. A probabilistic solution discovery algorithm for solving 0-1 knapsack problem. International Journal of Parallel, Emergent, and Distributed Systems, 2018, 33(6): 618 - 626.
[6] Hu Y, Wang Z, Zhang X. Steganography in social networks based on behavioral correlation. IETE Technical Review, 2020, 38(1): 93 - 99.
[7] Kantartopoulos P, Pitropakis N, Mylonas, A. Exploring adversarial attacks and defenses for fake Twitter account detection. Technologies, 2020, 8 (4): 64.
[8] Li S, Zhang X. Towards construction based data hiding: from secrets to fingerprint images. IEEE Transactions on Image Processing, 2019, 28(3): 1482 - 1497.
[9] Li S, H, Wang Z, Lost in the digital wild: hiding information in digital activities. Proceedings of the 2nd International Workshop on Multimedia Privacy and Security. Toronto, Canada: Associate for Computer Mair Coolinghinery, 2018: 27 - 37.
[10] Mesut A, Veri Sikiştirmada Yeni Yöntemler (Doktora Tezi), Trakya Üniversitesi Fen Bilimleri Enstitüsü, Bilgisayar Mühendisliği Anabilim Dalı, 2006. http://dspace.trakya.edu.tr/xmlui/bitstream/handle/trakya/590/0042520.pdf?sequence=1, Erişim 15.04.2022
[11] Pantic N, Husain M. Covert botnet command and control using Twitter. Proceedings of the 31st Annual Computer Security Applications Conference. Los Angeles: Associate for Computer Mair coolinghinery, 2015: 171 - 180.
[12] Subramanian B, Yesudhas H, Enoch G. Channel-based encrypted binary arithmetic coding in a wireless sensor network. Ingénierie des Systèmes d'Information, 2020, 25(2): 199 - 206.
[13] Wang Z, Zhang X, Yin Z. Joint cover-selection and payload-allocation by stenographic distortion optimization. IEEE Signal Process Lett, 2018, 25(10): 1530 -1534.
[14] Yan W, Min W, Jia L, Xiang X. Algorithmic decision analysis of 0-1 knapsack problem. Computer Knowledge and Technology, 2020, 16(04): 259 - 264.
[15] Zhang W, Qin Z, Feng Z, Liu J, Liu W, Tang X. Big data analysis for detection of web brute-force attack. Journal of Shenzhen University Science and Engineering), 2020, 37(S1): 44 - 49.
[16] Zhang X. Behavior Steganography in Social Network. Taiwan, China: Springer International Publishing, 2017: 21 - 23.
[17] Zhao X, Cheng Y, Zuo L, Fang Y. Design of CMI CODEC based on FPGA. Modern Information Technology, 2020, 4(19): 35 - 37.
[18] http://www.interfacebus.com/CMI_Encoding_Definition.html, Erişim: 15.04.2022

Araştırma Makalesi https://doi.org/10.46810/tdfd.1172635 Research Article

Türk Doğa ve Fen Dergisi
Turkish Journal of Nature and Science
www.dergipark.gov.tr/tdfd

An Ethnobotanical Research on Plants Used for Food Purposes in Bigadiç (Balıkesir-Turkey)

Gökhan TANAYDIN[1], Fatih SATIL[2], Uğur ÇAKILCIOĞLU[3]*

[1] Balıkesir University, Department of Plant and Animal Production, Altınoluk Vocational School, Balıkesir, Turkey
[2] Balıkesir University, Faculty of Arts and Sciences, Department of Biology, Balıkesir, Turkey
[3] Munzur University, Pertek Sakine Genç Vocational School, Tunceli, Turkey
Gökhan TANAYDIN ORCID No: 0000-0002-7222-1270
Fatih SATIL ORCID No: 0000-0002-4938-1161
Uğur ÇAKILCIOĞLU ORCID No: 0000-0002-3627-3604

** Corresponding author: ucakilcioglu@yahoo.com*

(Received: 08.09.2022, Accepted: 16.12.2022, Online Publication: 28.12.2022)

Keywords
Balıkesir,
Bigadiç,
Ethnobotany,
Food plants,
Traditional use

Abstract: In this study, the ethnobotanical properties of the plants used by the local people for food in Bigadiç province were investigated. The study was carried out in fifteen rural neighborhoods and two district markets. A total of 104 resource persons, 76 male and 28 female, were interviewed. These plants, which are used among the people, were also identified and collected in their natural environments and their herbariums were made. As a result of the research, it was determined that a total of 51 taxa belonging to 26 families in the region were used for food purposes. The first five families of plants used as food are as follows: Rosaceae (18%), Lamiaceae (12%), Cucurbitaceae (7%), Fabaceae (7%), Moraceae (7%) and others (%41). The first five genera, which are most commonly used by the public, are listed as follows: *Triticum* (21), *Sesamum* (19), *Origanum* (17), *Portulaca* (14) and *Vitis* (14). Mostly fruit/seed (32), leaf (17) and root/stem (3) parts of these plants are used by the public. In the study, the plants that people use as food mostly; eating in the kitchen (22), fruit and fruit juice (21), spice (7), medicinal tea (5), oil (4) and molasses/jam (3). As a result of the study, more diversity was observed in the use of wild plants as food, especially in rural.

Bigadiç (Balıkesir-Türkiye)'te Gıda Amaçlı Yararlanılan Bitkiler Üzerine Etnobotanik Bir Araştırma

Anahtar Kelimeler
Balıkesir,
Bigadiç,
Etnobotanik,
Geleneksel kullanım,
Gıda bitkileri

Öz: Bu çalışmada, Balıkesir ili Bigadiç ilçesinde yerel halkın gıda amaçlı kullandığı bitkilerin etnobotanik özellikleri araştırılmıştır. Çalışma, Bigadiç ilçesindeki on beş kırsalda bulunan mahalle ve merkezde iki semt pazarında gerçekleştirilmiştir. 76'sı erkek ve 28'i kadın toplam 104 kaynak kişi ile görüşülmüştür. Halk arasındaki kullanımı belirlenen bitkiler doğal ortamlarında tespit edilerek toplanmış ve herbaryum materyali haline getirilmiştir. Araştırma sonucunda bölgede 26 familyaya ait toplam 51 taksonun gıda amaçlı kullanıldığı tespit edilmiştir. Gıda olarak kullanılan bitkilerin familyalara göre dağılımında ilk 5 familya şu şekildedir: Rosaceae (%18), Lamiaceae (%12), Cucurbitaceae (%7), Fabaceae (%7), Moraceae (%7). Halk arasında en çok kullanımı belirlenen ilk beş cins ise *Triticum* (21), *Sesamum* (19), *Origanum* (17), *Portulaca* (14) ve *Vitis* (14)'tir. Bu bitkilerin daha çok meyve/tohum (32), yaprak (17) ve kök/gövde (3) bölümleri kullanılmaktadır. Çalışmada halkın gıda olarak yararlandığı bitkileri daha çok; yemek (22), meyve ve meyve suyu (21), baharat (7), tıbbi çay (5), yağ (4) ve pekmez/reçel (3) olarak değerlendirdikleri belirlenmiştir. Çalışma sonucunda, yabani bitkilerin gıda olarak kullanımında özellikle kırsalda daha fazla çeşitlilik görülmüştür.

1. INTRODUCTION

How plants affect people's culture and accumulation, how people use plants, how they are applied and how they are transferred to future generations have always been a matter of curiosity for researchers. However, studies on this subject have mostly been for the medicinal use of plants [1].

Due to its geographical location, being under the influence of different climates, geomorphological structure and the existence of different ecosystems, Turkey has a rich plant diversity. However, due to the fact that it has been home to different civilizations for thousands of years, a rich plant culture has been formed besides this rich plant diversity. For this reason, ethnobotanical studies that will reveal this rich plant usage culture in Anatolia are very important. There are many studies related to ethnobotanical research in our country [2-9].

However, in classical ethnobotanical studies, the use of medicinal plants among the public was investigated [3, 5, 10], whereas plants, in addition to their medicinal uses, have a widespread use in many stages of human life such as food, fuel and handicrafts [11].

Among the general ethnobotanical studies in our country, there are studies in which information about the use of plants as food is given. Koçyiğit (2005) found out that 40 of 99 plant taxa in Yalova were used as food [12]. Yucel et al. (2010) identified 25 taxa belonging to 18 families used as food in their research in Mihalıççık district of Eskişehir province [13]. Aktan (2011) identified plants used for food in his ethnobotanical study in Yenişehir (Bursa) district [14]. Ekren and Çorbacı (2021) stated that 116 taxa were used for food in their study in Rize [15]. In addition, Kıncal (2021) in Muğla province Ula district recorded the use of 69 taxa for food and spice purposes [16].

There are very few studies on the use of plants as food only. Yucel et al. (2010) identified the plants used as food in Mihalıççık district of Eskişehir province [13]. Korkmaz and Karakurt (2015) revealed the traditional use of natural food plants in the Kelkit district of Gümüşhane [17]. There are also some ethnobotanical studies in Balıkesir province and its surroundings that determine the use of plants for food purposes [7, 18-22].

However, ethnobotanical studies on only food types are very limited. In this area, Duran et al. (2001) demonstrated their characteristics of wild fruits during ethnobotanical studies of these plants in Balıkesir province [23]. İnci Aladı et al. (2019) studied wild fruits sold as food in Edremit market and their medicinal properties [24]. Kawarty et al. (2021) determined 62 taxa belonging to 23 families used as food in their study in Ballakayati (Northern Iraq - Erbil) where they gave traditional information about wild food plants [2].

In recent years, diet with natural food has gained importance. Today, fast food meals, foods prepared with various additives to maintain their freshness for a long time, and purified products cause many health problems such as low immunity, obesity and physical and mental diseases related to obesity. For this reason, people have turned to natural foods and organic products, and studies on the use of natural plants as food have become even more important.

In this study; Bigadiç district was chosen because of its rich flora and hosting different civilizations in the past. In the study, the species that the people of the district benefit from for food were determined.

2. MATERIAL AND METHOD

2.1. General Characteristics of the Research Area

Bigadiç district, which is our research area, is located in the southeast of Balıkesir province in the South Marmara part of the Marmara Region.

Bigadiç was established on the eastern edge of the Bigadiç Plain, where Simav Stream passes, and on the west-facing skirts of very steep sloping ridges. The land of the district consists of the deep valley opened by the Simav Stream, which has expanded from place to place and turned into a small Ovacik, and the west-facing slopes of the Alaçam Mountains to the east of this valley. Approximately 30% of the population lives in the city center and 70% in the rural areas.

Bigadiç district has been chosen as the study area because of its rich geographical features, rich plant existence and having hosted different civilizations in the past.

2.2. Method

Study; It was held in fifteen rural neighborhoods and two street markets selected from Bigadiç district between 2020-2021 (Figure 1).

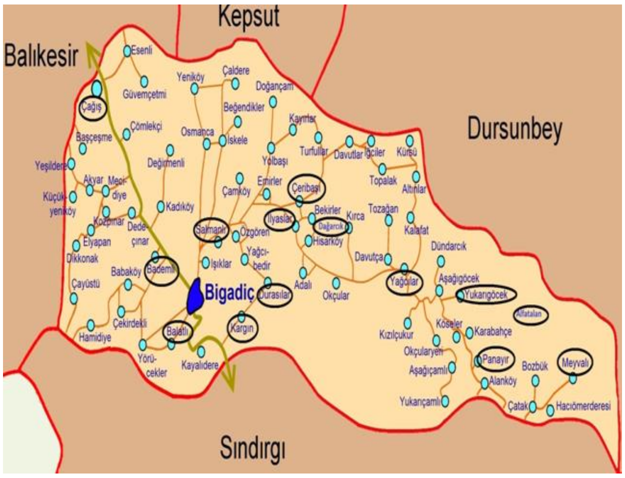

Figure 1. Bigadiç map and rural neighborhoods where the ethnobotanical study was conducted.

2.3. Source Contacts

Nearly all of Bigadiç's population consists of citizens of Manav and Yörük origin. This distribution was taken into consideration when selecting the rural neighborhoods and informants to be studied (Table 1).
104 resource people were interviewed in the rural neighborhoods visited in our research region (Table 1). Of these informants, 76 are male and 28 are female.

Table 1. Demographics of Informants.

Gender	**N**	**%**
Male	76	73.08
Female	28	26.92
Age	**N**	**%**
29-50	33	31.73
51-65	45	43.27
Over 65	26	25.00
Education Status	**N**	**%**
Reader-Writer	3	2.88
Primary school	37	35.58
High school	58	55.77
University	6	5.77

Rural Neighborhoods Visited	**Neighbourhood**	**Origin**
	Alfatalan	Manav
	Bademli	Manav
	Balatli	Manav
	Cagis	Mixed
	Ceribasi	Manav
	Dagarcık	Manav
	Durasilar	Manav
	Ilyaslar	Manav
	Iskele	Manav
	Kargın	Manav
	Meyvalı	Manav
	Panayır	Yörük
	Salmanli	Manav
	Yagcilar	Mixed
	Yukarigocek	Yörük

(N: Number of people)

2.4. Interview Methods

In the interviews with the informants (Figure 2A); Unstructured Interview, Semi-Structured Interview and Focus Group Interview methods were used.

Figure 2. A-Interview with source people, B-Market research.

2.5. The Market Research

Hanimeli and Thursday markets in Bigadiç, which is our research area, were visited periodically at different times and products that were sold and consumed as food were determined (Figure 2B).

2.6. Field Research and Plant Diagnostics

In the study, in order to see and identify the plants used as food on site, they went to the land together with the source people. Photographs of the plants seen in their natural habitats were taken and the collected specimens were turned into herbarium material. Herbarium specimens it has been preserved in the herbarium of the BAUN Faculty of Arts and Sciences with the number GT1001-1103. In the identification of plants, especially "Flora of Turkey and the East Aegean Islands" [25-26] were used in flora and ethnobotanical researches [7, 19, 27].

3. RESULTS AND DISCUSSION

As a result of the study, 51 taxa belonging to 26 families used as food by the Bigadiç people were determined. The family order of these taxa is Rosaceae (18%), Lamiaceae (12%), Cucurbitaceae (7%), Fabaceae (7%), Moraceae (7%) and other (41%) (Figure 3).

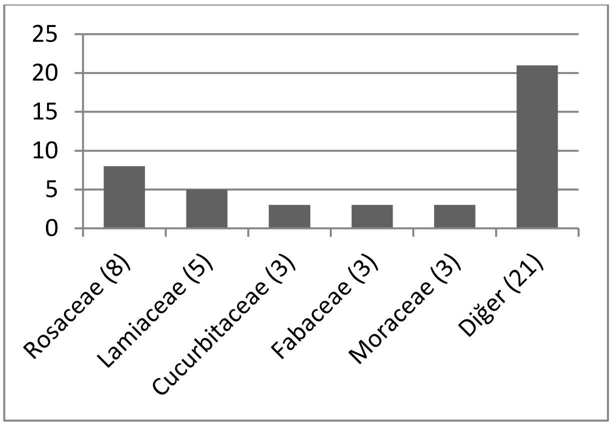

Figure 3. Distribution of taxa whose usage was determined according to families.

The plant species identified as a result of the study; family, Latin name, vernacular name, used part, usage pattern and herbarium number are given in Table 2.

Table 2. Ethnobotanical characteristics of plants used as food in Bigadiç District.

Family	**Taxon**	**Vernacular name**	**Used Part**	**Usage**	**Herbarium No**
Amaranthaceae	*Spinacia oleracea* L.	Ispanak	Leaf	Food	GT1081
Anacardiaceae	*Rhus coriaria* L.	Somak	Fruit	Spice	GT1020
Anacardiaceae	*Pistacia terebinthus* L.	Çitlembik, çetlemik	Fruit	Oil	GT1105
Apiaceae	*Anethum graveolens* L.	Günnem, dere otu	Leaf	Spice	GT1040
Asparagaceae	*Asparagus acutifolius* L.	Kuşkonmaz	Exile	Food	GT1095
Asteraceae	*Cichorium intybus* L.	Hindiba, acı hindiba	Leaf	Food	GT1111
Asteraceae	*Taraxacum microcephaloides* Soest	Karahindiba	Leaf	Food	GT1067
Brassicaceae	*Brassica oleracea* L.	Dürülgen, kelem, lahana	Leaf	Food	GT1019
Brassicaceae	*Raphanus raphanistrum* L.	Turp otu	Leaf	Food	GT1096
Cucurbitaceae	*Cucurbita pepo* L.	Aşkabağı	Fruit	Food	GT1049
Cucurbitaceae	*Citrullus lanatus* (Thunb.) Matsum. & Nakai	Çömez karpuz	Fruit	Food	GT1044
Cucurbitaceae	*Cucumis melo* L.	Serkele, topatan, kavun	Fruit	Food	GT1043
Ebenaceae	*Diospyros kaki* L.	Cennet hurması	Fruit	Food	GT1035
Elaeagnaceae	*Elaeagnus angustifolia* L.	İğde	Fruit	Food	GT1012
Fabaceae	*Phaseolus vulgaris* L.	Ak fasülye, Ayşe kadın, Şeker fasülye, Sırık fasülye	Fruit	Food	GT1060
Fabaceae	*Vicia faba* L.	Bakla	Fruit	Food	GT1100
Fabaceae	*Vigna unguiculata* subsp. *sesquipedalis* (L.) Verdc.	Börülce, Çatak börülcesi	Fruit	Food	GT1051
Fagaceae	*Castanea sativa* Mill.	Kestane	Fruit	Food	GT1091
Juglandaceae	*Juglans regia* L.	Ceviz	Fruit	Food	GT1030
Lamiaceae	*Mentha aquatica* L.	Deli nane	Leaf	Spice	GT1077
Lamiaceae	*Sideritis perfoliate* L.	Antalya adaçayı, Ballıbab, Minare otu	Flower Leaf	Tea	GT1031
Lamiaceae	*Origanum onites* L.	Taş kekiği, Kekik, Dağ kekiği, Akbaş kekik	Leaf Trunk	Tea, Spices	GT1112

Lamiaceae	*Mentha longifolia* subsp. *typhoides* (Briq.) Harley	Nane	Leaf	Tea, Spices	GT1045
Lamiaceae	*Origanum vulgare* L. subsp. *hirtum* (Link) letsw.	Nuz otu, Nuzlu ot, Kekik	Flower Leaf	Tea, Spices	GT1026
Malvaceae	*Abelmoschus esculentus* (L.) Moench	Bamya	Fruit	Food	GT1075
Malvaceae	*Malva sylvestris* L.	Ebegümeci	Leaf	Food	GT1086
Moraceae	*Morus nigra* L.	Karadut	Fruit	Food, Juice	GT1046
Moraceae	*Morus alba* L.	Dut	Fruit	Food	GT1036
Moraceae	*Ficus carica* L.	İncir	Fruit	Food	GT1011
Padaliceae	*Sesamum indicum* L.	Susam	Seed	Oil, Bigadiç Halva	GT1078
Papaveraceae	*Papaver somniferum* L.	Afyan, Ayfan, Haşhaş	Seed	Oil, Pastry	GT1037
Papaveraceae	*Papaver rhoeas* L.	Gelincik	Leaf	Food	GT1042
Poaceae	*Zea mays* L.	Mısır Darı	Fruit	The Fruit Is Boiled. Fame	GT1025
Poaceae	*Triticum durum* Desf.	Karakılçık buğdayı, Kılçıklı	Seed	Food, Flour, Keskek	GT1076
Polygonaceae	*Rumex patientia* L.	Alabada, efelek	Leaf	Food	GT1064
Polygonaceae	*Rumex acetocella* L.	Kuzu kulağı	Leaf	Food	GT1088
Portuguese	*Portulaca oleracea* L.	Semiz otu, Semizlik	Leaf	Food	GT1089
Ranunculaceae	*Nigella sativa* L.	Bayır otu, Çörek otu, Çör otu	Seed	Oil, Spices, Pastry	GT1072
Rhamnaceae	*Ziziphus jujuba* Mill.	Hünnap	Fruit	Food	GT1024
Rosaceae	*Rosa phoenicia* Boiss.	Kuşburnu	Fruit	Marmalade, Tea, Food	GT1058
Rosaceae	*Prunus armeniaca* L.	Kayısı	Fruit	Juice, Food	GT1004
Rosaceae	*Cydonia oblonga* Mill.	Ayva	Fruit	Food	GT1014
Rosaceae	*Prunus spinosa* L.	Güvem, Keçi eriği	Fruit	Food, Juice	GT1055
Rosaceae	*Rubus sanctus* Schreb.	Bayır kırantısı, Böğürtlen kırantı	Fruit	Food, Juice	GT1104
Rosaceae	*Prunus domestica* L.	Mürdüm eriği, Mürdümük	Fruit	Sherbet, Dried and Eaten	GT1050
Rosaceae	*Malus sylvestris* (L.) Mill.	Ağa alma, Almat, Saray elması, Şer elması, Şeytan elması, Elma	Fruit	Food	GT1057
Rosaceae	*Prunus divaricata* Ledeb	Hırsız almaz, Yeşil erik	Fruit	Food	GT1056
Solanaceae	*Solanum tuberosum* L.	Kumpur, Patates	Body	Food	GT1032
Solanaceae	*Lycopersicon esculentum* Mill.	İyişibalcan, Domates	Fruit	Food, Salad	GT1073
Urticaceae	*Urtica dioica* L.	Gıcırgen, Istırgan, Isırgan otu, Cıgirgen	Leaf	Food	GT1003
Vitaceae	*Vitis vinifera* L.	Üzüm	Fruit	Molasses, Food	GT1059

In Bigadiç district, the existence of rich forest, the fact that 70% of the people live in rural areas and the meeting of different ethnic origins have led to diversity in the use of plants as food. As a result of the study, a total of 51 taxa were determined that the Bigadiç people used as food. Among them, *Triticum* (21), *Sesamum* (19), *Origanum* (17), *Portulaca* (14) and *Vitis* (14) are the most widely used taxa. Mostly fruit/seed (32), leaf (17) and root/stem (3) parts of these plants are used. The people mostly benefited from these food plants as food (22), fruit and fruit juice (21), spice (7), medicinal tea (5), oil (4) and molasses/jam (3) (Figure 4).

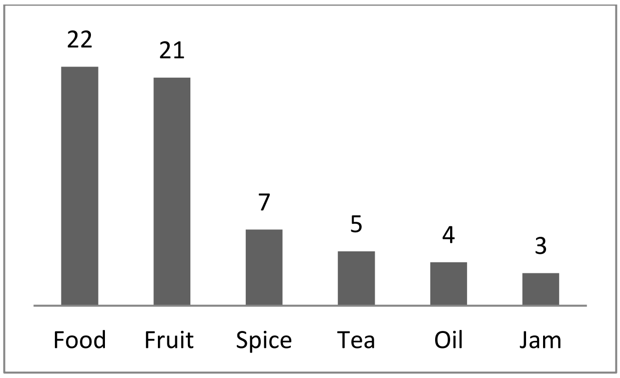

Figure 4. Distribution of taxa according to their usage patterns.

When we compare the Bigadiç data with similar studies conducted in the near vicinity, it is striking that the fruit and seed parts of the plants are used more (Table 3). The fruits and seeds of the plants used in our research area are used to make food, juice, salad, pastry, molasses, oil, spices and tea. In addition, the fruit and seed parts of the plants are eaten raw, fresh or dried.

Table 3. Comparison of the findings of our study area with the studies conducted in the immediate environment.

	Bigadiç [28]	Kazdagi [7]	Bandırma [18]	Burhaniye -Havran [19]	Yenişehir [14]	Alaçam Mountains [21]
Leaf	17	33	12	42	5	10
Fruit/Seed	32	52	15	50	32	28
Root/Stem	3	-	7	12	5	3
Spice	7	15	3	12	4	4
Tea	4	25	-	30	5	12
Plant Extract	-	13	-	-	2	-
Mushrooms	-	8	-	-	-	-
Above Ground	-	-	9	-	26	-
Total	51	153	41	140	70	41

It is seen that people from Manav and Yörük origin generally live in Bigadiç district. In the field of food, samples of these two origins were found in Bigadiç district. It has been observed that one of the two important values of the district, the keskek belongs to the Manav culture, and the halvah belongs to the Yörük culture. The traditionality of some plants used as food has been a cultural value of the district unlike others. In order to continue the traditions that have been going on for years; Wheat (*Triticum durum*), Sesame (*Sesamum indicum*) and Grape (*Vitis vinifera*) Food products obtained from plants are still obtained by traditional methods in the region.

Wheat Keskek dish, which is made using Turkish cuisine, is an example of an important tradition in the region. It is a deep-rooted legacy from the Ottoman period to these days. Keskek, a traditional dish, is served to guests at charity events, weddings, funerals or readings in our research area, Bigadiç (Figure 5).

Figure 5. Keskek and traditional village goodness.

In our study area, sesame plant is extensively used by the public. Sesame is consumed both raw and roasted and for breakfast by removing its oil. In addition, the sesame plant is used in the production of Bigadiç's famous halva. For this purpose, sesame seeds are roasted twice, then kneaded with celandine water and sweetened with sugar. Thus, a local halva is made, which is unique to the Bigadiç district. It has been done with the same method since the 1860s (Figure 6).

Figure 6. Bigadiç's famous tahini halva.

Grapes, another traditional plant widely used in the region, are squeezed by hand or with presses made from trees. It is boiled only in cauldrons used for making molasses. Especially in mountain villages, local people come together for a few days and produce molasses (Figure 7).

Figure 7. Traditional grape molasses making.

There is a need for national or international gastronomy organizations in order to transfer this rich plant usage culture of Bigadiç to future generations. Although there is currently an event called "Roasting Festival" by Bigadiç Municipality, it is insufficient to reflect Bigadiç's food culture. In this regard, there is a need for more professional organizations in cooperation with the Provincial Tourism Directorate of local administrations and the University. In addition, it is important that this rich plant usage culture is recorded and recorded as soon as possible.

4. CONCLUSION

In this study, we found edible 26 families and 51 plants have been determined. The present study showed of wild food plants as a sign of the cultural identity of local peoples and also reveals the importance of wild plants in building different methods of preparing and eating food. In our study, it is observed that uses of several of the food plants used are as stated in the literature.

Ethnobotanical studies with wild food plants are few. Therefore, this study may be an important source for further ethnobotanical studies in Turkey.

This article was reproduced from the master's thesis (Gökhan Tanaydın)

REFERENCES

[1] Yuen K, Ye Z, Fung S, Chan C, Jin D. SARS CoV2 and COVID 19: The most important research questions. Cell Biosci. 2020;10:1-5.

[2] Kawarty AMAMA., Behçet L, Çakılcıoğlu U. Traditional information on wild food crops of Ballakaati (Erbil-Northern Iraq). Afyon Kocatepe Univ J Sci Engineer. 2021;21(3):520-531.

[3] Cakilcioglu U, Khatun S, Turkoglu I, Hayta S. Ethnopharmacological survey of medicinal plants in Maden (Elazig-Turkey). J Ethnopharmacol. 2011;137(1):469-486.

[4] Kayabaşı Poyraz, N, Tümen G, Polat R. Ethnobotanical studies on useful plants in Manyas (Balıkesir/ Turkey) region. Biol Diver Conser. 2016;9(3):58-63.

[5] Polat R, Cakilcioglu U, Satıl F. Traditional uses of medicinal plants in Solhan (Bingöl-Turkey). J Ethnopharmacol. 2013;148(3):951-963.

[6] Sağıroğlu M, Arslantürk A, Akdemir ZK, Turna M. An ethnobotanical survey from Hayrat (Trabzon) and Kalkandere (Rize/ Turkey). Biol Diver Conser. 2012;5(1):31-43.

[7] Satıl F, Tümen G, Dirmenci T, Çelik A, Arı Y, Malyer H. Balıkesir Ethnobotanical Inventory Study in and Around Kazdağı National Park 2004-2006. TÜBA-KED Turkish Acad Sci J Cultural Invent. 2007;(5):171-199.

[8] Selvi S, Polat R, Çakılcıoğlu U, Celep F, Dirmenci T, Ertuğ ZF. An ethnobotanical review on medicinal plants of the Lamiaceae family in Turkey. Turk J Bot. 2022;46(4):283-332.

[9] Yalçın S, Akan H. Çakılcıoğlu U. Traditional uses of some medicinal plants in Suruç (Şanlıurfa-Turkey). Turk J Nature Sci. 2021;10(1):236-244.

[10] Selvi S, Satıl F, Polat R, Çakılcıoğlu U. A research on medicinal plants collected from Kazdağları (Balıkesir-Edremit) and sold in herbalists in the region, Kazdağları III. National Symposium. 2012;24(26):505-513.

[11] Ertug F. Contemporary plant Gathering in Central Anatolia: An Ethnoarchaeological and

ethnobotanical study. In this work: Öztürk, M., Seçmen, Ö., Görk G. (Edlr.). Proceedings of the 4. Plant Life in Southwest Asia Symposium, 945-962, Izmir; Ege University Press; 1996.
[12] Koçyiğit M. An ethnobotanical research in Yalova province. Istanbul University Institute of Health Sciences, Master Thesis. Istanbul; 2005.
[13] Yücel E, Güney F, Şengün İY. Wild plants consumed as food in Mihalıççık district, Eskişehir/Turkey, and consumption patterns of these plants. Biol Diver Conser. 2010;(3):158-175.
[14] Aktan T, Altan Y. Natural ornamental plants of new City (Bursa) cemeteries. Celal Bayar Univ. J Sci. 2011;7(2):31-39.
[15] Ekren E, ÇorbacI ÖL. Etnobotanik kullanım olanakları üzerine bir araştırma: Rize kentsel açık yeşil alanlar örneği. J of Anatolia Environ Animal Sci. 2021;6(4):487-497.
[16] Kincal S, Ceylan O, Görk G. Ethnobotanical features of Ula (Mugla/ Turkey) district. Biol Diver Conser. 2021;14(1):69-81.
[17] Korkmaz M, Karakurt E. Traditional uses of natural food plants in Kelkit (Gümüşhane) district. J Biol Sci Res. 2015;8(2):31-39.
[18] Onar S. Ethnobotany of Bandırma (A1 (A) Balıkesir) and its surroundings, Master Thesis, Çanakkale Onsekiz Mart Univ Institute Sci Technol, Çanakkale; 2006.
[19] Polat R, Satıl F. Balıkesir ethnobotanical studies in Havran and Burhaniye. TÜBA-KED Turk Academy of Sci J Cult Invent. 2010:8:65-100.
[20] Nath EÖ. Natural dye plants in Kepsut (Balıkesir, Turkey). Europ J Biol. 2015;74(2):25-32.
[21] Alkaç, SA. Some plants with economic importance and ethnobotanical features in the Bigadiç District of Alaçam Mountains (Balıkesir), Balıkesir Univ, Inst Sci, Department of Biology, Master's Thesis; 2013.
[22] Satıl F, Akçiçek E, Selvi S. An ethnobotanical study in and around Madra Mountain (Balıkesir/İzmir). Res J Biol Sci. 2008;1:31-36.
[23] Duran A, Satıl F, Tumen G. Wild fruits eaten in Balıkesir region and their ethnobotanical properties. J Herb Syst Bot. 2001;8:87-94.
[24] İnci Aladı H, Satıl F, Selvi S. Wild fruits left in the public bazaars of Edremit Gulf (Balıkesir) and their medicinal uses. Biol Diver Conser. 2019;12(1):89-99.
[25] Davis, PH. Flora of Turkey and the East Aegean Islands. Vol. 1-9. Edinburgh: Edinburgh University Press: 1965-1985.
[26] Güner A, Özhatay N, Ekim T, Başer KHC. Flora of Turkey and the East Aegean Islands. Vol. 11. Edinburgh; Edinburgh University Press; 2000.
[27] Nath EÖ, Kültür Ş. Natural dye plants in Savaştepe (Balıkesir, Turkey). J Fac Pharm Istanbul Univ. 2016;46(2):89-95.
[28] Tanaydın G. Bigadiç ilçesinin (Balıkesir) etnobotanik özellikleri. Balıkesir Univ, Inst Sci, Department of Biology, Master's Thesis; 2021.

Cilt 11, Sayı 4, Sayfa 148-154, 2022

Volume 11, Issue 4, Page 148-154, 2022

Araştırma Makalesi https://doi.org/10.46810/tdfd.994281 Research Article

Türk Doğa ve Fen Dergisi
Turkish Journal of Nature and Science
www.dergipark.gov.tr/tdfd

Localization of the Eigenvalues of Doubly Cyclic Z^+ Matrices

Murat SARDUVAN[1*], Hande NEZİROĞLU[2]

[1]Sakarya University, Faculty of Arts end Sciences, Department of Mathematics, Sakarya, Türkiye
[2]Sakarya University, Institute of Natural Sciences, Sakarya, Türkiye
Murat SARDUVAN ORCID No: 0000-0001-7049-8922
Hande NEZİROĞLU ORCID No: 0000-0003-1948-3068

Corresponding author: msarduvan@sakarya.edu.tr

(Received: 12.09.2021, Accepted: 18.12.2022, Online Publication: 28.12.2022)

Keywords
Doubly cyclic Z^+ matrix,
Localization of the Eigenvalues,
Zeros of a polynomial

Abstract: In this study, the results that determine the localization of the eigenvalues of $n \times n$ doubly cyclic Z^+ matrices with negative determinants are presented when $n \leq 4$, n $\mathbb{Z}$. While establishing these results, the fact that any eigenvalue of a matrix is a continuous function of entries of the matrix is used.

Çift Devirli Z^+ Matrislerin Özdeğerlerinin Yerleri

Anahtar Kelimeler
Çift devirli Z^+ matris,
Özdeğerlerin yerleri,
Bir polinomun sıfırları

Öz: Bu çalışmada $n \leq 4$, Z^+ olmak üzere, negatif determinantlı $n \times n$ boyutlu çift devirli Z^+ matrislerin özdeğerlerinin yerlerini belirleyen sonuçlar ortaya konulmuştur. Bu sonuçlar ortaya konulurken özdeğerlerin matris elemanlarının sürekli fonksiyonu olması gerçeği kullanılmıştır.

1. GİRİŞ

Bu çalışmada, $\mathbb{R}$, $\mathbb{R}^+$ ve C sembolleri, sırasıyla reel sayılar kümesini, pozitif reel sayılar kümesini ve kompleks sayılar kümesini göstermektedir. $M_n(F)$ ile elemanları F cisminin elemanları olan n boyutlu kare matrisler kümesi gösterilmektedir. $\det(A)$ ve $p(A)$ ile bir A kare matrisinin determinantı ve karakteristik polinomu işaret edilecektir. Bir $A \in M_n(\mathbb{C})$ matrisinin (j,j), $j = 1,2,\ldots,n$, ve $(j,j+1)$, $j = 1,2,\ldots,n-1$, indisli elemanlarının bulunduğu köşegenlere, sırasıyla, A matrisinin esas köşegeni ve süper köşegeni denir. Eğer $A \in M_n(\mathbb{R})$ matrisinin; esas köşegendeki, süper köşegendeki ve $(n,1)$ indisli elemanları tamamı ile sıfırdan farklı ve diğer elemanları sıfır ise A matrisine bir çift devirli matris (doubly cyclic matrix) veya kısaca DC matris denir [12]. Eğer bir $A \in M_n(\mathbb{R})$ matrisinin özdeğerlerinin reel kısmı pozitif ise matrise pozitif kararlı (positive stable) matris denir [8]. Eğer $A \in M_n(\mathbb{R})$ matrisinin esas köşegen üzerinde olmayan elemanları pozitif değilse, matrise Z matris, buna ek olarak eğer esas köşegen elemanları pozitifse, matrise Z^+ matris denir. Bir $A \in M_n(\mathbb{R})$ matrisi hem DC matris hem de Z^+ matris olma özelliğini sağlıyorsa bu matrise çift devirli Z^+ matris kısaca DCZ^+ matris denir. O halde her $j = 1,2,\ldots,n$, için $a_j, b_j > 0$ olmak üzere, DCZ^+ matrisler,

$$A=\begin{bmatrix} a_1 & -b_1 & 0 & 0 & \dots & 0 & 0 \\ 0 & a_2 & -b_2 & 0 & \dots & 0 & 0 \\ 0 & 0 & a_3 & -b_3 & \dots & 0 & 0 \\ \vdots & \vdots & \vdots & \ddots & & \vdots & \vdots \\ 0 & 0 & & \ddots & & \ddots & 0 \\ 0 & 0 & \vdots & \ddots & & a_{n-1} & -b_{n-1} \\ -b_n & 0 & & & & 0 & a_n \end{bmatrix} \quad (1)$$

biçimindedir. $a=\left(a_1\cdot a_2\cdot\ldots\cdot a_n\right)^{\frac{1}{n}}$ ve $b=\left(b_1\cdot b_2\cdot\ldots\cdot b_n\right)^{\frac{1}{n}}$ olmak üzere (1) tipli matrisler kümesi $DC(a,b)$ ile gösterilecektir. Ayrıca, $DC(a,b)$ kümesindeki matrislerin negatif determinantlı olanlarının da kümesi $DC\_(a,b)$ ile gösterilecektir. Eğer bir $A\in M_n(\mathbb{R})$ matrisi Z matris olup aynı zamanda pozitif kararlı ise ona M matris denir [12]. Bir $A\in M_n(\mathbb{C})$ matrisi için öz değerlerinin reel kısmı; pozitif olanların sayısı $s_+(A)$, negatif olanların sayısı $s_-(A)$ ve sıfır olanların sayısı $s_0(A)$ ile gösterilecektir. Bu üç sayı ile oluşan $s(A)=(s_+(A),\, s_-(A),\, s_0(A))$ üçlüsüne A matrisinin eylemsizliği (inertia) denir [12]. Burada bu sayılar belirlenirken özdeğerler katlı olduğunda katlılık sayısı da hesaba katılır. Bir $A\in M_n(\mathbb{C})$ matrisi için

$$\det\begin{bmatrix} a_{11} & a_{12} & \cdots & a_{1k} \\ a_{21} & a_{22} & \cdots & a_{2k} \\ \vdots & \vdots & \vdots & \vdots \\ a_{k1} & a_{k2} & \cdots & a_{kk} \end{bmatrix},\ k=1,2,\ldots,n\,,$$

sayısına A matrisinin bir başlıca esas minörü (leading principal minor) denir ve sabitlenmiş bir k değeri için bu sayı A^k_{LPM} ile gösterilecektir.

Hershkowitz ve Schneider [9] Z matrisler ve M matrislerin genelleştirilmiş sıfır uzayları üzerine çalışmışlardır. Bunu yaparken öncelikle bir M matrisin genelleştirilmiş sıfır uzayı için bir öncelikli baz teoremi ortaya koymuş ve ispatlamışlardır. Daha sonra bu teoremi Z matrisler için genişletip genelleştirmişlerdir. Yine Hershkowitz ve Schneider [10] Z matris denklemlerinin çözümleriyle de ilgilenmişlerdir. Şöyle ki; A bir Z matris, b bir negatif olmayan vektör olduğu durumda $Ax=b$ matris denkleminin çözümlerinin varlığı ve doğasını araştırmışlardır.

Kalman ve White [13] düşük dereceli polinomlar ile oluşturulmuş denklemlerin köklerinin o polinomlar ile ilişkili dairesel matrislerin özdeğerleri olduğunu göstermişlerdir.

Chandrashekaran ve arkadaşları [5] güçlü Z matris tanımı yapmışlar, ayrıca tersinir olan güçlü Z matris için Lipschitzian özelliğini sağlayıp sağlamadığını belirlemenin bir yolunu bulmuşlardır.

Jeffries ve arkadaşları [11] 4×4 boyutlu çift devirli matristen türetilebilecek bir matrisin $(1,3,0)$ eylemsizliğine sahip olduğunu ispat etmişlerdir. Bu ispat ettikleri sonucu, bir küçük kanser hücresi dinamikleri modelini analiz etmede kullanmışlardır. Boyut daha büyük olduğunda elde edilebilecek sonuçların da daha büyük modellerin analizinde yararlı olabileceğini belirtilmişlerdir. Dolayısıyla, çift devirli matrislerin biyoloji uygulamalarındaki önemini yaptıkları bu çalışmayla göstermişlerdir.

Bendito ve arkadaşları [2] çalışmalarında simetrik ve tersinir olmayan bir Jacobi M matrisinin Moore-Penrose tersinin ne zaman aynı zamanda bir M matris olduğunu karakterize etme problemini ele almışlardır. Bu problemin çözümünü kare matrislerin boyutu üç ve daha küçük olduğunda çözmüşler fakat boyutun dört ve daha yüksek olduğunda problemin çözümünün daha karmaşık bir hal aldığını görmüşlerdir. Çalışmalarının sonunda, matrislerin üzerine ekstra olarak üçgensellik koşulunu da ekleyip, herhangi n boyut için bir sonuç verebilmişlerdir.

Johnson ve arkadaşları [12] $DC(a,b)$ matrislerin sol yarı düzlemde olan özdeğerlerinin sayısını ele almışlardır. Bu çalışmada bu sonuç Teorem 1.1 olarak hatırlatılmaktadır. Teorem 1.1 ile böyle matrislerin sol yarı düzlemdeki özdeğerlerinin sayısı ile $a\mathrm{I}-bP$ matrisinin özdeğerlerinin sayısının aynı olduğuna dikkat çekmişlerdir. Hatta sonlu boyutlu genel durum için $a<b$ ise böyle matrislerin sol yarı düzlemdeki özdeğer sayısı özel bir aralıktaki tek tam sayı olabileceği açık problemini (bkz. Konjektür 1.2) ortaya atmışlardır. Bu aralık alttan 1 ile ve üstten $a\mathrm{I}-bP$ matrisinin sol yarı düzlemdeki özdeğer sayısı ile sınırlıdır. Daha sonra bu konjektür $a<b$ (yani negatif determinantlı olma) koşulu olmaksızın, dolayısıyla daha genel hali ile, [4]'te ispatlanmış ve burada Teorem 1.3 ile hatırlatılmıştır. Burada ve çalışmanın bundan sonraki kısmında P ile

$$P=\begin{bmatrix} 0 & 1 & 0 & \dots & 0 \\ 0 & 0 & 1 & \dots & 0 \\ \vdots & & \ddots & \ddots & \\ 0 & \dots & \dots & 0 & 1 \\ 1 & 0 & \dots & 0 & 0 \end{bmatrix}$$

matrisi gösterilmektedir.

Lu ve diğerleri [14] Markov zincirleriyle alakalı Wiener-Hopf problemlerinin incelenmesinde ortaya çıkan tersinir

M matrisli ikinci dereceden matris denkleminin sayısal çözümünü ele almışlardır. Bunu yaparken önce matris denklemini Riccati denklemine çevirip sabit nokta iterasyonu ile bu denklemi çözmüşlerdir.

Amster ve Idels [1] yüksek dereceli gecikmeli otonom olmayan modellerin parametrelerinden yararlanarak onların kararlılık analizlerinde M matrisleri kullanan bir algoritma tanımlamışlardır.

Brandts ve Cihangir [3] simetrik ters M matris problemlerini geometrik açıdan araştırmışlardır.

Guan [7] M matrisli cebirsel Riccati denkleminin sayısal çözümünü ele almıştır. Bu denklemin minumum ve negatif olmayan çözümlerini hesaplamak için değiştirilmiş ve doğrusallaştırılmış kapalı bir iterasyon yöntemi ortaya koymuş ve bu yöntemin etkinliğini göstermiştir.

Aşağıda bu makaleye esin kaynağı olan [12] ve [4] çalışmalarında bulunan bazı teoremler ve bir konjektür hatırlatılmaktadır.

Teorem 1.1. ([12, Theorem 1]) $a,b>0$ iken aşağıdaki ifadeler denktir:

1. $s_{-}\left(aI-bP\right)=1$,
2. $\cos\left(\dfrac{2\pi}{n}\right)<\dfrac{a}{b}<1$,
3. Tüm $A\in DC\left(a,b\right)$ matrisleri için $s_{-}\left(A\right)=1$ 'dir.

Konjektür 1.2. ([12, Conjecture]) $A\in DC\_\left(a,b\right)$ olması, $s_{-}\left(A\right)\le s_{-}\left(aI-bP\right)$ olmasını sağlar.

Teorem 1.3. ([4, Theorem 1.1]) $n\in\mathbb{N}$, $n\ge 2$, $a,b\in\mathbb{R}^{+}$ ve $A\in DC\left(a,b\right)$ olsun. Bu durumda A matrisinin negatif reel kısımlı özdeğerlerinin sayısı $aI-bP$ matrisinin negatif reel kısımlı özdeğerlerinin sayısını geçemez ve $A=aI-bP\in DC\left(a,b\right)$ almak $DC\left(a,b\right)$ kümesinin tüm elemanları için bir maksimum olarak üst sınır elde edilmesine imkân sağlar.

Teorem 1.1 ve Teorem 1.3'te bulunan A matrisleri (1) ile verilen DCZ^{+} matrislerdir. Bu çalışmada örneğin 4 boyut için

$$A=\begin{bmatrix} R_1 & -R_1 & 0 & 0 \\ 0 & R_2 & -R_2 & 0 \\ 0 & 0 & R_3 & -R_3 \\ -2R_4 & 0 & 0 & R_4 \end{bmatrix} \qquad (2)$$

çift devirli Z^{+} matrisini ele alınmaktadır. (2) ile verilen matriste Teorem 1.1 ve Teorem 1.3'te bulunan A matrislerinden farklı olarak (4,1) indisli eleman ekstra 2 katsayısını almakta ve böylece, matrisin negatif determinantlı oluşu garanti altına alınmaktadır. Yine (1) tipli matris için yapılan Teorem 1.1 ve Teorem 1.3'te özdeğerlerin yerleri $aI-bP$ matrisinin özdeğerleri ile ilişkilendirilerek belirlenirken, bu çalışmada bu ilişkilendirme yapılmaksızın (2) matrisi ve onun daha küçük boyutlu halleri için eylemsizlikler direkt olarak ortaya koyulmaktadır.

2. ÖN BİLGİLER

Teorem 2.1. (Gerschgorin Teoremi [15, Theorem 4]) $A=\left(a_{pq}\right)\in M_n\left(\mathbb{R}\right)$ olsun.

$$D_p=\left\{z\in\mathbb{C}:\left|z-a_{pp}\right|\le\sum_{q\ne p}\left|a_{pq}\right|\right\},\ p=1,\dots,n,$$

diskleri tanımlansın. Bu durumda

(a) A matrisinin tüm özdeğerleri $\bigcup_{p=1}^{n}D_p$ birleşim kümesinde bulunur.

(b) Eğer $\bigcup_{p=1}^{n}D_p$ kümesi k tane ayrık bağlantılı $E_1,\dots,E_k$ bölgelerin birleşimi ise ve $D_1,\dots,D_n$ disklerinin r tanesinin birleşimi E_r bölgesiyse bu durumda E_r bölgesi A matrisinin tam olarak r tane özdeğerini içerir, $r=1,\dots,k\le n$ [15].

Aşağıda verilenler Teorem 2.1'in direkt sonuçlarıdır. 150

Sonuç 2.2. $R_1,\ R_2,\ R_3,\ R_4\in\mathbb{R}^{+}$ olmak üzere (2) ile verilen A çift devirli Z^{+} matrisini ele alalım.

$$D_1=\left\{z\in\mathbb{C}:\left|z-R_1\right|\le R_1\right\},$$
$$D_2=\left\{z\in\mathbb{C}:\left|z-R_2\right|\le R_2\right\},$$
$$D_3=\left\{z\in\mathbb{C}:\left|z-R_3\right|\le R_3\right\},$$
$$D_4=\left\{z\in\mathbb{C}:\left|z-R_4\right|\le 2R_4\right\}$$

için A matrisinin tüm özdeğerleri $D=D_1\cup D_2\cup D_3\cup D_4$ kümesinde bulunur.

Sonuç 2.3. $R_1,\ R_2,\ R_3\in\mathbb{R}^{+}$ olmak üzere,

$$A=\begin{bmatrix} R_1 & -R_1 & 0 \\ 0 & R_2 & -R_2 \\ -2R_3 & 0 & R_3 \end{bmatrix} \qquad (3)$$

çift devirli Z^{+} matrisini ele alalım.

$$D_1=\left\{z\in\mathbb{C}:\left|z-R_1\right|\le R_1\right\},$$
$$D_2=\left\{z\in\mathbb{C}:\left|z-R_2\right|\le R_2\right\},$$

$$D_3 = \{z \in \mathbb{C} : |z - R_3| \le 2R_3\}$$

için A matrisinin tüm özdeğerleri $D = D_1 \cup D_2 \cup D_3$ kümesinde bulunur.

Sonuç 2.4. $R_1,\ R_2 \in \mathbb{R}^+$ olmak üzere,

$$A = \begin{bmatrix} R_1 & -R_1 \\ -2R_2 & R_2 \end{bmatrix} \tag{4}$$

çift devirli Z^+ matrisini ele alalım.

$$D_1 = \{z \in \mathbb{C} : |z - R_1| \le R_1\},$$
$$D_2 = \{z \in \mathbb{C} : |z - R_2| \le 2R_2\}$$

için A matrisinin tüm özdeğerleri $D = D_1 \cup D_2$ kümesinde bulunur.

Li ve Zhang'ın [15] çalışmalarının ilk sayfasında belirttiği gibi, Gerschgorin [6] çalışmasında, daha sonra Gerschgorin disk teoremi olarak adlandırılan teoremi ortaya koyarken aşağıda ifade edilen gerçeği kullandı. Burada Lemma 2.5 olarak ifade edilen bu gerçek bizim bu çalışmamızdaki ispat yöntemimizin esin kaynağı olacaktır.

Lemma 2.5. Bir matrisin özdeğerleri, karakteristik polinomun kökleridir ve bu kökler matris bileşenlerinin sürekli fonksiyonlarıdır [15].

3. ANA SONUÇLAR

Bir matrisin özdeğerlerin çarpımının o matrisin determinantına eşit olmasını ve önceki bölümde verilenleri kullanarak 4 ve daha küçük boyutlu çift devirli Z^+ matrislerin özdeğerlerinin yerleri için oluşturulan sonuçlar aşağıdaki gibidir.

Teorem 3.1. $R_1,\ R_2,\ R_3,\ R_4 \in \mathbb{R}^+$ olmak üzere, (2) ile verilen A çift devirli Z^+ matrisini ele alalım. Bu durumda $s(A) = (3,1,0)$'dır.

İspat. A matrisinin determinantı,

$$\det(A) = \det \begin{bmatrix} R_1 & -R_1 & 0 & 0 \\ 0 & R_2 & -R_2 & 0 \\ 0 & 0 & R_3 & -R_3 \\ -2R_4 & 0 & 0 & R_4 \end{bmatrix} = -R_1R_2R_3R_4 \tag{5}$$

olarak bulunur. Diğer taraftan, A matrisinin karakteristik polinomu

$$\begin{aligned} &\det(A - x\mathrm{I}) \\ &= x^4 + x^3(-R_1 - R_2 - R_3 - R_4) \\ &+x^2(R_3R_4 + R_2R_4 + R_2R_3 + R_1R_4 + R_1R_3 + R_1R_2) \\ &+x(-R_1R_2R_3 - R_1R_2R_4 - R_1R_3R_4 - R_2R_3R_4) \\ &-R_1R_2R_3R_4 \end{aligned} \tag{6}$$

şeklinde elde edilir. A matrisinin özdeğerlerinin eylemsizliğini belirlemek için, özdeğerlerin alabileceği değerlere göre olası tüm durumlar üzerinden aşağıdaki gibi inceleme yapılabilir.

1) Özdeğerlerin en az biri sıfır olsun. Bu durumda A matrisin özdeğerlerinin çarpımı, dolayısıyla determinantı sıfır olur. Oysaki (5)'ten $\det(A) < 0$ olduğunu biliniyor. Bu ise bir çelişkidir. O halde özdeğerlerin hiçbiri sıfır olamaz.

2) Özdeğerlerin hepsi pür imajiner olsun. Bu durumda $a,\ b \in \mathbb{R} - \{0\}$ ve $x_1 = ai$, $x_2 = -ai$, $x_3 = bi$, $x_4 = -bi$ için, $\det(A) = a^2b^2 > 0$ olur. Oysaki (5)'ten $\det(A) < 0$ olduğunu biliniyor. Bu ise bir çelişkidir. O halde tüm özdeğerler pür imajiner olamaz.

3) Özdeğerlerin iki tanesi pür imajiner iki tanesi pür kompleks olsun. Bu durumda $a,\ b,\ c \in \mathbb{R} - \{0\}$ ve $x_1 = a + ib,\ x_2 = a - ib,\ x_3 = ic,\ x_4 = -ic$ için, $\det(A) = (a^2 + b^2)c^2 > 0$ olur. Oysaki (5)'ten $\det(A) < 0$ olduğunu biliniyor. Bu ise bir çelişkidir. O halde özdeğerlerin iki tanesi pür imajiner iki tanesi pür kompleks olamaz.

4) Özdeğerlerin iki tanesi pür imajiner, iki tanesi reel olsun. Bu durumda $a,\ b,\ c,\ d \in \mathbb{R} - \{0\}$ ve $x_1 = ai,\ x_2 = -ai,\ x_3 = b,\ x_4 = c$ için $\det(A) = a^2bc$ olur. Dolayısıyla (5)'ten b ve c zıt işaretli olmalıdır. O halde genelliği bozmaksızın $\lambda,\ \mu \in \mathbb{R}^+$ için, özdeğerler $a = 1$ iken, $x_1 = i,\ x_2 = -i,\ x_3 = \lambda,\ x_4 = -\mu$ olarak alınabilir. Bu durumda karakteristik polinom,

$$\begin{aligned} p(A) &= (x - \lambda)(x + \mu)(x - i)(x + i) \\ &= x^4 + x^3(-\lambda + \mu) + x^2(1 - \lambda\mu) \\ &+x(-\lambda + \mu) - \lambda\mu \end{aligned} \tag{7}$$

olarak bulunur. (6) ve (7) ifadelerinin her ikisi de A matrisinin karakteristik polinomu olduklarından eşit olmalıdır. Buradan, sırasıyla x^3, x^2, x, x^0 içeren terimlerin eşitliğinden,

$$R_1 + R_2 + R_3 + R_4 = \lambda - \mu, \quad (8)$$

$$R_1R_2 + R_1R_3 + R_1R_4 + R_2R_3 + R_2R_4 + R_3R_4 = 1 - \lambda\mu, \quad (9)$$

$$R_1R_2R_3 + R_1R_2R_4 + R_1R_3R_4 + R_2R_3R_4 = \lambda - \mu, \quad (10)$$

$$R_1R_2R_3R_4 = \lambda\mu \quad (11)$$

elde edilir. (8) – (11) denklemlerinin sol yanlarını kısalık olsun diye sırasıyla B, C, D, E ile gösterelim. (9) ve (11)'den; $C + E = 1$ olur. Bu ifade ile birlikte (8) ve (10) denklemlerinin sağ taraflarının eşitliği göz önüne alındığında

$$(C+E)B = D \quad (12)$$

yazılabilir. Bu ifadenin sol tarafındaki CB ifadesi tekrar R_j'ler kullanılarak yazılırsa,

$$\begin{aligned}&(C+E)B\\ &= R_1^2(R_2+R_3+R_4) + R_2^2(R_1+R_3+R_4)\\ &+ R_3^2(R_1+R_2+R_4) + R_4^2(R_1+R_2+R_3)\\ &+3D+EB\end{aligned}$$

elde edilir. (12)'de bu ifade kullanılırsa

$$EB = -\begin{bmatrix} 2D + R_1^2(R_2+R_3+R_4) \\ +R_2^2(R_1+R_3+R_4) + R_3^2(R_4+R_1+R_2) \\ +R_4^2(R_1+R_2+R_3) \end{bmatrix}$$

bulunur. $R_j > 0$, $j = 1,2,3,4$ kabulü gereği yukarıdaki ifadede hem eşitliğin sol yanındaki EB çarpımı hem de eşitliğin sağında parantez içindeki ifadeler pozitif olmak zorundadır. Fakat bu durumda pozitif bir sayının negatif bir sayıya eşit olması durumu elde edilir ki bu bir çelişkidir. O halde özdeğerlerin iki tanesi pür imajiner, diğer iki tanesi ise reel olamaz.

Böylece, geometrik bakış açısıyla özdeğerler hiçbir zaman imajiner eksenin üzerinde olamayacaklardır. Çünkü imajiner eksen üzerinde 4×4 boyutlu matrisin pür imajiner özdeğere sahip olma durumlarının tamamı (dört tane pür imajiner özdeğere sahip olma ya da iki tane pür imajiner özdeğere sahip olma) incelenmiş ve bu durumların olamayacağı görülmüştür. Diğer taraftan örneğin, $j = 1,2,3,4$ iken $R_j = 1$ için özdeğerler yaklaşık olarak $-0,1892$, $2,1892$ ve $1,0000 \pm 1,1892i$ olur. O halde bu durum için $s(A) = (3,1,0)$ olur. Özdeğerlerin diğer olası durumlarını incelemeksizin Sonuç 2.2 ve Lemma 2.5 göz önüne alınsın. Özdeğerler R_j katsayılarının sürekli fonksiyonları olduğu ve imajiner eksende olamayacakları için R_j sayıları değiştikçe özdeğerlerden imajiner eksenin sağında olanlar sağda solunda olanlar ise eksenin solunda kalmaya devam edecektir. Dolayısıyla $s(A) = (3,1,0)$ olma durumu $R_j \in \mathbb{R}^+$, $j = 1,2,3,4$, sayıları için korunacaktır. Böylece ispat tamamlanır.

Not. Teorem 3.1'in ispatının 4. durumunda $a = 1$ almanın genelliği bozmayacağı ifade edilmiştir. Çünkü a direkt olarak kullanılmış olsaydı (7) denkleminin sağ tarafı

$$x^4 + x^3(-\lambda+\mu) + x^2(a^2 - \lambda\mu) + xa^2(-\lambda+\mu) - a^2\lambda\mu$$

şeklinde olurdu. İspat bu ifadedeki toplanan kısımların işaretlerine dayandığı için gelen bu a^2'li terimler bu kısımların işaretini, dolayısıyla ispatı değiştirmeyecektir.

Teorem 3.2. $R_1, R_2, R_3 \in \mathbb{R}^+$ olmak üzere, (5) ile verilen A çift devirli Z^+ matrisini ele alalım. Bu durumda $s(A) = (2,1,0)$'dır.

İspat. A matrisinin determinantı

$$\det(A) = \det\begin{bmatrix} R_1 & -R_1 & 0 \\ 0 & R_2 & -R_2 \\ -2R_3 & 0 & R_3 \end{bmatrix} = -R_1R_2R_3 \quad (13)$$

olarak bulunur. Diğer taraftan, A matrisinin karakteristik polinomu

$$\begin{aligned}\det(xI - A) &= x^3 + x^2(-R_1 - R_2 - R_3)\\ &+ x(R_1R_2 + R_2R_3 + R_1R_3) + R_1R_2R_3\end{aligned} \quad (14)$$

şeklinde elde edilir. A matrisinin özdeğerlerinin eylemsizliğini belirlemek için, özdeğerlerin alabileceği değerlere göre olası tüm durumlar üzerinden aşağıdaki gibi inceleme yapılabilir.

1) Özdeğerlerin en az biri sıfır olsun. Bu durumda A matrisinin özdeğerlerinin çarpımı, dolayısıyla determinantı sıfır olur. Oysaki (13)'ten $\det(A) < 0$ olduğu biliniyor. Bu ise bir çelişkidir. O halde özdeğerlerin hiçbiri sıfır olamaz.

2) Özdeğerlerin bir tanesi reel, iki tanesi pür imajiner olsun. Bu durumda, $a, b \in \mathbb{R} - \{0\}$ ve $x_1 = ai$, $x_2 = -ai$, $x_3 = b$ için $\det(A) = a^2b$ olur. Dolayısıyla (13)'ten $b < 0$ olmalıdır. O halde genelliği bozmaksızın $\lambda, \mu \in \mathbb{R}^+$ için, özdeğerler $x_1 = \mu i$, $x_2 = -\mu i$, $x_3 = -\lambda$ olarak alınabilir. Bu durumda karakteristik polinom

$$\begin{aligned} p(A) &= (x-\mu i)(x+\mu i)(x+\lambda) \\ &= x^3 + x^2\lambda + \mu^2 x + \lambda\mu^2 \end{aligned} \tag{15}$$

olur. (14) ve (15) ifadelerinin her ikisi de A matrisinin karakteristik polinomu olduklarından eşit olmalıdır. Burada x^2 içeren terimlerin eşitliğinden

$$R_1 + R_2 + R_3 = -\lambda \tag{16}$$

elde edilir. Bu ise R_1, R_2, $R_3 \in \mathbb{R}^+$ ve $\lambda \in \mathbb{R}^+$ kabulleri ile çelişir. O halde özdeğerlerin biri reel ve ikisi pür imajiner olamaz.

Böylece, geometrik bakış açısıyla özdeğerler hiçbir zaman imajiner eksenin üzerinde olamayacaklardır. Çünkü, imajiner eksen üzerinde 3×3 boyutlu matrisin pür imajiner özdeğere sahip olma durumlarının tamamı (iki tane pür imajiner özdeğere sahip olma) incelenmiş ve bu durumun olamayacağı görülmüştür. Diğer taraftan, örneğin $j=1,2,3$ iken $R_j = 1$ için özdeğerler yaklaşık olarak $-0,2599$ ve $1,6300 \pm 1,091i$ bulunur. Yani bu durum için $s(A) = (2,1,0)$ olur. Özdeğerlerin diğer olası durumlarını incelemeksizin Sonuç 2.3 ve Lemma 2.5 göz önüne alınsın. Özdeğerler R_j katsayılarının sürekli fonksiyonları oldukları ve imajiner eksen üzerinde olamayacakları için imajiner eksenin sağında olanlar sağda solunda olanlar ise eksenin solunda kalmaya devam edecektir. Dolayısıyla $s(A) = (2,1,0)$ olması $R_j \in \mathbb{R}^+$, $j = 1,2,3$, sayıları için korunacaktır.

Teorem 3.3. $R_1, R_2 \in \mathbb{R}^+$ olmak üzere, (6) ile verilen A çift devirli Z^+ matrisini ele alalım. Bu durumda $s(A) = (1,1,0)$ 'dır.

İspat. A matrisinin determinantı,

$$\det(A) = \det\begin{bmatrix} R_1 & -R_1 \\ -2R_2 & R_2 \end{bmatrix} = -R_1R_2 \tag{17}$$

olarak bulunur. Diğer taraftan, A matrisini karakteristik polinomu,

$$\det(A - x\mathrm{I}) = x^2 + x(-R_1 - R_2) - R_1R_2 \tag{18}$$

şeklinde elde edilir. A matrisinin özdeğerlerinin eylemsizliğini belirlemek için, özdeğerlerin alabileceği değerlere göre olası tüm durumlar üzerinden aşağıdaki gibi inceleme yapılabilir.

1) Özdeğerlerin en az biri sıfır olsun. Bu durum A matrisinin özdeğerlerinin çarpımı, dolayısıyla determinantı sıfır olur. Oysaki (17)'den $\det(A) < 0$ olduğunu biliniyor. Bu ise bir çelişkidir. O halde özdeğerlerin hiçbiri sıfır olamaz.

2) Özdeğerlerin ikisi de pür imajiner olsun. Bu durumda, $a \in \mathbb{R} - \{0\}$ ve $x_1 = ai$, $x_2 = -ai$ için, $\det(A) = a^2$ olur. Oysaki (17)'den $\det(A) < 0$ olduğunu biliniyor. Bu ise bir çelişkidir. O halde özdeğerler pür imajiner olamaz.

Böylece, geometrik bakış açısıyla özdeğerler hiçbir zaman imajiner eksenin üzerinde olamayacaklardır. Diğer taraftan, örneğin $j = 1,2$ iken $R_j = 1$ için özdeğerler yaklaşık olarak $2,4142$ ve $-0,4142$ olarak bulunur. Yani bu durum için $s(A) = (1,1,0)$ olur. Özdeğerlerin diğer olası durumlarını incelemeksizin Sonuç 2.4 ve Lemma 2.5'e dikkat edelim. Buradan özdeğerler R_j katsayılarının sürekli fonksiyonları olduğu ve imajiner eksende olamayacakları için imajiner eksenin sağındakiler sağda solundakiler ise eksenin solunda kalmaya devam edecektir. Dolayısıyla $s(A) = (1,1,0)$ olma durumu $R_j \in \mathbb{R}^+$, $j = 1,2$, sayıları için korunacaktır.

4. SONUÇLAR VE TARTIŞMA

Bilindiği üzere Teorem 1.1, Konjektür 1.2 ve Teorem 1.3 literatürde ([12] ve [4]) mevcut olan ve bu çalışma yapılırken esinlenilen sonuçlardır. Teorem 1.1 ile (1) tipli $A \in DC(a,b)$ matrisinin, yani bir çift döngülü Z^+ matrisin, sol yarı düzlemdeki özdeğer sayısının 1 olmasının gerek ve yeter koşulunun $aI - bP$ matrisinin sol yarı düzlemdeki özdeğer sayısının 1 olması olduğu gösterilmiştir. Aynı zamanda bu önermelerin her birinin gerek ve yeter koşulunun $\cos\left(\frac{2\pi}{n}\right) < \frac{a}{b} < 1$ önermesi olduğu da gösterilmiştir. Bu son koşulun $A \in DC(a,b)$ matrisinin üzerine konulma sebebinin aynı zamanda negatif determinantlı olmayı garanti etmek olduğuna dikkat ediniz. Konjektür 1.2'de ise " $A \in DC\_(a,b)$ olması durumunda (yani Teorem 1.1'deki A matrisinin üzerindeki koşullara, negatif determinantlı olma koşulunu direkt olarak ekleyerek) onun sol yarı düzlemdeki özdeğer sayısının üstten $aI - bP$ matrisinin sol yarı düzlemdeki özdeğer sayısı ile sınırlı olacağı" açık problem olarak bırakılmıştır. [4]'te mevcut olan Teorem 1.3 ise bu açık problemin, negatif determinantlı olma koşulu olmaksızın, dolayısıyla daha genel halinin, tüm $A \in DC(a,b)$ matrisleri için ispatlanmış halidir.

Bu çalışmada $n < 5$ iken (2) tipli negatif determinantlı çift döngülü Z^+ matrisler için sol yarı düzlemde yalnızca bir özdeğerin varlığı, diğer özdeğerlerin ise sağ yarı düzlemde olduğu gösterildi. Dolayısıyla, $n<5$ iken Konjektür 1.2 yeniden ispatlandı. Ancak Konjektür 1.2 ve diğer var olan sonuçlardan farklı olarak (1) tipli matris yerine (2), (3) ve (4) tipli matrisler ile çalışıldı. Yani dikkat edilirse çalışılan matrisin köşegen ve süper köşegen elemanlarında değişikliğe gidilmiş ve $(n,1)$ indisli elemanın önüne ekstra 2 katsayısı konulmuştur. Bu katsayının konulma sebebi matrisin negatif determinantlı olmasını garanti etmektir. Buradaki 2 katsayısının yerine 1'den büyük olan herhangi bir reel sayı da alınabilir. Hatta $(n,1)$ indisli elemanın önüne değil süper köşegen üzerindeki herhangi bir elemanın önüne de bu katsayı konulabilir. $(n,1)$ indisli elemanı bu katsayıyı koymak için seçmenin genelliği bozmayacağına dikkat ediniz.

Bu çalışmada verilen ispatlarda kullanılan yöntemin bir avantajı mertebesi 5'ten küçük olan matrisler için Teorem 1.3'ün [4]'te verilen ispatı ile kıyaslanmayacak kadar çok daha az emek gerektirmesidir. Böylece bu çalışmadaki ispat yöntemi kullanılarak boyutu 5'ten küçük olup örneğin negatif olmayan matrisler, çift devirli matrisler, vb. herhangi özel tipli matrisler için özdeğerlerin yerleri problemleri çalışılabilir. Dolayısı ile elde edilen sonuçlar ile herhangi bir boyuttaki matrisler için konjektürler oluşturulabilir. İspat yöntemimizin bir diğer avantajı ise (2) tipli matrisin özdeğerlerinin yerini başka bir matrisin özdeğerlerinin yeri ile ilişkilendirmeksizin direkt olarak belirleyebilmesidir. Zira Teorem 1.1 ve Teorem 1.3'te sonuçlar $aI-bP$ matrisi ile ilişkili olarak verilmiştir. Çalışmamızın bu anlamda başka çalışmalara esin kaynağı olacağını umuyoruz.

KAYNAKLAR

[1] Amster P, Idels L. New applications of M -matrix methods to stability of high-order linear delayed equations. Appl. Math. Lett. 2016;54:1-6.

[2] Bendito E, Carmona A, Encinas AM, Mitjana M. The M -matrix inverse problem for singular and symmetric Jacobi matrices. Linear Algebra Appl. 2012;436:1090-1098.

[3] Brandts J, Cihangir A. Geometric aspects of the symmetric inverse M -matrix problem. Linear Algebra Appl. 2016;506:33-81.

[4] Baker CE, Mityagin BS. Localization of eigenvalues of doubly cyclic matrices. Linear Algebra Appl. 2018;540:160-202.

[5] Chandrashekaran A, Parthasarathy T, Ravindran G. On strong Z -matrices. Linear Algebra Appl. 2010;432:964-969.

[6] Gerschgorin VS. Über die abgrenzung der eigenwerte einer matrix. Bulletin de L'Academie des Sciences de L'URSS. Classe des sciences mathématiques et naturelles. 1931;1:749-754.

[7] Guan J. Modified alternately linearized implicit iteration method for M -matrix algebraic Riccati equations. Appl. Math. Comput. 2019;347:442-448.

[8] Horn RA, Johnson CR. Topics in matrix analysis. Cambridge, Cambridge University Press; 1991.

[9] Hershkowitz D, Schneider H. On the generalized nullspace of M -matrices and Z -matrices. Linear Algebra Appl. 1988;106:5-23.

[10] Hershkowitz D, Schneider H. Solutions of Z -matrix equations. Linear Algebra Appl. 1988;106:25-38.

[11] Jeffries CD, Johnson CR, Zhou T, Simpson DA, Kaufmann WK. A flexible and qualitatively stable model for cell cycle dynamics including DNA damage effects. Gene Regulation and Systems Biology. 2012;1:55-66.

[12] Johnson CR, Price Z, Spitkovsky IM. The distribution of eigenvalues of doubly cyclic Z^+ -matrices. Linear Algebra Appl. 2013;439:3576-3580.

[13] Kalman D, White JE. Polynomial equations and circulant matrices. Amer. Math. Monthly. 2001;108(9):821-840.

[14] Lu L, Ahmed Z, Guan J. Numerical methods for a quadratic matrix equation with a nonsingular M -matrix. Appl. Math. Lett. 2016;52:46-52.

[15] Li CK, Zhang F. Eigenvalue continuity and Gersgorin's Theorem. Electron. J. Linear Algebra. 2019;35:619-625.

Cilt 11, Sayı 4, Sayfa 155-159, 2022 Volume 11, Issue 4, Page 155-159, 2022

Araştırma Makalesi https://doi.org/10.46810/tdfd.1178856 Research Article

Türk Doğa ve Fen Dergisi
Turkish Journal of Nature and Science
www.dergipark.gov.tr/tdfd

Contributions to the Knowledge of Dytiscidae (Insecta: Coleoptera) Fauna of Batman Province

Medeni AYKUT[1*], Sadreddin TUSUN[2]

[1] Dicle University, Ziya Gökalp Education Faculty, Maths and Science Education Department, Diyarbakır, Türkiye
[1] Dicle University, Ziya Gökalp Education Faculty, Maths and Science Education Department, Diyarbakır, Türkiye
Medeni AYKUT ORCID No: 0000-0001-6824-1394
Sadreddin TUSUN ORCID No: 0000-0002-0696-4244

**Corresponding author: medeniaykut@hotmail.com*

(Received: 27.09.2022, Accepted: 24.11.2022, Online Publication: 28.12.2022)

Keywords
Diving Beetles
Coleoptera,
Dytiscidae,
Faunistic

Abstract: The present study was carried out between September-2018 and June-2019 in Batman Province which is located in South-eastern Region with the aim of determination of the species of family Dytiscidae (Predaceous diving beetles). The specimens were collected from 39 different localities of Batman province and its districts. 23 species belonging to 11 genera of family Dytiscidae were recorded from the study area. Twenty of the 23 identified species were new records for the Batman province.

Batman İli Yırtıcı Dalgıç Böcekleri (Coleoptera: Dytiscidae) Faunasına Katkılar

Anahtar Kelimeler
Dalgıç Böcekleri,
Kın Kanatlılar,
Dytiscidae,
Faunistik

Öz: Güneydoğu Anadolu Bölgesinde yer alan Batman ilinin Dytiscidae (Yırtıcı dalgıç böcekleri) familyasına ait türlerin belirlenmesine yönelik yapılan bu çalışma Eylül-2018 ile Haziran-2019 tarihleri arasında gerçekleştirilmiştir. Böcek örnekleri Batman ili ve ilçelerini kapsayan 39 farklı istasyondan toplanmıştır. Çalışma alanından Dytiscidae familyasının 11 cinsine ait 23 tür tespit edilmiştir. Tespit edilen türlerin 20'si Batman ili için yeni kayıt özelliği göstermektedir.

1. INTRODUCTION

The family Dytisicdae Leach, 1815 is an important component of the aquatic life. The members of the family are known as ‘‘predaceous diving beetles’’ and they could generally be found in all freshwater habitats such as; small streams, puddles, springs, rainwater puddles, etc.

In current the family is represented by 182 genera and approximately 4600 species around the world [1]. In Palearctic region where Türkiye is located these values are; 80 genera and around 650 species [2].

So far, in Türkiye numerous field studies have been conducted with the relation of the family Dytiscidae. As a result of mentioned studies a total of 165 species belong to 28 genera have been recorded, from of these 38 are endemic for Türkiye [3-23]. According to our literature searches up to now just one study has been carried out in Batman province [22]. According to our investigations, only tree species from Batman [*Deronectes kabilcevz* Aykut, Yıldırım, Tusun & Fery, 2019, *Deronectes propedoriae* Aykut, Yıldırm, Tusun & Fery, 2019 and *Deronectes evelynae* Fery & Hosseinie, 1998] have been reported so far.

With this study we tried to determine the species of Batman province belong to the family Dytiscidae.

2. MATERIAL AND METHOD

2.1. Description of the Study Area

Batman province is located in the Dicle Section of the Southeastern Anatolia Region of Türkiye. Batman province has five districts, these are; Sason, Kozluk, Beşiri, Hasankeyf and Gercüş. Of these, Sason district is located in the Eastern Anatolia Region. While the city center has an altitude of 550 meters, the north and northeast of the city have high steep mountains and rough terrain. Southern parts of the province are less mountainous, rugged and have an altitude compared to the northern parts. Batman province is surrounded by Muş province in the north, Diyarbakır province in the west, Bitlis and Siirt provinces in the east and Mardin province in the south (Figure 1.) [24].

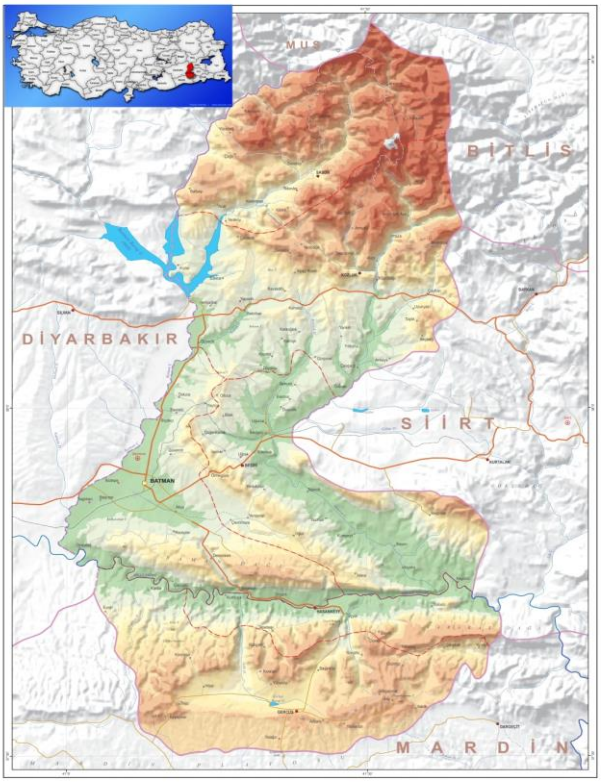

Figure 1. Map of study area, Batman province, Türkiye

2.2. Material and Methods

The specimens were collected from 39 different fresh water habitats (Table 1.) of Batman province and its districts using nets with a mesh diameters of 0.5 - 1 cm between September - 2017 and June - 2019. The handheld GPS tool (Magellan Explorist 610) was used for the coordinates and altitude information's of the localities. 70% ethyl alcohol solution was used at spot for fixation and preservation of collected specimens. In laboratory a small paintbrush was used to remove the clay and muddy substances on the surfaces of collected specimens. The specimens which collected from the study area have been deposited in the private collection of the correspond author at Dicle University, Ziya Gökalp Education Faculty, Diyarbakır, Türkiye.

3. RESULTS

Totally 934 adult specimens of 23 species in 3 subfamilies and 11 genera of family Dytiscidae were collected and described from the study area. Of 23 identified species in Batman province, 20 are new for the study area. By now, 23 dytiscid species are known from Batman province. The determined species and their locality data are listed below:

Family: DYTISCIDAE Leach, 1815

Subfamily: Agabinae Thomson, 1867
Tribe: Agabini Thomson, 1867
Genus: *Agabus* Leach, 1817
***Agabus biguttatus* (Olivier, 1795)**
Material examined and locality information: B2, 5 ex.; B4, 3 ex.; B6, 3 ex.; B9, 5 ex.; B11, 2 ex.; B14, 3 ex.; B16, 7 ex.; B19, 6 ex.; B24, 8 ex.; B27, 3 ex.; B29, 2 ex.; B33, 6 ex.; B36, 3 ex.; B38, 1 ex.

***Agabus bipustulatus* (Linnaeus, 1767)**
Material examined and locality information: B2, 3 ex.; B3, 2 ex.; B4, 2 ex.; B6, 5 ex.; B13, 6 ex.; B15, 4 ex.; B18, 4 ex.; B21, 5 ex.; B23, 3 ex.; B25, 4 ex.; B27, 2 ex.; B29, 3 ex.; B31, 2 ex.; B32, 1 ex.; B34, 2 ex.; B39, 5 ex.

***Agabus conspersus* (Marsham, 1802)**
Material examined and locality information: B1, 2 ex.; B4, 3 ex.; B7, 4 ex.; B11, 7 ex.; B14, 3 ex.; B17, 2 ex.; B20, 5 ex.; B22, 7 ex.; B26, 4 ex.; B30, 3 ex.; B33, 2 ex.; B37, 1 ex.

***Agabus nebulosus* (Forster, 1771)**
Material examined and locality information: B2, 3 ex.; B5, 4 ex.; B8, 5 ex.; B11, 5 ex.; B13, 3 ex.; B18, 2 ex.; B21, 5 ex.; B24, 5 ex.; B26, 2 ex.; B28, 5 ex.; B30, 3 ex.; B31, 1 ex.; B32, 6 ex.; B38, 2 ex.

Subfamily: Hydroporinae Aubé, 1836
Tribe: Bidessini Sharp, 1880
Genus: *Bidessus* Sharp, 1880
***Bidessus calabricus* (Guignot, 1957)**
Material examined and locality information: B1, 5 ex.; B3, 7 ex.; B7, 3 ex.; B11, 7 ex.; B13, 4 ex.; B16, 8 ex.; B18, 13 ex.; B21, 10 ex.; B25, 13 ex.; B28, 3 ex.; B31, 5 ex.; B33, 2 ex.; B35, 3 ex.; B37, 3 ex.; B38, 9 ex.

Genus: *Deronectes* Sharp, 1882
***Deronectes evelynae* Fery & Hosseinie, 1998**
Material examined and locality information: B10, 5 ex.
***Deronectes kabilcevz* Aykut, Yıldırım, Tusun & Fery, 2019**
Material examined and locality information: B10, 7 ex.

***Deronectes propedoriae* Aykut, Yıldırım, Tusun & Fery, 2019**
Material examined and locality information: B10, 5 ex.

Genus: *Hydroglyphus* Motschulsky, 1853
***Hydroglyphus geminus* (Fabricius, 1792)**
Material examined and locality information: B2, 6 ex.; B7, 3 ex.; B12, 3 ex.; B14, 5 ex.; B19, 7 ex.; B23, 4 ex.; B28, 3 ex.; B32, 4 ex.; B39, 3 ex.

Table 1. Location of the sampling sites of Batman province where the specimens were found.

Abbreviation	Sampling sites	Coordinates	Altitude (m)
B1	Batman, Sason district, Boğazkapı village	38^{0}21'34"N, 41^{0}26'53"E	886
B2	Batman, Sason district, Taşyuva village	38^{0}21'57"N, 41^{0}28'51"E	1326
B3	Batman, Sason district, Çalışırlar village	38^{0}23'19"N, 41^{0}29'07"E	1075
B4	Batman, Sason district, Kınalı village	38^{0}24'58"N, 41^{0}28'49"E	974
B5	Batman, Sason distyrict, Derince village	38^{0}26'19"N, 41^{0}28'36"E	1009
B6	Batman, Sason district, Sarıkız village	38^{0}25'58"N, 41^{0}34'21"E	1496
B7	Batman, Sason district, Karayün village	38^{0}24'52"N, 41^{0}35'07"E	1647
B8	Batman, Sason district, Karaağaç village	38^{0}24'59"N, 41^{0}34'41"E	1702
B9	Batman, Sason district, Meşeli village	38^{0}25'49"N, 41^{0}28'48"E	1027
B10	Batman, Sason district, Dereiçi village	38^{0}30'32"N, 41^{0}31'53"E	735
B11	Batman, Kozluk district entrance	38^{0}09'57"N, 41^{0}28'27"E	694
B12	Batman, Kozluk district, Merga stream	38^{0}11'51"N, 41^{0}30'42"E	667
B13	Batman, Kozluk district , İnişli village	38^{0}13'32"N, 41^{0}29'36"E	954
B14	Batman, Kozluk district, Bekirhan Küllük stream	38^{0}08'50"N, 41^{0}18'22"E	649
B15	Batman, Kozluk district, Parmakkapı village	38^{0}06'48"N, 41^{0}14'57"E	638
B16	Batman, Kozluk district, Konaklı village	38^{0}08'10"N, 41^{0}16'39"E	655
B17	Batman, Kozluk district, Geyikli village	38^{0}13'05"N, 41^{0}26'05"E	948
B18	Batman, Beşiri district, Yaylıca village	37^{0}59'48"N, 41^{0}13'55"E	710
B19	Batman, Beşiri district, Bilek village	37^{0}58'49"N, 41^{0}15'51"E	703
B20	Batman, Beşiri district, Bahçeçayırı township	37^{0}57'28"N, 41^{0}20'28"E	560
B21	Batman Beşiri district, Durucak village	38^{0}00'32"N, 41^{0}19'58"E	583
B22	Batman Beşiri district, Yontukyazı village	37^{0}52'59"N, 41^{0}19'32"E	681
B23	Batman, Beşiri stream	37^{0}53'55"N, 41^{0}17'52"E	754
B24	Batman -Hasankeyf road, 27. Km	37^{0}45'24"N, 41^{0}16'09"E	673
B25	Batman, Hasankeyf district, Suçeken village	37^{0}43'58"N, 41^{0}18'51"E	541
B26	Batman, Hasankeyf district, Sinniboğaz stream	37^{0}44'28"N, 41^{0}25'56"E	625
B27	Batman, Hasankeyf district, Akyar picnic area	37^{0}39'21"N, 41^{0}27'05"E	738
B28	Batman, Hasankeyf district, Gürbüz village	37^{0}38'22"N, 41^{0}25'43"E	826
B29	Batman, Batman Thermal area	38^{0}21'58"N, 41^{0}11'12"E	836
B30	Batman, Batman thermal road	38^{0}21'43"N, 41^{0}10'02"E	902
B31	Batman, Karayün village	37^{0}50'33"N, 41^{0}06'51"E	645
B32	Batman, Güvercin village	37^{0}56'28"N, 41^{0}10'39"E	687
B33	Batman, Gercüş district, Karalan village	37^{0}36'53"N, 41^{0}18'23"E	826
B34	Batman, Gercüş district, Esentepe village	37^{0}36'17"N, 41^{0}17'08"E	776
B35	Batman, Gercüş district, Yücekök village	37^{0}35'59"N, 41^{0}19'55"E	928
B36	Batman, Gercüş district entrance	37^{0}34'41"N, 41^{0}23'39"E	922
B37	Batman, Gercüş district, Özler village	37^{0}34'39"N, 41^{0}25'19"E	978
B38	Batman, Gercüş district, Yamanlar village	37^{0}33'10"N, 41^{0}27'46"E	1122
B39	Batman, Gercüş district, Koçak village	37^{0}33'58"N, 41^{0}31'52"E	1193

Hydroglyphus pusillus **(Fabricius, 1781)**
Material examined and locality information: B4, 2 ex.; B9, 3 ex.; B15, 3 ex.; B21, 5 ex.; B22, 1 ex.; B25, 4 ex.; B26, 1 ex.; B30, 2 ex.; B33, 4 ex.; B37, 5 ex.

Tribe: Hydroporini Aubé, 1836
Genus: *Nebrioporus* Régimbart, 1906b
Nebrioporus stearinus stearinus **Kolenati, 1845**
Material examined and locality information: B1, 2 ex.; B3, 5 ex.; B5, 3 ex.; B6, 7 ex.; B8, 2 ex.; B9, 1 ex.; B12, 2 ex.; B27, 13 ex.; B35, 2 ex.

Genus: *Scarodytes* Gozis, 1914
Scarodytes halensis **(Fabricius, 1787)**
Material examined and locality information: B2, 2 ex.; B4, 2 ex.; B5, 1 ex.; B7, 4 ex.; B9, 3 ex.; B11, 2 ex.; B13, 6 ex.; B16, 12 ex.; B18, 6 ex.; B20, 8 ex.; B22, 3 ex.; B24, 1 ex.; B26, 4 ex.; B28, 3 ex.; B30, 5 ex.; B32, 4 ex.; B34, 2 ex.; B38,2 ex.

Genus: *Hydroporus* Clairville, 1806
***Hydroporus discretus* (Fairmaire and Brisout, 1859)**
Material examined and locality information: B1, 2 ex.; B5, 3 ex.; B14, 3 ex.; B17, 4 ex.; B23, 2 ex.; B31, 3 ex.; B33, 5 ex.

***Hydroporus planus* (Fabricius, 1782)**
Material examined and locality information: B2, 3 ex.; B5, 1 ex.; B8, 1 ex.; B12, 2 ex.; B13, 3 ex.; B16, 1 ex.; B21, 1 ex.; B24, 2 ex.; B27, 2 ex.; B29, 4 ex.; B34, 3 ex.

***Hydroporus pubescens* (Gyllenhal, 1808)**
Material examined and locality information: B1, 3 ex.; B3, 1 ex.; B5, 1 ex.; B6, 3 ex.; B8, 3 ex.; B9, 2 ex.; B15, 4 ex.; B18, 4 ex.; B22, 2 ex.; B26, 2 ex.; B30, 5 ex.; B31, 3 ex.; B36, 2 ex.; B29, 3 ex.

***Hydroporus tessellatus* (Drapiez, 1819)**
Material examined and locality information: B1, 2 ex.; B3, 2 ex.; B7, 1 ex.; B11, 1 ex.; B14, 1 ex.; B16, 2 ex.; B19, 2 ex.; B21, 4 ex.; B24, 5 ex.; B27, 3 ex.; B30, 3 ex.; B33, 1 ex.; B39, 1 ex.

Genus: *Graptodytes* Seidlitz, 1887
***Graptodytes flavipes* (Olivier, 1795)**
Material examined and locality information: B2, 2 ex.; B4, 5 ex.; B6, 3 ex.; B8, 3 ex.; B12, 4 ex.; B17, 6 ex.; B20, 3 ex.; B23, 6 ex.; B26, 3 ex.; B29, 7 ex.; B32, 9 ex.; B35, 7 ex.

Genus: *Hydrovatus* Motschulsky, 1853
***Hydrovatus cuspidatus* (Kunze, 1818)**
Material examined and locality information: B2, 1 ex.; B5, 1 ex.; B7, 2 ex.; B8, 2 ex.; B12, 1 ex.; B15, 2 ex.; B19, 3 ex.; B24, 1 ex.; B34, 2 ex.; B37, 1 ex.

Tribe: Hygrotini Portevin, 1929
Genus: *Hygrotus* Stephens, 1828
***Hygrotus confluens* (Fabricius, 1787)**
Material examined and locality information: B7, 2 ex.; B16, 3 ex.; B23, 4 ex.; B32, 1 ex.; B38, 1 ex.

***Hygrotus inaequalis* (Fabricius, 1777)**
Material examined and locality information: B3; 5 ex.; B5, 3 ex.; B6, 5 ex.; B9, 14 ex.; B11, 8 ex.; B12, 7 ex.; B14, 3 ex.; B15, 2 ex.; B18, 6 ex.; B20, 2 ex.; B23, 4 ex.; B25, 2 ex.; B26, 6 ex.; B27, 3 ex.; B29, 5 ex.; B32, 11 ex.; B35, 6 ex.; B36, 4 ex.; B39, 8 ex.

***Hygrotus saginatus* (Schaum, 1857)**
Material examined and locality information: B1, 2 ex.; B4, 17 ex.; B9, 8 ex.; B13, 4 ex.; B16, 4 ex.; B22, 3 ex.; B24, 6 ex.; B28, 2 ex.; B29, 13 ex.; B33, 1 ex.

Subfamily: Laccophilinae Gistel, 1848
Tribe: Laccophilini Gistel, 1848
Genus: *Laccophilus* Leach, 1815
***Laccophilus hyalinus* (De Geer, 1774)**
Material examined and locality information: B2, 2 ex.; B4, 3 ex.; B8, 6 ex.; B9, 2 ex.; B12, 4 ex.; B17, 4 ex.; B19, 3 ex.; B20, 3 ex.; B22, 4 ex.; B26, 8 ex.; B31, 1 ex.; B35, 3 ex.; B38, 2 ex.

***Laccophilus minutus* (Linnaeus, 1758)**
Material examined and locality information: B2, 3 ex.; B6, 6 ex.; B9, 3 ex.; B15, 8 ex.; B18, 2 ex.; B22, 4 ex.; B27, 7 ex.

4. DISCUSSION AND CONCLUSION

In 39 different freshwater habitats of Batman province 23 species belong to 11 genera of family Dytiscidae were recorded. With this study a total of 934 specimens were collected and identified. Of these *Hygrotus inaequalis* (Fabricius, 1777) was the most dominant (11, 13%), followed by *Bidessus calabricus* Guignot, 1957 (10, 06%), *Scarodytes halensis* (Fabricius, 1787) (7, 49%), *Hygrotus saginatus* (Schaum, 1857) (6, 42%), *Graptodytes flavipes* (Olivier, 1795) (6, 21%) and *Agabus biguttatus* (Olivier, 1795) (6, 1%). *Deronectes evelynae* Fery & Hosseinie, 1998, *D. kabilcevz* Aykut, Yıldırım, Tusun & Fery,2019 and *D, propedoriae* Aykut, Yıldırım, Tusun & Fery,2019 has an abundance of less than 1%. *Hygrotus inaequalis*, *Scarodytes halensis* (Fabricius, 1787), *Agabus bipustulatus* (Linnaeus, 1767), *Bidessus calabricus* Guignot, 1957, *Agabus biguttatus* (Olivier, 1795) and *A. nebulosus* (Forster, 1771) were the most widespread species found in our study area. These mentioned six species were found respectively; *H. inaequalis* in 19, *S. halensis* in 18, *A.bipustulatus* in 16, *B. calabricus* in 15, *A. biguttatus* and *A. nebulosus* in 14 sites. *Deronectes evelynae*, *D. kabilcevz* and *D, propedoriae* were restricted to a single site each.

Acknowledgement

This study was supported by the Research Fund of Dicle University (DUBAP), project no ZGEF.17.014. This study was presented orally in summary in 5 th International Eurasian Conference on Biological and Chemical Sciences (EurasianBiochem 2022) held online on 23-25 November, Ankara, Türkiye.

REFERENCES

[1] Nilsson AN, Hájek J. A world catalogue of the family Dytiscidae (Coleoptera, Adephaga). World Wide Web Electronic Publication; 2022 [Cited 2022 September 5]. Available from: http://www.waterbeetles.eu/

[2] Nilsson AN, Hájek J. Catalogue of Palearctic Dytiscidae (Coleoptera). World Wide Web Electronic Publication; 2022 [Cited 2022 September 5]. Available from: http://www.waterbeetles.eu/

[3] Erman ÖK, Erman O. First records of *Oreodytes* Seidlitz, 1887 (Dytiscidae, Coleoptera) from Turkey: *Oreodytes septentrionalis* (Gyllenhel, 1826) and *Oreodytes davisii* (Curtis, 1831). Turk J Zool. 2002; 26(3): 295-299.

[4] Erman ÖK, Erman O. First record of *Graptodytes bilineatus* (Sturm, 1835) (Coleoptera, Dytiscidae) from Turkey. Turk J Zool. 2004; 28(1): 87- 90.

[5] Erman ÖK, Fery H. *Hydroporus neclae* sp. n. from north-eastern Turkey, a new member of the memnonius-group of *Hydroporus* Clairville

(Coleoptera: Dytiscidae). Zootaxa. 2006; 1355: 39-47.
[6] Darılmaz CM, Kıyak S. Checklist of Gyrinidae, Haliplidae, Noteridae and Dytiscidae of Turkey (Coloptera: Adephaga). J Nat Hist. 2009; 43(25): 1585 -1636.
[7] Darılmaz MC, Kıyak S. New and Rare Water Beetles (Coleoptera: Haliplidae: Dytiscidae) for the Fauna of Turkey. Acta Zool Bulg. 2010; 62(1): 99-102.
[8] Fery H, Erman OK. Five new species of the *longulus*-group of *Hydroporus* Clairville, 1806 from north-eastern Turkey (Coleoptera: Dytiscidae). Zootaxa. 2009; 2033: 1-12
[9] Fery H. New species of the *Hydroporus longulus*-group from Iran, Armenia and Turkey with a synopsis of the group (Coleoptera: Dytiscidae). Acta Entomol Mus Natl Pragae, 2009; 49(2): 529-558.
[10] Fery H, Hendrich L. *Hydroporus esersi* sp. n., a new diving beetle from southern Turkey (Coleoptera, Dytiscidae, Hydroporinae). Zootaxa. 2011; 2909: 38-46.
[11] Fery H, Hendrich L. *Ilybius enpalaiatheka* spec. nov. from Anatolia, Turkey, with a revised key to males of the *Ilybius erichsoni* and *chalconatus* groups. Spixiana. 2011; 34: 39-46.
[12] Fery H, Przewoźny M. *Ilybius thynias* sp. n. from European Turkey (Coleoptera: Dytiscidae). Zootaxa. 2011; 2740: 59-67.
[13] Hájek J, Šťastný J, Boukal M, Fery, H. Updating the eastern Mediterranean Deronectes (Coleoptera: Dytiscidae) with the description of two new species from Turkey. Acta Entomol Mus Natl Pragae. 2011; 51: 463-476.
[14] Hernando C, Aguilera P, Castro A, Ribera I. A new interstitial species of the *Hydroporus ferrugineus* group from north-western Turkey, with a molecular phylogeny of the *H. memnonius* and related groups (Coleoptera: Dytiscidae: Hydroporinae). Zootaxa. 2012; 3173: 37-53.
[15] Vorst O, Fery H. *Hydroporus emergens* sp. n. from south-western Turkey (Coleoptera: Dytiscidae). Tijdschr Entomol. 2014; 157: 145-149.
[16] Aykut M, Fery H. *Scarodytes costatus* nov. sp. from the Bingöl Province in Turkey, the first species of the genus with costate elytra (Insecta: Coleoptera: Dytiscidae: Deronectina). Linz Biol Beitr. 2017; 49: 395–414.
[17] Aykut M. The Diving Beetle Fauna of Diyarbakır and Bingöl Provinces, Turkey (Coleoptera: Dytiscidae) with a New Record. Pakistan J Zool. 2018; 50 (1): 65-74.
[18] Aykut M, Taşar GE, Fery H. *Deronectes taron* sp. n. from the eastern Anatolian region of Turkey (Coleoptera, Dytiscidae, Hydroporinae). Zootaxa. 2018; 4422 (2): 403-410.
[19] Darılmaz MC, Polat A, İncekara Ü. Faunistic study on aquatic Coleoptera of the Eastern Mediterranean Region of Turkey. Turk J Fish Aquat Sci. 2018; 19(5): 409-421.
[20] Erman ÖK, Taşar GE, Aykut M, Kurt K. First record of *Hydaticus histrio* Clark, 1864 (Coleoptera, Dytiscidae) from Turkey. Acta Biologica Turcica. 2018; 31(4): 174-177.
[21] Aykut M, Taşar GE. Contributions to the knowledge of Adephagan fauna in Adıyaman Province, Turkey (Coleoptera: Dytiscidae, Gyrinidae, Haliplidae and Noteridae). Mun Ent Zool. 2018; 13: 249-255
[22] Aykut M, Yıldırım İH, Tusun S, Fery H. *Deronectes kabilcevz* sp. n. and *D. propedoriae* sp. n. from south-eastern Anatolia (Turkey) (Coleoptera, Dytiscidae, Hydroporinae). Zootaxa. 2019; 4691 (1): 5-10.
[23] Aykut M, Taşar GE, Fery H. *Bidessus anatolicus adiyaman* ssp. n. from Adyaman province, southern Turkey (Coleoptera, Dytiscidae, Bidessini). Zootaxa. 2021; 5027(4): 563-575.
[24] Tuğluk ME, Özfidan T. 2022. Batman ili köy ve bağlı yerleşim birimleri yer adları üzerine bir değerlendirme. Hikmet-akademik edebiyat dergisi. 2022; 16: 464-487.